

ANALYSIS OF THE 2015 SAGAVANIRKTOK RIVER FLOOD: ASSOCIATED PERMAFROST DEGRADATION
USING INSAR AND CHANGE DETECTION TECHNIQUES

By

Mark Timothy McClernan, A.A., B.S.

A Thesis Submitted in Partial Fulfillment of the Requirements

for the Degree of

Master of Science

in

Geophysics

University of Alaska Fairbanks

August 2020

APPROVED:

Franz Meyer, Committee Chair

Simon Zwieback, Committee Member

Clifton Minter, Committee Member

Paul McCarthy, Chair

Department of Geosciences

Kinchel Doerner, Dean

College of Natural Science and Mathematics

Anupma Prakash, Provost and Executive Vice Chancellor

Abstract

In 2015, the Sagavanirktok River experienced a sequence of high, early-winter temperatures that lead to a buildup of aufeis. The buildup displaced the spring runoff causing widespread flooding. Flood waters inundated the surrounding tundra introducing heat into ground ice-baring soils. The Sagavanirktok River flood was caused by an extensive ice dam that developed the previous winter. The first flooding pulse started in April 2015, when an aufeis obstruction diverted river water to the surface. The obstruction caused flooding along 24 km of the Dalton Highway and its surroundings, necessitating a prolonged highway closure and emergency repairs. A second flooding pulse was caused by annual spring runoff in May 2015, which was driven by rapid snowmelt due to warm seasonal temperatures. The washed-out highway had to be closed again.

Field investigations showed that thermal erosion of ice wedges in the tundra adjacent to the Dalton Highway caused local subsidence by several meters. However, the full environmental impact of the flood has not yet been quantified regionally or temporally. Thermokarst formation, can cause rapid ecological and environmental changes. Thawing of permafrost can lead to terrain instability as the melting of ground ice induces subsidence and loss of soil strength. The processes involved in permafrost degradation are complex, as is predicting terrain stability and the associated impacts to permafrost surrounding infrastructure. The immediate impact of the 2015 Sagavanirktok River flood is evident, which caused rapid terrain collapse in the vicinity of the Dalton Highway and the Trans-Alaska Pipeline near Deadhorse, North Slope Borough, Alaska.

Thermal degradation of permafrost can be expressed as the change in the surface-microtopography over several years following a flood. Change detection, digital elevation model

differencing, and InSAR were employed within the area of interest to understand the extent of the flood and deformation within inundated areas. To determine the likely impacted areas within the area of interest and expanse of the flood, an unsupervised change detection technique of high resolution TerraSAR-X and Sentinel-1 amplitude images was utilized. The topographic deformation analysis to determine the motion on the ground surface used a short baseline subset InSAR analysis of Sentinel-1 data during the summer season following the Sagavanirktok River flooding events. Additional deformation analysis was conducted with ALOS-2 data for annual comparison of the 2015 to 2019 summers. TanDEM-X digital elevation model differencing compared surface models generated from before and after the Sagavanirktok River flood. Elevation model differencing would identify the absolute change between the acquisition time of the surface models. A joint data analysis between deformation and differenced elevation models analyzed the contrast within inundated and flood-unaffected areas; thus, the changes and impact to the permafrost following the 2015 Sagavanirktok River flood.

The Sagavanirktok River flood highlights the vulnerability of ice-rich permafrost to flooding. A change in the vicinity of the Sagavanirktok River Delta to the hydrological cycle led to widespread increases in terrain instability. Analysis of summer season deformation data suggested inundated permafrost areas showed lower seasonal deformation in years following the flood. Analysis of annual deformation shows permafrost subsidence intensified in inundated areas in the years following the flood. Digital elevation model differencing produced a statistically ambiguous result. This research illustrates the value of combining TerraSAR-X, TanDEM-X, Sentinel 1, and ALOS-2 microwave remote sensing missions for evaluating widespread surface changes in arctic environments. However, annual deformation data proved the most usable tool in observing the changing permafrost ecosystems around the Sagavanirktok River.

Table of Contents

	Page
<i>Abstract</i>	<i>iii</i>
<i>Table of Contents</i>	<i>v</i>
<i>List of Figures</i>	<i>vii</i>
<i>List of Tables</i>	<i>ix</i>
<i>List of Acronyms.....</i>	<i>x</i>
<i>Acknowledgments</i>	<i>xi</i>
<i>Chapter 1 Introduction.....</i>	<i>1</i>
1.1 Background	1
1.2 The 2015 Sag River Flood Event	3
1.3 Hypothesis	8
1.4 Organization	10
<i>Chapter 2 Overview of Study Area</i>	<i>11</i>
2.1 Area of Interest	11
2.2 Climate.....	12
2.3 Topography.....	14
2.4 Geomorphology	16
2.4.1 Permafrost	16
2.4.1.2 Brooks Range Foothills Permafrost.....	21
2.4.1.3 Massive Ground Ice	21
2.4.1.4 Segregated Ground Ice and Pore Ice	24
2.4.2 Permafrost Thaw-Related Landforms in the AOI.....	28
2.4.2.1 Ice Wedge Polygons.....	28
2.4.2.2 Thermokarst.....	30
2.4.3 Vegetation.....	30
2.5 Hydrology	31
2.6 Geologic Setting	31
2.7 Surficial Geology and Soils	36
<i>Chapter 3 Data and Methods.....</i>	<i>41</i>
3.1 Radar Imaging from Space	41
3.1.1 Overview of Synthetic Aperture Radar History	41
3.1.2 Radar and Synthetic Aperture Radar	43
3.1.3 Synthetic Aperture Radar Principles.....	45
3.1.4 SAR Image Characteristics, Geometry, and Speckle	45
3.1.5 Multilooking	49

3.2 Interferometric Synthetic Aperture Radar	50
3.2.1 Interferometric Synthetic Aperture Radar Principles	50
3.2.2 InSAR-based Topographic Mapping and Height of Ambiguity.....	53
3.2.3 Relative Terrain Motion: Differential Interferometry	54
3.2.4 Coherence	55
3.2.5 Atmospheric Effects and Other Error Sources.....	55
3.3 SAR Data Sets Used In This Thesis	56
3.3.1 Sentinel-1.....	56
3.3.2 ALOS-2.....	59
3.3.3 TerraSAR-X and TanDEM-X.....	61
3.3.4 Ancillary Data	62
3.4 Work flows.....	64
3.4.1 Pairwise Change Detection	64
3.4.2 Seasonal Short-Baseline InSAR	68
3.3.3 Multi-Year Short-Baseline Subset InSAR	77
3.4.4 DEM Differencing.....	80
3.4.5 Dataset Comparison and Analysis Approach.....	87
<i>Chapter 4 Results and Interpretation.....</i>	<i>89</i>
4.1 Results	89
4.1.1 Estimating Flood Water Inundation.....	89
4.1.2 Seasonal Surface Deformation Results	97
4.1.2.1 Summer 2017 Surface Deformation Results	97
4.1.2.2 Summer 2018 Surface Deformation Results	105
4.1.2.3 Summer 2019 Surface Deformation Results	112
4.1.3 Annual Surface Deformation Results	119
4.1.4 Summary DEM Differencing Results	132
4.2 Joint Data Analysis	135
4.2.1 Analysis of the Eastern Sag River Focus Area	135
4.2.2 Analysis of the Dalton Highway Channel Analysis Area	143
4.2.3 Analysis of the Sag River Eastern Terrace Focus Area.....	148
4.3 Interpretation of Data.....	154
<i>Chapter 5 Conclusions</i>	<i>157</i>
5.1 Change Detection Conclusions and Limitations.....	158
5.2 SBAS InSAR Deformation Conclusions and Limitations	159
5.3 DEM Differencing Conclusions and Limitations.....	160
5.4 Data Comparisons.....	161
5.5 Suggestions for Further Study	161
<i>References.....</i>	<i>165</i>

List of Figures

	Page
Figure 1.1: Regional map of the location of the AOI.....	2
Figure 1.2: Permit map of the winter 2014 seismic survey.....	5
Figure 2.1: General location map of the Sag River AOI.....	11
Figure 2.2: Ecoregion map of the State of Alaska.....	13
Figure 2.3: TanDEM-X elevation map of the Alaska Northern Slope and the AOI.....	15
Figure 2.4: Distributed stable soil temperatures of Alaska.....	17
Figure 2.5: Schematic temperature profile of permafrost terminology	18
Figure 2.6: Permafrost distribution in the State of Alaska	20
Figure 2.7: Diagram showing the evolution of ice wedges	23
Figure 2.8: Yedoma distributions in Alaska	25
Figure 2.9: General soil horizons of upper layers of permafrost.....	27
Figure 2.10: Ice volume of segregated ground ice and pore ice by geologic lithofacies and terrain	27
Figure 2.11: Schematic diagram of ice wedges and ice wedge polygon landscapes	29
Figure 2.12: Discharge plot of the Sag River from 2014 to 2019.....	32
Figure 2.13: Temperature plot showing the 2014-2015 winter temperatures.....	32
Figure 2.14: Cross-section and generalized geologic stratigraphy of the Alaska North Slope	33
Figure 2.15: Generalized stratigraphic column of the Alaska North Slope	34
Figure 2.16: Surficial Geologic Map of the Beachy Point Quadrangle used in this study	39
Figure 3.1: Geometry of the typical side-looking SAR imaging platform	44
Figure 3.2: Geometric distortions of SAR images and their relationship to the acquisition geometry	46
Figure 3.3: SAR image speckle	48
Figure 3.4: Geometry of spaceborne InSAR interferometry	52
Figure 3.5: Image showing the full swath of a Sentinel-1 interferometric wide-mode SAR.....	57
Figure 3.6: Processing method for change detection analysis.....	64
Figure 3.7: Processing method for SBAS InSAR analysis	70
Figure 3.8: Baseline plot of the 2017 summer SBAS InSAR data set.....	72
Figure 3.9: Baseline plot of the 2018 summer SBAS InSAR data set.....	73
Figure 3.10: Baseline plot of the 2019 summer SBAS InSAR data set.....	74
Figure 3.11: Points of interest of the Sag River Delta	75
Figure 3.12: Baseline plot of the annual, 2015-2019, annual InSAR data set	80

Figure 3.13: Processing flow diagram for absolute TDX DEM generation in GAMMA	81
Figure 3.14: Coherency derived water mask for DEM differencing.....	82
Figure 3.15: DLR TanDEM-X 12 m ² DEM used to reference topographic data.....	84
Figure 3.16: TanDEM-X 12 m ² pre-flood DEM used for DEM differencing.....	85
Figure 3.17: Focus areas for data comparison in inundated and flood-unaffected areas	88
Figure 4.1: Estimate of the first flood pulse from the 2015 Sag River Flood.....	90
Figure 4.2: Inset maps of the first flood pulse estimate from the 2015 Sag River Flood.....	92
Figure 4.3: Estimate of the second flood pulse from the 2015 Sag River Flood.....	93
Figure 4.4: Inset maps of the second flood pulse from the 2015 Sag River Flood.	95
Figure 4.5: Estimates of the first and second flood pulses and the common area covered by both	96
Figure 4.6: Inset maps showing estimates of both flood areas are outlined in Figure 4.5	97
Figure 4.7: Histogram of relative deformation of the AOI during summer 2017	98
Figure 4.8: Summer 2017 subsidence and master amplitude image.....	99
Figure 4.9: Seasonal 2017 summer subsidence.....	100
Figure 4.10: Inset maps showing estimates of 2017 summer season deformation	102
Figure 4.11: Plot showing the deformation within selected locations for the 2017 summer season	103
Figure 4.12: Histogram of relative deformation of the AOI during summer 2018	105
Figure 4.13: Summer 2017 subsidence and master amplitude image.....	107
Figure 4.14: Seasonal 2018 summer subsidence.....	108
Figure 4.15: Inset maps showing estimates of summer 2018 season deformation	109
Figure 4.16: Plot showing the deformation at several locations for the 2018 summer season.....	110
Figure 4.17: Histogram of relative deformation of the AOI during summer 2019	112
Figure 4.18: Summer 2019 subsidence and master amplitude image.....	114
Figure 4.19: Seasonal 2019 summer subsidence.....	115
Figure 4.20: Inset maps showing estimates of the summer 2019 season deformation	116
Figure 4.21: Plot showing the deformation at POI locations for the 2019 summer season	117
Figure 4.22: Histogram of cumulative annual relative deformation of the AOI	120
Figure 4.23: ALOS-2 cumulative deformation for the 2015-2019 period	121
Figure 4.24: ALOS-2 Cumulative Annual subsidence from 2015 to 2019 with insets	122
Figure 4.25: Inset maps showing estimates of ALOS-2 cumulative annual deformation	123
Figure 4.26: Histogram of high-pass filtered cumulative annual relative deformation of the AOI	126
Figure 4.27: ALOS-2 Gaussian high-pass filtered annual deformation	127

Figure 4.28: ALOS-2 Gaussian high-pass filtered annual deformation with insets	128
Figure 4.29: Inset maps showing estimates of high-pass filtered ALOS-2 annual deformation.....	130
Figure 4.30: ALOS-2 cumulative annual deformation of unique structures.....	131
Figure 4.31: Plot showing the deformation of POI locations within the AOI	132
Figure 4.32: Preflood - May 27, 2015 DDEM.....	134
Figure 4.33: Pre-flood - June 21, 2015 DDEM	136
Figure 4.34: June 21, 2015 - December 5,2016 DDEM.	137
Figure 4.35: December 5,2016 - February 2017 DDEM	138
Figure 4.36: Location of the eastern channel focus area and abandoned floodplain	139
Figure 4.37: Averaged time series of deformation of abandoned floodplain	141
Figure 4.38: Distribution of a TDX DDEM of the pre-flood average DEM and the June 21, 2015 DEM...	143
Figure 4.39: Location of the Dalton Highway focus area and analyzed geologic formation.....	144
Figure 4.40: Averaged time series of deformation of alluvial terraces west of the Dalton Highway.....	146
Figure 4.41: Data distribution of three TDX DDEMs within the Dalton Highway focus area	148
Figure 4.42: Location of the Sag River western terrace focus area and analyzed geologic formation....	150
Figure 4.43: Averaged time series of deformation of the Sag River western terrace focus area	151
Figure 4.44: Distribution of two TDX DDEMs sampling the Sag River western terrace focus area	153

List of Tables

	Page
Table 1.1: Timeline of the Sag River flood recorded by ADOT&PF	6
Table 1.2: Summary of the data analyses utilized	9
Table 2.1: Summary of geologic facies and lithologic descriptions of the Beachy Point Quadrangle	38
Table 3.1: List of major SAR development innovations and highlights.....	42
Table 3.2: List of available SAR scenes utilized in the change detection analysis	58
Table 3.3: List of scenes utilized in InSAR analysis.....	60
Table 3.4: List of TDX Scenes utilized for DEM generation	63
Table 3.5: Summary of the surficial geology at points of interest in the AOI	76
Table 4.1: Summary of observations recorded in each of the focus areas	154

List of Acronyms

ASF	Alaska Satellite Facility	IW	Interferometric Wide
ADOT&PF	Alaska Department of Transportation and Public Facilities	JAXA	Japan Aerospace Exploration Agency
AOI	Area of Interest	JPL	Jet Propulsion Lab
ALOS-2	Advanced Land Observing Satellite-2	NOAA	National Oceanic and Atmospheric Administration
cfs	cubic feet per second	NASA	National Aeronautics and Space Administration
CoSSc	Coregistered Single Look Slant Range Complex	POI	Point of interest
DAAC	Distributed Active Archive Center	RAR	Real Aperture Radar
DEM	Digital Elevation Model	RC	radiometrically corrected
DDEM	Differenced DEM	S1	Sentinel-1
DLR	German Aerospace Center	Sag	Sagavanirktok
EEC	enhanced ellipsoid corrected	SAR	Synthetic Aperture Radar
ESA	European Space Agency	SBAS	Short Baseline Subset
ERS	European Space Agency Radar Satellite	SLC	Single Look Complex
EW	Extra-wide swath	SRTM	Shuttle Radar Topography Mission
GC	Geometrically corrected	TDX	TanDEM-X: TerraSAR-X add-on for Digital Elevation Measurement
GDAL	Geospatial Data Abstraction Library	TOPS	Terrain Observation with Progressive Scan
GIAnt	Generic InSAR Analysis Toolbox	TSX	TerraSAR-X
H	Horizontal	UAF	University of Alaska, Fairbanks
HoA	Height of Ambiguity	USD	United States Dollar
HH	Horizontal Transmit and Receive	USGS	United States Geological Survey
HyP3	Hybrid Pluggable Processing Pipeline	VH	Vertical transmit and Horizontal Receive
InSAR	Interferometric Synthetic Aperture Radar	V	Vertical
		VV	Vertical Transmit and Receive

Acknowledgments

Thanks to the Geomatics Office of the National Geospatial-Intelligence Agency for continued funding and financial support in completion of this project. I thank GeoNorth Information Systems for retasking of the TerraSAR-X satellite and for providing data and support for this project. German Aerospace Center, (DLR) provided access to TanDEM-X DEM and CoSSc data under permits XTI_GEOS7449 and DEM_GEOL2889 and is appreciated. Special thanks to Franz Meyer, Simon Zwieback, and Clifton Minter for support and guidance and providing this project in an expedited timeframe. Special thanks friends, family, and the anonymous reviewers who helped complete the thesis writing. It was greatly appreciated.

This page was intentionally left blank.

Chapter 1 Introduction

1.1 Background

The Sagavanirktok (Sag) River is located on the Alaska North Slope, an Arctic region underlain by continuous permafrost (Figure 1.1). In 2015, the Sag River experienced a sequence of environmental conditions that led to flooding. These conditions included high, early-winter temperatures and aufeis (from the German word meaning sheet or planar ice) build up, which resulted in the early arrival of spring breakup (river ice breakup). The warm temperatures caused thaw, generating aufeis. Under the right conditions, aufeis can form significant blockages in river channels. A buildup of aufeis blocked large portions of the Sag River, which displaced the early spring runoff causing widespread flooding. Warm flood waters inundated the surrounding permafrost and introduced thermal energy into the soil resulting in thaw of the ground ice in the active layer. The full environmental impact of the flood, to date, has not been studied in detail. This research attempts to quantify the regional impact using multiple remote sensing methods.

Ice wedges are the most widespread form of massive ground ice in north polar regions. Ice wedge melting, or thermokarst formation, can cause rapid ecological and environmental changes (Alaska Division of Homeland Security & Emergency Management, 2018). These changes can include differences in soil chemistries, vegetation diversity, groundwater movement, and widespread topographical variations. Flood waters can transfer thermal energy to the ground, which can lead to degradation of permafrost and result in changes in the overlying microtopography (Shur, 1988; Abolt, et al., 2015).

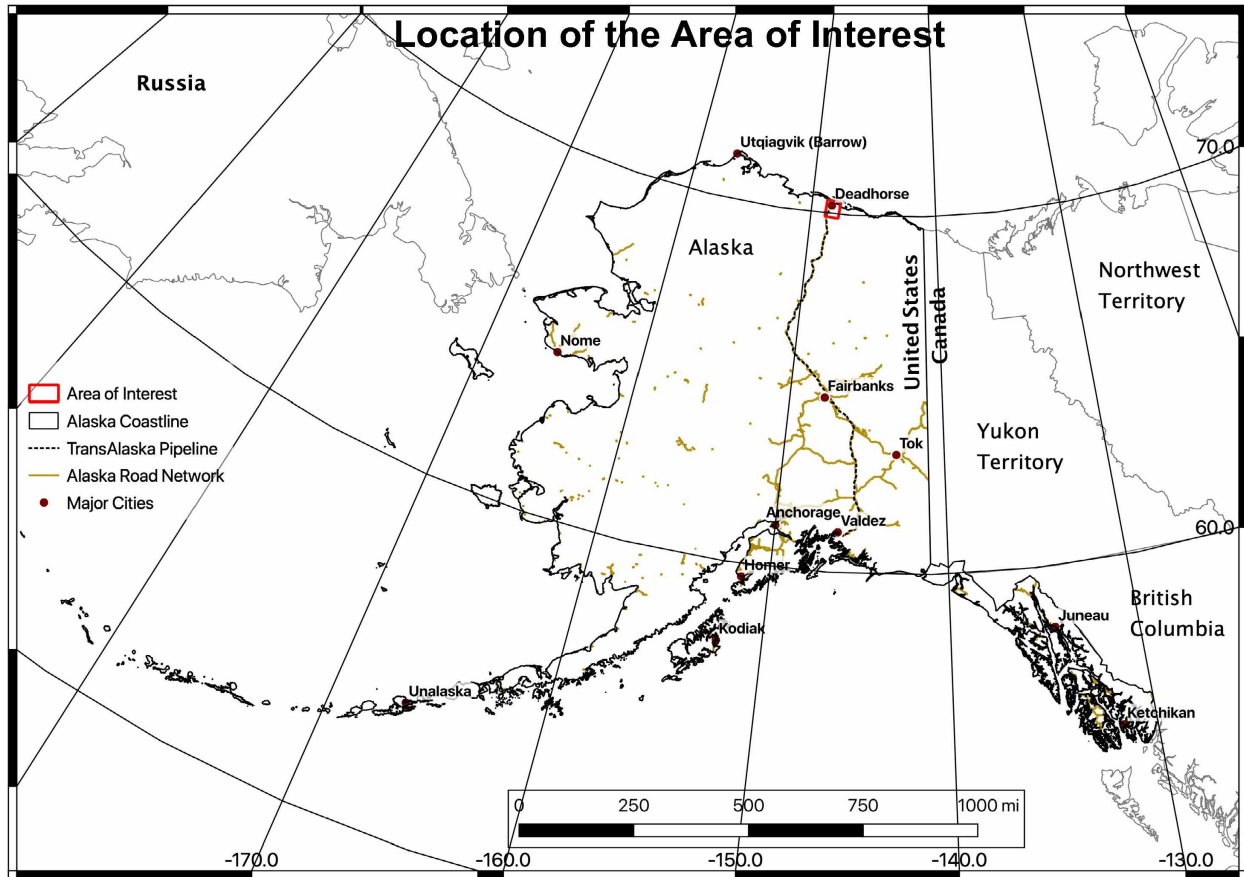


Figure 1.1: Regional map of the location of the AOI. AOI shown in red. TransAlaska Pipeline dashed in black. Alaska extended road network shown in gold. The Dalton Highway extends from Fairbanks to Deadhorse, Alaska.

To understand the timing of impacts and deformation within the Area of Interest (AOI), three analytical methods were utilized to evaluate the surface change: change detection; deformation analysis; and Digital Elevation Model (DEM) differencing. The AOI is spatially confined to the permafrost environments near the Sag River watershed. To determine the flood-impacted areas within the AOI and map the expanse of the flood, an unsupervised multiscale change detection approach supported with high resolution TerraSAR-X (TSX) and TanDEM-X (TDX) Synthetic Aperture Radar (SAR) amplitude imagery was utilized. The deformation analyses included: 1) a Short Baseline Subset (SBAS) Distributed Scatters Interferometric SAR (InSAR) analysis of Sentinel-1 (S1) Single Look Complex (SLC) data for each of the 2017, 2018, and 2019 summers, and 2) an SBAS InSAR analysis using Advanced Land Observing

Satellite 2 (ALOS-2) SLC data comparing the 2015 through 2019, summers sampled annually. DEM differencing compared TDX DEMs before and after the flood event. The Sag River Delta is home to Prudhoe Bay, a highly active oil field since the 1960s. The Sag River flood posed a significant risk to large oil industry infrastructure and ongoing operations.

This thesis intends to understand the regional expanse and subsequent temporal impacts of the 2015 Sag River flood on the regional permafrost environment.

1.2 The 2015 Sag River Flood Event

Aufeis is ice that crystalizes within the river channel or along the floodplain from consecutive water overflows during subfreezing temperatures (Wanty et al., 2007). Aufeis formation is a significant river hazard for the Alaska North Slope and can become a complicated problem to mitigate in permafrost regions (Shur et al., 2015). River flooding can be expected in areas where there is a buildup of aufeis. Aufeis formation is a common phenomenon occurring in arctic braided rivers. One way aufeis forms is from upwelling flow collecting behind river icing that induces further icing upstream (Zufelt and Daly, 2006). Aufeis also forms as a result of ground-water discharge into stream channels along river shorelines near springs. Ice formation occludes river discharge, perturbing the steady-state condition, and causing an incremental rise in the hydrologic head until discharge continues above the previously formed ice (Wanty et al., 2007). While natural channel levees normally contain the flooding, ice jams or thick accumulations of aufeis generated during cold winters can result in an almost total channel blockage within the river's path (Zufelt and Daly, 2012). The following paragraphs provide an overview of the 2015 Sag River flooding events in more detail. Table 1.1 summarizes the timeline of the 2015 Sag River flooding events recorded by the Alaska Department of Transportation and Public Facilities (ADOT&PF), which attempted to minimize the flooding impact to keep the Dalton Highway open.

Aufeis formation is a natural phenomenon common in arctic regions or induced by human activity with the right environmental conditions (Wilkins, 2004). During the 2014 winter oil exploration season, prior to the floods, a seismic shoot was conducted distal to the Sag River Delta channel apex (Table 1.1) (Figure 1.2) (Alaska Department of Natural Resources, 2014). Temporary roads were constructed across the Sag River to allow heavy equipment access along select river crossings. Winter access roads are typically temporary ice roads that are poured in place. During road construction, snow is compacted or removed. Snow acts as a natural insulation barrier, and its removal releases heat from the soil. Removal of heat from the soil lowers the temperature of the ground, forcing deep freezing. Increased frost in the soil can displace water flowing in delta regions, increasing the chance for overflows (Shur et al., 2015). Any winter river flow under the Sag River surface ice can be naturally obstructed, but the ice road increased the probability of overflows. The actual effect of the seismic survey on the extent of the Sag River flood was debated among cold-climate civil engineers and is not yet quantified and documented (Shur et al., 2015).

The 2015 Sag River flood was exacerbated by a sequence of heavy snowfall and high temperatures that created extensive aufeis that expanded for miles (Ajadi, 2017). Late February through early March 2015 experienced warmer temperatures than normal (Toniolo, 2017). Warm periods have been attributed to increased soil pore pressures and subsequent formation of aufeis even when temperatures remain below freezing (Kane, 1981). The abnormal winter warmth in 2015 coincided with river overflows, intensifying the formation of aufeis (Toniolo, 2017). Weather records, showed precipitation during the 2014-2015 winter was above average (Toniolo, 2017). The increased precipitation during winter was frozen and stored in the upper drainage basin until an early spring brought warm temperatures. The increased temperatures caused early spring runoff into the Sag River while widespread aufeis was still present in the delta region (Toniolo, 2017).

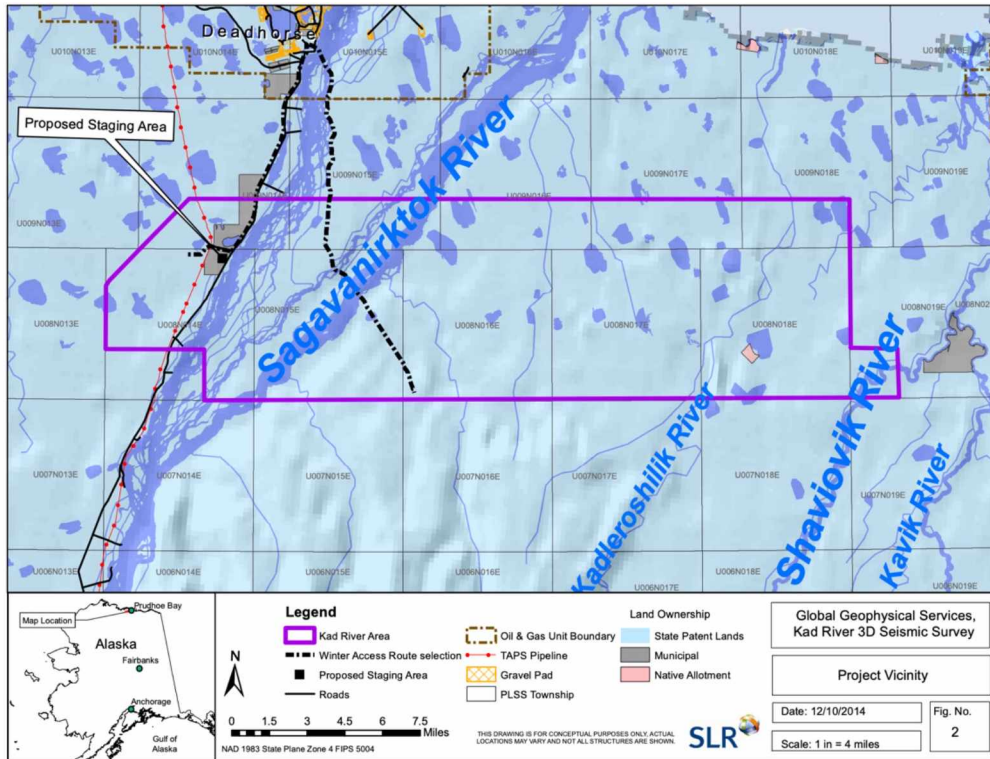


Figure 1.2: Permit map of the winter 2014 seismic survey. From Alaska permit MLUPNS 14-007.

The first flooding pulse of the 2015 Sag River flooding events was initially recorded in late March, 2015 by ADOT&PF, who attempted to minimize Sag River overflows on the Dalton Highway (Table 1.1). The Dalton Highway is a 644-km haul road connecting the Prudhoe Bay oilfield to the Alaskan Highway System beginning just north of Fairbanks, Alaska (Figure 1.1). The Dalton Highway supports the oil industry by providing a transportation route for maintenance, workers, and drilling supplies (Toniolo, 2017). The first flooding pulse was caused by winter overflows (Shur et al., 2015; Toniolo, 2017). The overflows submerged the Dalton Highway in excess of one meter. The first flood was challenging to mitigate as refrozen overflow created a solid barrier on the highway. Overflows began to block traffic on the highway in early April, resulting in two closures of the highway and a disaster declaration issued by Governor Bill Walker. April 11, 2015, ADOT&PF mobilized an emergency response campaign constructing snow dams along the side of the highway and digging canals to redirect water to

Table 1.1: Timeline of the Sag River flood recorded by the Alaska Department of Transportation and Public Facilities (ADOT&PF) (Alaska Department of Transportation and Public Facilities, 2015).

2015 Sagavanirktok River Flood Timeline and Response	
Existing Circumstances	
Fall 2014	Heavy rain events in the Brooks Range.
Winter 2014-2015	Higher than normal precipitation in the upper Sag River watershed. Winter overflows of water reached the surface.
ADOT&PF Log of the First Flooding Event	
Mar 20, 2015	Highway milepost 396-405 – ADOT&PF begins working with Alyeska Pipeline Service Company to minimize overflow from the Sag River. The river was overflowing the highway in eight locations. The largest overflow was 1/3 meter deep above the road grade and 60 meters long.
Mar 30, 2015	Mitigation efforts continued until storm forced repair work to cease.
Mar 30-Apr 4, 2015	Overnight closure March 30 due to storm. The Highway was reduced to one lane with traffic control through April 4.
Apr 5, 2015	Aufeis formation caused flooding and prolonged closure of the highway, south of Deadhorse, Alaska.
Apr 5, 2015	Over 1,100 haul trucks backlogged behind the flooded region resulted in an emergency response from the ADOT&PF.
Apr 7, 2015	Alaska State Governor Walker declares state disaster.
Apr 8, 2015	Defense industry response, Geonorth LLC responded to the flooding event providing radar images of the damaged and flood impacted regions to ADOT&PF.
Apr 11, 2015	Crews begin work to dig canals to divert water and reinforce berms along the road.
Apr 12-Apr 13, 2015	Highway reopens one lane to limited, pre-authorized traffic.
Apr 14, 2015	Trenching operations intercept and divert water away from the road.
Apr 14-Apr 28, 2015	The Dalton Highway fully reopens to all loads.
ADOT&PF Log of the Second Flooding Event	
May 5, 2015	Warmer temperatures start to melt snow and ice on the road.
May 5-May17, 2015	Spring river breakup arrives with another round of aufeis flooding.
May 17, 2015	The Dalton Highway is closed. Overflow of the highway exceeds one meter in one location.
May 21, 2015	Flooding reaches Deadhorse, Alaska. Governor Walker declares second state disaster.
May 24-May 25, 2015	Water level begins to recede substantially, near mile marker 394.
May 28, 2015	Water level returns to almost normal levels. ADOT&PF repair work begins.
June 5, 2015	The road repaired and reopened to all traffic.

flow downriver instead of over the highway (Table 1.1) (Alaska Department of Transportation and Public Facilities, 2015). The highway reopened on April 14, 2015 and remained open until April 28, 2015 (Table 1.1).

The second flooding pulse, occurring on May 5, 2015, covered a greater area than the previous flood (Table 1.1). This second flood pulse was caused by higher than normal temperatures, resulting in early spring runoff in the upper Sag River watershed (Table 1.1) (Shur et al., 2015; Toniolo, 2017). High, early season flow reached the lower delta and was displaced by widespread aufeis that had formed during the 2014-2015 winter and first flooding event. At peak flow, the flood inundated a 38-km length of the Dalton Highway and caused a 13-day closure from May 17 to May 28, 2015. On May 21, 2015, a second state disaster declaration was issued by Governor Walker when the flooding reached the town of Deadhorse, Alaska (Table 1.1). The water level dramatically receded on May 24, 2015 and by May 28, 2015, and had returned to almost normal levels. The Dalton Highway was heavily damaged. ADOT&PF made initial repairs to the road, but, in 2016, ADOT&PF reconstructed and raised the road to mitigate recurrent flooding (Alaska Department of Transportation and Public Facilities, 2015).

The two flooding events cost the State of Alaska approximately \$17M USD in emergency construction funds and disrupted the oil and gas industry on the Alaska North Slope. (Coffey, 2018). While economic effects were calculable, the impact of the 2015 Sag River flood on the permafrost environment remained difficult to quantify. The tundra and underlying permafrost are temperature-sensitive environments that thaw and degrade with higher surface temperatures. The flooding introduced water into the permafrost region adjacent to the river. The consequences of these floods have produced soil stability issues and, in select eroded locations, have resulted in complete thawing of ice wedges and slope failure at several study sites (Shur et al., 2015). The floodwaters introduced

thermal energy over a broad area of tundra surrounding the Sag River. Thawing of permafrost can lead to widespread change in the hydrologic cycle, including variable changes in water storage and changes to the surface topography (Walvoord et al., 2016). This thesis study investigated the regional impact of the flood on the ground ice by analyzing the topographic deformation in areas inundated by the flood.

1.3 Hypothesis

The objective of this thesis is to characterize the impact of both flooding events on the permafrost of the Sag River lower watershed. SAR was used for its ability to detect small shifts in signal phase. These shifts can indicate changes in topographic height of the ground with high precision (McCandless and Jackson, 2004; Woodhouse, 2015). Additionally, SAR is daylight independent, ensuring accurate data acquisition when the satellite passes over the AOI (McCandless and Jackson, 2004; Woodhouse, 2015). SAR is an active source imaging platform and has the intrinsic capability of consistent monitoring, independent of cloud cover or weather conditions (McCandless and Jackson, 2004; Woodhouse, 2015). Phase and amplitude data are returned with each image acquisition providing powerful information for observing Earth's topography and deformation (Woodhouse, 2015). As such, analysis with SAR is a compelling option for quantifying and studying the regional permafrost deformation impacted by the 2015 Sag River flood.

This study centers on the following question: *What was the response of the Sag River Delta region after the 2015 flooding in terms of deformation and topographic change?*

To answer this question, this thesis analyzed the response of deformation and topographic change within specific inundated and flood-unaffected focus areas. To mitigate contributing factors, it was assumed that additional systematic difference prior or after the flood. A combination of data

sourced from TSX and TDX, S1, and ALOS-2 satellites were utilized to understand permafrost and ground ice degradation on the Alaska North Slope. The AOI contains a high degree of heterogeneity. A joint data analysis between each data set was conducted in focus areas selected based on homogeneity and similarity of environments to minimize the effect of the variable environment. The joint data analysis accompanied the mean deformations within inundated and flood unaffected areas with the goal of determining differences. Ideally this comparison would be able to show a difference between inundated and flood-unaffected areas; however, there is a high degree of variability and existing permafrost degradation already present in the AOI. This thesis investigated the following four methods to understand the regional disturbance and temporal deformation (Table 1.2).

Table 1.2: Summary of the data analyses utilized.

<i>Analysis</i>	<i>Method</i>
Change detection to track the progression and total accumulation areas of ice and water during the 2015 Sag River flood to determine impacted areas using high resolution TSX, TDX, and S1 SAR georeferenced amplitude imagery.	Time series change detection and image classification (Ajadi et al., 2019)
SBAS InSAR analysis using S1 SAR SLC data to understand the seasonal permafrost subsidence and changes in the active layer.	SBAS InSAR (Berardino et al., 2002; Agram et al., 2012).
An SBAS InSAR analysis of ALOS-2 SAR SLC data imagery to understand the annual deformation within the region.	SBAS InSAR (Berardino et al., 2002; Agram et al., 2012).
DEM differencing of temporal TDX DEMs to understand the seasonal and yearly topographic change throughout the time series. Differential InSAR methods of TDX data will be utilized to generate the multi-temporal DEMs.	Differenced DEMs generated from InSAR techniques (Werner et al., 2000).

First, flood inundated areas were identified using TSX, TDX and S1 amplitude images using change detection to identify areas that are most likely to have been impacted (Table 1.2). Second, deformation was investigated for the summer season, with S1 SLC data to monitor the seasonal active layer thaw of the permafrost (Table 1.2). Seasonal deformation was investigated to determine if areas affected by flooding experienced change in their summer thaw behavior. Third, annual subsidence was

evaluated to understand the time topography change associated with the flooding event. The annual subsidence analysis utilizes ALOS-2 SLC data (Table 1.2). Fourth, analysis of topographic change was conducted just before and just after the flood using Digital Elevation Model (DEM) differencing.

1.4 Organization

The thesis is organized in five chapters. Chapter 1 describes the 2015 Sag River flooding event and the motivation for this study along with the study question, goals, and objectives of this research. Chapter 2 discusses the AOI including its geologic, geomorphologic, and hydrological setting. Chapter 3 provides details on the data sets used, outlines the workflow, and explains the methods used to meet the research objectives. Chapter 4 presents results and discusses interpretations based on relevant scenarios. Chapter 5 discusses conclusions and limitations of the study along with recommendations for future work.

Chapter 2 Overview of Study Area

2.1 Area of Interest

This study focused on the Sag River Delta area. The AOI is confined from the Sag River Delta channel apex in the south to the Arctic Ocean in the north (Figure 2.1). To capture the full spatial extent of the two flood pulses, the AOI is limited to the Kuparuk River in the west and the Kadleroshilik River in the east. This delineation gives the AOI complete coverage of the Lower Sag River watershed. The Sag River Delta is located north of the Brooks Range in the geographical center of the North Slope Borough near the town of Deadhorse, Alaska and the Prudhoe Bay oilfield (Figure 2.1). The red box in Figures 1.1 and 2.1 outlines the AOI and is bounded between points 70.38016183°N, -148.78084222°W in the northwest and 69.88176430°N, -147.80006924°W in the southeast.

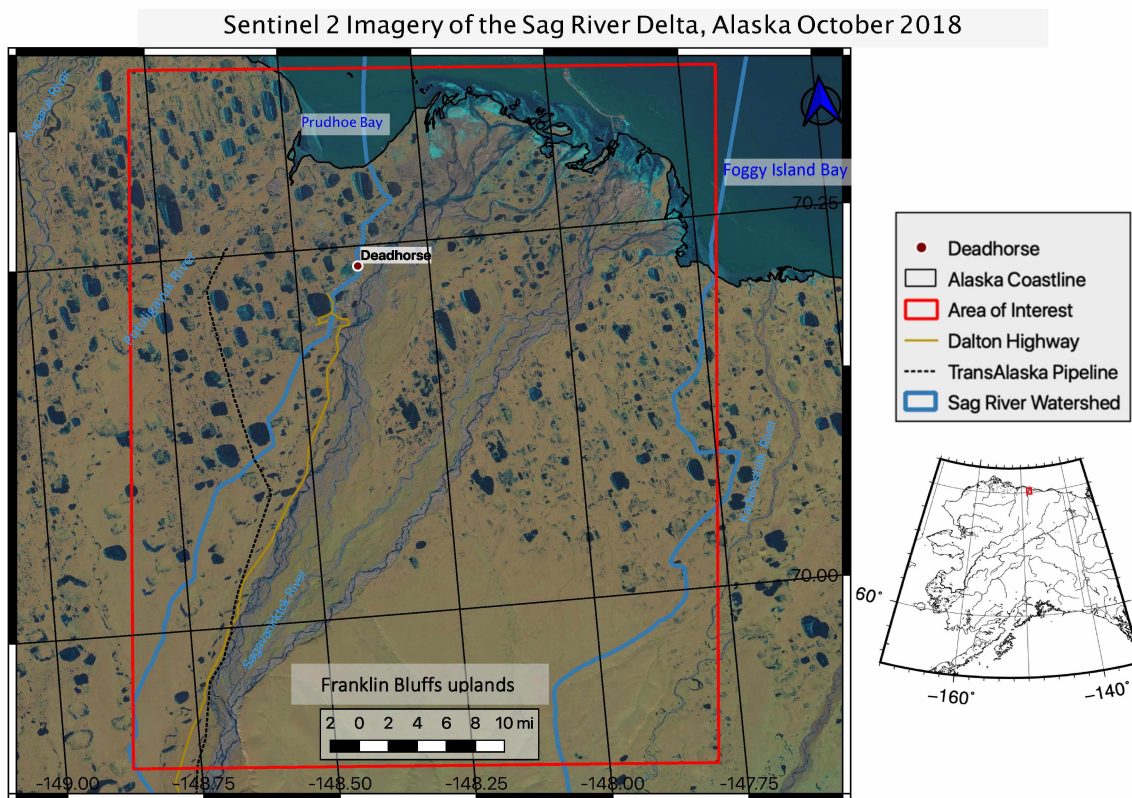


Figure 2.1: General location map of the Sag River AOI. Background shows October 4, 2018 Sentinel 2 imagery of the Sag River Delta. Data displayed in Alaska Albers Projection. Coordinate system grid shown in WGS84.

The Sag River is the most accessible river in the Alaska Northern Slope and has several environmental monitoring stations installed along its path. A majority of these monitoring stations were installed by the ADOT&PF and the University of Alaska, Fairbanks (UAF) after the 2015 Sag River flood. The most commonly referenced weather/temperature station utilized in peer-reviewed scientific papers is the UAF Franklin Bluff Station (Toniolo, 2017), located just outside of the AOI, south of the Sag River Delta at coordinates 69.7167° N, 148.6833° W. Additionally, the U.S. Geological Survey (USGS), has a stream gage station (Gage ID: 159080000) along the Sag River at the TransAlaska Pipeline pump station 3, south of the AOI (Federal Priority Streamgage Program; 2019). To characterize the long-term impact of flooding on the lower Sag River, this study included the extended watershed of the Sag River from the delta distributary channel apex to the terminus of the delta (red boundary in Figure 1.1 and 2.1).

2.2 Climate

Alaska contains 32 unique ecoregions (Figure 2.2). These regions are defined by large areas of land with vegetation and species diversity that share ecological similarities (Feirer, 2004). The Sag River watershed flows through three ecoregions: 1) Beaufort Arctic Coastal Plain; 2) Brooks Range Foothills; and 3) Brooks Range Highlands (Kane, 2014; Toniolo, 2017). Although the Sag River watershed is contained within these three ecoregions, this study focuses on the delta region, contained in the Beaufort Coastal Plain and adjacent to the Brooks Range Foothills within the AOI (Figure 2.1).

The Beaufort Coastal Plain is a treeless, windswept terrain that extends across the northern coast of Alaska into the Yukon Territory (Figure 2.2) (Feirer, 2004). This ecoregion is characterized by an abundance of lakes, wetlands, and permafrost-related features. The coastal plain gradually ascends from the Arctic Ocean into the southern Brooks Range Foothills (Figure 2.3). The general drainage pattern of the Sag River is subparallel braided river channels that flow northward to the Arctic Ocean

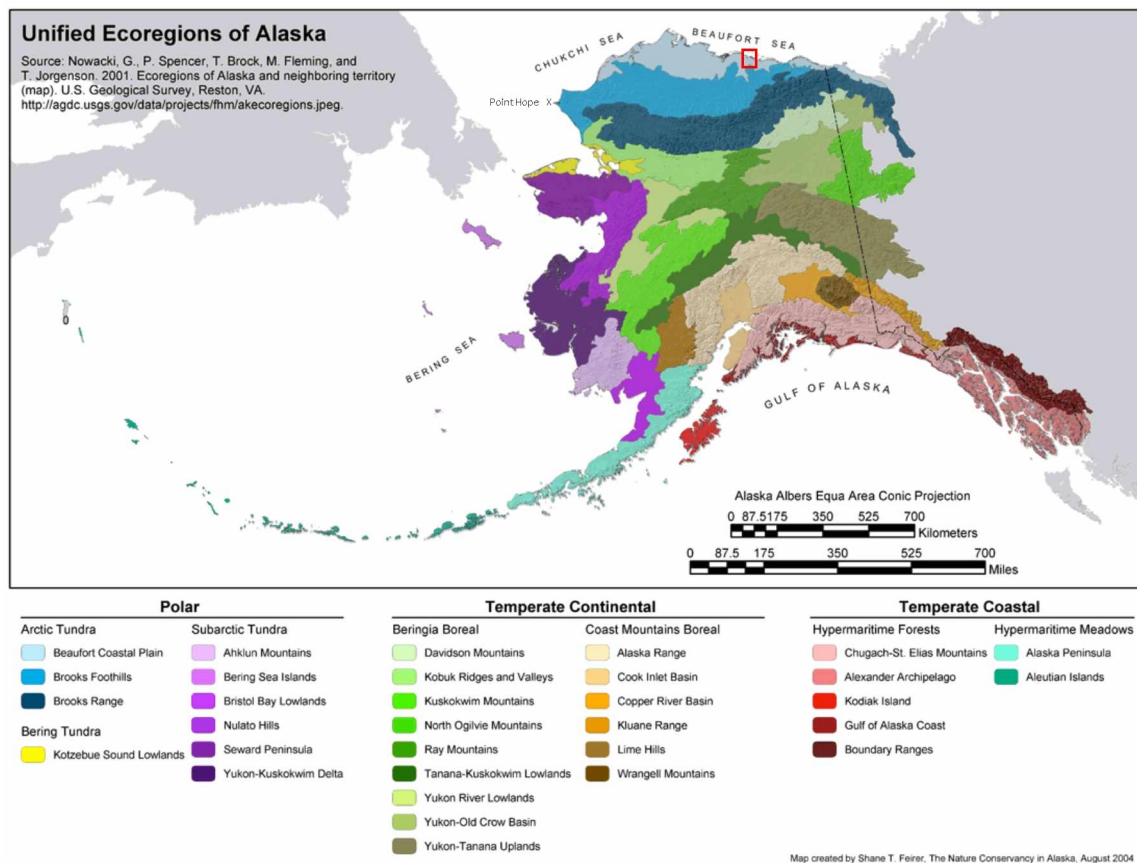


Figure 2.2: Ecoregion map of the State of Alaska. The AOI, red outline, contains the Beaufort Coastal Plain and an exposure of the Brooks Range Foothills (From Feirer, 2004).

(Bolin, 1959). Smaller streams dry up or freeze solid in the winter. Thousands of shallow rectangular lakes cover the lowland landscape, up to 50% of exposed surface area (Figure 2.1) (Hodel, 1986; Feirer, 2004). The presence of oversaturated soils, up to 82% by surface area, gives the coastal plain its classification as a wetland. Precipitation along the coastal plain is generally low at 10 to 15 cm annually (Figure 2.1) (Hodel, 1986; Feirer, 2004). Most precipitation occurs during the winter in the form of snow (Feirer, 2004). The average annual winter temperature ranges from -30°C to -20°C, and summer temperature averages 8°C (Gallant et al., 1995).

The southeastern portion of the study contains a small exposure of the Brooks Range Foothills that steps down into the AOI (Figures 2.1, 2.2, and 2.3). This ecoregion spans from Point Hope, Alaska to just west of the U.S.-Canadian border (Figure 2.2). The Brooks Range Foothills have a broad rolling hill expression. Generally, the foothills exhibit tight ridges, buttes, and mesas separated by alluvial valleys and glacial valleys (Feirer, 2004). Lakes and ponds are uncommon in this ecoregion. Rivers typically have multiple defined incised channels that are notable when compared to the coastal plains (Gallant et al., 1995). Rivers in northern Alaska generally flow northward, from the Brooks Range across the foothills to lower elevations (Figure 2.2) (Gallant et al., 1995). Many of the rivers freeze to their base in the winter and form aufeis. Aufeis deposits may last into the late summer (Feirer, 2004). The climate is a dry polar desert which is typically warmer and more humid than in the Beaufort Coastal Plain and the Brooks Range ecoregions (Feirer, 2004). The average annual precipitation ranges from 15 cm to 25 cm. Average winter temperatures range between -28°C and -20°C. Summer temperatures range between 0.5°C and 13°C. Freezing can occur at any time of the year, but the mid-summer period of July and August are mostly frost free (Hodel, 1986; Gallant et al., 1995).

2.3 Topography

The topography within the AOI is signified by the same ecological regions listed in Section 2.2, consisting of the Beaufort Coastal Plain, the Brooks Range Foothills, and the Brooks Range. The Beaufort Coastal Plain is relatively flat, with typical ground slopes less than 1° gradient. The land rises from the Arctic Ocean to the Brooks Range Foothills at approximately 182 meters above sea level (Figures 2.2 and 2.3) (Rawlinson, 1993; Gallant et al., 1995). The Beaufort Coastal Plain is generally described as a broad wedge landmass that narrows to the north. This wedge contains mesas, rolling hills, and anticlines in the south, then becomes relatively flat in the northern regions (Figure 2.3) (Rawlinson, 1993; Gallant et al., 1995). Large rectangular lakes are visible throughout the ecoregion (Gallant et al., 1995; Feirer, 2004).

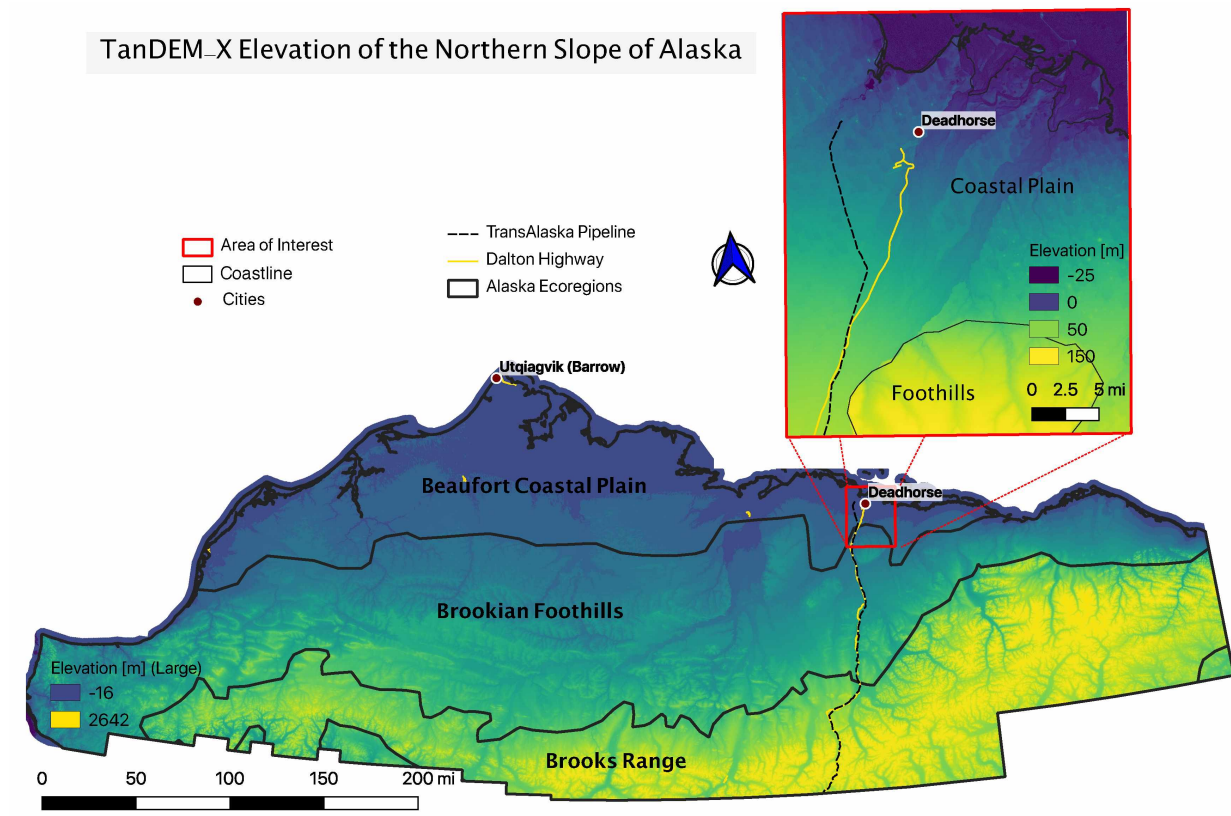


Figure 2.3: TanDEM-X elevation map of the Alaska Northern Slope and the AOI. Lower map shows the 90 m² resolution elevation data of the North Slope Borough. The inset map shows the 12 m² resolution TDX elevation data. Relevant Alaskan ecoregion zones are labeled on both maps.

These lakes are typically 1 meter to meter in depth (Gallant et al., 1995). Many of these lakes have characteristically steep shorelines, reaching 9 meters from rim edge to lake base (Pelletier et al., 2018). Shorelines are susceptible to slumping and slope failure (Pelletier et al., 2018). Permafrost related features dominate the terrain and isolated pingos rise from the ground up to 70 meters (Gallant et al., 1995). Sparse sand dunes also form along the coastline (Feirer, 2004).

The Sag River is headwatered in the Brooks Range. The Sag River continues north across the Brooks Range Foothills. The foothills are divided into northern and southern sections based on geography and geology (Gallant et al., 1995). Elevations of the southern Brooks Range Foothills section

closest to the Brooks Range are typically less than 810 meters above sea level (Figures 2.2 and 2.3). Typical ground slope averages between 0° and 5° gradient. The topography contains many high relief mesas, irregular buttes, and long ridges with intermixed plateaus and plains (Gallant et al., 1995). Elevations in the northern section of the Brooks Range Foothills are less than 60 meters. The Brooks Range Foothills terrain is hilly, consisting of broad east-west trending ridges. Mesa-like uplands are also prominent throughout the landscape (Gallant et al., 1995). The topography of the Brooks Range to the south is mountainous. The Brooks Range ecoregion lies outside the AOI.

The topography within the AOI (Figures 2.1 and Figure 2.3) shows a clear distinction between the Brooks Range Foothills and the Beaufort Coastal Plain. The Brooks Range Foothills have a maximum height of 152 meters above sea level within the AOI. The Beaufort Foothills quickly descend into the coastal plain. The Beaufort Coastal Plain in the AOI has a minimum elevation of 0 meters at sea level and a maximum elevation of 62 meters in the foothills (Figure 2.3). The boundary between an extension of foothills and the coastal plain in the AOI shows a cliff with relief ranging from 27 meters to 64 meters. The Sag River trifurcates into three primary braided channels in the delta region. The broad channels have depths of 3 to 8 meters. The deepest sections in the river channel are confined to isolated depressions that are significantly deeper than the natural flowline gradient of the channel (Figure 2.3).

2.4 Geomorphology

2.4.1 Permafrost

The ground (rock, soil, and ice) is classified as permafrost once it remains below 0°C in place for at least two years (Permafrost Subcommittee, 1988). The shallowest layer, known as the active layer, is defined as the top layer of ground subject to annual thawing and freezing in an area underlain by permafrost (Permafrost Subcommittee, 1988). Below the active layer lies the permafrost table, a

temperature-defined horizon or upper boundary of the permafrost (Permafrost Subcommittee, 1988).

Taliks, unfrozen waterbodies, may also lie below the active layer.

Frozen ground can be either seasonal or perennial. The difference between seasonal and perennial frost is seasonal frost thaws in summer. Seasonal freezing in areas without permafrost involves one-sided freezing from the surface downward. Seasonal freezing within permafrost areas is often two-sided, from the subsurface perennial frost and surface (French and Shur, 2010). In general, mean annual temperature of permafrost in its stable thermal state is lowest at the permafrost table and increases with the depth of the local geothermal gradient (French and Shur, 2010). Stable average ground temperatures for Alaska are shown in Figure 2.4. Within the AOI, the stable ground temperature ranges between -10°C and -8°C , measured at depths of 20 to 30 meters (Jorgenson et al., 2008).

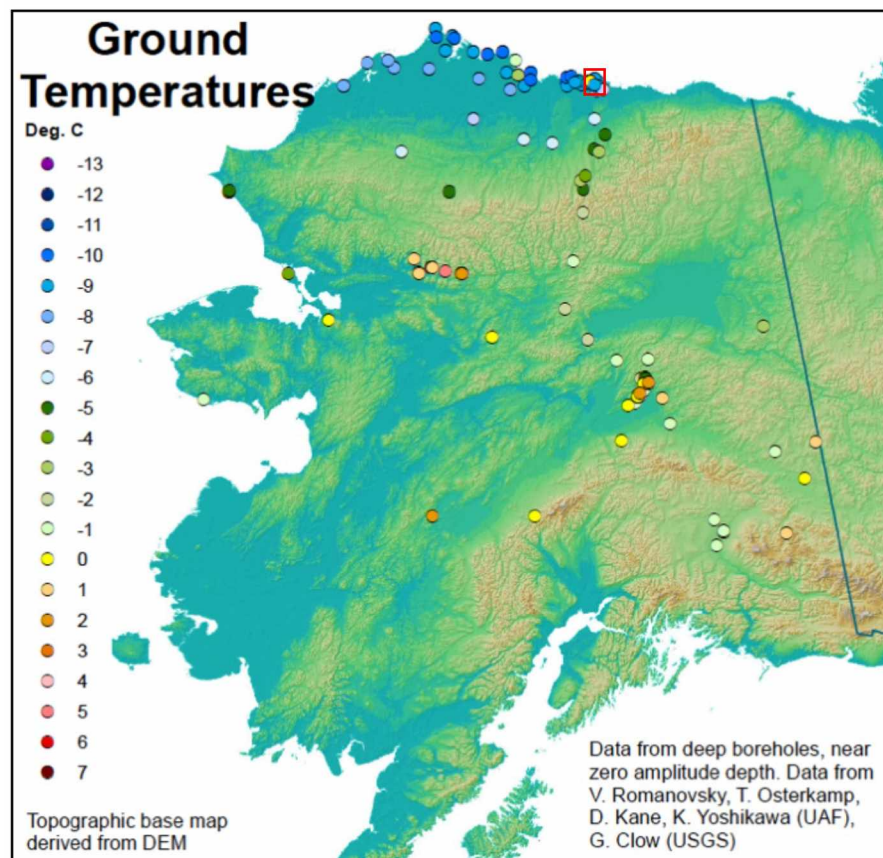


Figure 2.4: Distributed stable soil temperatures of Alaska. AOI shown in red (From Jorgenson et al., 2008).

Figure 2.5 shows a temperature profile of permafrost environment relative to the freezing point and the state of water versus depth. The funnel-shaped area within the curved lines in Figure 2.5 shows a typical maximum summer and minimum winter soil temperature profile in permafrost. As the seasons change, the temperature profile above the depth of zero annual amplitude will change relative to the surface temperature. During summer months, the temperature profile exceeds 0°C (right half funnel-shaped temperature profile, Figure 2.5). The soil thickness between the ice-nucleation temperature, and the ground surface defines the thickness of the active layer (Figure 2.5) (Permafrost Subcommittee, 1988). During the winter, the temperature profiles fall below 0°C , and the active layer refreezes. Below the depth of zero annual amplitude, the temperature is in steady state and equivalent to the local geothermal gradient. With greater depth, the temperature increases with the local geothermal gradient. At a certain depth, the temperature profile will exceed 0°C , marking the base or lower limit of the permafrost (Figure 2.5).

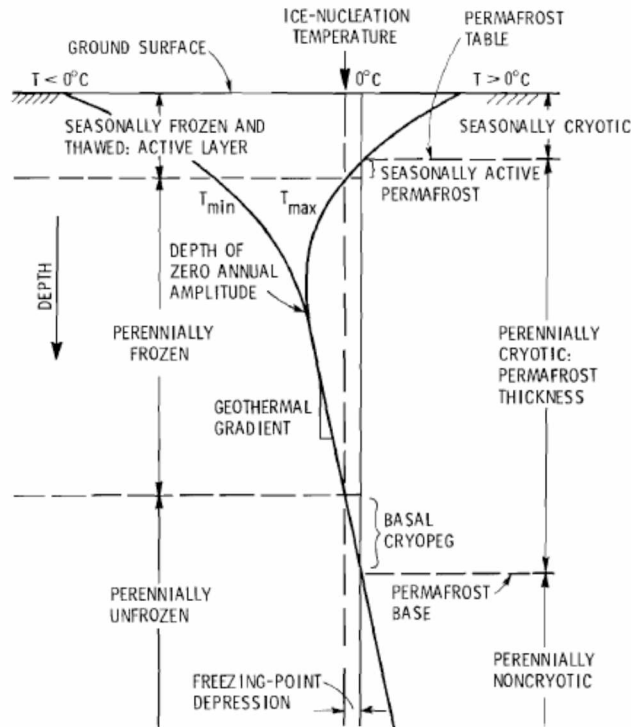


Figure 2.5: Schematic temperature profile of permafrost terminology. Depth of temperature profile plotted relative to freezing point and the state of water in a generalized permafrost environment. The associated naming conventions are placed at their corresponding relative depths (From Permafrost Subcommittee, 1988).

Permafrost is not completely frozen solid. Taliks are layers or bodies of unfrozen ground in permafrost (Permafrost Subcommittee, 1988). Taliks can have temperatures above or below freezing and have been observed in the AOI (Williams, 1970; Permafrost Subcommittee, 1988). Individual taliks are a major source of groundwater in the continuous permafrost (Rawlinson, 1983). In the Sag River area, taliks could be used for a year-round source of clean water supply for the Prudhoe Bay Oilfields (Rawlinson, 1983). Ground water discharge from taliks can influence aufeis formation (Rawlinson, 1983).

The maritime climate of the Beaufort Coast Plain actively maintains permafrost (Rawlinson, 1993). However, arctic amplification has been noted to affect permafrost stability by warming the permafrost. On the Yukon Coastal Plain, east of the Beaufort Coastal Plain, the average temperature has risen -15°C over the past 100 years (Figure 2.2) (Couture et al., 2018). Temperature stability of the Arctic Coastal Plain is essential for the long-term stability of numerous permafrost features such as ice wedges, ice wedge polygons, thaw lakes, rivers, pingos, and yedoma (Feirer, 2004). Within the AOI, oil and gas well logs indicate the presence of permafrost to depths of 659 meters (Figure 2.6) (Jorgenson et al., 2008). The sediments on the Alaska North Slope contain various types of ground ice in high volumes including: 1) pore ice; 2) segregated ice; and 3) massive ice (Kanevskiy et al., 2013). Surface morphology determines the distribution and amount of ice in the permafrost in the coastal plain. The ice is mostly concentrated in the topmost layers of the permafrost. The near-surface sediments contain segregated ice and ice wedges accounting for up to 85% of the groundmass by volume (Rawlinson, 1993). Natural or induced disturbances to the critical temperature environment of permafrost can produce a degradation of permafrost structures and uneven changes in the microtopography of the ground surface. Disturbances can be further complicated as topographic lowering can cause preferential erosion or ponding of water (Rawlinson, 1993).

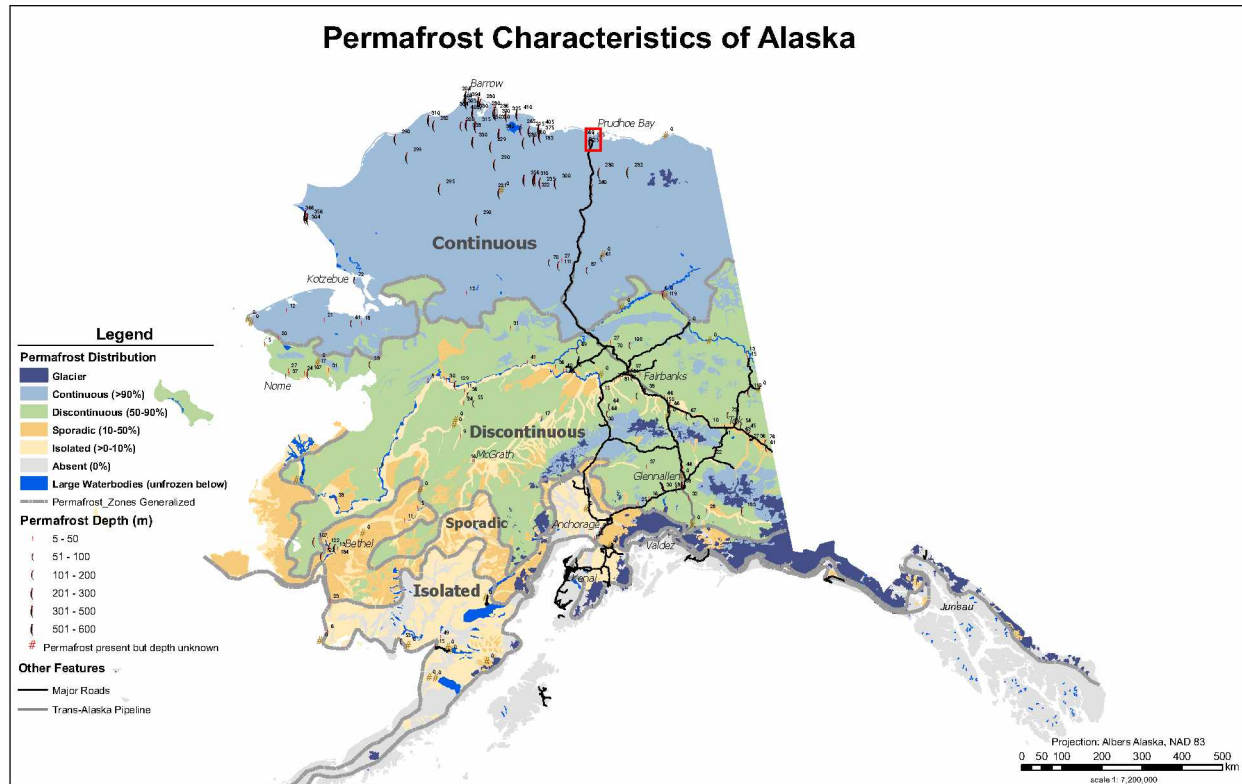


Figure 2.6: Permafrost distribution in the State of Alaska. Associated permafrost thicknesses and classification are shown (Modified Jorgenson et al., 2008). The three thicknesses listed in the AOI are 660, 595, and 625 meters.

2.4.1.1 Coastal Plain Permafrost

The Beaufort Coastal Plain is within a zone of continuous permafrost where the ground has been permanently frozen (Figures 2.2 and 2.6) (Rawlinson, 1993; Jorgenson et al., 2008). At the Prudhoe Bay oilfields, the ground temperatures are typically around -10°C (Rawlinson, 1993; Jorgenson et al., 2008). Local bodies of water warm the surface, thawing the underlying permafrost (Rawlinson, 1993). Under some rivers, the seasonal thaw may be deeper than that of areas of the surrounding river area, and taliks may be present (Gallant et al., 1995). The active layer within this ecoregion varies between 0.5 to 1.0 meters, depending on the soil texture (Rawlinson, 1993; Gallant et al., 1995). This region is characterized by pingos, ice wedges, ice wedge polygons, peat ridges, and frost boils. Permafrost is continuous throughout this region (Feirer, 2004; Jorgenson et al., 2008).

Submarine permafrost likely exists within the northern marine sections of the AOI such as Prudhoe Bay or Foggy Island Bay (Rawlinson 1993). However, the evaluation of the subsea permafrost has no bearing on the objective of this study and is outside of the scope of evaluation.

2.4.1.2 Brooks Range Foothills Permafrost

The Brooks Range Foothills is a relatively featureless terrain having a thick mat of permafrost with many ice-related features (Gallant et al., 1995). These ice-related features included gelifluction lobes, pingos, and ice wedge polygon networks. Permafrost impedes drainage, causing high soil saturation. Soils typically have a thick organic horizon. The permafrost active layer is typically less than 1 meter thick (Feirer, 2004).

Permafrost documentation in this ecoregion is limited. A majority of the reviewed scientific papers contain similar descriptions of Brooks Range Foothills permafrost as discussed in the previous paragraph. Ice wedge polygons were visible within the Brooks Range Foothills portion of the AOI indicating the presence of ice wedges (Figure 2.1). A UAF monitoring station is located near the Franklin Bluffs, in the Beaufort Coastal Plain, outside of the Brooks Range Foothills (Figure 2.1). Descriptions of the coastal plain permafrost at this monitoring station are documented in the coastal region discussion of the study (Section 2.4.1.1).

2.4.1.3 Massive Ground Ice

Massive ground ice is a general term that describes large volumes of ground ice, including ice wedges, pingo ice, buried ice, and large ice lenses (Permafrost Subcommittee, 1988). Within the Beaufort Coastal Plain, the Brooks Range Foothills and the AOI, the most common form of massive ice are ice wedges.

Ice wedge formation occurs during arctic winters. Plunging temperatures cause the contraction of the surface soils which creates cracks in the tundra (Leffingwell, 1915; 1919; O'Neill and Christiansen, 2018). Water and snow fill these cracks in the ground. In the subsequent winter, when temperatures drop below freezing, the newly introduced water freezes and expands creating a vertical vein of ice, which widens the crack (Leffingwell, 1915). Over successive winters, the cycle of cracking, water infilling, and freezing continues. After hundreds to thousands of years, epigenetic ice will develop its wedge shape (Figure 2.7). Surface cracking tends to occur in the ice rather than the surrounding sediments due to the lower tensile strength of the ice, as compared with the surrounding soil column (Lachenbruch, 1962; Mackay, 1983). The subsurface of the Sag River region is classified as ice-rich permafrost due to a high volume of ground ice in the upper 3 meters of the permafrost. A majority of this ice is contained within ice wedges (Rawlinson, 1993).

The three types of ice wedges are: 1) epigenetic; 2) syngenetic; and 3) anti-syngenetic. Within the Beaufort Coastal Plain of the AOI, the most common form of ice wedge is epigenetic (Kanevskiy et al., 2017). There is potential for syngenetic ice wedge formation in the AOI near alluvial terraces or small channels in the Sag River Delta. Documentation of anti-syngenetic ice wedges in the Sag River Watershed has not been found in the literature.

Epigenetic ice wedges are formed in existing permafrost regions (Figure 2.7). These were younger than the host strata. Since the ice wedges grow seasonally with water filling cracks at the center of the wedge, the center ice is younger than the edges of the wedge. Epigenetic wedges tend to widen as they grow, warping the surface around them (Mackay, 1990). Most ice wedges in the AOI were epigenetic.

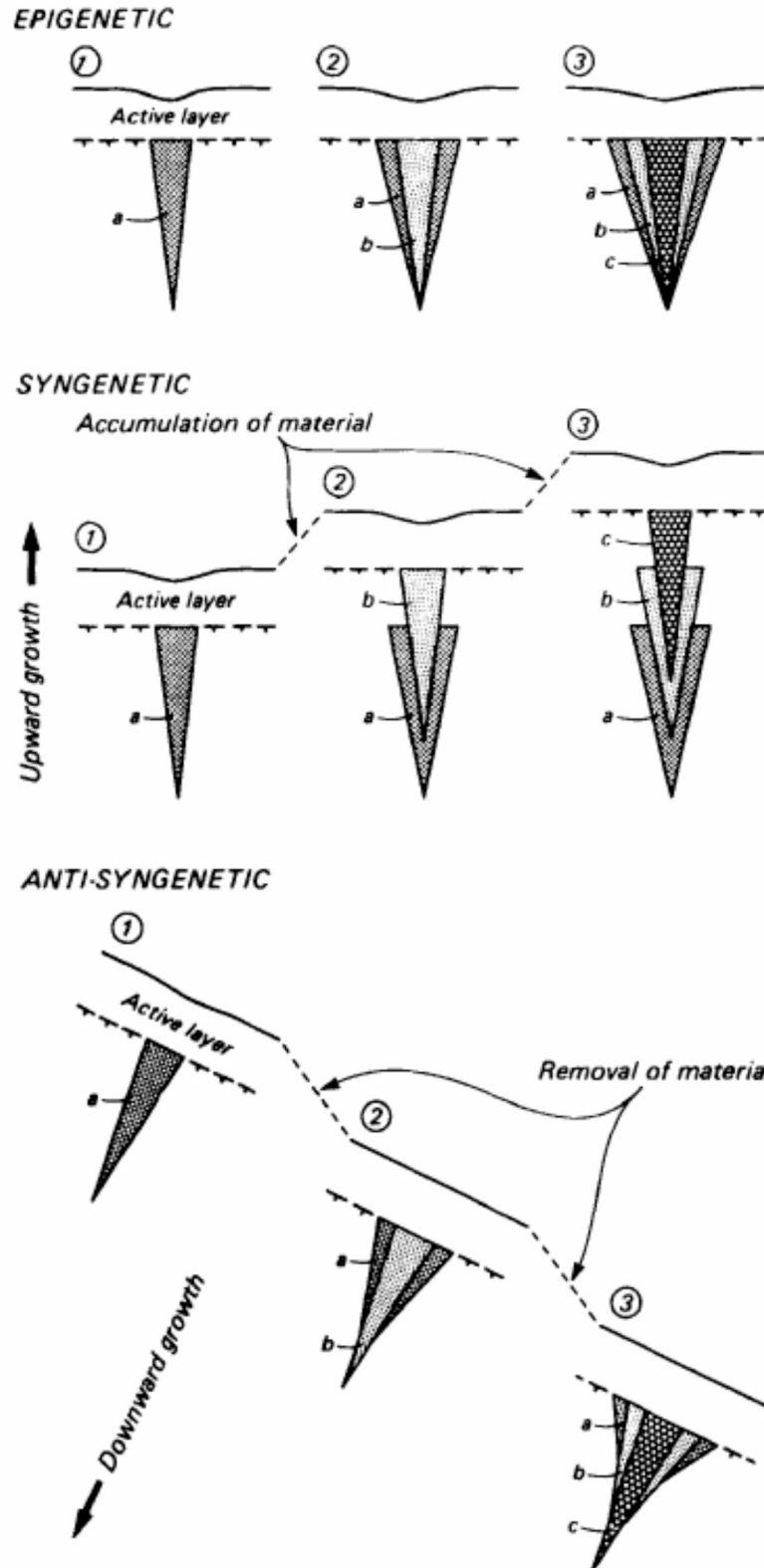


Figure 2.7: Diagram showing the evolution of ice wedges. Evolution of epigenetic, syngenetic, anti-syngenetic ice wedges are shown. Three general growth stages are shown: Stage 1 is the youngest formation of ice; followed by stage 2; and stage 3 shows the oldest formation (Form Mackay, 1990).

Syngenetic ice wedges grow in response to the permafrost surface rising resulting from the accumulation of material on the ground surface (Figure 2.7). The accumulated material can be alluvium from rivers, peat generated from a tundra polygon, or gelifluction deposits accumulating at the bottom of a slope. If the ice wedge grows at the same rate of material deposition, the ice wedge is classified as a syngenetic ice wedge. Ice on the edges of the wedge or deeper underground will be older in age (Mackay; 1990). As such, syngenetic ice grows vertically from the center of the wedge.

Anti-syngenetic ice only grows in eroding areas where the ground surface is lowered by the removal of material (Figure 2.7). The removal of material is typically from mass wasting or erosion. If the growth contraction and ice expansion keeps pace with the removal of material, the wedge will grow to greater depths. The growth conditions are opposite to syngenetic ice wedges. As material is removed, growth at the top of the ice wedge is truncated by thaw at the surface. Favorable conditions in the ground allow the ice wedge to grow downwards. The age of anti-syngenetic ice wedges increases from bottom to top (Figure 2.7) (Mackay, 1990).

Yedoma is an extreme form of wedge ice that forms in permafrost with high ice content. Yedoma is a superficial deposit that ranges in typical thickness from 9 meters to 30 meters, but has been observed to be up to 50 meters thick. Ice wedges usually penetrate the entire thickness of yedoma (Kanevskiy et al., 2011). The presence of yedoma has not been identified in the literature within the AOI (Figure 2.8) (Kanevskiy et al., 2011).

2.4.1.4 Segregated Ground Ice and Pore Ice

A form of ground ice occurring on the Beaufort Coastal Plain is segregated ground ice. Segregated ground ice forms initially when water moves toward the freezing plane by cryosuction. Thus,

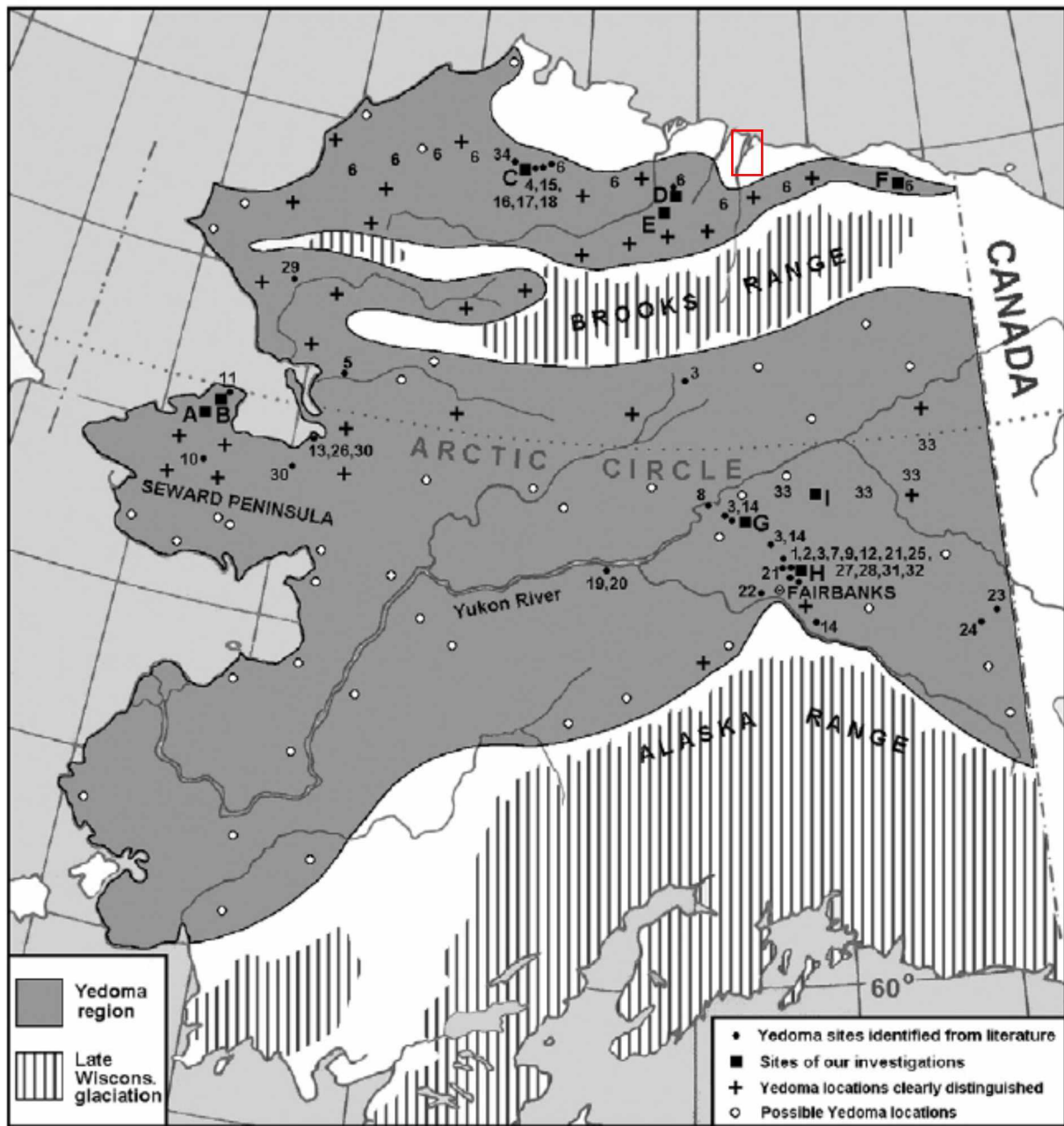


Figure 2.8: Yedoma distributions in Alaska. Red box outlines the AOI (From: Kanevskiy et al., 2011).

ice accumulates as thin ice lenses in soils and rock near the freezing plane (French and Shur, 2010).

Segregated ground ice is visible to the eye and will vary in thickness from a few millimeters to several meters thick (French and Shur, 2010). As ice accumulates, wedging forces the soil or rock apart.

Segregated ground ice tends to form parallel to the surface. As it expands, pressure is exerted. This pressure plays a key role in frost wedging, the frost-induced fracturing of soils, and frost heaving. Segregated ground ice is common in all arctic regions (Kanevskiy, 2013).

Pore ice forms in the capillary space between sediment grains and is also referred to as interstitial or cement ice (French and Shur, 2010). Pore ice is the bonding material that holds grains together. Pore ice is typically not visible and can range from well-bonded with excess ice to poorly cemented and friable (French and Shur, 2010).

The four-layer permafrost model, which contains an intermediate layer, is shown in Figure 2.9.B. The intermediate permafrost layer forms when the active layer is distributed. Intermediate permafrost layers are abundant throughout the Beaufort Coastal Plain (Kanevskiy et al., 2013). Intermediate permafrost layer disturbance is caused by the termination of sedimentation, changes in surface conditions, or other factors. With the accumulation of organic material on the surface, a portion of the active layer will join the permafrost. While this process takes centuries, the intermediate permafrost layer becomes ice-rich. During formation of the intermediate permafrost layer, the surface will rise due to perennial frost heave resulting from the accumulation of aggregational ice (Kanevskiy et al., 2013).

Segregated ground ice and pore ice forms between ice wedges within the top 2 to 3 meters of soil. Generally, segregated ground has been observed to contain ice up to 70% of the total soil by volume (Jorgenson, 2011; Kanevskiy, 2013). The volume and distribution of segregated ice is closely related to soil texture (Jorgenson, 2011). Segregated ground ice and pore ice volumes are highest in massive organic soils and lowest in layered sands (Jorgenson, 2011). See Figure 2.10 for geomorphic unit and terrain descriptions with observed ice volumes across the coastal plain (Jorgenson, 2011). Along the

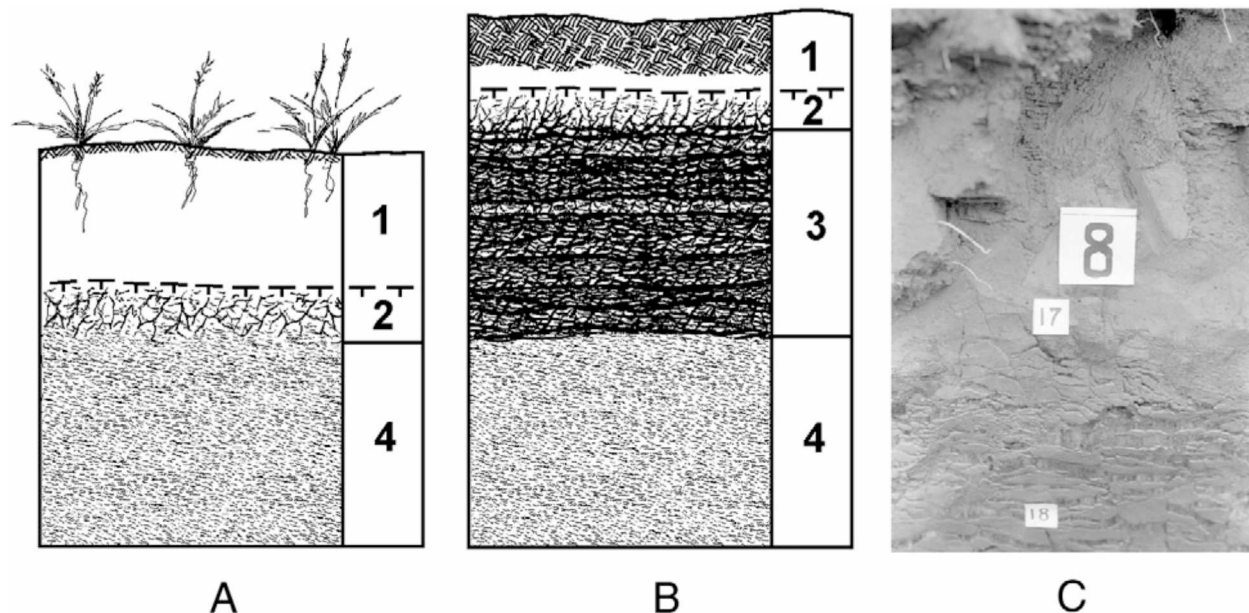


Figure 2.9: General soil horizons of upper layers of permafrost. A three-layer model is shown in Inset A; showing 1) active layer; 2) transient layer; and 4) permafrost. The four-layer model shown in Inset B contains two layers in the transition zone. Layers are as follows: 1) active layer; 2) transient layer; 3) intermediate layer containing aggregational ice; and 4) permafrost. Inset C is a photo showing the four-layer model horizons (From French and Shur, 2010).

Sag River, inactive floodplains have thick accumulations of fine-grained sediments and abundant ground ice. The fine-grained soils in these locations support the formation of ataxitic textured ice, occupying up to 80% of the soil by volume (Jorgenson, 2011).

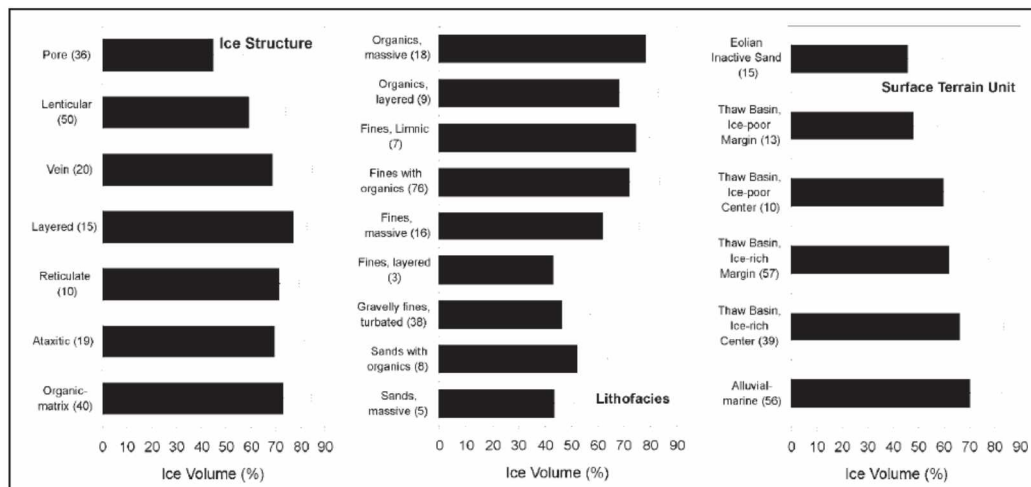


Figure 2.10: Ice volume of segregated ground ice and pore ice by geologic lithofacies and terrain. Ice volume (%) of segregated ground ice and pore ice by geologic lithofacies and terrain units are shown (From Jorgenson, 2011).

2.4.2 Permafrost Thaw-Related Landforms in the AOI

Variations between the summer and winter climates of the Beaufort Coastal Plain and Brooks Range Foothills play an important role in modifying their landforms (Rawlinson, 1993). Thawing of the permafrost is the primary driver of these changes. The impacted permafrost features include ice wedge polygons, thermokarst, and localized formations of other types of ice.

2.4.2.1 Ice Wedge Polygons

Permafrost systems and ice wedge activity dominate the Arctic landscape with polygonal surface expressions (Kanevskiy et al., 2013). These surface expressions can be hidden under a flat topography or can be expressed as depressions or mounds in the microtopography (Figure 2.11). Multiple ice wedges create isolated polygonal blocks (Leffingwell, 1915) and are often referred to as ice wedge polygons (Lachenbruch, 1962). As the epigenetic ice wedges grow in the subsurface, pressure is exerted on adjacent soil columns, deforming the surface into raised rims (Lachenbruch, 1962). Soil warping from ice wedge expansion can enclose a polygon with rims, creating a low-centered polygon (Figure 2.11). The rims of low-centered polygons tend to block surface water from entering the ice wedge depression; thus, in the summer these polygons are likely to pond water (Liljedahl et al., 2012). The capacity of low-center polygons to hold water is dependent on the thermal and physical properties of the soil surrounding the polygon and the shape of the permafrost table. Thaw may generate exaggerated permafrost tables under waterlogged ice wedge polygons. If the surrounding permafrost table remains frozen the low-centered polygon may remain completely isolated from the groundwater system (Abolt et al., 2015). If ice wedge development has not distorted rims of the surface of the ice wedge, the polygon is considered flat. Orthogonal ice wedge polygons commonly occur in drained lake basins, downflows of river floodplains, or river terraces. Non-orthogonal ice wedge polygons have shown little modification from lacustrine or fluvial processes (Rawlinson, 1993).

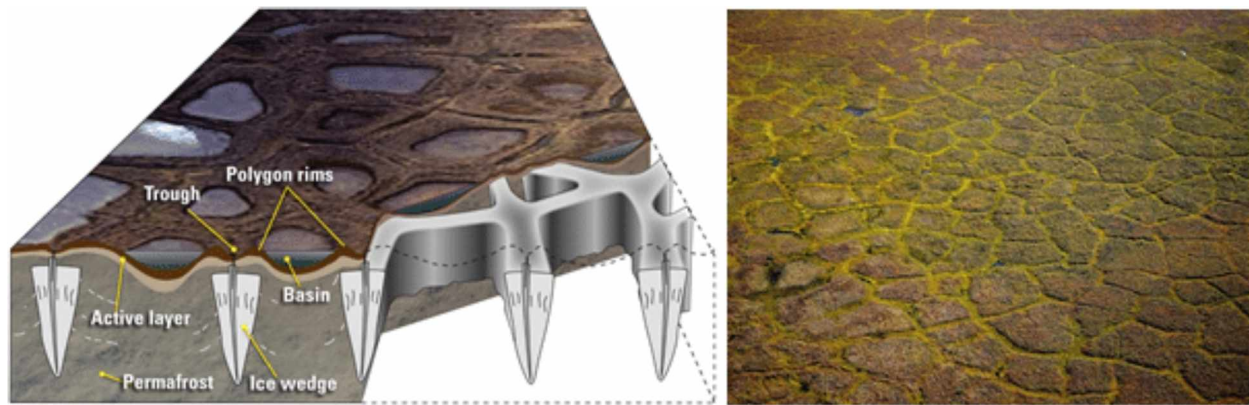


Figure 2.11: Schematic diagram of ice wedges and ice wedge polygon landscapes (From Martin et al., 2016).

Ice wedge polygons can be low-centered (concave) or high-centered (convex), depending on where the center is in relation to the rim height (Rawlinson, 1993). The occurrence of high-, flat-, or low-centered ice wedge polygons are related to the soil material that form them. Low-centered polygons form in material that has a finite shear strength when thawed, such as peat or silt. High-centered polygons form when the material is more fluid when thawed, such as some peats, silts, or clays; these polygon features are produced from degradation (Rawlinson, 1993). Low-centered polygons are thought to convert to high-centered polygons when undergoing increases in climatic temperatures (Walker et al. 2014). The warming ice wedges leave behind a sunken trough causing the center of the polygon to appear raised (Abolt et al., 2015). Ice wedge polygon type conversion can also be caused by the breakdown of the low center polygon rims, as portions of the neighboring ice wedges will begin to degrade from the new influx of melt. Melt could cause the troughs at polygon boundaries to subside below the center polygon elevation (Abolt et al., 2015). High-centered polygons are typically well drained and retain little water in the polygon center due to their soil properties and geometry. An example of high-centered permafrost polygons is near Utqiagvik, Alaska (Wainwright, et al., 2015). Thermal influx can cause wide-spread degradation of ice wedge systems. These disturbances can be natural, including forest fires, erosion, and reservoir drainage, or manmade, typically relating to power

generation or resource extraction. Ice wedge polygons, and thus, ice wedges, can be observed throughout the coastal plain and the AOI (Figure 2.1 and 2.11).

2.4.2.2 Thermokarst

Thermokarst formation is the process by which characteristic landforms result from the thawing of ice-rich permafrost (Permafrost Subcommittee, 1988). As a consequence of changing climatic conditions on the surface, when the upper layer of the permafrost experiences warming, the seasonal thawing processes can trigger increased subsidence unevenly on the surface and polygon transformation to high-centered polygons. These topographic expressions and processes are examples of permafrost degradation and thermokarst formation (Shur, 1988; Abolt, et al., 2015). Ice wedges and their polygons are critical structural components of the soil column. If seasonal thaw reaches a sufficient depth, the top of the massive ice will melt for the rest of the summer. The intermediate permafrost layer usually contains a thin layer of ice between the active layer and the ice wedges, and usually helps protect the massive ice from seasonal variability. Disturbance to the soil can increase the thickness of the active layer. The ponding of water in troughs can result in ice loss (Pullman et al., 2007). It has been observed that water drainage can become channelized through ice wedge networks (Pullman et al., 2007). Ice wedges are extremely vulnerable to changing surface conditions (Jorgenson et al., 2015). In 2015, 34% of the tundra, at select monitoring sites, in the Sag River Delta region contained thermokarst (Abolt et al., 2015).

2.4.3 Vegetation

Vegetation in the Beaufort Coastal Plain is strongly influenced by the microtopography. Microtopography influences drainage patterns redirecting groundwater drainage. Wet and oversaturated soils are common within this ecoregion (Figure 2.2). The most common plants are various

grasses and sedges (Gallant et al., 1995). Drier soils occur in locations where the ground is more exposed to sunlight or where the ground surface has sufficient topographic relief to allow drainage. Changes in topographic relief are seen at bluffs and rims along lakes, rivers, or ice wedge polygons. Dwarf shrubs grow in these drier soils (Gallant et al., 1995). The Brooks Range Foothills area is primarily vegetated with various grasses and a dwarf shrub community (Gallant et al., 1995).

2.5 Hydrology

The Sag River is the second largest river on the Alaska North Slope with a watershed covering an area of 1,489,000 hectares (Milner, et al., 2005; Toniolo, 2017). The river flows from its headwaters at Accomplishment Creek in the Brooks Range, emerging from the Philip-Smith Mountains and flowing north across the Brooks Range Foothills to the Arctic Ocean (Milner, et al., 2005). Discharge in the summer season typically exceeds 10,000 cubic feet per second (cfs) (Federal Priority Streamgauge Program; 2019). During the winter season discharge is estimated to be as low as 150 cfs (Figure 2.12) (Federal Priority Streamgauge Program; 2019). Arctic braided streams typically freeze solid to the river base in the winter with the exception of deep pools and river channels in deltas (Milner, et al., 2005). River discharge is highly dependent on climatic conditions such as the ambient temperature (Figure 2.13) (Hodel, 1986). Spring river breakup typically occurs in late May and winter freeze up begins in late September (Hodel, 1986). The Prudhoe Bay tidal range has a relatively small impact on the landscape. The tide ranges between -1.05 meter and +1.25 meters from sea level with a mean range of ± 0.16 meter (Tides and Current Station 9497645) (National Oceanic and Atmospheric Administration, 2020).

2.6 Geologic Setting

The sediments of the Alaska North Slope, including the Beaufort and Chukchi Continental Shelves, were deposited as passive margin sediments, rift sediments, pelagic sediments, volcanoclastics,

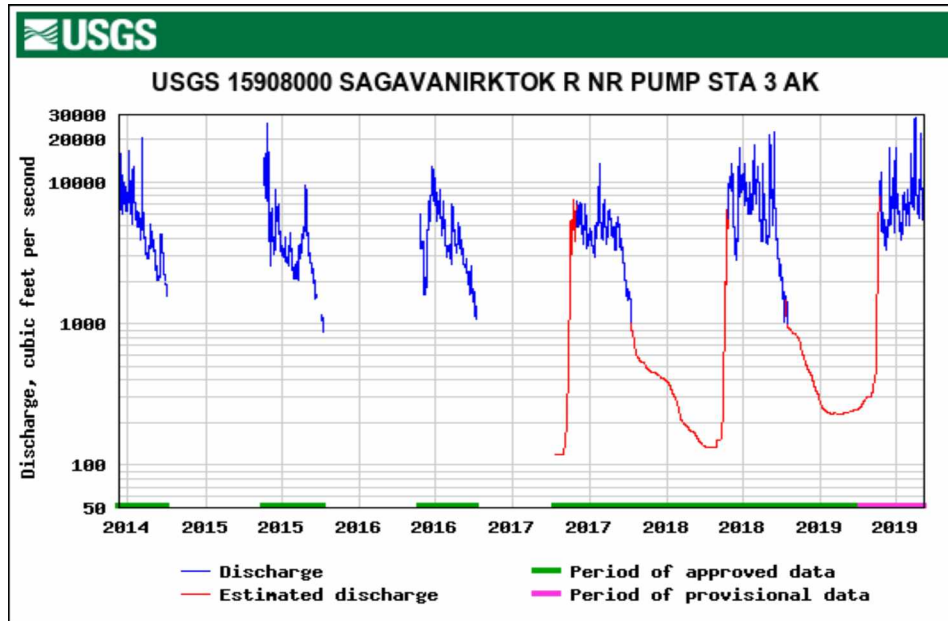


Figure 2.12: Discharge plot of the Sag River from 2014 to 2019. Graph shows the measured (blue) and estimated (red) discharge of the Sag River flow reported from the TransAlaska Pipeline pump station 3. Data from USGS streamgauge station 15908000 (Federal Priority Streamgauge Program, 2019).

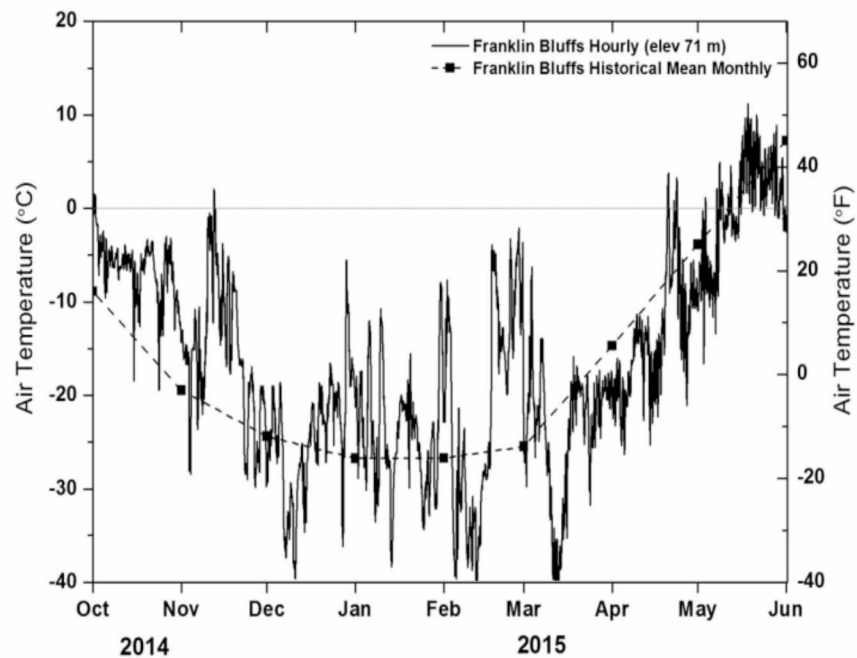


Figure 2.13: Temperature plot showing the 2014-2015 winter temperatures. The 2014-2015 shown as solid line. Winter season temperatures are compared to the historical monthly mean shown as dashed line. Data collected at UAF Franklin Bluffs station (From Toniolo, 2017).

and foreland-basin deposits. The sediments were sourced from the North American Craton (Jorgenson, 2011; Schenk et al., 2011). The terrane is subdivided into two geologic structures, the Colville Basin, and the North Slope Subterrane (Figure 2.14). The Colville Basin overlies the North Slope Subterrane and is a foreland basin of Cretaceous-Tertiary age that filled with sediments shed from the Brooks Range (Jorgenson, 2011). The North Slope Subterrane is comprised of Cretaceous and older rocks underlying the Colville Basin and much of the Brooks Range. Compression of the Arctic Alaska Plate during the Mid-Cretaceous was produced by the combined forces of terrane accretion at the southern margin of the Arctic Alaska Plate and rift-zone expansion in the marine basin bordering the Arctic Alaska Plate to the north. The resulting deformation formed the Brooks Range thrust-fault belt, the foreland Colville River Basin, and Barrow Arch (Jorgenson, 2011). In the literature, the geology of the North Slope has been subdivided into four mega-sequences of emplacement: 1) Franklinian; 2) Ellesmerian; 3) Beaufortian; and 4) Brookian sequences (Figure 2.14 and 2.15) (Houseknecht and Bird, 2005).

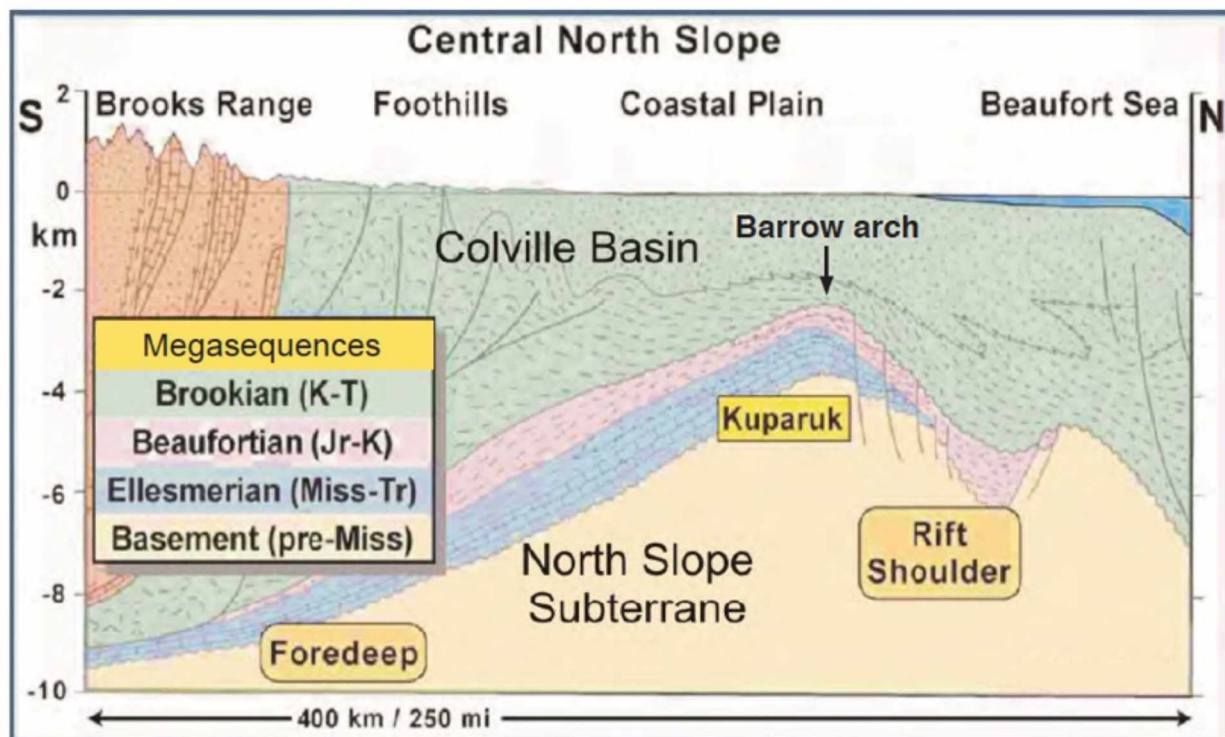


Figure 2.14: Cross-section and generalized geologic stratigraphy of the Alaska North Slope (From Jorgenson, 2011).

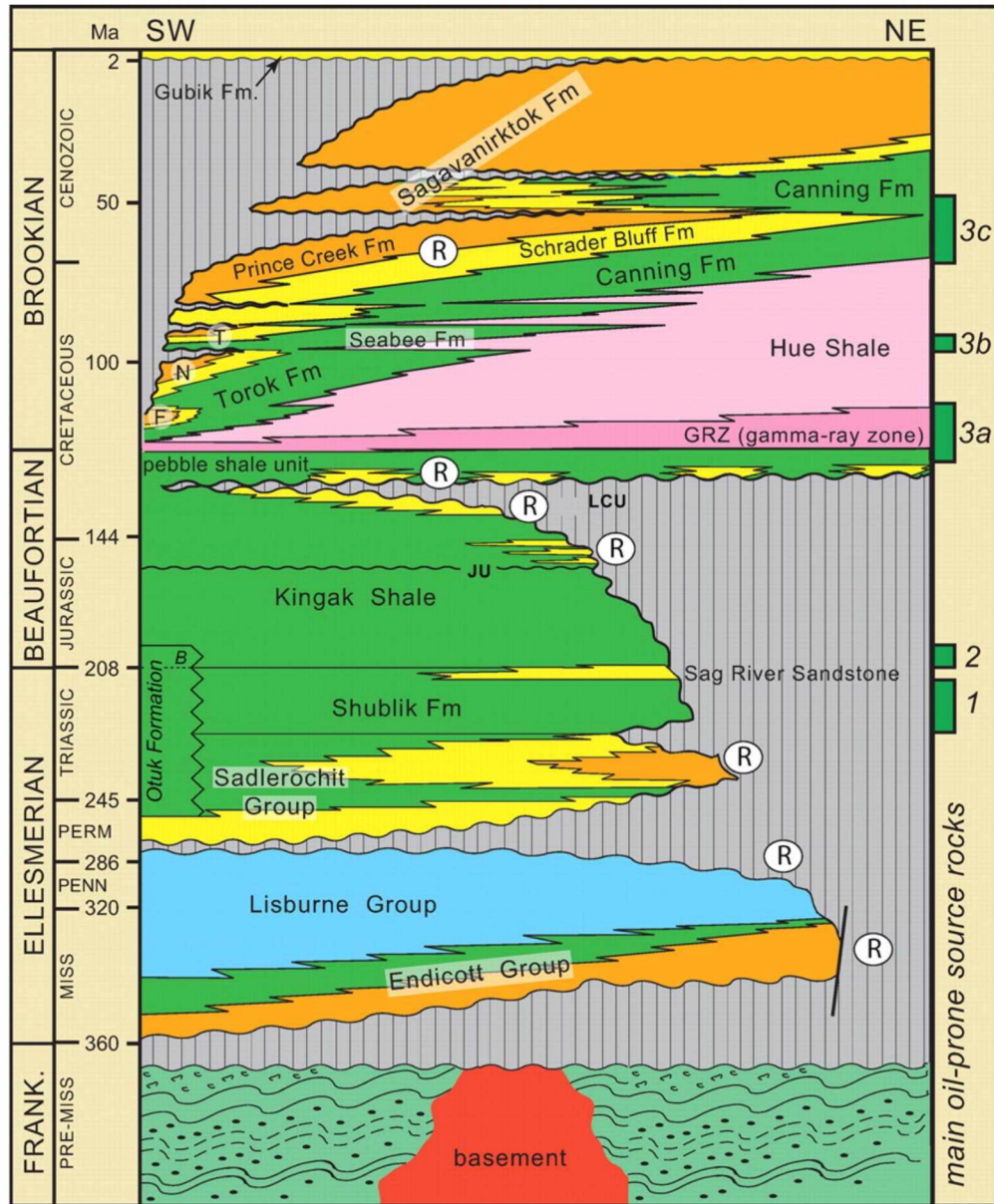


Figure 2.15: Generalized stratigraphic column of the Alaska North Slope (From Houseknecht and Bird, 2005).

The earliest sequence, the Pre-Mississippian Franklinian consists of Devonian and older aged strata. During this time, the Alaska Northern Slope was a stable continental shelf. These rocks have been compressed and metamorphosed into the thermogenic gas window. These strata and the underlying

crystalline rocks represent the economic basement units in most of the Alaska North Slope (Figures 2.14 and 2.15) (Houseknecht and Bird, 2005).

The Ellesmerian sequence consists of carbonate shallow marine to nonmarine siliclastic deposits spanning the Early Mississippian to the Late Triassic. Sediments were shed from a south-facing continental margin into the Barrow Arch from a north-lying continent and pinch out to the north. Sediments greatly thicken to the west near the Hannah Trough. The Devonian and Mississippian have been interpreted as synrift deposits while post-Mississippian deposition is interpreted as thermal sag deposits (Figures 2.14 and 2.15) (Houseknecht and Bird, 2005). Many of the oil and gas source rocks were deposited during this time. However, maturation did not occur until the Beaufortian and Brookian sequences.

The Beaufortian sequence spans from the early Jurassic to the early Cretaceous and is signified by the opening of the Canada Basin and the creation of the Barrow Arch. This sequence consists of stratigraphically complex synrift deposits and extension-generated horst and graben structures throughout the basin. This sequence contains multiple unconformities including the breakup unconformity. This unconformity truncates older sediments onto the Barrow Arch. The diachronous contact has generated the migration pathway to many of the Alaskan petroleum reservoirs (Figure 2.14 and 2.15) (Houseknecht and Bird, 2005).

The Brookian sequence spans from the Early Cretaceous to the Late Tertiary periods. Large volumes of sediment were generated from the Brooks Range uplift and deposited as clinoforms, filling the Colville Foreland Basin. This sequence consists of sediments ranging from short-traveled marine mudstones to long-traveled turbidite deposits. Deposition during this time compressed the basin,

generating the heat needed for thermal maturation of source rocks (Figure 2.14 and 2.15) (Houseknecht and Bird, 2005).

2.7 Surficial Geology and Soils

The Tertiary sediments of the Sagavanirktok Formation discontinuously underlie the sediments of the Gubik Formation in the AOI. The Sagavanirktok Formation is defined at Franklin Bluffs as poorly consolidated conglomerate, sandstone, siltstone, and lignite coal exposed along the east side of the Sag River (Bolin, 1959; Mull et al., 2003) (Figure 2.1). All sediments overlying the Prince Creek Formation and underlying the Gubik Formation are designated as the Sagavanirktok Formation (Figure 2.14) (Rawlinson, 1993). The Sagavanirktok Formation is subdivided from oldest to youngest, into the Sagwon, White Hills, Franklin Bluffs, and Nuwuk Members, respectively (Mull et al., 2003).

The Late Paleocene to early Eocene White Hills Member is composed of 49 meters of well-rounded, cobble-sized clasts of gray quartzitic sandstone, white quartz, and chert (Mull et al., 2003). The early Eocene Franklin Bluffs Member is composed of poorly consolidated siltstone, sandstone, and poorly sorted conglomerate with chert clasts. The Franklin Bluffs Member is largely exposed at the Franklin Bluffs, in the southern AOI (Figure 2.1) (Mull et al., 2003). These members outcrop east of the Colville River and west of the U.S.-Canada Border and at the Franklin Bluffs. Outcrops are typically at an elevation higher than the coastal plain and are considered an extension of the Brooks Range Foothills. Surface exposures of the White Hills Member and the Franklin Bluffs Member of the Sagavanirktok Formation are located within the AOI at Franklin Bluffs.

Overlying the Sagavanirktok Formation is the Pleistocene Gubik Formation (Figure 2.15). This formation is comprised of 12 meters to 15 meters of primarily marine sediments and is defined as all

late Pliocene and Quaternary unconsolidated marine and nonmarine sediments on the coastal plain (Rawlinson, 1993). The Gubik is exposed throughout the Arctic Coastal Plain and extends into the shallow, continual shelf, terminating at the Arctic Ocean shelf break (Bolin, 1959).

A majority of the geologic formations are east-west striking and decrease in age northward from the Brooks Range to the Arctic Ocean (Hodel, 1986). The Quaternary river sediments are mostly flat-lying, and exposed along the banks of the Sag River, and associated gravel bars (Keller et al., 1961). The geology of the Sag River bed contains two predominant lithologies, marine and sedimentary rocks (Hodel, 1986); both lithologies are composed of rounded sand to boulder-sized sediment.

The superficial geology of the Alaska North Slope was well documented by Rawlinson (1993). The Rawlinson (1993) superficial geology report contains the most complete and up-to-date geologic report of the surficial geology on the Alaska North Slope. A current project at the Alaska Division of Geology and Geophysical Surveys (DGGs) is remapping areas in the Rawlinson report and modernizing the maps in ESRI vector format and will likely be completed in late 2020 (Alaska Division of Geology and Geophysical Surveys, 2019). There is a high degree of variation along the Beaufort Coastal Plain. In general, the sediments are modern coastal deposits, glaciomarine, fluvial and glaciofluvial, from lacustrine processes of drained lake basins, or eolian (Rawlinson, 1993; Jorgenson et al., 2008). This study used the Rawlinson (1993) surficial geologic map to define the surficial sediments (Figure 2.16). See Table 2.1 for a summary of sediment types.

The sediments of the Alaska North Slope are considered permafrost to depths of 659 meters in the Sag River Delta (Hodel, 1986; Jorgenson et al., 2008). Here, thickness of the active layer is largely dependent on the superficial deposits at the surface, and the amount of solar radiation received and

Table 2.1: Summary of geologic facies and lithologic descriptions of the Beachy Point Quadrangle. Units are summarized from Rawlinson (1993). Corresponding map is shown in Figure 2.16.

	<i>General Surficial Lithology and Map Unit</i>	<i>Summarized Descriptions</i>
1	Active Marine (Qb, Qtf, Qsm, W)	<i>Settings:</i> beach, tidal-flats, saltwater-marshes, open water. <i>Typical lithologies:</i> gravelly sand, moderate to well-sorted silt and fine sand in quiescent environments. sparse to no surface vegetation.
2	Deltaic (Qd, Qdi, Qda)	<i>Settings:</i> active, inactive, and abandoned deltaic deposits. <i>Typical lithologies:</i> silt to fine sand, interbedded with sparse to massive peat.
3	Lacustrine (Qt, Qti)	<i>Settings:</i> thaw-lake, and ice-rich thaw lake deposits. <i>Typical lithologies:</i> peat, pebbly silt, and fine sand, often cryoturbated and contains segregated ice or ice wedges.
4	Fluvial (Qf, Qfi, Qfa, Qat, Qaf, Qau, Qsg)	<i>Settings:</i> active, inactive, and abandoned flood plain, alluvial terrace, alluvial fan, undifferentiated alluvium, and alluvial-plain deposits. <i>Typical lithologies:</i> silt to gravel, flatlining or mounded. often contains gravel or peat. high degree of variation, see Rawlinson (1993) for detailed descriptions
5	Eolian (Qs, Qsd)	<i>Settings:</i> sand cover and sand dune deposits. <i>Typical lithologies:</i> fine to medium sand. dunes are vegetated and contain pore ice, up to 2 meters in height.
6	Colluvial (Qrg, Qc)	<i>Settings:</i> retransported granular deposits and undifferentiated colluvium. <i>Typical lithologies:</i> poorly to moderately sorted silt and sand. gravel is common.
7	Terrace (QtF, QtE, QtD, QTtC, QTtB, QTtA, Tgs)	<i>Settings:</i> alluvial terrace and marine terrace deposits and undifferentiated gravelly sand. <i>Typical lithologies:</i> predominately fluvial silty sand with granules and pebbles. minor clay present.
8	Outwash (Qso, Qo)	<i>Settings:</i> silt and sand over gravel and gravel. <i>Typical lithologies:</i> eolian silt and fine sands over glaciofluvial gravel, stratified silt pebble cobble and boulder gravel.
9	Glacial (Qsgt ₃ , Qgt ₃ , Qsgt ₄ , Qgt ₃ , Tg)	<i>Settings:</i> silt and sand till, and gravel plain. <i>Typical lithologies:</i> eolian and colluvial silt, gravel.
10	Gravel (QTsg, QTg('), QTgm).	<i>Settings:</i> gravel plain <i>Typical lithologies:</i> silt and sand over gravel, gravelly sand, sand, silt, and clay.
11	Bedrock (Ts, Tmg, Tsmg, Tsg).	<i>Settings:</i> undifferentiated siltstone, shale, and sandstone, diamicton, silt and muddy conglomerate. <i>Typical lithologies:</i> see Sagavanirktok Formation description in section 2.7.

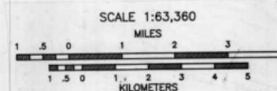
Figure 2.16: Surficial Geologic Map of the Beachy Point Quadrangle used in this study. AOI outlined in red (From Rawlinson, 1993).



GEOLOGY ADAPTED BY S.E. RAWLINSON AND S.A. HARRIS, 1989-1992;
RAWLINSON AND S.A. HICKMOTT, 1993-1995; HICKMOTT AND RAWLINSON, 1996;
AND RAWLINSON, 1998-1999
BASE MAP FROM U.S. GEOLOGICAL SURVEY BEECHY POINT A-1, 1968, REVISED 1970;
A-2, 1968, REVISED 1970; B-1, 1968, REVISED 1970; B-2, 1968, REVISED 1970.

SURFICIAL-GEOLOGY MAP OF THE BEECHY POINT A-2, A-3, B-2,
AND B-3 QUADRANGLES, ALASKA

by S.E. Rawlinson
1993



native vegetation. In the Sag River Delta, the active layer west of the river can exceed 70 cm in thickness and ranges from 35 cm to 65 cm and up to 200 cm east of the Sag River (Hodel, 1986; Nelson, et al., 1997). The active layer above a permafrost table has low water storage capacity of surface melt and may have large runoff from meltwater or rainfall (Bolin, 1959).

Chapter 3 Data and Methods

3.1 Radar Imaging from Space

SAR is an active source imaging technique where a sensor emits microwave pulses to illuminate the ground and records the echoes returned to the sensor (Woodhouse, 2015). For the past 30 years, SAR has been implemented globally in applications of Earth Remote Sensing (Moreira et al., 2013). SAR satellite imaging provides, depending on the sensor, on-demand or fixed acquisition data of the ground surface with daylight and weather independence (Moreira et al., 2013; Woodhouse, 2015). This chapter introduces SAR and its properties and applications, as well as provides overviews of the methods used in this study. For the purposes of this study only spaceborne SAR was utilized.

3.1.1 Overview of Synthetic Aperture Radar History

Investigation of SAR imaging originated in the 1940s, when the United States Army began looking for an active source surveillance imaging platform (Engineering and Technology History, 2019). Radar was chosen for its ability to penetrate cloud cover and illuminate its target, allowing it to capture images at night (Uys, 2016). One of the initial problems was designing an antenna long enough to provide useful resolution (Uys, 2016). Prior to this time, radar was popular for obtaining aerial images of the ground because of its weather and daytime independence. Innately, radar antennas needed to be long for focusing purposes (Woodhouse, 2015). In 1951, Carl Wiley, of the Goodyear Aircraft Company (today Lockheed Martin), observed a correspondence between emitted microwaves and the Doppler shift of the reflected signal (Table 3.1). Wiley concluded through frequency analysis that the along-track width of the physical beam allowed for a higher-resolution image (McCandless and Jackson, 2004). Wiley's investigations developed into the Doppler beam-sharpening concept (Table 3.1) (McCandless and Jackson, 2004). Doppler beam-sharpening enabled the transition from real aperture radar (RAR)

imaging to SAR imaging, resulting in a significant downsizing of antenna length and making SAR more versatile (Uys, 2016).

Table 3.1 List of major SAR development innovations and highlights (From: McCandless and Jackson, 2004).

DATE	DEVELOPMENT
1951	Carl Wiley of Goodyear postulates the Doppler beam-sharpening concept.
1952	University of Illinois demonstrates the beam-sharpening concept.
1957	University of Michigan produces the first SAR imagery using an optical correlator.
1964	Analog electronic SAR correlation demonstrated in non-real time (University of Michigan).
1969	Digital electronic SAR correlation demonstrated in non-real time (Hughes, Goodyear, Westinghouse).
1972	Real-time digital SAR demonstrated with motion compensation (for aircraft systems).
1978	First space-borne SAR NASA/JPL SEASAT satellite. Analog downlink; optical and non-real-time digital processing.
1981	Shuttle Imaging Radar series starts - SIR-A. Non-real-time optical processing on ground.
1984	SIR-B. Digital downlink; non-real-time digital processing on ground.
1986	Space-borne SAR Real-time processing demonstration using JPL Advanced Digital SAR processor (ADSP).
1987	Soviet 1870 SAR is placed in earth orbit.
1990	Magellan SAR images Venus.
1990	Evolution of SAR begins in space; Soviet ALMAZ (1991), European ERS-1 (1991), Japanese JERS-1 (1992), SIR-C (1994), ERS-2 (1995), Canadian RADARSAT-1 (1995), SRTM (2000), ENVISAT (2002).

In 1952, researchers at the University of Illinois developed beam-sharpening and autofocus concepts for microwave images, demonstrating the Doppler beam-sharpening concept (Table 3.1) (McCandless and Jackson, 2004; Engineering and Technology History, 2019). In 1953, the University of Michigan began a special project to develop the optical processing of SAR imaging. This method was first deployed in 1957 on an airborne SAR platform (Table 3.1) (McCandless and Jackson, 2004; Uys, 2016).

In 1974, the National Oceanic and Atmospheric Administration (NOAA) and engineers from the National Aeronautics and Space Administration (NASA) Jet Propulsion Laboratory (JPL) began exploring the possibilities of oceanic observations using a satellite carrying a SAR. SAR's wavelengths make it sensitive to small changes in surface roughness and able to measure displacements with accuracies in the millimeter range, making it ideal for monitoring ocean surface wave patterns and currents. The 1978 launch of the Seasat Satellite was the first spaceborne deployment of SAR. Seasat operated for 105 days until a short circuit disabled its power system (McCandless and Jackson, 2004; Uys, 2016). Since that time, SAR sensors have been deployed on numerous spaceborne platforms including a NASA space shuttle deployment (McCandless and Jackson, 2004).

3.1.2 Radar and Synthetic Aperture Radar

Basic radar self-illuminates a target location by transmitting a series of microwaves pulses (McCandless and Jackson, 2004; Woodhouse, 2015). The pulses are reflected from the illuminated area and collected by the radar receiver (McCandless and Jackson, 2004; Woodhouse, 2015). By measuring the time difference between the emitted pulse and the returned signal, the radar is able to determine the precise distance to the reflected object (McCandless and Jackson, 2004). The down-range resolution of radar is determined by its ability to discern multiple distinct objects in the range direction. However, multiple objects must be separated by a certain distance for their signal to be resolved. If two objects are located within the same resolution area, the return signal will be a compound contribution from both objects (McCandless and Jackson, 2004).

The geometry and basic terminology of satellite SAR imagery are presented in Figure 3.1. Most SAR imaging platforms are side-looking with a look-angle, θ_l , anywhere from $\sim 20^\circ$ to $\sim 50^\circ$ from nadir (Figure 3.1). Microwave pulses are transmitted in a slant direction and recorded over the flight path

(Woodhouse, 2015). These pulses are recorded and stitched together to form an image (Woodhouse, 2015). Due to the side-looking geometry of the sensor, the microwave energy returned from the initial microwave pulse is from backscatter or reflection. High-energy returns, or bright areas, are caused by microwaves reflected directly back at the sensor, whereas low-energy returns, or dark areas, are caused by microwave scatter, absorption, or reflection away from the sensor.

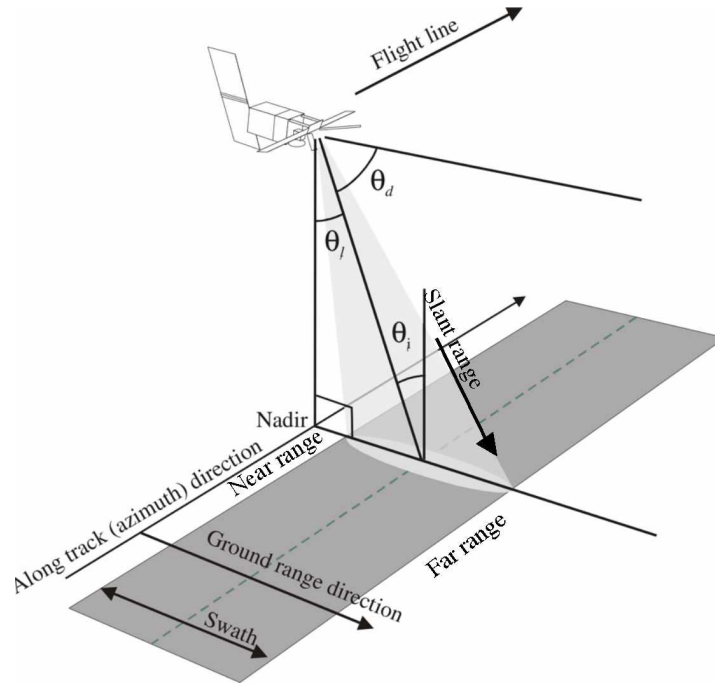


Figure 3.1: Geometry of the typical side-looking SAR imaging platform. Geometry shown in a strip map imaging mode. Note that a thin microwave beam is pulsed in the slant range, in the look- angle, θ_l , of the sensor and θ_i is the incident angle. The swath area (dark gray) is illuminated by microwave pulses (light gray). Continued imaging along the flight line allows for the construction of a 2D image (From Woodhouse, 2015).

The sensor's synthetic aperture length is dependent on the distance the SAR sensor travels while imaging a target, which, for strip map imaging modes, is the width of the antenna and the distance to the imaged object. Typically, the larger the synthetic aperture, the higher the resolution of the image. The simplified equitation for the azimuth resolution of SAR is

$$\rho_a = \frac{D}{2}, \quad [\text{m}] \quad (1)$$

where ρ_a is the azimuth resolution and D is the length of the antenna (Woodhouse, 2015). This property allows SAR sensors to create high-resolution images from acquisitions with relatively small antennas (McCandless and Jackson, 2004). The synthetic aperture has the unique property of increasing in length as the down range distance to the target grows. This allows for consistent image resolution along the azimuth direction of the image (McCandless and Jackson, 2004).

3.1.3 Synthetic Aperture Radar Principles

Figure 3.1 also displays the typical ‘strip map’ imaging mode of a side-looking imaging platform. As the satellite continues along its flight path, a microwave pulse is emitted to the ground and reflected back to the satellite sensor. The imaged area is relatively narrow along the swath. The light gray shaded area in Figure 3.1 shows the footprint of the imaged area for a single pulse (McCandless and Jackson, 2004; Woodhouse, 2015). Image data are stored in a buffer aboard the satellite before being downlinked. Signal processing of each point target includes weighting, shifting, and summing of microwave pulses. Signal processing constructs an image by placing the total energy response obtained in the focusing process on a particular target at the position in the image corresponding to that target (McCandless and Jackson, 2004).

3.1.4 SAR Image Characteristics, Geometry, and Speckle

A SAR image has several characteristics that make it unique when compared to optical images (McCandless and Jackson, 2004). The positions of a SAR image appear distorted with a gritty appearance. SAR samples, like all radar, have a precise measured time between an emitted microwave pulse and its reflection. A microwave pulse extends from the sensor, to the Earth, and back to the sensor. The time delay associated with the signal return is converted to distance. SAR samples its data in the range direction to the ground surface. The regular sampling interval of the SAR sensor does not

correspond to equal area sample spacing on the Earth's surface. Instead, the sample spacing is a function of the sensor's grazing angle, which varies depending on the location in a ground range referenced image (Figure 3.2). Sample spacing increases with shallow grazing angles and decreases with steeper grazing angles. However, the same image acquisition would have equal sample spacing when observed in radar slant range.

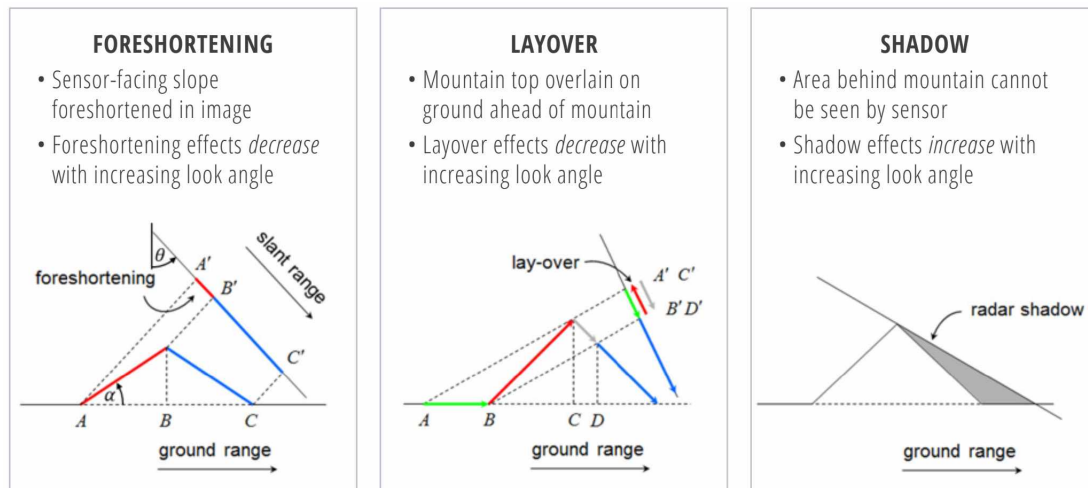


Figure 3.2: Geometric distortions of SAR images and their relationship to the acquisition geometry. Left shows foreshortening. Middle shows layover. Right shows shadow. (From Meyer, 2019).

An oblique incident angle contributes to several geometric artifacts present in the microwave images. Terrain variation, such as mountains or tall structures in urban areas, cause radar foreshortening, layovers, and shadows (Figure 3.2) (McCandless and Jackson, 2004). The geometric distortions are corrected using geometric terrain correction algorithms. Additionally, radiometric distortion causing over-brightening of sensor-facing slopes are corrected for using radiometric correction algorithms. Radar foreshortening, layover, and shadow artifacts can be caused by variations in the terrain, particularly in mountainous regions and in urban areas (Figure 3.2). These image artifacts depend largely on the viewing geometry of the sensor and the incident angle of the radar pulse (Natural Resources Canada, 2015; Woodhouse, 2015). Unlike flat areas, regions of variable terrain have a returned signal that can look compressed after an image is formed. This is due to the oblique imaging

geometry of the SAR sensor in slant-range of the sensor rather than the true horizontal distance along the ground. SAR sensors only record distance. From the perspective of a sensor, the recorded data would represent perceived distance with artifacts influenced from terrain geometry (Figure 3.2).

An example of the geometric artifacts is foreshortening, shown in Figure 3.2 (middle sketch). The sketch describes how sensor-facing slopes will be projected into a narrow range interval when observed with a side-looking radar (Natural Resources Canada, 2015; Woodhouse, 2015; Meyer, 2019). The amount of foreshortening depends both on the system's look angle θ_l , and on the slope of the earth surface α . Depending on the angle of the hillside or mountain slope in relation to the incidence angle of the radar beam, the severity of foreshortening will vary. The geometric shift will cause the slope facing the sensor to appear compressed. Similarly, the slope facing away from the sensor appears to be extended. It reaches its maximum if $\theta_l \rightarrow \alpha$; i.e. maximum foreshortening occurs when the radar beam is perpendicular to the slope such that the slope, the base, and the top are imaged simultaneously (Natural Resources Canada, 2015).

Layover is an extreme case of foreshortening. In layover situations, the tops of mountains are imaged ahead of their base (Natural Resources Canada, 2015; Woodhouse, 2015) (Figure 3.2, left pannel). Layover will also cause the sensor to return values indicating that the top is drastically diverged from its reference location and appears closer to the sensor "laying over" the bottom of the structure (Figure 3.2) (Natural Resources Canada, 2015). Layover usually occurs on steep slopes in mountainous regions, cliffs, or tall structures.

The third artifact in SAR imagery is radar shadow. Radar shadow is caused when the topography blocks the microwave signal from illuminating the target. This area will appear black in images (Figure

3.2, right panel) (Natural Resources Canada, 2015). Radar shadow effects are almost always associated with both foreshortening and layover because of obstructing terrain or buildings (Woodhouse, 2015). Shadow is commonly associated with large look angles (Woodhouse, 2015). Correcting for radar shadow is not possible because no signal is returned from that location to the sensor (Natural Resources Canada, 2015).

Radar images are subject to speckle noise that creates a 'gritty' pattern. Speckle is caused by interference from the many scattering echoes within a resolution cell (Natural Resources Canada, 2015; Woodhouse, 2015). Speckle noise is not random but an inherent property of all coherence imaging systems. Figure 3.3 shows an example of speckle noise. One correction technique for speckle noise reduction uses an extra processing step known as multi-looking (Moreira, 2013). Multi-looking is discussed in section 3.1.6.

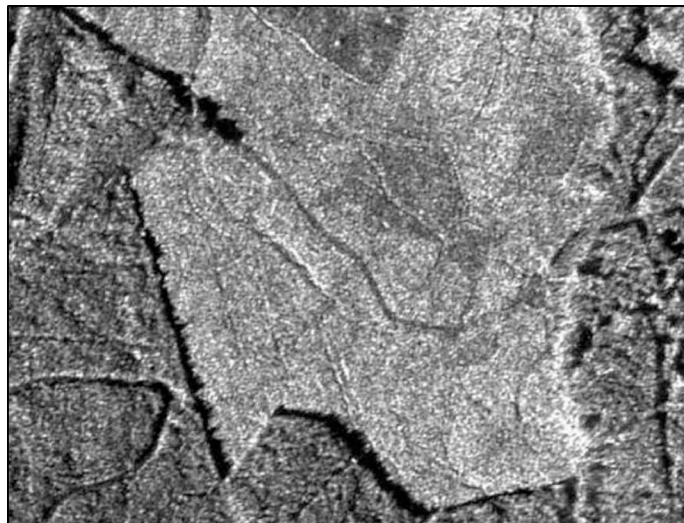


Figure 3.3: SAR image speckle. The gritty appearance appearing in this SAR image is due to speckle. Here, the image shows the signal response of a forested area (From Woodhouse, 2015).

Speckle is a byproduct of signal backscatter and the microwave interactions with the ground. There are three types of backscatter that can dominate an image: double bounce; surface; and volume

scattering (Woodhouse, 2015). The types of backscatter can be determined in the reflected signal by the type of surface the microwave pulse interacts with. For example, double bounce scattering occurs when a building or vertical object causes the incoming signal to bounce from the ground to the vertical surface and back to the sensor completing a double bounce scattering. Surface scattering is caused by the roughness or smoothness of the surface relative to the wavelength used by the radar. Volume scattering is a signature caused by a thick material like snow or a forest canopy where signal energy can be reflected, absorbed, or transferred within the material (Woodhouse, 2015). Additionally, signals can be reflected away or absorbed. Often, areas covered in standing water create little signal return and appear black in SAR images. Calm water in a terrestrial setting is a smooth surface that causes the microwave to be absorbed or bounce away from the sensor on return.

3.1.5 Multilooking

Multilooking is the process that improves radiometric resolution at the expense of spatial resolution. In SAR, the time between microwave pulse transmit and receive is used to generate the aperture length (Woodhouse, 2015). The theoretical full SAR resolution is achieved when using one look, i.e., when dedicating the full synthetic aperture to image every target on the surface (Woodhouse, 2015). Multilooking is an averaging process that creates several different sub-images in an area by partitioning the data acquired with the full synthetic aperture into several shorter, non-overlapping pieces. These images are then averaged together to obtain a full final image (Woodhouse, 2015). Multilooking is conducted in either the azimuth direction, range direction, or both azimuth and range directions simultaneously (McCandless and Jackson, 2004). Multiple measurements allow multilooking to sample the same underlying mean data independently with each look (Woodhouse, 2015). This process is commonly utilized to reduce image speckle (McCandless and Jackson, 2004).

3.2 Interferometric Synthetic Aperture Radar

Comparing phase measurements between two or more SAR images separated either temporally or spatially; forms the basis of Interferometric SAR (InSAR). InSAR is a method that allows for sub-centimeter measurements of surface displacement in the look direction of the satellite (McCandless and Jackson, 2004). This thesis utilized InSAR to observe change and to apply the two separate analyses within the AOI: 1) measuring surface deformation and 2) measuring surface topography changes.

3.2.1 Interferometric Synthetic Aperture Radar Principles

InSAR is an advanced method of radar ranging conducted by comparing the phase component of two or more separate SAR images. The first application of InSAR was the topographic mapping conducted in the 1970s as an alternative to topographic mapping from aerial photography (Graham, 1974). Graham (1974) provided a comparison between traditional mapping methods and the potential of using airborne InSAR for terrain mapping. The accuracy of a radar-produced topographic map was within the accuracy tolerances of a hand drawn map. Seasat, a SAR imaging satellite, was launched in 1978 to demonstrate the ability of spaceborne InSAR data acquisition. InSAR research during the 1980s used airborne sensors to analyze individual study areas with a focus on topographic mapping. This early research suggested that InSAR could be used from spaceborne platforms for greater accuracy than maps drawn from stereo-photography (Goldstein et al., 1988; Zebker and Goldstein, 1986).

Prior to the 1990s, InSAR analysis was mostly restricted to topography mapping due to limitations in computational power. The unavailability of computers with enough memory to process InSAR data and the limited access to SAR data, made it difficult for InSAR to gain popularity. Over the next few years, with the progression of computer technology and more satellites launched with SAR antennas, such as the European Space Agency (ESA) Remote Sensing satellites (ERS), the availability of

data to the general public was increased (Uys, 2016). A defining moment of the success of InSAR was the Shuttle Radar Topography Mission (SRTM), which produced the world's first near-global DEM (Rodriguez et al., 2005).

An alternative use of InSAR is for surface displacement mapping (Gabriel et al., 1989). Gabriel et al. (1989) were the first to analyze surface displacement using data sources from the Seasat mission to track the displacement of the ground in the Imperial Valley, California. The development of InSAR and its capabilities were improved with the launch of ERS-1 in 1991. ERS-1 was the first radar satellite launched by the ESA in a polar orbit that provided the remote sensing community with a long-time series of repeat data coverage. The accuracy of InSAR and its applications to geodetic science modeling were demonstrated by Massonnet et al. (1993). In this case, InSAR was able to detect the displacement of the 1999 Landers earthquake, 7.9 Mw, near Landers, California, with a fine spatial resolution and high precision (Massonnet et al., 1993). Currently, InSAR analysis has developed into a product where many locations around the globe are actively monitored for surface displacement (ASF, 2019). Global monitoring is done with many sensors, but ESA's Sentinel-1 is currently the most publicly accessible (ASF, 2019).

An understanding of the physics of SAR is required to understand the various aspects associated with InSAR. InSAR works based on the concept of comparing microwave phase delay. Phase delay can be found by calculating the phase difference for every image pixel between two unique points in time from two different acquisitions. The following is a description of the basic principle of InSAR summarized from Uys (2016). This property of comparing phase measurements is exploited by comparing two different SAR images in space (topography) or in time (deformation) (Woodhouse, 2015). If the surface deforms between the acquisition times, for instance due to glacier motion, ground water extraction, active

volcanism or seismic events, the surface deformation will express a phase difference between the SAR images acquired and can be analyzed in the interferogram. Several corrections to the data must be applied once the initial phase difference map interferogram is formed. There are several contributions to the observed phase difference of an image, ϕ , and is defined as follows:

$$\phi_{i,j} = \phi_{i,j,defo} + \phi_{i,j,flat} + \phi_{i,j,topo} + \phi_{i,j,atm-s} + \phi_{i,j,atm-t} + \phi_{i,j,orbit} + \phi_{i,j,noise}, \quad (2)$$

Where i, j are images in a data stack of SAR scenes such that $i < j$. The measured phase difference will contain information on the changes in topographic height between the SAR scenes encoded in $\phi_{i,j,topo}$, and the flat Earth phase, $\phi_{i,j,flat}$, and surface deformation between the image acquisition times $\phi_{i,j,defo}$ (McAlpin et al., 2017). In addition to changes in surface measurements, ϕ is also affected by atmospheric changes such as stratification, $\phi_{i,j,atm-s}$, and water vapor content, $\phi_{i,j,atm-t}$, orbital errors, $\phi_{i,j,orbit}$, and random noise $\phi_{i,j,noise}$. See Section 4 of McAlpin et al. (2017) and Woodhouse (2015) for more information. An example of the typical InSAR geometry is shown in Figure 3.4. The two main applications of InSAR (topographic mapping and deformation mapping) are described below.

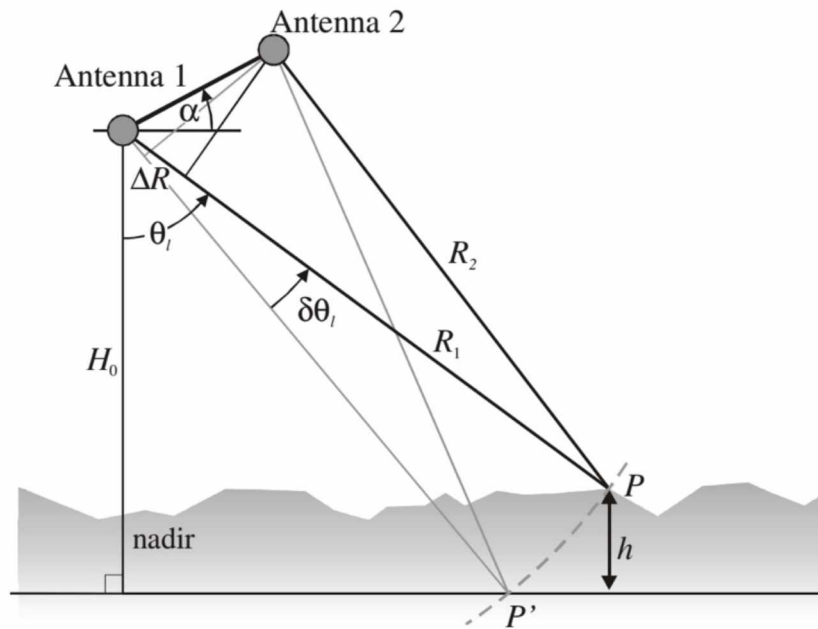


Figure 3.4: Geometry of spaceborne InSAR interferometry (From, Woodhouse, 2015).

3.2.2 InSAR-based Topographic Mapping and Height of Ambiguity

InSAR is a tool that is commonly utilized for topographic mapping (European Space Agency, 2007). Topographic mapping is commonly done with single pass interferometry (Natural Resources Canada; 2015). Two SAR images are acquired at the same time and coregistered together for processing. The advantage of single pass interferometry is that the temporal baseline (the time difference between the acquisition times of the interferometric partner images) is minimized and the coherence during the acquisition will remain relatively high. Terrain altitude measurements, thus, a topographic surface, can be extracted through the interferometric topographic phase, $\phi_{i,j,topo}$ (European Space Agency, 2007). The sensitivity and relationship of $\phi_{i,j,topo}$ and topographic height, h , is given by

$$\phi_{i,j,topo} = \frac{4\pi}{\lambda} * \frac{B_{i,j,\perp}}{r * \sin(\theta)} h, \quad (3)$$

Where $B_{i,j,\perp}$ is the perpendicular baseline between SAR scenes i and j . r is the sensor to target range, θ is the look direction, and λ is imaging the wavelength of the sensor (McAlpin et al., 2017). Processing of the phase requires flat Earth phase removal, $\phi_{i,j,flat}$, interferogram flattening to scale the topography to height, and phase unwrapping. The measured phase can be modeled to produce a topographic surface, DEM, between two SAR scenes. Change can be assessed by differencing DEMs produced using these properties.

The height of ambiguity, h_a , defined as the altitude difference corresponding to an interferometric phase change of 2π in the interferogram after it has been flattened (ESA, 2007; Takashi et al., 2019). h_a is defined as

$$h_a = \frac{\lambda * \sin(\theta)}{2B_{i,j,\perp}}, \quad (4)$$

Where the height of ambiguity is a measurement that is inversely proportional to the perpendicular baseline of an interferogram (European Space Agency, 2007; Woodhouse, 2015).

The height of ambiguity provides a value relating to the sensitivity of the satellite configuration. Longer baselines, are equivalent to a more accurate height measurement because the phase noise is equivalent to smaller DEM errors (Takashi et al., 2019). Depending on the mapping required, it may be advantageous to have a smaller or larger height of ambiguity. With a smaller height of ambiguity, the data are more sensitive to topography (European Space Agency, 2007). A larger height of ambiguity is less sensitive to decoration (European Space Agency, 2007).

3.2.3 Relative Terrain Motion: Differential Interferometry

Differential interferometry is commonly conducted to model small ground displacements (European Space Agency, 2007; Woodhouse, 2015). The principle behind differential InSAR is measuring the phase difference between acquisitions to from different points in time. If the ground has not moved, the microwave of the returned signal will not be shifted, and deformation-related phase contributions are close to zero (Woodhouse; 2015). However, if there is localized change, phase difference between the ground and its new position will result in a phase offset induced by the change in range. The phase offset is then utilized to extract the displacement of the ground (Woodhouse; 2015). Measuring the deformation phase difference, $\phi_{i,j,defo}$, and the sensitivity of the measurement is given by

$$\phi_{i,j,defo} = \frac{4\pi}{\lambda} * (d_j - d_i), \quad (5)$$

where $d_j - d_i$ represent the surface deformation, $\Delta d_{i,j}$ between SAR acquisition time i and j (McAlpin et al., 2017).

Differential InSAR is commonly referred to as repeat pass interferometry. In this method, SAR scenes are acquired over a temporal baseline on a scale of days to years depending on the motion of the observed location. With a changing temporal baseline, the deformation can be investigated on a specific timescale of interest (Woodhouse; 2015).

3.2.4 Coherence

SAR image coherence measures the fixed relationship between waves in a beam of electromagnetic radiation. Two microwaves of radiation are coherent when they are in phase. That is, they vibrate in unison. In terms of the application to radar, the term coherence is also used to describe systems that preserve the phase of the received signal (European Space Agency, 2007). Coherence is a limiting factor in InSAR as changing surface conditions can cause signal decorrelation. Additional errors can be caused by coherence loss. Coherence loss can be due to soil moisture or vegetation. InSAR requires invariant surface conditions to maintain phase coherence for differential phase measurements. Temporal variations in surface dielectric properties are common over permafrost areas due to changes in vegetation, soil moisture, and snowpack. Such variations can easily cause loss of coherence (Liu, 2010).

3.2.5 Atmospheric Effects and Other Error Sources

Despite the weather independence of SAR, phase data can contain numerous effects from the transmission of microwaves through the atmosphere. The atmosphere is a medium that can cause errors within repeat pass InSAR and within DEMs at the scale of tens of centimeters (Ding, et al., 2008). Single pass DEM errors are reduced as both images are acquired simultaneously, minimizing the effects a changing atmosphere will have on shifting the signal phase (Nonaka, et al., 2018). These effects are usually accumulated from the off-nadir sensor transition of microwaves through the troposphere and the ionosphere. Electromagnetic waves are delayed when they travel through the troposphere. Phase difference error can surpass the phase difference produced by deformation on the ground, yielding a value higher or lower than the correct value. This issue has been addressed with temporal and coherence filtering (Agram et al., 2012). The ionosphere can accelerate the phases of electromagnetic waves when they travel through the medium producing a phase shift (Ding et al., 2008). The ionosphere

is a dispersive medium affecting the radar signals proportionate to the square of the wavelength (Curlander and McDonough, 1991). Orbital errors in the path of the satellite can produce an additional long wavelength trend in phase.

3.3 SAR Data Sets Used In This Thesis

This thesis utilizes multiple data sets to test the study question and subsequent research questions. Data sets include: 1) German Aerospace Center (DLR) enhanced ellipsoid corrected (EEC), radiometrically corrected (RC), geometrically corrected (GC) TSX and TDX X-band imagery; 2) TSX slant-range SLC data and amplitude data; 3) TDX mission multi-temporal SLC data and amplitude data; 4) the ESA S1 C-band amplitude imagery and SLC data; and 5) Japan Aerospace Exploration Agency (JAXA) ALOS-2 PALSAR-2 L-Band SLC data.

3.3.1 Sentinel-1

The Sentinel-1A satellite orbits the Earth in a near-polar sun-synchronous orbit, repeating its coverage every 12-days. Sentinel-1B, an identical satellite to Sentinel-1A, was launched in 2016 in the same orbit, 180° degrees out of phase. The combination of these satellite orbits offers a 6-day repeat cycle (ESA, 2019). However, a majority of the images utilized in this study were acquired from the Sentinel-1A satellite at a 12-day repeat cycle. The data used were acquired in Sentinel-1's wide swath (IW) mode in a type of ScanSAR acquisition mode called Terrain Observation with Progressive Scan (TOPS) SAR. The basic function of TOPS SAR is of a pivoting antenna to scan a desired image path (Figure 3.5). This system is designed to have the same coverage as traditional ScanSAR images but with a nearly uniform signal-to-noise ratio and distributed target ambiguity ratio (ESA, 2019). The Sentinel-1A and 1B systems carry C-band radar sensors that can operate in various polarimetric modes including: 1) single polarization (vertical (V) transmit and vertical (V) receive: (VV) or horizontal (H) transmit and horizontal

(H) receive: (HH)) or 2) in dual polarization, (HH+HV or VV+VH), modes. SLC and amplitude data from the S1 satellites were retrieved from the Sentinel-1 data archives of the NASA Alaska Satellite Facility (ASF), NASA's Distributed Active Archive Center (DAAC) for SAR data. S1 amplitude data are used with change detection techniques to map the flood extent of the 2015 Sag river flooding. S1 SLC data are used to measure seasonal surface deformation patterns in the Sag river environment.

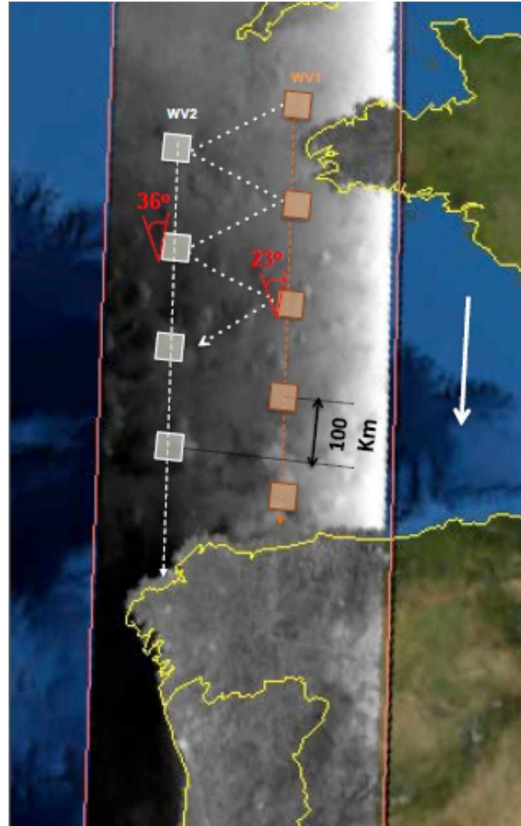


Figure 3.5: Image showing the full swath of a Sentinel-1 interferometric wide-mode SAR. White arrow shows the orbit direction of the satellite. The image acquisition is obtained by Terrain Observation with Progressive Scan (TOPS) SAR, where the antenna is pivoted to facilitate wide-swath coverage at high spatial resolution. The general path that the antenna takes to capture each image is shown along the white dashed line. The radar antenna is initially oriented toward the area indicated by the orange squares and then pivots back and forth between the orange and white sub-swaths to facilitate large area coverage. These sub-images are then compiled into the final IW-mode, bordered by orange lines.

S1 amplitude data were geocoded and fully radiometrically calibrated using ASF's automatic Hybrid Pluggable Processing Pipeline (HyP3) system (Hogenson et. al, 2016) to generate co-registered image time series for the 2015 flood season. 2015 was the first year of S1 operation, and there were

only a limited number of amplitude images available at the beginning of the 2015 Sag River flood. See Table 3.2 for a list of amplitude images utilized in this study. S1 images available in the Sag River Delta during the flood were a mixture of IW and EW mode data. The spatial resolution of S1 EW images is approximately 20 m x 40 m recorded over a 400 km swath. Within the HyP3 system, these data were geocoded to a ground sampling of 30 m x 30 m. The higher-resolution IW data were sampled at 10 x 10 m spacing.

Table 3.2: List of available SAR scenes utilized in the change detection analysis. Resolution of images are in meters.

Dataset	Sensor	Index	Band	Type	Polarization	Image Mode	Resolution
TerraSAR-X	TSX	2015-04-08	X	Amplitude	HH	Strip Map	(3,3) [m,m]
	TSX	2015-04-13	X	Amplitude	HH	Strip Map	(3,3)
	TSX	2015-04-19	X	Amplitude	HH	Strip Map	(3,3)
	TSX	2015-04-22	X	Amplitude	HH	Strip Map	(3,3)
	TSX	2015-04-24	X	Amplitude	HH	Strip Map	(3,3)
	TSX	2015-04-24	X	Amplitude	HH	Strip Map	(3,3)
	TSX	2015-04-27	X	Amplitude	HH	Strip Map	(3,3)
	TSX	2015-05-03	X	Amplitude	HH	Strip Map	(3,3)
	TSX	2015-05-05	X	Amplitude	HH	Strip Map	(3,3)
	TSX	2015-05-07	X	Amplitude	HH	Strip Map	(3,3)
	TSX	2015-05-08	X	Amplitude	HH	Strip Map	(3,3)
	TSX	2015-05-10	X	Amplitude	HH	Strip Map	(3,3)
	TSX	2015-05-11	X	Amplitude	HH	Strip Map	(3,3)
	TSX	2015-05-13	X	Amplitude	HH	Strip Map	(3,3)
Sentinel-1	S1	2015-05-23	C	Amplitude	HH	EW	(30,30)
	S1	2015-05-28	C	Amplitude	HH	IW	(10,10)
	S1	2015-05-30	C	Amplitude	HH	IW	(10,10)

S1 images were included in the change detection data stack, see section 3.4.1 for details on its inclusion. To account for missing time between TSX and TDX image acquisitions during critical portions of the flood, S1 scenes were introduced into the high resolution TSX amplitude data set for change detection analysis, see section 3.4.1 for details on its inclusion. For consistency, the S1 data included in the change detection were provided in HH polarization to match polarization of the other images used in change detection (Figure 3.2).

Initial InSAR processing of S1 SLC images was also performed using ASF's HyP3 processing system, see section 3.4.2 for details. Topographic correction of these interferograms was done using a best available DEM layer compiled from 1 arc-second SRTM data as well as DEM National Elevation Dataset (NED) sources. More information on the DEMs used by HyP3 can be found in Meyer et al. (2018). The interferograms created using HyP3 were used to analyze the sub-seasonal deformation within the AOI. Surface deformation was derived using a SBAS time-series method that is described in more detail in Section 3.3.2. To facilitate SBAS processing, HyP3 data were analyzed using the cloud-based SAR data analysis platform OpenSARLab (<https://opensarlab.asf.alaska.edu/>). This platform was developed at the ASF to enable the analysis of large volume SAR without requiring data download and local computer infrastructure. S1 SLC data were only available in the AOI for the 2017 to 2019 summer seasons (May to August). No SLC data were available prior to the 2017 summer within the AOI. For a list of InSAR scenes refer to Table 3.3.

3.3.2 ALOS-2

PALSAR-2 is the L-band radar sensor aboard the ALOS-2 earth observation satellite. ALOS-2 was launched in 2014 and operates in a near sun-synchronous orbit at an altitude of 628km (Kramer, 2002). The satellite has an orbit cycle of approximately 14 days and has the capability to be left- or right-looking depending upon how the satellite is tasked. The sensor operates in a transmit and receive mode where the polarization can be selected as single (HH/VV/HV), dual (HH + HV; VV + VH), quad (HH + HV + VV + VH), or compact polarized (Tx: oriented 45° from the sensor long axis, Rx: H or V). L-band offers many advantages over other SAR frequency bands, mostly related to higher penetration into vegetation covers, leading to improved interferometric coherence and related improved capabilities in mapping surface deformation (Kramer, 2002).

Table 3.3: List of scenes utilized in InSAR analysis.

InSAR							
Dataset	Sensor	Image acquisition date	Band	Type	Polarization	Image Mode	Resolution
Sentinal 1	S1A	2017-05-17	C	SLC	VV	IW	(80,80) 4x20 multilooked
	S1A	2017-05-29	C	SLC	VV	IW	(80,80) 4x20 multilooked
	S1A	2017-06-10	C	SLC	VV	IW	(80,80) 4x20 multilooked
	S1A	2017-06-22	C	SLC	VV	IW	(80,80) 4x20 multilooked
	S1A	2017-07-04	C	SLC	VV	IW	(80,80) 4x20 multilooked
	S1A	2017-07-16	C	SLC	VV	IW	(80,80) 4x20 multilooked
	S1A	2017-07-28	C	SLC	VV	IW	(80,80) 4x20 multilooked
	S1A	2017-08-09	C	SLC	VV	IW	(80,80) 4x20 multilooked
	S1A	2017-08-21	C	SLC	VV	IW	(80,80) 4x20 multilooked
	S1A	2017-09-02	C	SLC	VV	IW	(80,80) 4x20 multilooked
	S1A	2017-09-14	C	SLC	VV	IW	(80,80) 4x20 multilooked
	S1A	2017-09-26	C	SLC	VV	IW	(80,80) 4x20 multilooked
	S1A	2018-05-24	C	SLC	VV	IW	(80,80) 4x20 multilooked
	S1A	2018-06-05	C	SLC	VV	IW	(80,80) 4x20 multilooked
	S1A	2018-06-17	C	SLC	VV	IW	(80,80) 4x20 multilooked
	S1A	2018-07-11	C	SLC	VV	IW	(80,80) 4x20 multilooked
	S1A	2018-07-23	C	SLC	VV	IW	(80,80) 4x20 multilooked
	S1A	2018-08-04	C	SLC	VV	IW	(80,80) 4x20 multilooked
	S1A	2018-08-16	C	SLC	VV	IW	(80,80) 4x20 multilooked
	S1A	2018-08-28	C	SLC	VV	IW	(80,80) 4x20 multilooked
	S1A	2018-09-09	C	SLC	VV	IW	(80,80) 4x20 multilooked
	S1B	2018-09-27	C	SLC	VV	IW	(80,80) 4x20 multilooked
	S1A	2019-05-07	C	SLC	VV	IW	(80,80) 4x20 multilooked
	S1A	2019-05-19	C	SLC	VV	IW	(80,80) 4x20 multilooked
	S1A	2019-05-31	C	SLC	VV	IW	(80,80) 4x20 multilooked
	S1A	2019-06-12	C	SLC	VV	IW	(80,80) 4x20 multilooked
	S1A	2019-06-24	C	SLC	VV	IW	(80,80) 4x20 multilooked
	S1A	2019-07-06	C	SLC	VV	IW	(80,80) 4x20 multilooked
	S1A	2019-07-18	C	SLC	VV	IW	(80,80) 4x20 multilooked
	S1A	2019-07-30	C	SLC	VV	IW	(80,80) 4x20 multilooked
	S1A	2019-08-11	C	SLC	VV	IW	(80,80) 4x20 multilooked
	S1A	2019-09-04	C	SLC	VV	IW	(80,80) 4x20 multilooked
	S1A	2019-09-16	C	SLC	VV	IW	(80,80) 4x20 multilooked
	S1A	2019-09-28	C	SLC	VV	IW	(80,80) 4x20 multilooked
ALOS 2	PALSAR-2	2015-08-05	L	SLC	HH	Stripmap	(10,10) 6x10 multilooked
	PALSAR-2	2016-08-17	L	SLC	HH	Stripmap	(10,10) 6x10 multilooked
	PALSAR-2	2017-08-16	L	SLC	HH	Stripmap	(10,10) 6x10 multilooked
	PALSAR-2	2018-08-01	L	SLC	HH	Stripmap	(10,10) 6x10 multilooked
	PALSAR-2	2018-08-29	L	SLC	HH	Stripmap	(10,10) 6x10 multilooked
	PALSAR-2	2019-07-31	L	SLC	HH	Stripmap	(10,10) 6x10 multilooked
	PALSAR-2	2019-08-28	L	SLC	HH	Stripmap	(10,10) 6x10 multilooked

To capture the annual deformation signal within the AOI and to arrive at annual deformation measurements, all available PALSAR-2 strip map SLC data were utilized within the AOI. This data set

includes at least one annual image acquisition during August 2015 to 2019. SLC data indexing was restricted to the summer in the Sag River region to minimize the effect of snowy winters. Refer to Table 3.3 for information on acquisition dates.

3.3.3 TerraSAR-X and TanDEM-X

TerraSAR-X (TSX) and its twin satellite, TanDEM-X (TDX), are operated by the DLR to perform high-resolution SAR imaging and terrain mapping (Kramer, 2002). TSX data acquisitions began in 2007 to provide high-resolution X-band data available for a wide spectrum of scientific applications. The TSX mission was enacted with two goals: 1) provide the scientific community with multimode X-Band SAR data. A spectrum of supported scientific disciplines included hydrology, geology, climatology, oceanography, environmental monitoring, disaster monitoring and DEM Generation and Interferometry (Kramer, 2002); and 2) establishment of a commercial market for X-Band frequency imagery in Europe to support future projects (Werninghaus, 2004). The TDX mission began in 2010. The mission utilized the TSX and TDX satellites flying in close formation to image the same location at approximately the same time. This mission was augmented to the original TSX mission. The combination of these satellites in the TDX mission is beneficial because the desired interferometric baselines are produced in a highly reconfigurable constellation and the coherence is maximized. The satellites fly in a tandem, helical orbit crossing at the north and south poles (Kramer, 2002). The horizontal baseline and vertical baselines can range between 200-500 m depending on the orbit location. The satellites operate in X-band frequency at an approximate altitude of 513 km at the equator. The TSX and TDX strip map imaging mode provides images with an average resolution of 3 m x 3 m (Kramer, 2002).

The Arctic Geodata Cooperative under the direction of GeoNorth has provided this project with 17 high resolution (9 m²) repeat pass EEC, RC, GC, TSX and TDX amplitude images with partial coverage

of the Sag River. These images span the time range from April 13, 2015 to May 13, 2015. Repeat coverage of these images ranges from one to six days, averaging two days, during the flooding event. These data provide coverage during the first pulse of flooding but fail to fully capture the second pulse of flooding as these data are HH polarized and sensitive to scattering (Table 1.1 and 3.3) (Woodhouse, 2015).

Bistatic or Coregistered Single Look Slant Range Complex (CoSSc) data were utilized for InSAR processing. CoSSc data are acquired by TSX and TDX satellites flying in close configuration. CoSSc data were acquired by these satellites to support the development of multi-temporal DEMs for a subsequent analysis of topographic changes related to the 2015 Sag River floods. Eighty-three CoSSc images were provided by DLR, licensed under DLR permit number XTI_GEOS7449. A majority of the scenes were acquired during 2012 and 2015. Few images are available in the flooded area during 2016 and 2017. Images were screened based on their coverage area, acquisition time outside of the flood, and the height of ambiguity. The maximum height of acceptable ambiguity was set at ± 50 m, based on the noise level in the DEMs. The list of scenes utilized for DEM generation are listed in Table 3.4.

3.3.4 Ancillary Data

Additional high-resolution, (12 m x 12 m) TDX DEMs were provided by DLR under permit number DEM_GEOL2889. ESRI shapefiles were acquired from the Alaska Department of Natural Resources State Geo-Spatial Data Clearinghouse (<http://www.asgdc.state.ak.us/>). These layers include political boundaries, the Alaska Coastlines, Alaska State Watershed Map, and USGS historical maps and location names. Meteorological information was sourced from the UAF Franklin Bluffs monitoring station (Toniolo, 2017).

Table 3.4: List of TDX Scenes utilized for DEM generation. Height of Ambiguity listed as HOA.

Dataset	Sensor	Image acquisition date	Band	Type	Polarization	Orbit	Orbit type	Orbit Height	Image Mode	Resolution	Inclination	HOA
TanDEM-X	TMX1	2011-01-26 X	CoSSc	HH			sun-synchronous polar	319 mi	Strip Map	(10,10)	97.44	-48.283591
	TMX1	2011-01-26 X	CoSSc	HH			sun-synchronous polar	319 mi	Strip Map	(10,10)	97.44	-47.754292
	TMX1	2011-02-12 X	CoSSc	HH			sun-synchronous polar	319 mi	Strip Map	(10,10)	97.44	-45.874101
	TMX1	2011-02-12 X	CoSSc	HH			sun-synchronous polar	319 mi	Strip Map	(10,10)	97.44	-46.133402
	TMX1	2011-03-06 X	CoSSc	HH			sun-synchronous polar	319 mi	Strip Map	(10,10)	97.44	-46.993773
	TMX1	2011-03-06 X	CoSSc	HH			sun-synchronous polar	319 mi	Strip Map	(10,10)	97.44	-47.925846
	TMX1	2011-03-06 X	CoSSc	HH			sun-synchronous polar	319 mi	Strip Map	(10,10)	97.44	-47.410564
	TMX1	2012-05-13 X	CoSSc	HH			sun-synchronous polar	319 mi	Strip Map	(10,10)	97.44	-35.782143
	TMX1	2012-05-13 X	CoSSc	HH			sun-synchronous polar	319 mi	Strip Map	(10,10)	97.44	-35.560082
	TMX1	2012-07-02 X	CoSSc	HH			sun-synchronous polar	319 mi	Strip Map	(10,10)	97.44	37.2168307
	TMX1	2012-07-02 X	CoSSc	HH			sun-synchronous polar	319 mi	Strip Map	(10,10)	97.44	-36.68208
	TMX1	2012-07-02 X	CoSSc	HH			sun-synchronous polar	319 mi	Strip Map	(10,10)	97.44	-37.031261
	TMX1	2012-08-04 X	CoSSc	HH			sun-synchronous polar	319 mi	Strip Map	(10,10)	97.44	-36.964422
	TMX1	2012-08-04 X	CoSSc	HH			sun-synchronous polar	319 mi	Strip Map	(10,10)	97.44	-37.446474
	TMX1	2012-08-04 X	CoSSc	HH			sun-synchronous polar	319 mi	Strip Map	(10,10)	97.44	-37.229201
	TMX1	2013-05-11 X	CoSSc	HH			sun-synchronous polar	319 mi	Strip Map	(10,10)	97.44	-58.3605879
	TMX1	2013-05-11 X	CoSSc	HH			sun-synchronous polar	319 mi	Strip Map	(10,10)	97.44	-58.477709
	TMX1	2013-05-11 X	CoSSc	HH			sun-synchronous polar	319 mi	Strip Map	(10,10)	97.44	-58.09661
	TMX1	2015-05-21 X	CoSSc	HH			sun-synchronous polar	319 mi	Strip Map	(10,10)	97.44	8.13991356
	TMX1	2015-05-21 X	CoSSc	HH			sun-synchronous polar	319 mi	Strip Map	(10,10)	97.44	8.21533769
	TMX1	2015-05-21 X	CoSSc	HH			sun-synchronous polar	319 mi	Strip Map	(10,10)	97.44	7.95433326
	TMX1	2015-05-22 X	CoSSc	HH			sun-synchronous polar	319 mi	Strip Map	(10,10)	97.44	16.0610431
	TMX1	2015-05-22 X	CoSSc	HH			sun-synchronous polar	319 mi	Strip Map	(10,10)	97.44	-23.813856
	TMX1	2015-05-22 X	CoSSc	HH			sun-synchronous polar	319 mi	Strip Map	(10,10)	97.44	16.4389746
	TMX1	2015-05-22 X	CoSSc	HH			sun-synchronous polar	319 mi	Strip Map	(10,10)	97.44	-23.435373
	TMX1	2015-05-22 X	CoSSc	HH			sun-synchronous polar	319 mi	Strip Map	(10,10)	97.44	-24.015974
	TMX1	2015-05-22 X	CoSSc	HH			sun-synchronous polar	319 mi	Strip Map	(10,10)	97.44	16.673552
	TMX1	2015-05-23 X	CoSSc	HH			sun-synchronous polar	319 mi	Strip Map	(10,10)	97.44	6.37055433
	TMX1	2015-05-23 X	CoSSc	HH			sun-synchronous polar	319 mi	Strip Map	(10,10)	97.44	25.8714269
	TMX1	2015-05-23 X	CoSSc	HH			sun-synchronous polar	319 mi	Strip Map	(10,10)	97.44	26.9411636
	TMX1	2015-05-26 X	CoSSc	HH			sun-synchronous polar	319 mi	Strip Map	(10,10)	97.44	0.26808351
	TMX1	2015-05-26 X	CoSSc	HH			sun-synchronous polar	319 mi	Strip Map	(10,10)	97.44	5.10077529
	TMX1	2015-05-26 X	CoSSc	HH			sun-synchronous polar	319 mi	Strip Map	(10,10)	97.44	5.18233299
	TMX1	2015-05-27 X	CoSSc	HH			sun-synchronous polar	319 mi	Strip Map	(10,10)	97.44	12.157901
	TMX1	2015-05-27 X	CoSSc	HH			sun-synchronous polar	319 mi	Strip Map	(10,10)	97.44	11.9492494
	TMX1	2015-05-27 X	CoSSc	HH			sun-synchronous polar	319 mi	Strip Map	(10,10)	97.44	12.3938709
	TMX1	2015-05-28 X	CoSSc	HH			sun-synchronous polar	319 mi	Strip Map	(10,10)	97.44	-20.750905
	TMX1	2015-05-28 X	CoSSc	HH			sun-synchronous polar	319 mi	Strip Map	(10,10)	97.44	21.7624041
	TMX1	2015-05-28 X	CoSSc	HH			sun-synchronous polar	319 mi	Strip Map	(10,10)	97.44	-20.44404
	TMX1	2015-05-28 X	CoSSc	HH			sun-synchronous polar	319 mi	Strip Map	(10,10)	97.44	-20.976839
	TMX1	2015-05-28 X	CoSSc	HH			sun-synchronous polar	319 mi	Strip Map	(10,10)	97.44	21.251083
	TMX1	2015-05-30 X	CoSSc	HH			sun-synchronous polar	319 mi	Strip Map	(10,10)	97.44	-8.2716749
	TMX1	2015-05-30 X	CoSSc	HH			sun-synchronous polar	319 mi	Strip Map	(10,10)	97.44	-8.1349251
	TMX1	2015-06-01 X	CoSSc	HH			sun-synchronous polar	319 mi	Strip Map	(10,10)	97.44	7.91976463
	TMX1	2015-06-01 X	CoSSc	HH			sun-synchronous polar	319 mi	Strip Map	(10,10)	97.44	8.10392688
	TMX1	2015-06-01 X	CoSSc	HH			sun-synchronous polar	319 mi	Strip Map	(10,10)	97.44	8.17756841
	TMX1	2015-06-02 X	CoSSc	HH			sun-synchronous polar	319 mi	Strip Map	(10,10)	97.44	23.9464941
	TMX1	2015-06-02 X	CoSSc	HH			sun-synchronous polar	319 mi	Strip Map	(10,10)	97.44	-23.366463
	TMX1	2015-06-02 X	CoSSc	HH			sun-synchronous polar	319 mi	Strip Map	(10,10)	97.44	16.3622209
	TMX1	2015-06-02 X	CoSSc	HH			sun-synchronous polar	319 mi	Strip Map	(10,10)	97.44	-23.745798
	TMX1	2015-06-02 X	CoSSc	HH			sun-synchronous polar	319 mi	Strip Map	(10,10)	97.44	15.9867056
	TMX1	2015-06-02 X	CoSSc	HH			sun-synchronous polar	319 mi	Strip Map	(10,10)	97.44	16.593233
	TMX1	2015-06-04 X	CoSSc	HH			sun-synchronous polar	319 mi	Strip Map	(10,10)	97.44	3.649144
	TMX1	2015-06-04 X	CoSSc	HH			sun-synchronous polar	319 mi	Strip Map	(10,10)	97.44	1.82715407
	TMX1	2015-06-04 X	CoSSc	HH			sun-synchronous polar	319 mi	Strip Map	(10,10)	97.44	42.9873148
	TMX1	2015-06-07 X	CoSSc	HH			sun-synchronous polar	319 mi	Strip Map	(10,10)	97.44	12.1703854
	TMX1	2015-06-07 X	CoSSc	HH			sun-synchronous polar	319 mi	Strip Map	(10,10)	97.44	12.4051209
	TMX1	2015-06-07 X	CoSSc	HH			sun-synchronous polar	319 mi	Strip Map	(10,10)	97.44	11.9615191
	TMX1	2015-06-08 X	CoSSc	HH			sun-synchronous polar	319 mi	Strip Map	(10,10)	97.44	20.7461313
	TMX1	2015-06-08 X	CoSSc	HH			sun-synchronous polar	319 mi	Strip Map	(10,10)	97.44	21.2356458
	TMX1	2015-06-08 X	CoSSc	HH			sun-synchronous polar	319 mi	Strip Map	(10,10)	97.44	-20.972572
	TMX1	2015-06-08 X	CoSSc	HH			sun-synchronous polar	319 mi	Strip Map	(10,10)	97.44	21.7462514
	TMX1	2015-06-08 X	CoSSc	HH			sun-synchronous polar	319 mi	Strip Map	(10,10)	97.44	-20.439469
	TMX1	2015-06-15 X	CoSSc	HH			sun-synchronous polar	319 mi	Strip Map	(10,10)	97.44	42.8043174
	TMX1	2015-06-15 X	CoSSc	HH			sun-synchronous polar	319 mi	Strip Map	(10,10)	97.44	43.4532246
	TMX1	2015-06-15 X	CoSSc	HH			sun-synchronous polar	319 mi	Strip Map	(10,10)	97.44	41.6455805
	TMX1	2015-06-21 X	CoSSc	HH			sun-synchronous polar	319 mi	Strip Map	(10,10)	97.44	-8.1275622
	TMX1	2015-06-21 X	CoSSc	HH			sun-synchronous polar	319 mi	Strip Map	(10,10)	97.44	-8.2636824
	TMX1	2016-10-22 X	CoSSc	HH			sun-synchronous polar	319 mi	Strip Map	(10,10)	97.44	-66.429091
	TMX1	2016-10-22 X	CoSSc	HH			sun-synchronous polar	319 mi	Strip Map	(10,10)	97.44	-66.744704
	TMX1	2016-10-22 X	CoSSc	HH			sun-synchronous polar	319 mi	Strip Map	(10,10)	97.44	-66.130893
	TMX1	2016-12-05 X	CoSSc	HH			sun-synchronous polar	319 mi	Strip Map	(10,10)	97.44	-63.250258
	TMX1	2016-12-05 X	CoSSc	HH			sun-synchronous polar	319 mi	Strip Map	(10,10)	97.44	-63.558112
	TMX1	2016-12-05 X	CoSSc	HH			sun-synchronous polar	319 mi	Strip Map	(10,10)	97.44	-63.87953
	TMX1	2016-12-10 X	CoSSc	HH			sun-synchronous polar	319 mi	Strip Map	(10,10)	97.44	69.57571479
	TMX1	2016-12-10 X	CoSSc	HH			sun-synchronous polar	319 mi	Strip Map	(10,10)	97.44	-69.45674
	TMX1	2017-01-29 X	CoSSc	HH			sun-synchronous polar	319 mi	Strip Map	(10,10)	97.44	-64.803141
	TMX1	2017-01-29 X	CoSSc	HH			sun-synchronous polar	319 mi	Strip Map	(10,10)	97.44	-65.523098
	TMX1	2017-01-29 X	CoSSc	HH			sun-synchronous polar	319 mi	Strip Map	(10,10)	97.44	-65.204603
	TMX1	2017-02-03 X	CoSSc	HH			sun-synchronous polar	319 mi	Strip Map	(10,10)	97.44	3.0292494
	TMX1	2017-02-09 X	CoSSc	HH			sun-synchronous polar	319 mi	Strip Map	(10,10)	97.44	43.3585985
	TMX1	2017-02-09 X	CoSSc	HH			sun-synchronous polar	319 mi	Strip Map	(10,10)	97.44	43.0069478
	TMX1	2017-02-14 X	CoSSc	HH			sun-synchronous polar	319 mi	Strip Map	(10,10)	97.44	46.6989475
	TMX1	2017-02-14 X	CoSSc	HH			sun-synchronous polar	319 mi	Strip Map	(10,10)	97.44	46.3479784

3.4 Work flows

3.4.1 Pairwise Change Detection

The pairwise change detection approach developed by Ajadi et al. (2019) was utilized to map changes in auefis and open water extent between consecutive SAR image acquisitions (Figure 3.6). The approach combines pre-processing approaches such as log-ratio image formation and curvelet transform-based image filtering with an unsupervised image classification system to classify the progression of water within the Sag River Delta on TSX, TDX, and S1 images. These data contribute to the thesis objective of determining the environmental changes associated with the 2015 Sag River flooding events, by identifying flood areas susceptible to topographic change and long-term surface deformation. The input for the pairwise change detection is an image stack acquired throughout the

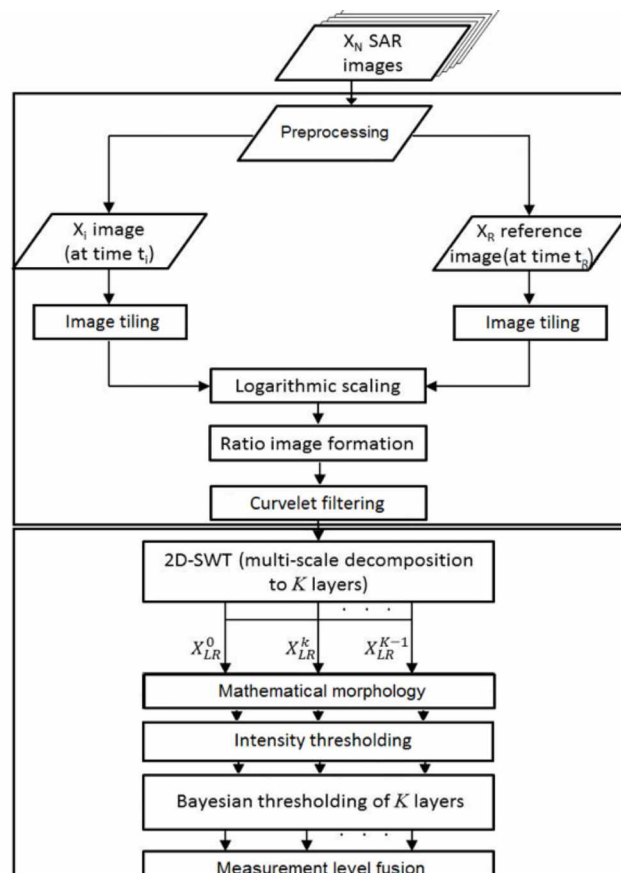


Figure 3.6: Processing method for change detection analysis. From Ajadi et al. (2019).

time of the flood. The output are maps showing: 1) the total water accumulation during the first pulse of flooding and 2) the total area inundated by the second pulse of flooding (Table 1.1).

Images were clipped to the AOI, removing excess data outside of the AOI, using the Geospatial Data Abstraction Library (GDAL) programming. The dielectric properties of water and ice allows for the quick identification of water and ice in radar remote sensing imagery. To enhance this effect, the log-ratio of subsequently-acquired image pairs is taken by dividing one image by the next image in time; thus, the log transform of the quotient is taken to produce a scaled image. New open water areas and new aufeis were scaled accordingly with the images appearing bright or dark depending on how the images were divided from each other. In this analysis, areas of new flood waters were bright and contained high positive values, and areas of new aufeis were dark and contained low to near zero values (Figure 3.6). Figure 3.6 shows Ajadi et al.'s (2019) unsupervised change detection method utilized in this study. Highlights of this method are as follows: 1) Speckle reduction using non-local filtering methods. 2) Multi-scale decomposition using 2D-SWT of the input images to generate image instances with varying resolutions and signal-to-noise ratios. 3) modeling of the probability density function of the change map at each resolution level as a sum of two or more Gaussian distributions. and 4) delineate the boundary of the changed region using measurement level fusion techniques. These techniques used the posterior probability of each class at each multi-scale image to compose a final change detection map. Ajadi et al. (2019) tested five different techniques including (i) product rule fusion; (ii) sum rule fusion; (iii) max rule fusion; (iv) min rule fusion; and (v) majority voting rule fusion; this thesis utilized the product rule (Figure 3.6)

The log-ratio calculation was repeated for every time step in the series. In locations where an image footprint is outside the coverage area of a comparison image, the image was saved and the log-

ratio calculations were repeated with the next available image with a similar footprint. The process was repeated until 80 percent of the original image was comparable with the next available image. The process was created to maximize image comparison within the image stack to model the change.

Log-ratio data have values near zero for pixels that have not changed between the acquisition of the two images. The exact value for no-change pixels can vary between each image pair depending on other environmental factors that may have occurred. In order to normalize the image distribution throughout the image time series, mean values of the log-ratio image are calculated and the mean value from all pixels is subtracted. The results are log-ratio data centered on zero.

Log-ratio data were processed through the Ajadi change detection method (Ajadi et. al., 2019). MATLAB and its matrix manipulation were used for this processing. Images were loaded and tiled with a height and width of 4096 by 4096 pixels using the GDAL `gdal_retile` tool. The height and width were assigned to this range (2^{12} by 2^{12}) to maximize processing speed in the various transforms applied to the data.

The curvelet transform of the data were used to filter the images in the data stack. The curvelet transform is utilized for image noise filtering, as it retains linear features while preserving curvature and edges. The curvelet transform coefficients are hard thresholded, a statistical method which either keeps or removes values of wavelet coefficients. Hard thresholding is applied when a frequency coefficient is larger than the Gaussian noise deviation. A discrete curvelet inverse transform then generates a denoised image.

The multiscale wavelet decomposition was then implemented with the MATLAB swt2 function, using a biorthogonal wavelet deconvolution to 6 levels. A 7th level of the wavelet deconvolution is included as the original image (Ajadi et. al., 2019). Deconvolution produces a data stack where the original log-ratio image contains reduced noise. The most geographical detail and the lowest resolution contains the residual noise and the least geometric detail. Each layer contains information to determine a multiscale representation of the change which can be queried in a numerical weighting system.

A probabilistic Bayesian approach was utilized to calculate the posterior probability that a pixel belongs to one of the three image classes. These classes are: 1) no-change; 2) new water; and 3) new ice (new aufeis). A classification result was created for each resolution level in the wavelet-based image pyramid. The approach is described further by Ajadi and modified for this thesis (Ajadi et al., 2019). Fusion of the multi-scale classification results were completed with a product rule of each image's posterior probability of change. Each map location was identified as no change, new water, or new ice. Ajadi et al.'s (2019) method produced a classified raster of the classifications. A time-series classification of raster images was produced showing these classifications. Visual checks were applied against the corresponding log-ratio images and corrections were applied manually, as needed. The final classification data were then vectorized to produce shapefiles capturing the surface waters during the time of the flooding events. Vector files were merged during the timeframe of the two Sag River flood pulses (Table 1.1).

Areas inundated by both floods were exposed to more flood water, which likely introduced more thermal energy into the ground. A geospatial intersection between the first and second flood pulses was conducted with QGIS vector tools to estimate the common area that was inundated twice.

Ajadi's (2019) overall method provided a relatively quick means of classifying image pairs to identify augeis and flood waters. This image set provided the thesis with the necessary location information of flooded areas. In addition to documenting the flooding events, these maps were useful to analyze surface deformation identified in flood affected areas.

Open water areas become easily identifiable by comparing the vectorized data with the log-ratio image. Errors become easily identifiable as the flood mask would either not include areas with the desired signature in the log-ratio image or include areas in the log-ratio image with the incorrect desired signature. Incorrectly classified areas in the flood masks were corrected using vector editing tools within QGIS. Incorrect classification manifests in individual image tiles where the new water and ice distributions are not equal. Water mask correction was conducted visually for every timestep in the data set. Visual inspection allowed for the correction of large objects such as lakes or individual overflows. The 1:24000 map scale only permitted corrections to the most obvious features. Small bodies of water adjacent to flood waters could have been thawed, inundated, or affected by the flood. As such, small bodies of water were kept in the flood mask to account for any possible flood influence.

3.4.2 Seasonal Short-Baseline InSAR

For the 2017 to 2019 summer seasons, SBAS InSAR analysis on available S1 SLC data were used to capture the seasonal deformation. The unwrapped interferograms produced an accumulative deformation map of each summer season. In this thesis, SBAS InSAR utilizes a beta release of the HyP3 software for interferogram generation and the Generic InSAR Analysis Toolbox (GIANT) for SBAS-type time series analysis (Agram et al., 2012; Hogenson et al., 2016).

Seasonal deformation of the Sag River surface was investigated for the 2017, 2018, and 2019 summer seasons utilizing SBAS InSAR processing with S1 SLC data. The summer season was selected as a five-month period of May 1 to October 1. Data from the month of September was included to account for the full melt season before the winter onset. The 2015 and 2016 summers were not analyzed due to an absence of SLC data within the AOI during that time. The following sections discuss the processing and results of SBAS InSAR from the analyzed summer seasons.

All SLC scenes were referenced to one another without filtering the temporal and perpendicular baselines. Interferograms were generated in HyP3 using the GAMMA Remote Sensing method (Werner et al., 2000). A 20 x 4 HyP3 multi-look setting was applied in azimuth and slant range, respectively, to achieve approximately square pixels and reduce noise in the phase observables. The interferograms and coherence maps were visually inspected for quality assurance. Interferogram pixels with high atmospheric noise, unwrapping errors, or low coherence outside of the Sag River region were removed from the data set. The interferograms were then uploaded into the ASF OpenSARLab (<https://opensarlab.asf.alaska.edu/>) for time series processing using GIANt. The SBAS processing workflow followed the recommended processing steps as described in the GIANt user manual (Figure 3.7) (Agram et al., 2012). The default SBASInvert.py script was applied to invert the interferograms for line-of-sight (LOS) deformation time series information. This analysis used a 2-month temporal filter and a variable coherence filter ranging between 0.1 and 0.3. A reference point was selected in a floodplain northwest of the Sag River at latitude 70.20223292°N, longitude -148.34786692°W. This reference location was also selected by Liu et al. (2010) because barren floodplains show high coherence in most of the interferograms. The reference location was also selected because of its low levels of erosion and deposition. The proximity to the river and the presence of gravel generally limit the formation of ground ice at this location, further guaranteeing a consistent stable reference point with reduced frost heave

and subsidence from thawing. To constrain the effect of orbital ramps within the data, the data set was leveled by fitting a plane with a least-squares regression to high coherent points within the data set (coherence greater than 0.997) that are assumed to have negligible deformation. The 2D planes were then subtracted from the deformation data. This process was repeated for every timestep in the data series.

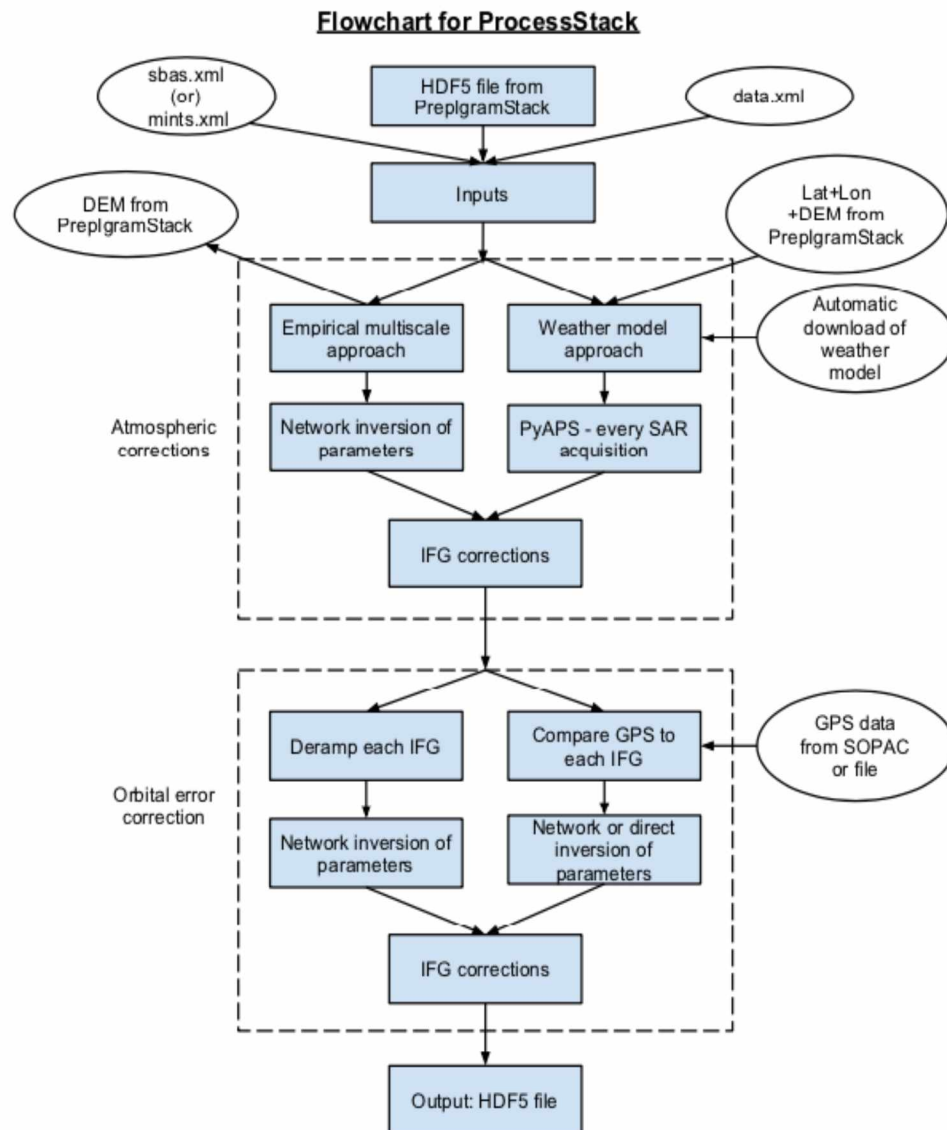


Figure 3.7: Processing method for SBAS InSAR analysis. From Agram, 2012.

The flat topography of the Sag River Delta and the general nature of permafrost environments allow surrounding soils to confine the deformation to the vertical direction. At this point all data are in LOS deformation. To convert to vertical deformation, the incident angle map data were utilized to transform the data from LOS to vertical deformation. The final products are seasonal vertical deformation maps over the AOI for the 2017 to 2019 summer seasons.

Error estimation from the SBAS method is conducted using a jackknifing method built into GIAN libraries (Agram et al., 2012). Similar to bootstrapping, jackknifing is utilized to estimate the variance and bias in a sample (Nisbet et al., 2018). The basic methodology of jackknifing involves a leave-one-out strategy of the estimation of the mean in a data set of m number interferograms from an n number of unique scenes. GIAN creates an n number of models built on the data set with different factors left out of each model (Agram et al., 2012). A separate inversion is conducted with the data set discluding the missing factor to produce a unique result. This process is continued by eliminating different sets of observations (Nisbet et al., 2018). Results of jackknifing are an assemblage of solutions can be interpreted to produce summary information (Nisbet et al., 2018). The estimates of all models are then aggregated into a single estimate of error (Agram et al., 2012; Nisbet et al., 2018).

Data processing parameters for the 2017 summer are as follows: S1 data were processed from May 29, 2017 to September 26, 2017. Eleven unique SAR scenes were utilized over this period. SLCs were consistently acquired every 12 days during the observation period. Data were referenced to a master image, May 29, 2017, for processing (Figure 3.8). Initially all possible interferogram combinations were generated from the eleven available scenes. No temporal baseline or perpendicular baseline threshold was utilized to reduce the interferogram count. Interferogram quality was filtered by visual inspection of the interferogram phase noise and by consulting the corresponding coherence plot.

Images showing unwrapping errors or atmospheric noise contained in interferograms were removed from the data stack. Coherence values less than 0.4 in flood-inundated areas were removed. After these data selection steps, 24 interferograms remained for surface deformation analysis (Figure 3.8). An SBAS InSAR approach was applied to invert the deformation time series from the data. A 2-month temporal filter and a coherence threshold of 0.3 was applied during processing.

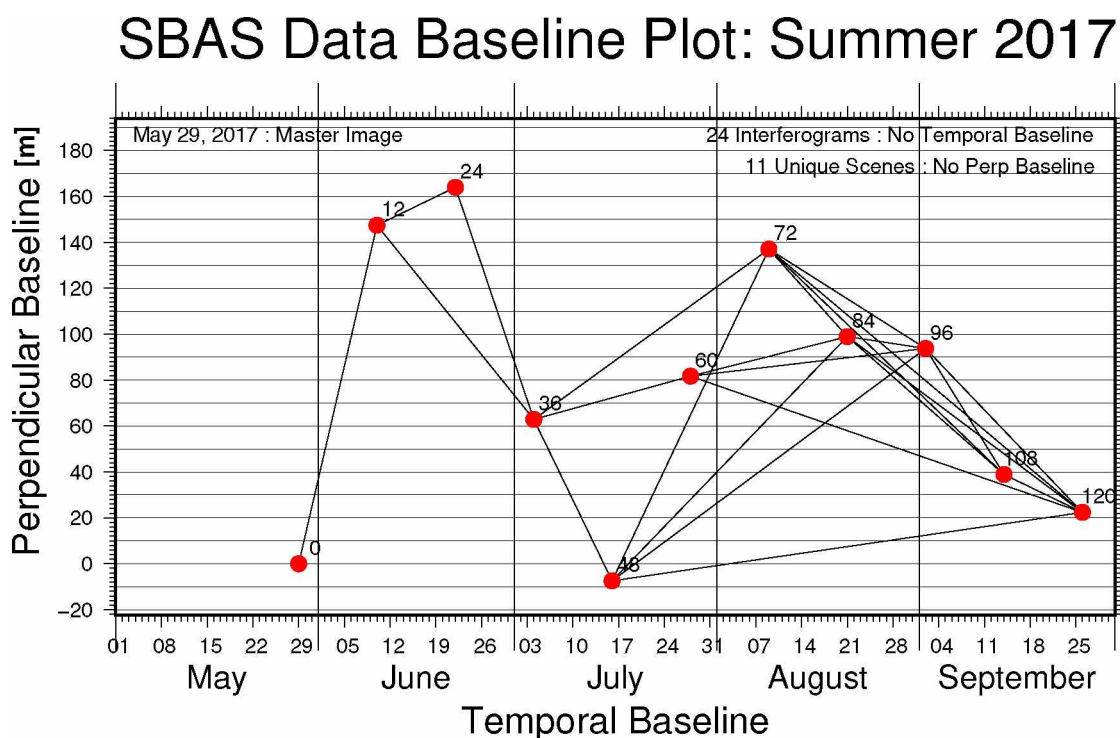


Figure 3.8: Baseline plot of the 2017 summer SBAS InSAR data set. Images referenced to master image, May 29, 2017, defined as day 0 in the figure. The annotated numbers show days after the acquisition of the master image.

Data processing steps for the 2018 summer are as follows: S1 data were processed for the period of July 11, 2018 to September 9, 2018. Six unique SAR scenes were utilized over this period. SLCs were consistently acquired every 12 days during the observation period. All other 2018 scenes prior to July 11, 2018 were not utilized due to low coherence within the AOI causing widespread decorrelation in most early summer SAR Scenes. The data meeting the requirements for processing were referenced to a master image, July 11, 2018, for processing (Figure 3.9). Initially all possible interferogram combinations

were generated from the six available scenes. No temporal baseline or perpendicular baseline threshold were utilized to reduce the interferogram count. Interferogram quality was filtered by visual inspection of the interferogram and corresponding coherence plots. Images showing unwrapping errors or atmospheric noise contained in interferograms were removed from the data stack. Coherence values less than 0.4 in flood inundated areas were removed. Ten interferograms passed these inspection steps and were utilized (Figure 3.9). An SBAS InSAR approach was used to derive deformation time series referenced to the first image in the stack. Data were processed using a 1-month temporal filter and a coherence threshold of 0.1 was used in the SBAS process.

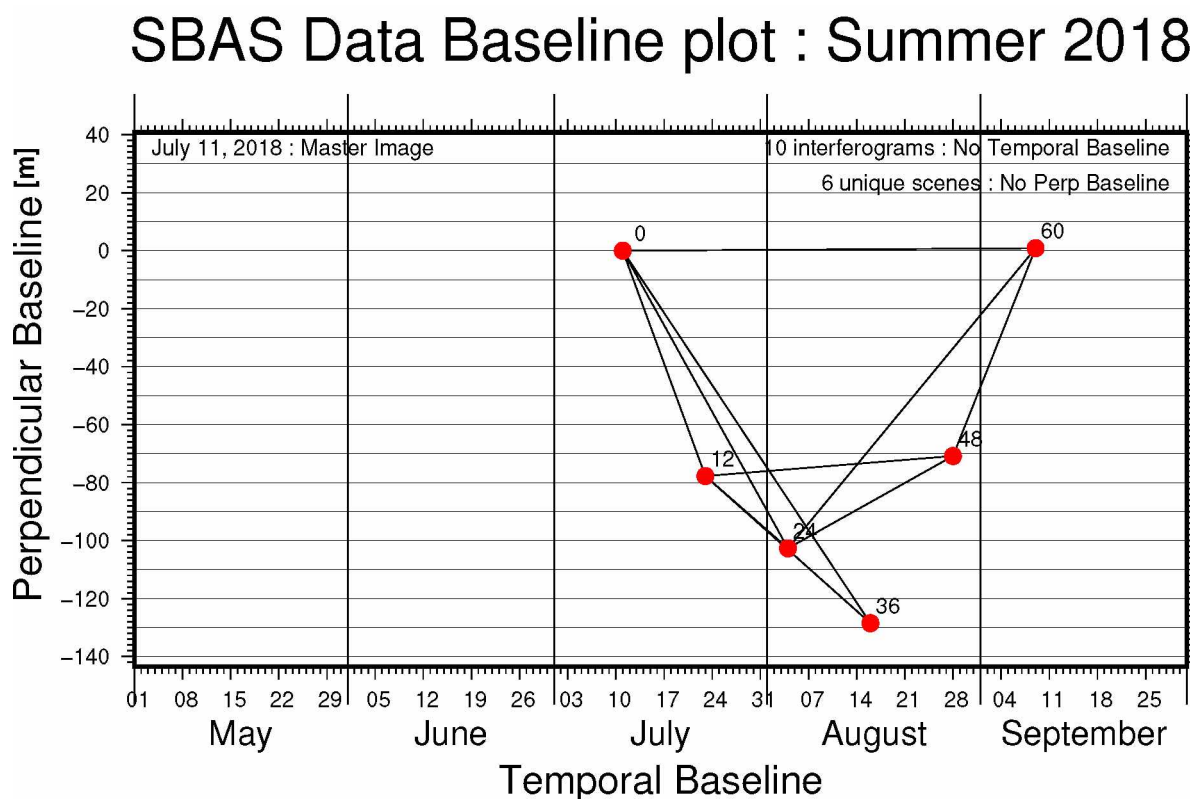


Figure 3.9: Baseline plot of the 2018 summer InSAR data set. Images referenced to master image, July 11, 2018, defined as day 0 in the figure. The annotated numbers show days after the acquisition of the master image.

Data processing steps for the 2019 summer were S1 data were processed from May 31, 2019 to September 29, 2019 similarly to the sampling period as the other summers. Ten unique SAR scenes were

utilized for this period. SLCs were consistently acquired every 12 days during the observation period except for a dropped acquisition on August 23, 2019. Data were referenced to a master image, May 31, 2019, for processing (Figure 3.10). All possible interferogram combinations were generated from the available ten scenes. No temporal baseline or perpendicular baseline threshold was utilized to reduce the interferogram count. Interferogram quality was filtered by visual inspection of the interferogram and corresponding coherence plot. Interferograms containing unwrapping errors or atmospheric noise contained in interferograms were removed from the data stack. Additionally, coherence values less than 0.4 in flood-inundated areas were removed. Fifteen interferograms remained after these selection steps and were used for SBAS-type InSAR analysis. A 2-month temporal filter and a coherence threshold of 0.3 was applied.

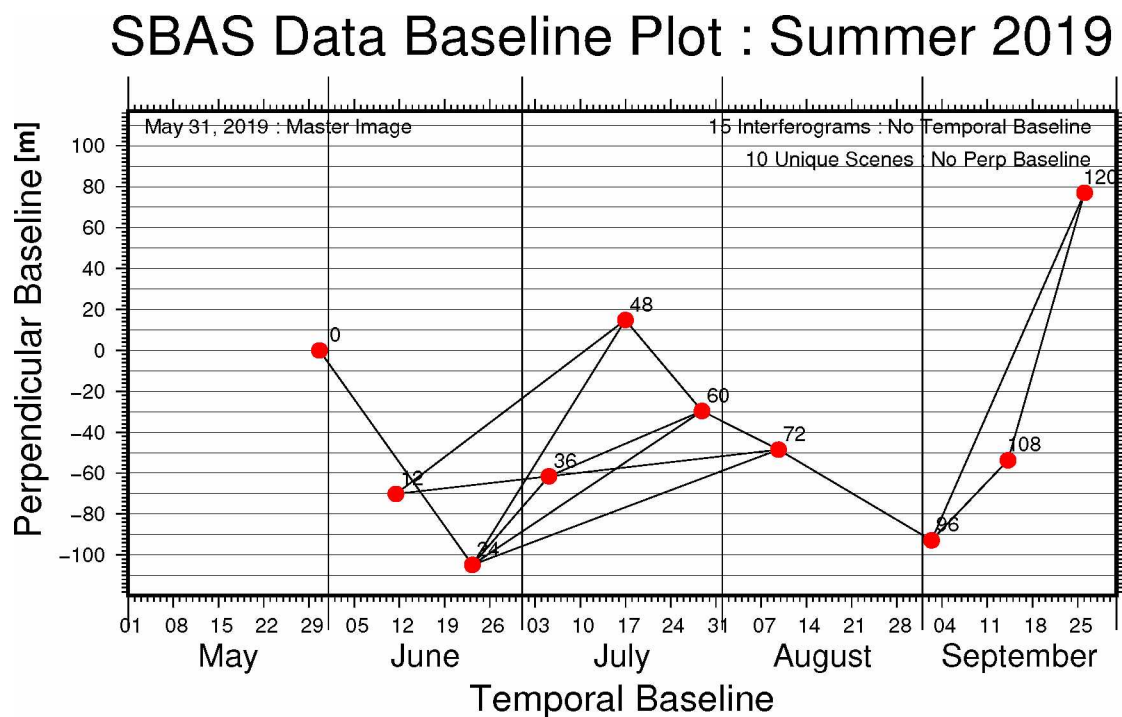


Figure 3.10: Baseline plot of the 2019 summer InSAR data set. Images referenced to master image, May 31, 2019, defined as day 0 in the figure. The annotated numbers show days after the acquisition of the master image.

To assist in quantifying the effect of the flood on seasonal surface deformation patterns, seven points of interest (POI) were selected based on spatial analyses in the AOI (Figure 3.11). The seven POIs that were selected in the AOI show the deformation throughout the Sag River at several temporal steps. Points were placed at locations inside and outside the flood zones. See Table 3.5 for surficial geologic description of each point. Notable POIs are: POI 1, POI 2, and POI 3 were selected in known inundated zones; POI 4 is placed on an oil pad. POI 5 and POI 6 were selected in areas for which flooding was not observed. POI 7 was placed at an abandoned floodplain with dune deposits and is the SBAS InSAR reference location (Figure 3.11). The results of the seasonal deformation analyses will be presented and discussed in Section 4.1.2.

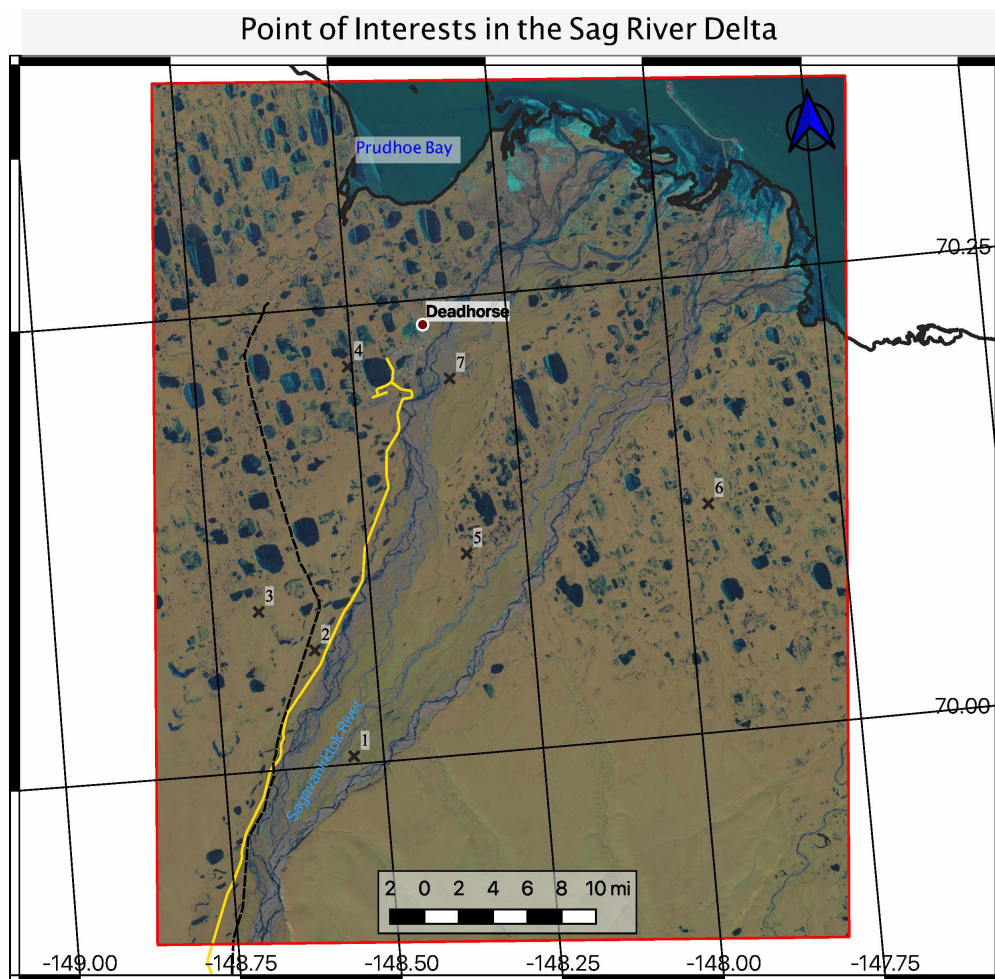


Figure 3.11: Points of interest (POI) of the Sag River Delta. Surficial geology at the POIs are summarized in Table 3.5.

Table 3.5: Summary of the surficial geology at points of interest in the AOI (Figure 3.11) (Rawlinson, 1993).

<i>POIs</i>	<i>Geological Unit (Figure 2.16)</i>	<i>Lithology (Rawlinson 1993)</i>	<i>Site Description (Figure 2.1)</i>
Point 1	Qfa (abandoned flood plain)	Peat and pebbly silt to fine sand. Mixtures or interbeds of all three. Peat up to 1 meter in thickness. Clasts are sub-rounded to rounded. Often cryoturbated. Unit rarely exceeds 3 meters. Indistinct scarps. Sharp contact with underlying layers with fluvial channels. Unit is continually frozen barring segregated ice or ice wedges that thaw to depths of 2/3 meter in summer. Unit floods infrequently.	Elevated surface marked by the presence of various grasses. Surface supports tundra and includes exposure of low-centered ice wedge polygons. Infrequent lakes and large arroyos. Affected by 2015 flooding.
Point 2	Qat (alluvial terrace)	Peat and pebbly silt to fine sand. Mixtures or interbeds of all three. Upper unit of peat up to 1 meter, often cryoturbated and vertically foliated. Deposited by fluvial processes. Sand typically underlies unit. Fine sand underlies unit. Sharp contact with channel. Channels usually contain pebbly to cobbly, sub-rounded to rounded sand. Unit is continually frozen barring segregated ice and ice wedges that thaw to depths of 2/3 meters in summer. Unit floods frequently due to proximity to river.	Location bounded by the TransAlaska Pipeline and Dalton Highway. Lakes and surface water are common along the flanks of the pipeline and highway. Various grasses. Surface supports tundra and includes exposure of low-centered ice wedge polygons. Large arroyos connect drainages in location Affected by 2015 flooding.
Point 3	Qau (undifferentiated alluvium)	Peat and silt to fine sand. Mixtures and interbeds of all three. Underlain by mixes of sand or gravel. Peat and peat rich pebbly silt compose the upper layers of this unit averaging 1 meter by noted up to 38 cm in thickness. Sediments cryoturbated and vertically foliated. Pebbly sand and silt comprises the bottom 3 meters of this unit. Unit is continually frozen barring segregated and ice wedges that thaw to depths of 2/3 meter in summer. Unit floods frequently due to proximity to river.	Location is in flat open location west of the Dalton Highway. Numerous lakes and flooded ice wedge polygons are noted through the local expanse of this unit. Various grasses are present in this unit. Confined drainages are rare within this location. Affected by 2015 flooding.
Point 4 and Point 6	Qsg (alluvial plain)	One to 1.3 meters of pebbly fine-eolian sand at the surface. Interbeds of pebbly silt. Interbeds noted close the thaw basins. Unlain by pebbly fine to medium sand and gravel. Unit has been noted to be up to 15 meters in thickness. Gravel averages 3 cm in diameter. Cobbles and boulders are common at the base of this unit. Units continually frozen barring segregated ice and ice wedges that thaw to depths of 2/3 meter in summer. Ice wedges common in the upper 3 meters of this section. Unit floods frequently due to proximity to river.	Point 4 is located on top of a large oil pad (Prudhoe Bay Unit 13). Fill added to environment to support road and pipeline construction and drilling operation. Deadhorse, Alaska within 1.6 km of location. Low-centered polygons area adjacent to manmade structures. Polygons appear to contain water at the borders. Large thaw lakes surround this location. Not affected by flooding. Point 6 is placed east of the River drainage and away from manmade structures. Low-centered polygons area adjacent to man mad structures. Polygons appear to contain water at the borders. Large thaw lakes surround this location. A small tributary flow near this location.
Point 5	Qt (Thaw Lake)	Peat and pebbly silt to fine sand. Mixture and interbeds of all sediments. Sediments rarely exceed 2 meters. Scarps bounding this unit are distinct. Ice wedges common in the upper 3 meters of this section. Unit floods frequently due to proximity to river.	Point 5 is located in thaw lake. Location show a depression with a shape equivalent to the lake surrounding it. Qt sediments extend from Qau and Qfa, recognizable in surface imagery. Irregular shaped lakes are resented around this point. Flooded ice wedge Not affected by 2015 flooding.
Point 7	Qsd (Sand Dune)	Fine to medium sand derived from barren location. Dunes up to 6 meters high. Dunes are longitudinal trending northeast to southwest. Pore ice is common in vegetated dunes. Seasonally thawed up to 1meter in depth. Reworked yardangs are common. Unit may seasonally flood.	Location is at an inactive floodplain east of the airport at Deadhorse, Alaska. Ice wedge polygons are not noted in surface drainages are small and infrequent. InSAR reference location in center of deposit. Not affected by 2015 flooding.

3.3.3 Multi-Year Short-Baseline Subset InSAR

To analyze the annual deformation, ALOS-2 level 1.1 data were downloaded from the JAXA Earth Observation Data Utilization Promotion Platform. In total, seven acquisitions were available for the AOI within the targeted time period (Figure 3.2). ALOS-2 carries an L-Band, 1270 MHz, radar antenna. L-band signals have longer wavelengths compared to the Sentinel-1 C-band data and provide more penetration power than C- and X-band radar (Global Forest Observation Initiative, 2018). L-Band showed high coherence in the AOI, permitting the formation of annual interferograms. Unwrapped interferograms were generated with the GAMMA Sensing Software using the standard 2-pass differential interferometry work-flow followed by a minimum cost function unwrapping procedure (Werner et al., 2000). The GInT software was used to derive time series of surface deformation estimates from the ALOS-2 interferograms.

Unwrapped interferograms were generated for image pairs with up to an approximately 4-year temporal baseline. During processing, the images were coregistered and 6 x 10 multilooking was applied. Subsequently, the interferometric phase was unwrapped using GAMMA's minimum cost flow approach. Low coherence areas were masked, including lakes and large sections of the Sag River channels.

To remove the topographic phase from each interferogram, the topographic phase was simulated from a high-resolution TDX DEMs of the AOI. The TDX DEM was projected into radar coordinates to match the footprint of the radar images. The unwrapped phase was simulated from this DEM using baseline information from the image pair and the phase simulation program. The scaled topographic phase was then subtracted from each interferogram. The resulting interferogram stack contained the differential phase between the two ALOS-2 acquisitions. The phase was converted to

surface elevation to produce a topographic correction for the TDX DEM to the timeframe the CoSSc data were acquired.

The produced interferograms were visually checked for unwrapping errors and georeferencing issues. Comparing the produced interferograms from 2015 and 2019 exhibited multiple unwrapping errors. Uncorrectable interferograms with unwrapping errors were removed from the data set.

The interferograms, coherence maps, LOS files, incident angle files, and amplitude images were uploaded into the ASF OpenSARLab for processing using GfANt (Figure 3.7). The data were processed in the same manner as the S1 data with GfANt software. A 0.3 coherence threshold was applied to the data to select reliable pixels for which deformation was derived. Jackknifing error estimation was applied similarly as described in Section 3.4.2. The resulting deformation was converted from LOS to vertical deformation by assuming that the deformation was laterally confined. The data were de-ramped using the deformation values of the high coherence areas with coherence values greater than 0.95. The reference location was assigned at the mudflat east of the airport at Deadhorse, Alaska; the same location utilized for processing the S1 data sets.

Within the deformation data, there were years that contained two acquisitions that were earlier and later than the acquisitions in other years. For the years where there were more than one acquisition, the deformation was averaged together to produce an average deformation for that year. The data were filtered spatially using a Gaussian smoothing filter and smoothed temporally using a two-year Savgol filter (Press and Teukolsky, 1990).

A high-pass filter was applied to the final deformation map to remove the long period signals present within the deformation map. For this step, a Gaussian high-pass filter was applied to the data using a fast Fourier transformation. Long period frequencies with an area greater than 41,044,434.1 m² (3985.8 m in east-west x 3277.8 m in north-south) were removed from the data set. A final filtered map was produced from this additional step.

Deformation between 2015 and 2019 was processed from August 5, 2015 to August 28, 2019. SLCs were consistently acquired annually. During 2018 and 2019, an acquisition was not available for the mid-August range. To substitute the deformation signal for mid-August, two acquisitions were acquired at the beginning and end of August and deformation rates calculated from these acquisitions were averaged. Data were referenced to the master image, August 5, 2015, for processing (Figure 3.11). Initially all possible interferogram combinations were generated from the seven available scenes. No perpendicular or temporal baseline threshold was utilized to reduce the interferogram count. Interferogram quality was filtered by visual inspection of the interferograms and corresponding coherence plots. Interferograms containing unwrapping errors or atmospheric noise were removed from the data stack. The interferograms removed from the data stack were the 4-year, 2015 to 2019, interferograms. Using these filters, 21 interferograms were selected for further processing (Figure 3.12). An SBAS InSAR processing approach was applied to invert deformation time series from the available data. GIANt specific processing parameters included a coherence threshold of 0.3 was a 2-year temporal filter.

Seven POIs were utilized from time series and spatial analyses in the AOI (Figure 3.11). The seven POIs were selected as the same points utilized in S1 deformation maps. See Table 3.5 for geologic description of the POIs. Results from this analysis are summarized in Sections 4.1.2 and 4.1.3.

Figure 10 is a plot showing the Perpendicular Baseline [m] versus Temporal Baseline for the August 5, 2015 : Master Image. The plot displays 21 interferograms (No Temporal Baseline) and 7 unique scenes (No Perp Baseline). The x-axis represents the Temporal Baseline from 2015 to 2019, and the y-axis represents the Perpendicular Baseline from -350 to 150 m. Red dots mark specific points, and lines connect them, illustrating the relationship between temporal and perpendicular baselines.

Point Label	Approx. Temporal Baseline (Year)	Approx. Perpendicular Baseline [m]
0	2015.0	0
378	2016.0	-120
742	2017.0	-70
1092	2018.0	-80
1120	2018.0	-170
1484	2019.0	-190
1456	2019.0	-310

3.4.4 DEM Differencing

Using the TSX and TDX satellites, an individual DEM can be produced for each image acquisition date. GAMMA Remote Sensing Software was employed for this process. The process is outlined in Figure 3.13. The CoSSc data were utilized to produce an interferogram. These scenes underwent 2x2 multi-looking to scale the data to the approximate resolution of the reference DEM. The 12 m² TDX DEM was

utilized as the reference surface for all DEM products. To remove the flat Earth phase from the data, a simulated flat Earth phase generated from the reference DEM was projected into radar coordinates and subtracted from the interferogram. Unwrapping of the interferogram was conducted using the GAMMA minimum cost flow algorithms. The unwrapped interferograms were then converted to a differential height value (difference between reference DEM and true height). To remove any ramps and offsets in the differential height map, a least-squares fit plane was subtracted from the surface using GDAL. The detrended data were then added back to the reference DEM to produce a series of absolute DEMs.

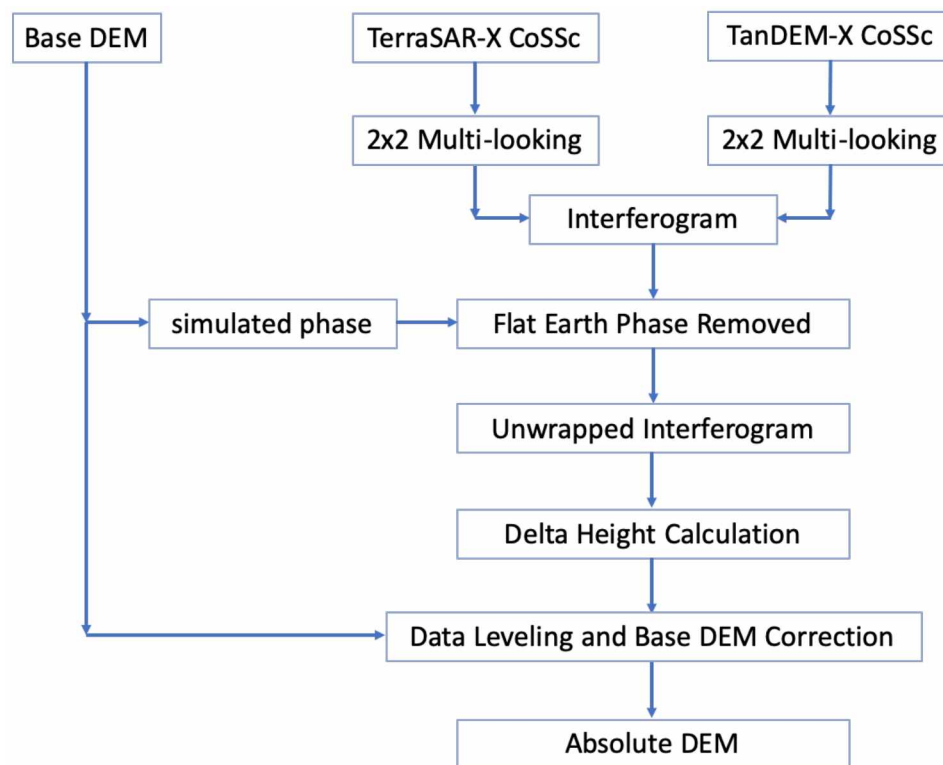


Figure 3.13: Processing flow diagram for absolute TDX DEM generation in GAMMA.

Areas of open water typically cause signal decorrelation and generate noise. A water mask was generated from low coherence areas using thresholding. A coherence threshold of 0.4-0.6 was utilized. Pixel values exceeding this selected threshold were designated land and pixel values below this threshold were designated water. The water mask was generated from the coherence maps from ALOS-

2 and S1 SLC data. A range of coherence threshold values was due to the variability of each SAR scene. A water mask was produced from each coherence map. As this thesis is focused on the change that occurred along the Beaufort Coastal Plain, the Franklin Bluffs Foothills in the southeastern AOI were masked out. Removing the Franklin Bluffs Foothills also minimized the effect of foreshortening and possible layover generated from the terrain. The mask is shown in Figure 3.14, and was applied to every absolute DEM generated by the GAMMA Remote Sensing software.



Figure 3.14: Coherency derived water mask for DEM differencing. Franklin Bluffs were also masked to remove the Brooks Range foothills terrain and possible errors.

DEMs can contain small shifts relative to each other. These small horizontal or vertical shifts between DEMs can introduce bias that will lead to large inaccurate estimations of vertical differences between the DEMs. To mitigate bias, all DEMs are coregistered to each other using the Python3.7 software library “pybob”, developed by Nuth and Kääb (2011). Coregistration compares the elevation differences with the terrain slope and aspect of the points where notable differences are measured. Shifts between the DEMs are modeled and adjusted at these locations leading to more accurate estimations of the differences between two elevation models. DEMs undergoing coregistration were adjusted in three iterations according to the Nuth and Kääb (2011) recommendations. A final correction was applied to each temporal TDX DEM pair with coregistration prior to DEM differencing.

In order to produce a pre-event reference DEM, all available pre-event DEMs were averaged together before the coregistration. The averaged DEM was produced by taking the mean for all available 2011, 2012, and 2013 DEMs using the GDAL mosaic tool. The averaged elevation data were coregistered to DLR’s TDX 12 m² resolution DEM (Figure 3.15). The pre-flood DEM is shown in Figure 3.16. The averaged surface represented topography unaffected by flooding was used as a reference to compare change from the flooding event. Slight differences are contained in the pre-flood average DEM (Figure 3.16) compared to DLR’s TDX 12 m² DEM (Figure 3.15). Notable differences are image boundaries signified by missing data, a large depression near the eastern shoreline of Prudhoe Bay, and small isolated depressions occurring throughout the AOI (Figures 3.15 and 3.16).

Multi-temporal DEMs with heights of ambiguity $\geq \pm 50$ m and those acquired during the Sag River flood period were removed from the analysis. The December 5, 2016 DEM was acquired in a critical time after the flooding events and allows for comparison of over 1 year later. The DEM was the only DEM acquired in 2016 that did not contain horizontal data shifts. If the DEM contained a shift or unresolvable

TanDEM-X Reference DEM

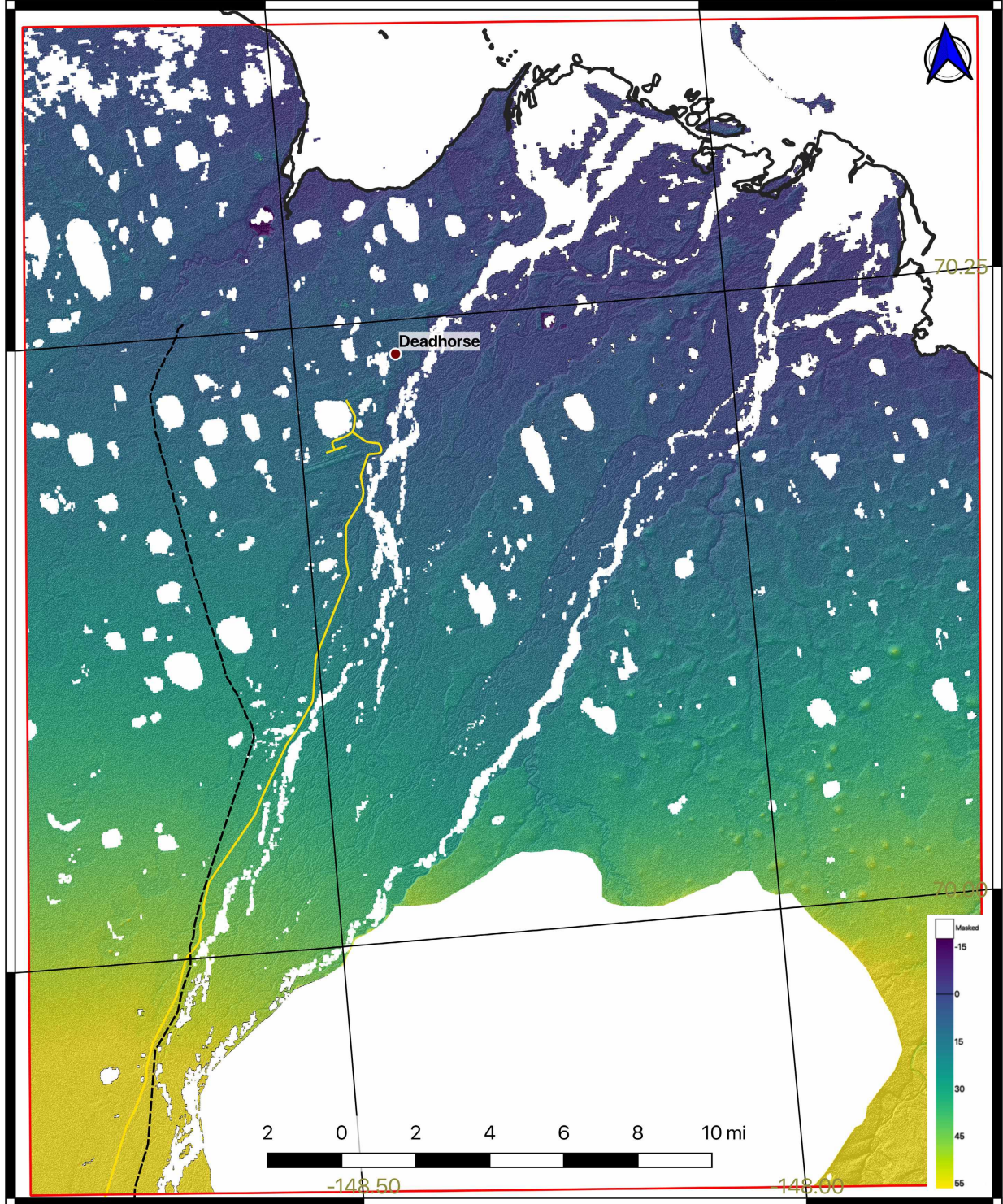


Figure 3.15: DLR TanDEM-X 12 m² DEM used to reference topographic data. Dalton Highway (yellow) and TransAlaska Pipeline (black-dashed) are shown. Colors indicate elevation in meters.

Pre-2015 Sagavarnirktok River Flooding

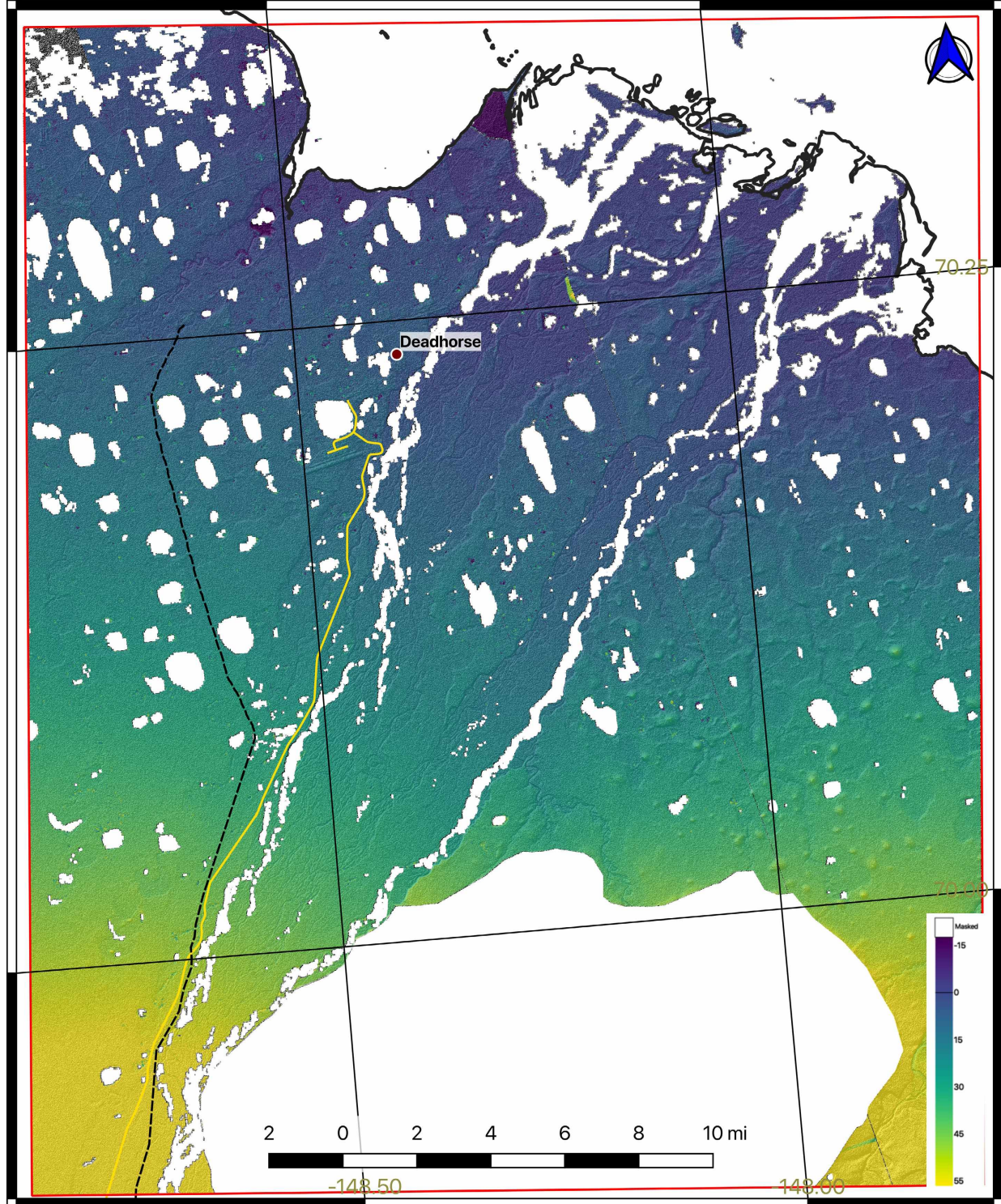


Figure 3.16: TanDEM-X 12 m² pre-flood DEM used for DEM differencing. Dalton Highway (yellow) and TransAlaska Pipeline (black-dashed) are shown. Colors indicate elevation in meters.

unwrapping issues, the DEM was also removed from the data set. Shifted data from 2017 were kept in the data set because there was only a single acquisition available for that year. A water mask was applied over the flooded areas (Figure 3.14).

DEM differencing was achieved by coregistering a slave DEM, later acquisition, to a master DEM, first acquisition, prior to differencing. A total of 48 DEMs met the height of ambiguity thresholding requirements. Of the 48, 16 DEMs were acquired during the 2011, 2012 and 2013 summers and were averaged together in a pre-flood DEM. Two DEMs were acquired during the 2016 winter, one DEM was acquired in the 2017 winter, and the remaining 29 DEMs were acquired during the 2015 summer. To limit the analysis, this thesis focused on four time frames: i) pre-flood DEM to May 27, 2015, ii) pre-flood DEM to June 21, 2015, iii) June 21, 2015 to December 5, 2016, and iv) December 5, 2016 to February 2017. See Table 1.1 for timing relationship to the flood. Note differenced DEM (DDEM) coverage varies throughout the AOI. Areas of missing data are analyzed in the joint data analysis section (Section 4.2) by including additional DDEMs differencing the pre-flood average DEM to the iv) June 8, 2015, v) December 5, 2016, and vi) May 21, 2015 DEMs.

Shifts and data ramps were present in the data after coregistration. To remove these long periods signals, a high-pass filter was applied to the final DDEM. A Gaussian high-pass filter was utilized. Long period signals with an area greater than $14,775,996.3 \text{ m}^2$ (1966.7 m in east-west x 2391.5 m north-south) were removed from the data set. Final, filtered differenced elevation models were produced from this additional step. A total of 48 DDEMs were high-pass filtered.

3.4.5 Dataset Comparison and Analysis Approach

A high degree of spatial variability is present within the AOI. Variability in the AOI included differences in the surficial geology, quantity of ice content, local area hydration, thermokarst presence, and several others. Due to the high environmental variability of the AOI, the thesis focused the analysis of the data to a limited number of areas. Analyzed areas were selected for interpretation based on their similar surficial geology and to contain inundated and flood-unaaffected areas.

The focus areas are shown in Figure 3.17. A statistical comparison of each area was conducted within each geologic formation to compare inundated and flood-unaaffected locations (Section 4.2). Data sets were masked to inundated and flood-unaaffected areas of the same geologic formation within the same focus area for analysis. Geologic formations that were mostly or completely inundated were omitted. The parameter of each surficial geologic formation was drawn with QGIS geometry tools within each focus area. The shapefile of each formation was clipped with the flood mask producing a polygon of flooded areas per geologic formation in each focus area. The flood-unaaffected areas in each formation were identified with a symmetric difference between the flooded areas per geologic formation and the original digitized surficial geologic formation. These steps produced shapefiles of inundated and flood-unaaffected areas for each geologic formation in the focus areas. Violin plots were utilized to display the mean, first and third quartiles of data distribution, and the kernel density, describing the distribution of deformation measurements, and associated population across the deformation time series. An individual test of each focused area to the study question was conducted. A summary of focus area analysis provided in Section 4.3.

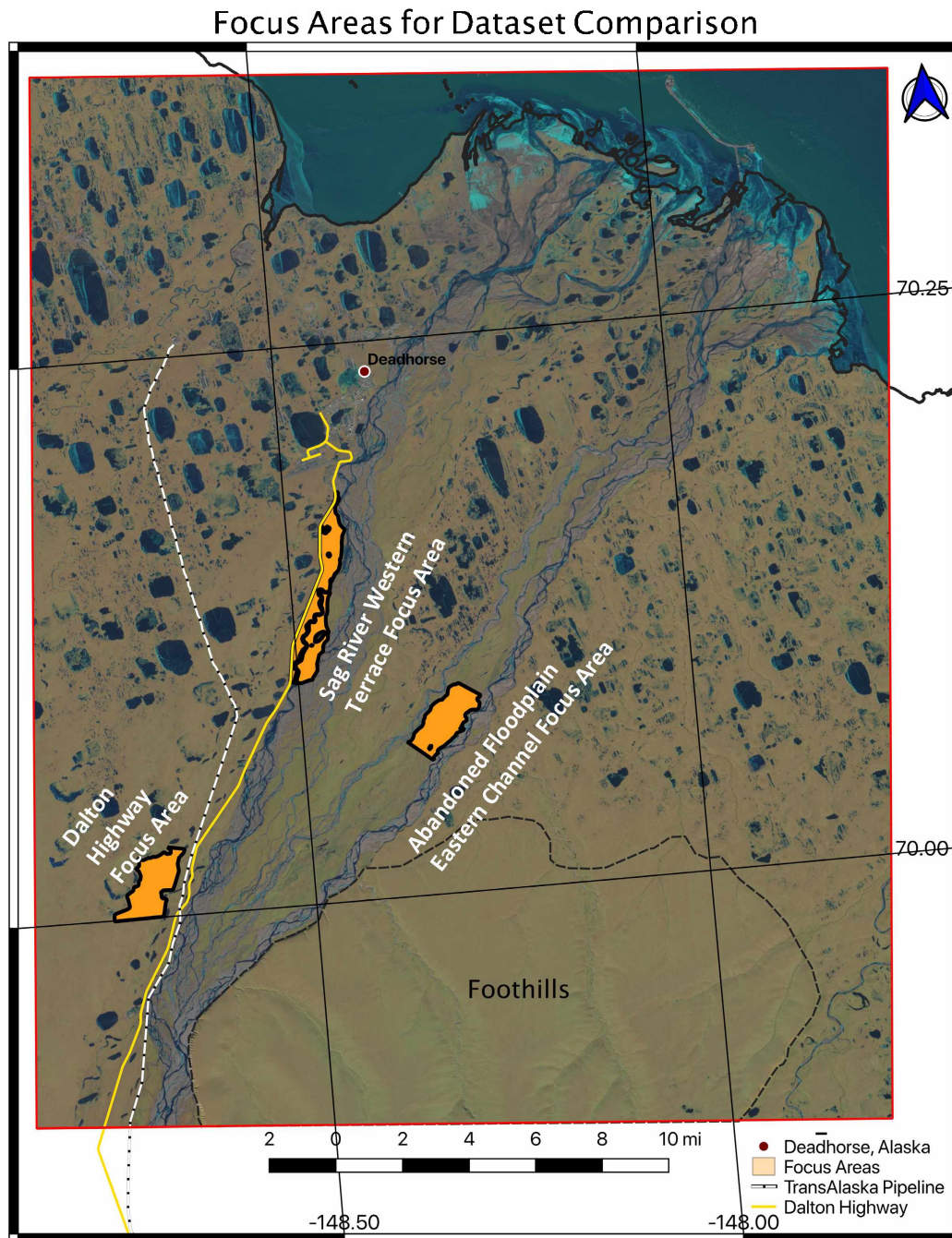


Figure 3.17: Focus areas for data comparison in inundated and flood-unaffected areas. October 2016 Sentinal 2 optical images shown in background.

Chapter 4 Results and Interpretation

4.1 Results

4.1.1 Estimating Flood Water Inundation

The first flood pulse of the Sag River was observed in the data starting April 4, 2015 and continued through April 26, 2015. Figure 4.1 shows the estimate of the first flood pulse extent. The exposed surface water of the first flood pulse was estimated to cover 12,955.9 hectares, or 5% of the total area of the AOI. The flood waters were mostly confined within the Sag River channels and stretched west of the Dalton Highway. Figure 4.1 shows the total surface water exposed during the first flood pulse in purple.

Known issues with the estimate include errors from missing data and false positives. Missing data is caused by two effects: data undersampling and image boundaries. Undersampling is related to the limited temporal sampling of the flooding event by the available SAR data. Through undersampling, the peak of the flood period may have been missed, leading to potential underestimation of the maximum flood extent. This most likely affected the second flood pulse more than the first due to the mix of data from the TSX and S1 sensors. TSX images were acquired with a range of every 2 to 6 days while S1 was acquired every 12 days. Image boundaries in the data set did not always cover the flood completely. In the areas where flood waters were partially covered, a linear artifact would be produced in the classified area. The produced maps show surface water including false positives related to thaw processes present during the time of the flood. Thaw of snow and ice results in pooling surface water whose radar signature can mimic that of flooded terrain. Notable features of the estimated extent of the first flood pulse are described in the following paragraphs.

April 2015, First Sagavanirktok River Flood Pulse

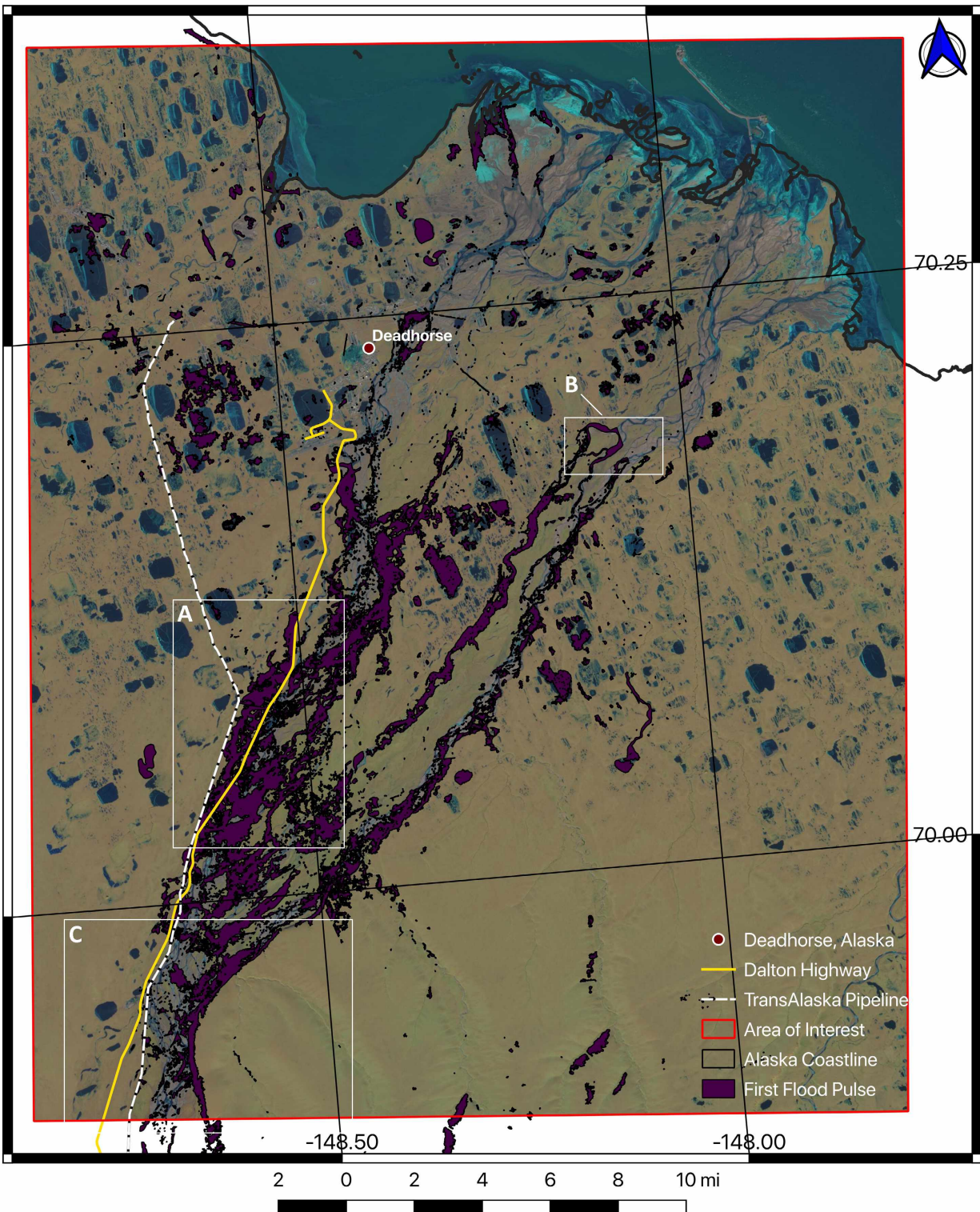


Figure 4.1: Estimate of the first flood pulse from the 2015 Sag River Flood. Boxes outline inset maps shown in Figure 4.2. Inset A shows the flooding breaching the Dalton Highway. Inset B shows a linear processing artifact. Inset C shows a false positive at a cliff face near the Franklin Bluffs.

An overflow of the first flood pulse and water inundation area was noted in the western flanks of the Sag River's westernmost channel (area of Inset A, Figure 4.1). Specifically, the overflow breached the slightly raised Dalton Highway in areas just north of the crossing point of the TransAlaska Pipeline and the Dalton Highway (area of Inset A, Figure 4.1). An alluvial terrace that extends west of the channel to the TransAlaska Pipeline was inundated by the flood. This flood pulse spread west to the TransAlaska Pipeline in areas where the pipeline paralleled the Dalton Highway but remained on its eastern side of the TransAlaska Pipeline (Figure 4.1). Additional overflows appeared in inactive floodplains and terraces throughout the river margins.

Figure 4.2 shows multiple insets of areas of specific interest including: A) flooding breaching the Dalton Highway; B) edge artifacts encountered; and C) a major false positive encountered on the Franklin Bluffs western cliff face. Again, open water surfaces not directly related to the flood were included in the results as it could not be determined if the flood did or did not affect these areas. Such surfaces are mostly comprised of numerous lakes and small tributaries (Figure 4.2). The Dalton Highway flooding appeared to inundate the common area between the TransAlaska Pipeline and the highway. The flood water traveled along the western edge of the Dalton Highway but did not cross the TransAlaska Pipeline (Figure 4.2.A). Straight borders or delineations were present within the estimated flood mask (Figure 4.1 and 4.2.B). These linear artifacts were caused by missing data at image boundaries (Figure 4.2.B). A 7.25 km-long false positive was discovered in the data. This error was located along the cliff face in the southern AOI between the Sag River and Franklin Bluffs (Figure 4.2.C). This error was caused by signal amplitude greatly increasing in two of the analyzed images on the cliff face creating a similar signature to the signature new water areas. The cliff face signature could be related to layover of SAR data (Figure 4.2.C).

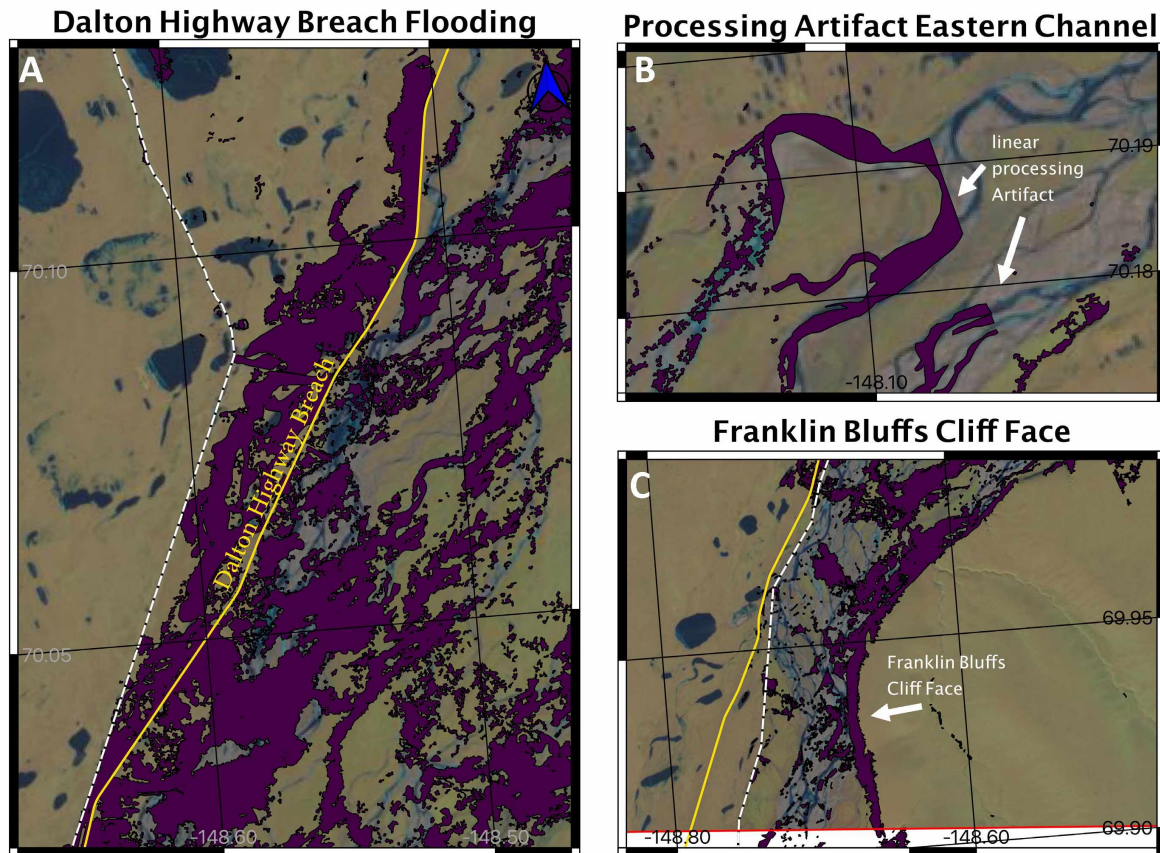


Figure 4.2: Inset maps of the first flood pulse estimate from the 2015 Sag River Flood. Inset locations outlined with white boxes as shown in Figure 4.1. Purple areas outline the estimate of the first 2015 Sag River flood pulse. Inset A shows flooding breaching the Dalton Highway. Inset B shows an edge artifact from an image boundary encountered during processing. Inset C show the false positive at the Franklin Bluffs cliff face. Refer to Figure 4.1 for the legend.

The second flood pulse was observed in the data starting in early May 2015 and continuing through May 28, 2015. Figure 4.3 shows the estimate of the second flood pulse extent. The second flood pulse inundated a broader area. The exposed surface water of the second flood pulse was estimated at 56,079.4 hectares, or 26% of the total area of the AOI (Figure 4.3). Figure 4.3 shows the total surface water exposed during the second flood pulse in green.

May 2015, Second Sagavanirktok River Flood Pulse

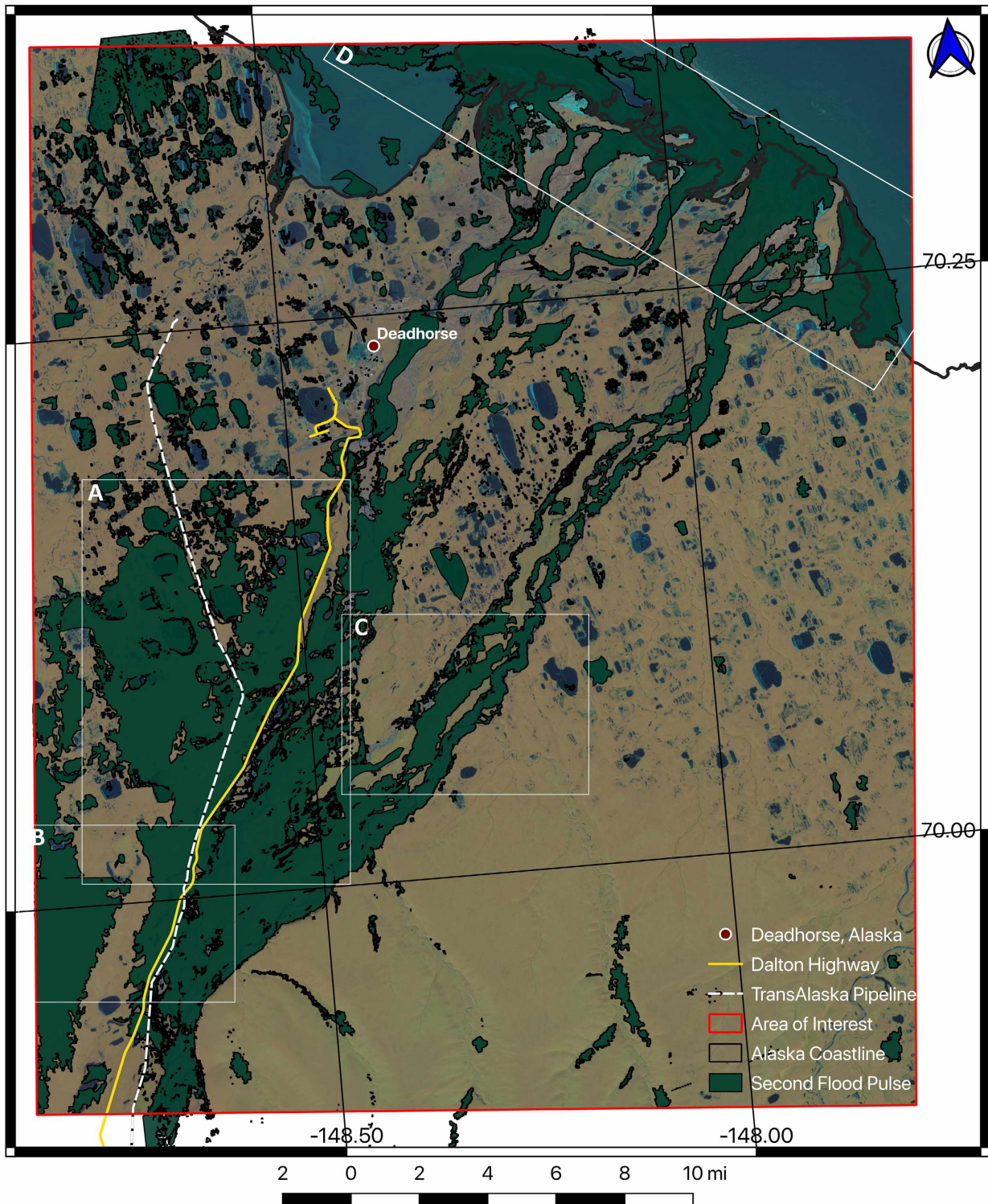
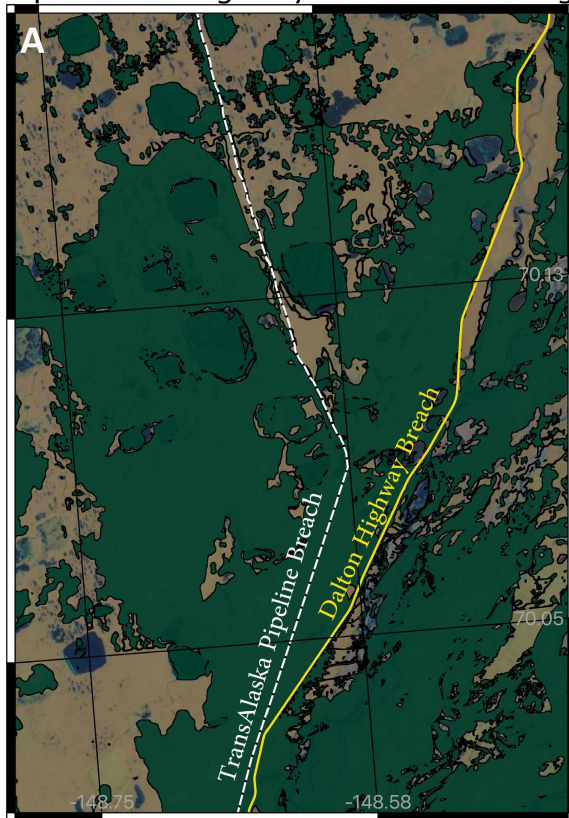


Figure 4.3: Estimate of the second flood pulse from the 2015 Sag River Flood. Boxes outline inset maps in Figure 4.4. Inset A shows waters breaching the Dalton Highway and TransAlaska Pipeline. Inset B shows a processing artifact. Inset C shows overflow between the eastern river channels. Inset D shows false positives at the terminus of the Delta.

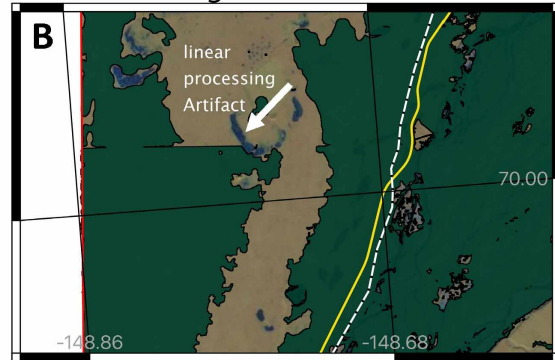
Figure 4.4 shows multiple insets of areas of specific interest including: A) floodwaters that breached the Dalton Highway and the TransAlaska Pipeline; B) an edge artifact encountered; C) overflow between the eastern channels; and D) false positives in the maritime areas of Prudhoe Bay in the northern AOI. The second flood pulse breached west of the Dalton Highway and the TransAlaska Pipeline throughout the AOI (Figure 4.3 and 4.4.A). Missing data were present in the AOI and are commonly associated with a linear boundary in the mapped flood mask (Figure 4.4.B). All data were clipped to the western and eastern expanse of the AOI. The clipped data failed to capture a portion of the second flood pulse's inundation extent to the west of the AOI and are displayed as a straight border on the edges of flood mask. Many large abandoned floodplains between the Sag River channels were submerged during the second flood pulse. An eastern channel overflow measuring 16 km by 0.8 km is shown in Figure 4.4.C. False positives in the flood mask contain surface water unrelated to the flood. These false positives are most prominent at the terminus of the Sag River Delta and along but also present in the ocean areas of Prudhoe Bay of the northern AOI (Figure 4.4.D)

The two pulses of the 2015 Sag River flood inundated common areas within the AOI (Figure 4.5). The total common area covered 8,472.1 hectares, or 3.8% of the AOI. The common inundated areas appeared similar to the footprint of the first flood pulse (Figures 4.1 and 4.3). The common area was mostly confined to the Sag River channels. Areas outside of the river channels included the overflow breaching the Dalton Highway to the west from the first flood pulse, but did not include the flooding that breached west of the TransAlaska Pipeline during the second flood pulse (Figure 4.6.A). A single linear artifact was located in the northwestern Sag River channels in Figure 4.6.B. Data coverage of the first flood pulse was limited east of this location. The major false positive at the Franklin Bluffs cliff face was included in the flood mask, but its eastern extent was reduced (Figure 4.6.C).

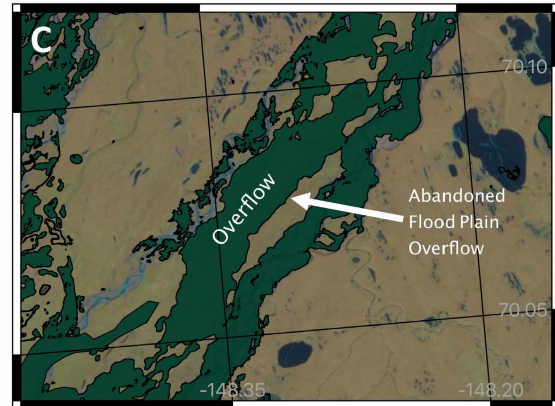
Pipeline and Highway Breached Flooding



Processing Artifact Western AOI



Eastern Channel Overflow



Sag River False Positives at the Delta Terminus

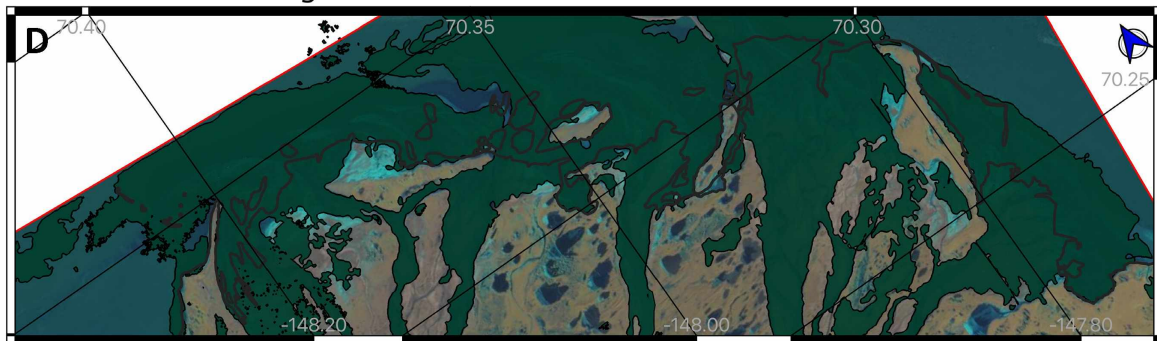


Figure 4.4: Inset maps of the second flood pulse from the 2015 Sag River Flood. Inset locations outlined with white boxes as shown in Figure 4.3. Green areas outline the estimate of the second 2015 Sag River flood pulse. Inset A shows flood water breaching the Dalton Highway and TransAlaska Pipeline. Inset B shows a linear processing artifact encountered in the study. Inset C shows the overflow over an abandoned floodplain between the Sag River eastern channels. Inset D shows the false positives at the terminus of the Sag River Delta. Note Inset D is rotated 30° to the west. Refer to Figure 4.3 for the legend and inset plot orientations.

Common Areas of the Sagavanirktok River Flood Pulses

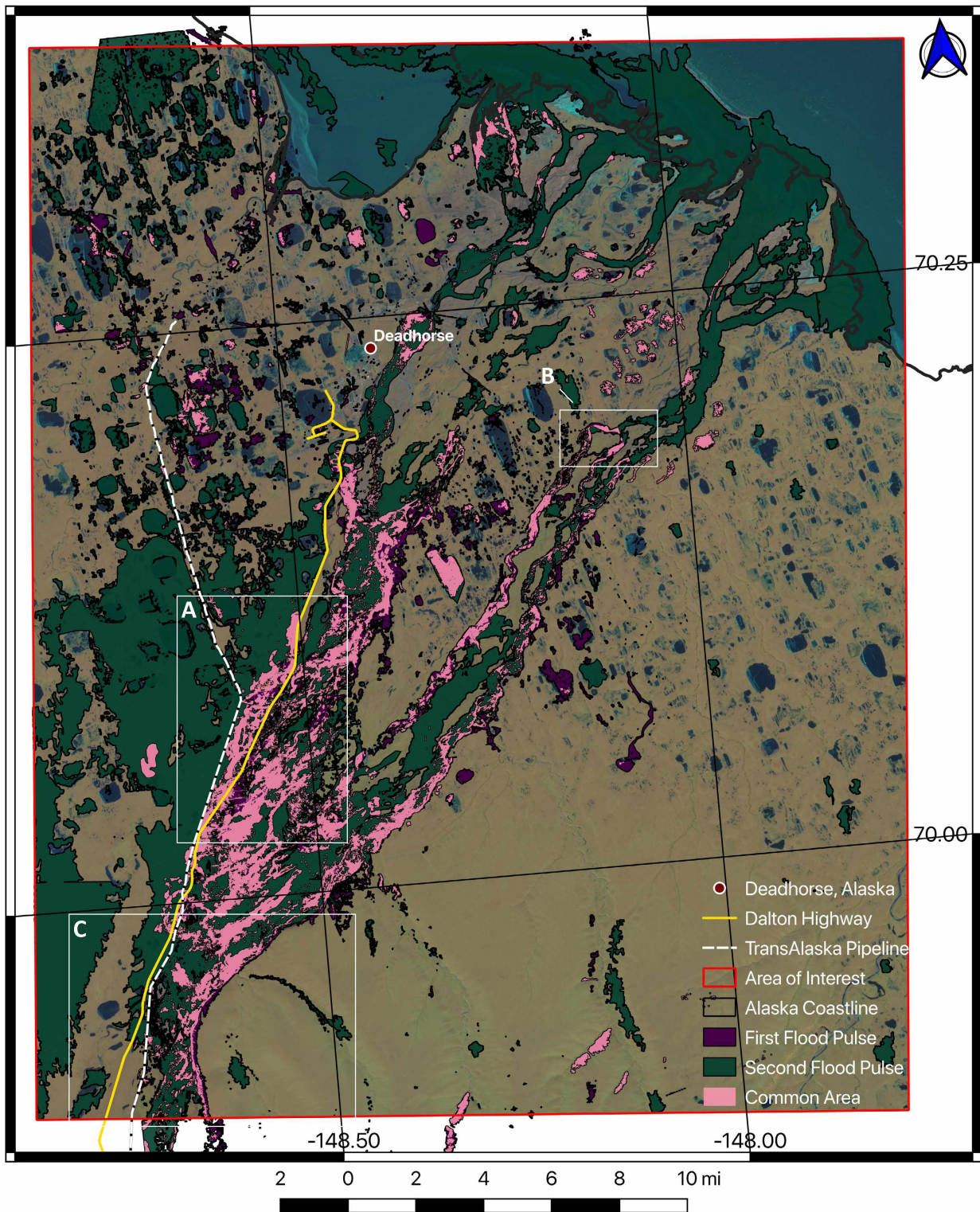
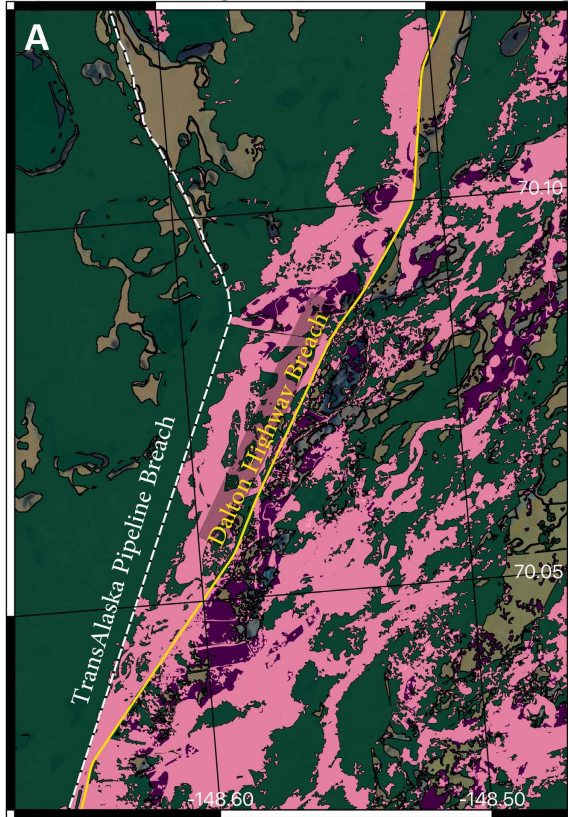
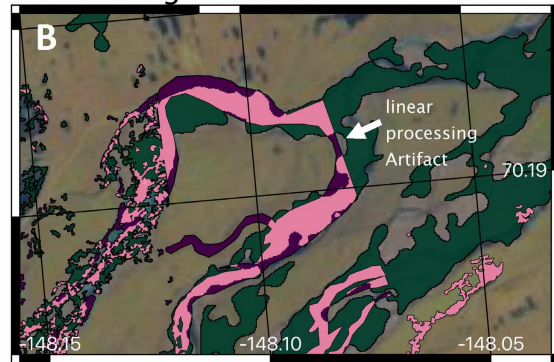


Figure 4.5: Estimates of the first and second flood pulses and the common area covered by both estimates. Boxes outline inset maps in Figure 4.6. Inset A shows flooding breaching the Dalton Highway and TransAlaska Pipeline. Inset B shows a processing artifact. Inset C shows the Franklin Bluffs cliff face.

Pipeline and Highway Breached Flooding



Processing Artifact Eastern Channel



Franklin Bluffs Cliff Face

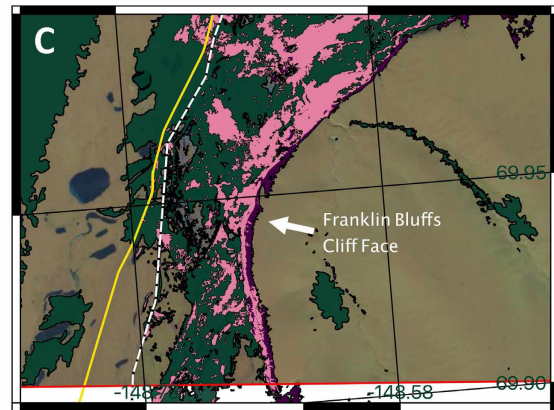


Figure 4.6: Inset maps showing estimates of both flood areas are outlined in Figure 4.5. Inset locations are outlined with white boxes in Figure 4.5 as white boxes. Purple areas outline the estimate of the first 2015 Sag River flood pulse. Green areas outline the second flood pulse. Yellow areas were covered by both flooding events. Inset A shows the major overflow over the Dalton highway and an example of a thawed tributary. Inset B shows a linear processing artifact encountered in the study. Inset C show the false positive at the Franklin Bluffs cliff face.

4.1.2 Seasonal Surface Deformation Results

4.1.2.1 Summer 2017 Surface Deformation Results

The estimated cumulative summer 2017 deformation data ranged between -53 mm and +44 mm over a five-month (May 1 to October 1) period (Figure 4.6). Mean deformation was -14 mm. The mode was -21 mm. A bimodal distribution of the data shows average subsidence of -18.5 mm and uplift of +3.0 mm in the local maxima (Figure 4.6). See Figure 4.6 for histogram distribution of deformation.

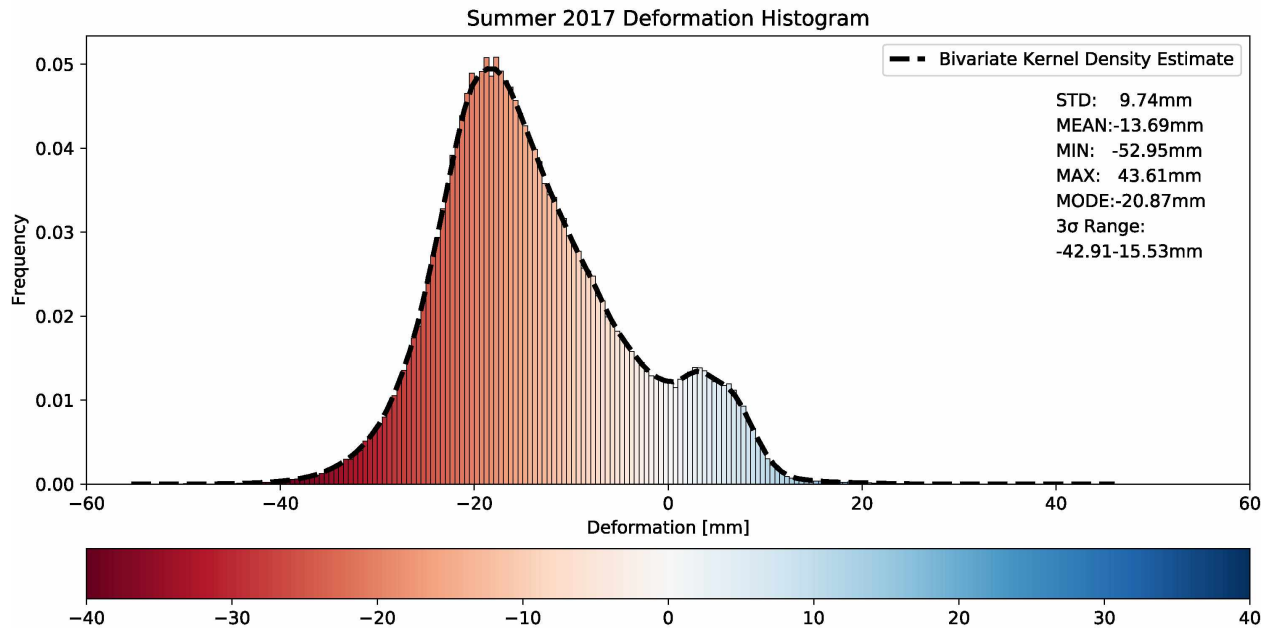


Figure 4.7: Histogram of relative deformation of the AOI during summer 2017. Pixel values in millimeters. Bins sampled every 0.5 mm. Bivariate kernel estimate of deformation shown with dashed line.

The estimated cumulative summer 2017 deformation map is shown in Figure 4.8. An annotated version of the deformation map is shown as Figure 4.9. Deformation had a high degree of variability across the AOI. The following sections discuss key areas of 2017 deformation data.

Key inset areas outlined in Figure 4.9 are shown in Figure 4.10. For consistency, the same areas are discussed for each InSAR product before discussing the unique signatures of each data set. The focus areas are as follows: A) along the alluvial terrace in the flood breach zone west of the Dalton Highway and the alluvial terrace in the flood breach zone southwest of the TransAlaska Pipeline; B) an abandoned alluvial plain between the eastern Sag River channels (see POI 1; Figure 3.12); C) an alluvial terrace in the southwestern AOI; D) an inactive floodplain east of the airport at Deadhorse, Alaska; and E) at manmade structures, infrastructure, and dwellings. See Figure 4.10 for inset figures.

Inset A shows breach flooding areas east of the Dalton Highway and southwest of the TransAlaska Pipeline (Figure 4.10.A). The Dalton Highway breach area showed deformation from -37 to

Deformation of Summer 2017

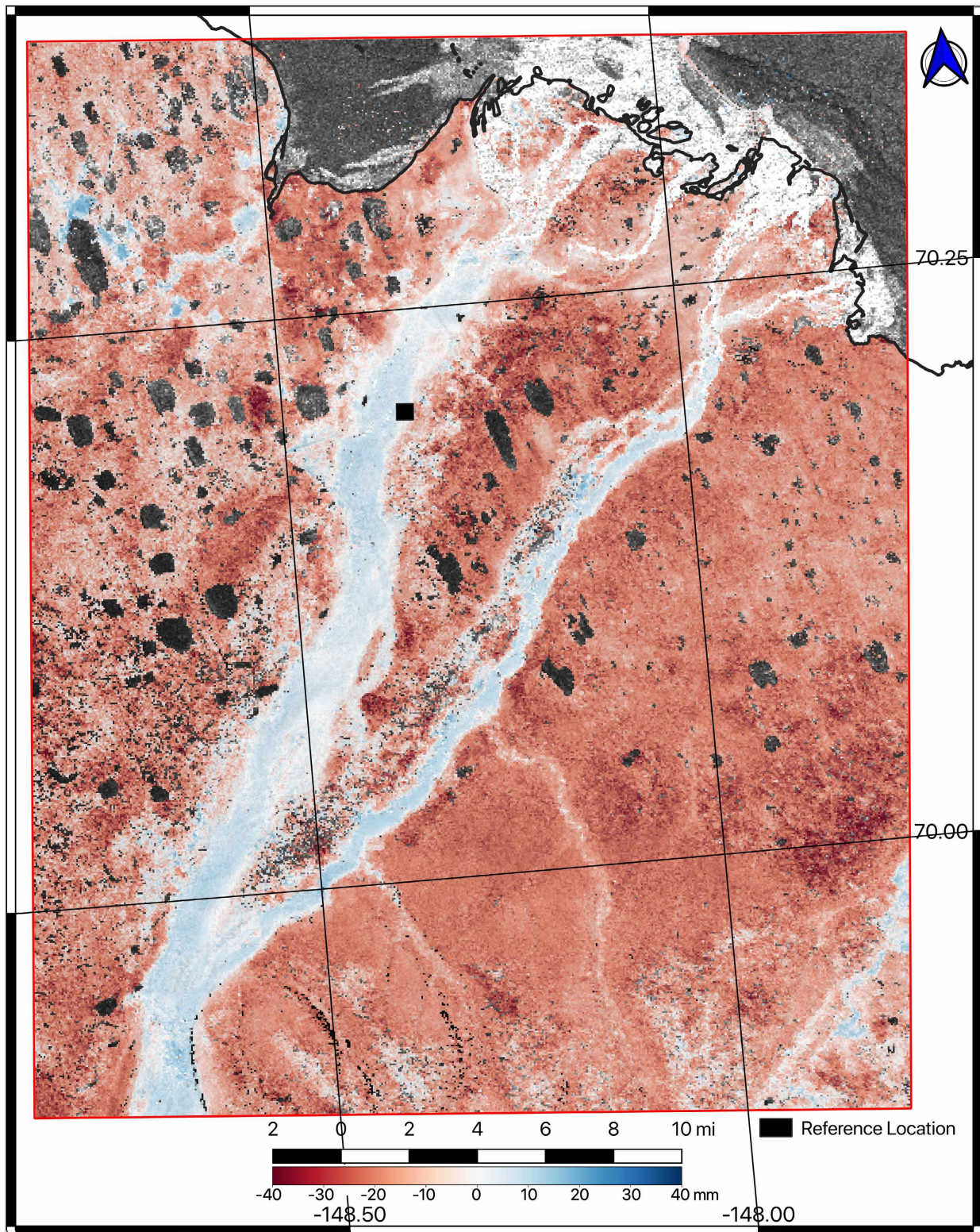


Figure 4.8: Summer 2017 subsidence and master amplitude image. AOI outlined in red. Coastline shown in black. S1 amplitude image of May 29, 2017 shown in background. Annotated version of the map shown in Figure 4.9.

Deformation of Summer 2017

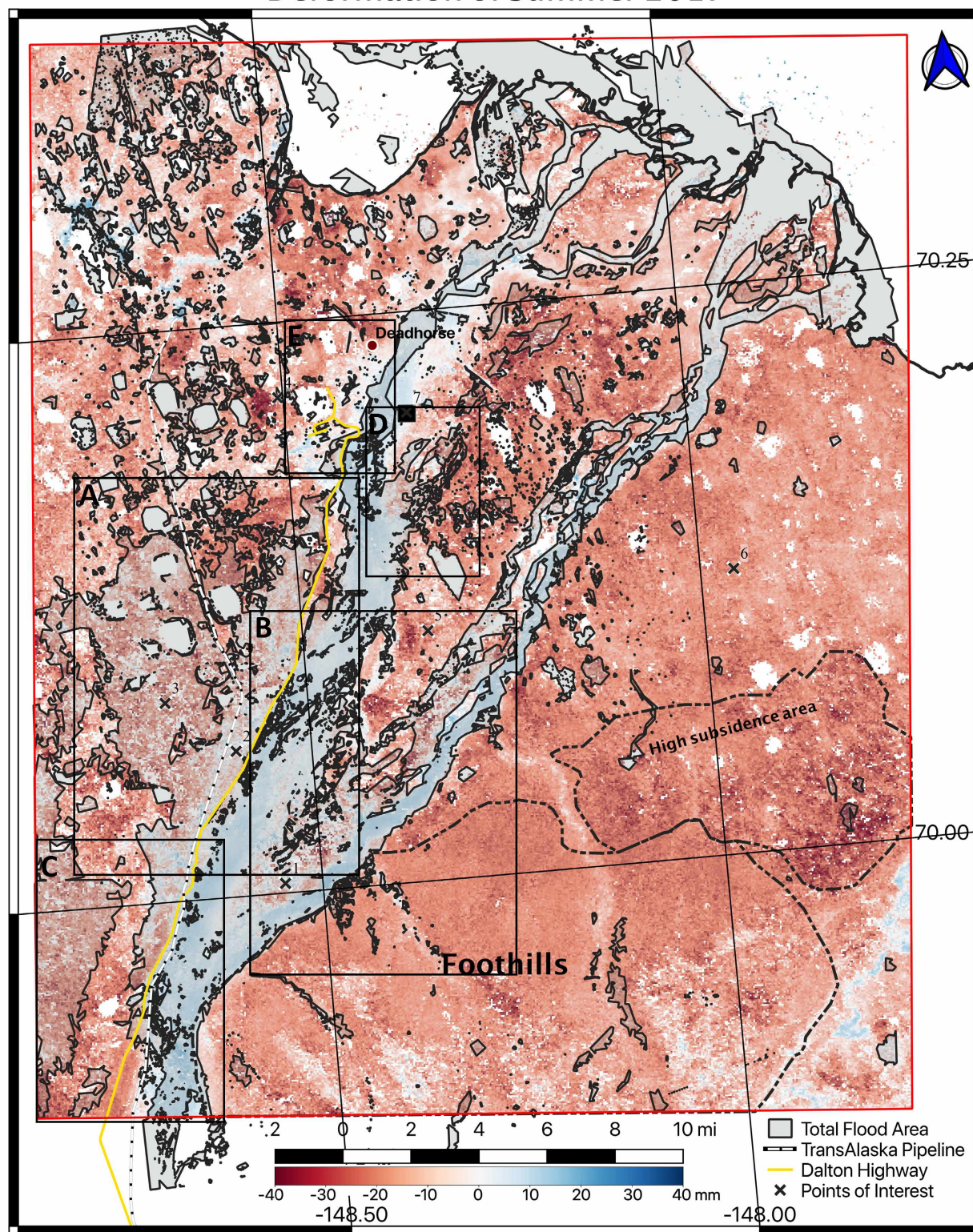


Figure 4.9: Seasonal 2017 summer subsidence. Xs show sampled locations of deformation (Figure 4.11). Light gray covers the total 2015 Sag River flooded area (Figure 4.5). Boxes outline inset maps (Figure 4.10).

+18 mm (Figure 4.10.A). The data showed more subsidence, -5 mm to -15 mm, closest to the Dalton Highway, and lower subsidence to the west of the breach area. Areas masked due to low coherence were distributed throughout this area. The Dalton Highway breach, when compared to the areas in the northwest, showed lower deformation amplitudes. The TransAlaska Pipeline breach area showed a deformation range of -43 mm to +12 mm (Figure 4.10.A). POI 2 is contained within the Dalton Highway breach zone and showed gradual subsidence up to -8 mm (Figure 4.11). Within 0.4 km west of the TransAlaska Pipeline, the data showed relative uplift. This uplift trend occurred west of the pipeline and it trends to the northwest. Most of the TransAlaska Pipeline, breach area showed relative subsidence with sparse areas masked due to low coherence. Deformation in the TransAlaska Pipeline breach area was slightly higher in magnitude when compared to areas just west of the Dalton Highway breach area. POI 3 is contained within the pipeline breach and showed a subsidence up to -18 mm. The highest rate of subsidence occurs in September 2017 (Figure 4.11).

Inset B shows a 27-km by 2.4-km abandoned alluvial floodplain between the eastern channels of the Sag River (Figure 4.10.B). Deformation within inundated areas showed a range from -50 mm to +20 mm, or were masked due to low coherence. Geographically, the deformation discussed in the abandoned floodplain occurs between the Sag River eastern channels. Flood-unaaffected areas on the abandoned floodplain had more positive values in deformation, ranging from -30 mm to +25 mm. The highest subsidence occurred near the center of the abandoned floodplain northeast of POI 1 (see northeast of POI 1 on the -148.5 meridian, Figure 4.10.B). POI 1 showed a deformation time series with a gradual subsidence up to -5 mm (Figure 4.11). POI 5 is contained in a flood-unaaffected area of the northern reaches of inset B. Subsidence at POI 5 was up to -35 mm (Figure 4.11). The greatest rate of deformation at POI 5 took place in July 2017 (Figure 4.11).

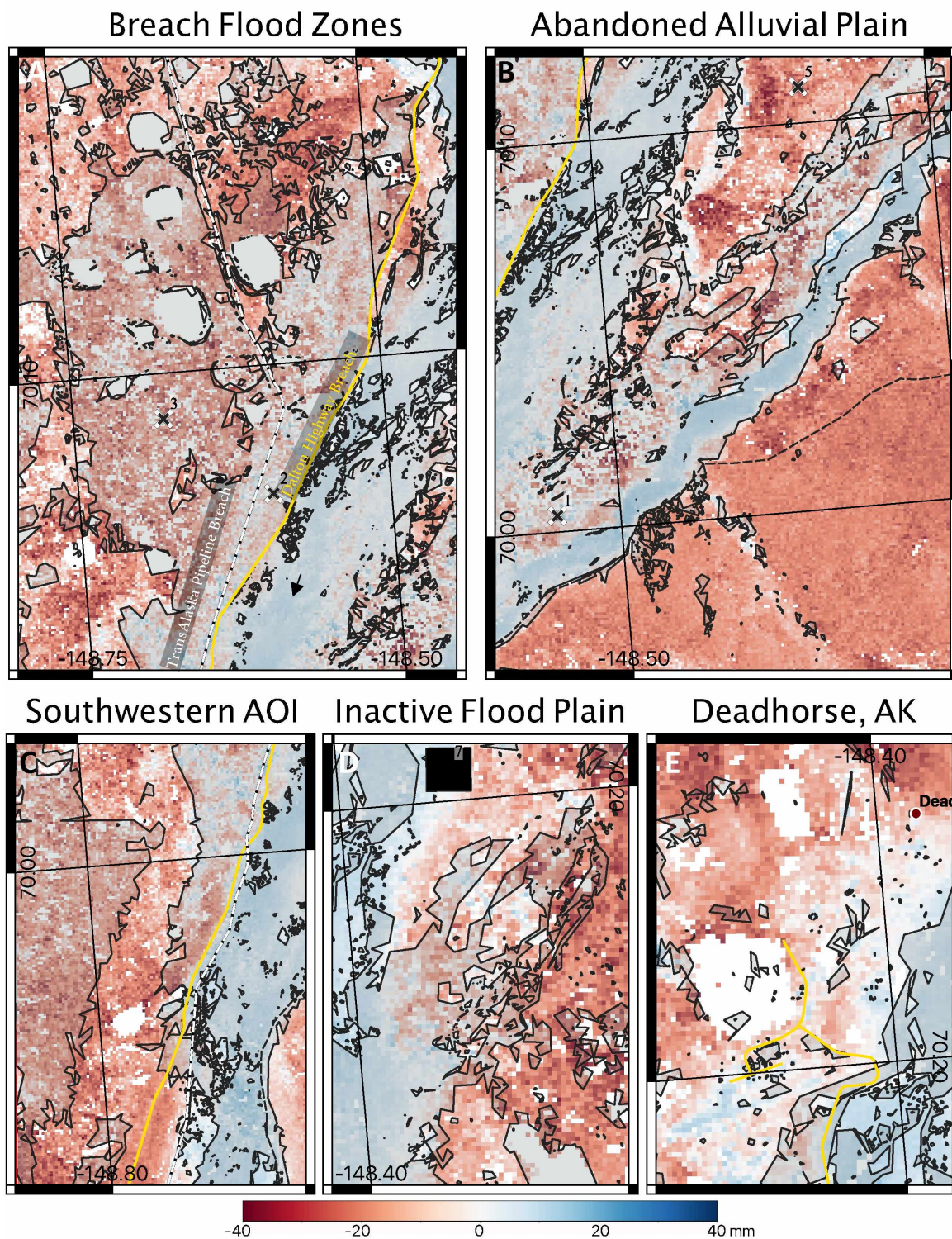


Figure 4.10: Inset maps showing estimates of 2017 summer season deformation. Insets outlined in Figure 4.9. Inset A shows the Dalton Highway and the TransAlaska Pipeline breach areas. Inset B shows an abandoned alluvial plain between the eastern Sag River channels. Inset C shows an alluvial terrace in the southwestern AOI. Inset D shows an inactive floodplain east of the airport at Deadhorse, Alaska. Inset E shows manmade structures at Deadhorse. Flood mask shown in gray. See Figure 4.9 for legend.

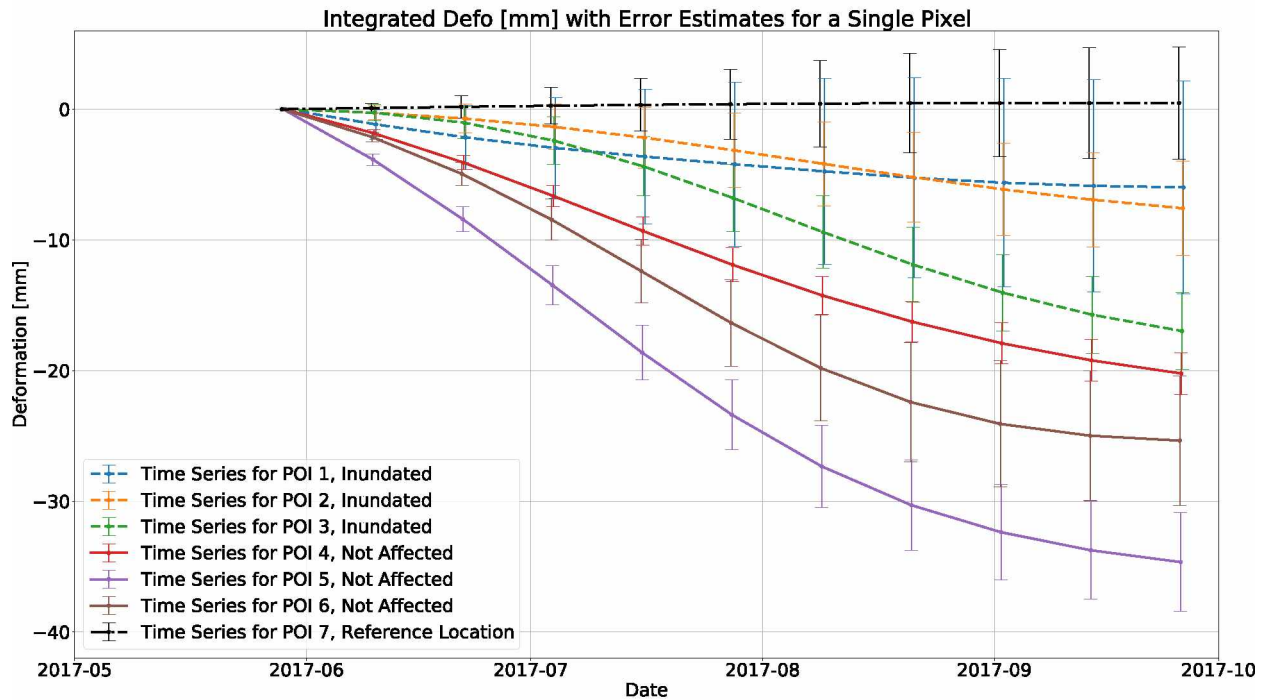


Figure 4.11: Plot showing the deformation within selected locations for the 2017 summer season. POIs 1,2, and 3 were affected by the 2015 Sag River flooding. POIs 4,5, and 6 were not affected. POI 6 is placed away from the AOI. The reference area location is labeled at POI 7 in the deformation plot. The deformation signal was processed with a 2-month temporal filter. See Figures 3.9 and 4.9 for locations of the POIs.

Inset C shows an alluvial terrace in the southwestern AOI. Deformation had a negative trend ranging from +8 mm to -35 mm (Figure 4.10.C). Deformation had a uniform signature within inset C. Areas of highest subsidence were isolated and sparse in their relationship to each other (Figure 4.10.C).

Inset D shows an inactive floodplain east of the airport at Deadhorse, Alaska (Figure 4.10.D). Deformation ranged from +18 mm to -40 mm. A majority of the deformation was subsidence in the range of -5 mm to -20 mm that appears lower when compared to the surrounding land (Figure 4.10.D). POI 7, the reference location, is contained within inset D. All deformation data were referenced to POI 7 and, as such, had little deformation. Over the area of POI 7 the deformation showed +1 mm of uplift and was zero within the margin of error (Figure 4.11).

Inset E shows manmade infrastructure in the vicinity of Deadhorse, Alaska (Figure 4.10.E). A majority of the manmade features consist of equipment yards, well pads, and dwellings. They predominantly show uplift ranging from 0 mm to +20 mm. The Deadhorse airport runway showed uplift of +5 mm to +10 mm (Figure 4.10.E). POI 4 is located just west of Inset E at an oil pad (Figure 4.9). POI 4 was not inundated and showed slightly higher subsidence, -20 mm, than the inundated POIs, and showed a more linear subsidence behavior than other POIs (Figure 4.11).

Deformation in the AOI during summer 2017 contained some additional interesting signatures: Subsidence in a 16-km-wide by 12-km long area noted in the eastern portion of the AOI just north of the base of the Franklin Bluffs foothills was noted to have a 3-sigma subsidence range between -6 mm and -40 mm (see outlined area labeled “High subsidence area” in Figure 4.9). Spotty locations of uplift were infrequent along the coastal plain (areas shaded in blue in Figure 4.9). Many of these uplift locations were located at manmade structures including oil pads, wells, and temporary roads. Generally, the summer season subsidence was highest in locations away from lakes or manmade objects (Figure 4.9). For instance, the highest subsidence in the AOI occurred just west of POI 4 with a subsidence of -30 mm to -44 mm (Figure 4.9). This site was located away from manmade features and was not affected by flooding (Figure 4.9).

A time series of deformation at select points of interest (POI) spread across the AOI is shown in Figure 4.11 and processed with a 2-month temporal filter. Subsidence was most rapid in July. POIs 1 and 2 showed seasonal subsidence in the range of -6 mm and -7 mm. The deformation difference between inundated areas, POIs 1 and 2, and flood-unaffected-areas, POIs 5 and 6, is just over -10 mm. POI 4 is located adjacent to a well pad and shows the highest subsidence of -20 mm. POI 7 is the reference point

and only shows less than +1 mm of uplift over its averaged area and is zero within the margin of error (Figure 4.11).

4.1.2.2 Summer 2018 Surface Deformation Results

The estimated cumulative deformation from summer 2018 ranged between -15 and +15 mm over a three-month (July 1 to October 1) period (Figure 4.12). Mean deformation was -1 mm. The mode was -4 mm. A frequency distribution of the data showed a signal maximum at an average subsidence of -1 mm (local maximum, Figure 4.12). See Figure 4.12 for the histogram distribution for the deformation for summer 2018.

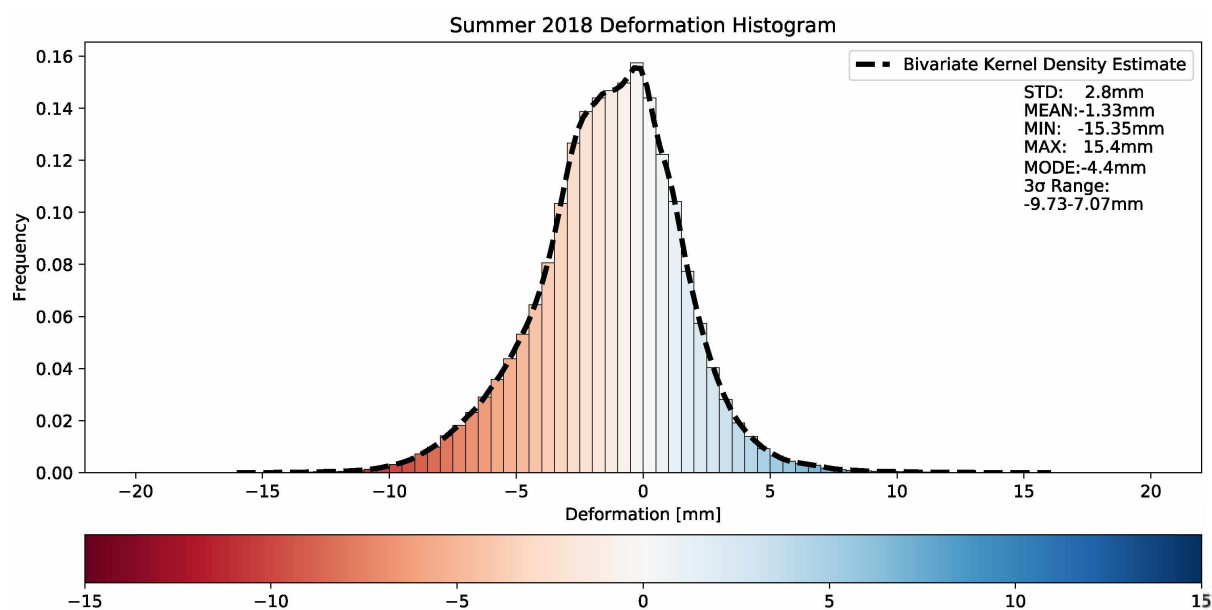


Figure 4.12: Histogram of relative deformation of the AOI during summer 2018. Pixel values in millimeters. Bins sampled every 0.5 mm. Bivariate kernel estimate of deformation shown with dashed line.

The cumulative deformation for the summer 2018 is shown in Figure 4.13. An annotated version of Figure 4.13 is shown in Figure 4.14. The summer 2018 data showed a broad trend of uplift in the southwestern and northeastern corners of the AOI. The center of the AOI, stretching from the southwest to the northeast of the AOI, displayed subsidence.

Key inset areas outlined in Figure 4.14 are shown in Figure 4.15. The areas discussed are the same areas utilized in the 2017 seasonal analysis.

Inset A covers the breached flooding areas west of the Dalton Highway and the TransAlaska Pipeline (Figure 4.15.A). The Dalton Highway breach shows deformations ranging from -10 mm to +2 mm in the areas where the Dalton Highway and the TransAlaska Pipeline are less than 2.4 km apart. POI 2 is contained within this location (Figure 4.15.A). The time series of deformation at POI2 shows gradual subsidence to a cumulative subsidence of -2 mm (Figure 4.16). The majority of the subsidence occurred in the late-July to early-August 2018 timeframe and decreased in late August 2018. A broad area in the center of the map displayed deformation ranging from -3 to +6 mm. The TransAlaska Pipeline breach area showed no clear deformation trend or distinction from the surrounding area. Here, deformation ranged from -11 mm to +4 mm. The majority of the Dalton Highway breach subsided. A small uplifted area was located on the western side of the pipeline towards the northwest (Figure 4.15.A). Many locations within the TransAlaska Pipeline breach area were masked in areas with lakes and small bodies of water. POI 3 is located within the TransAlaska Pipeline breach (Figure 4.15.A). POI 3 showed a gradual cumulative subsidence of -4 mm. The greatest rate of subsidence occurred through August 2018 and began to slow in September 2018 (Figure 4.16).

Inset B shows an abandoned alluvial floodplain between the eastern Sag River channels (Figure 4.15.B). Within the vicinity of POI 1, the deformation showed an uplift ranging from 0 mm to +7 mm along the northwestern half of the abandoned floodplain. An uplifting trend is located along the southeastern half of the abandoned floodplain and showed deformation ranging from a maximum value of +6 mm but with values as low as -6 mm. Uplift and subsidence largely occurred on opposite sides and displayed a trend across the abandoned floodplain. POI 1 is located on the abandoned floodplain at the

Deformation of Summer 2018

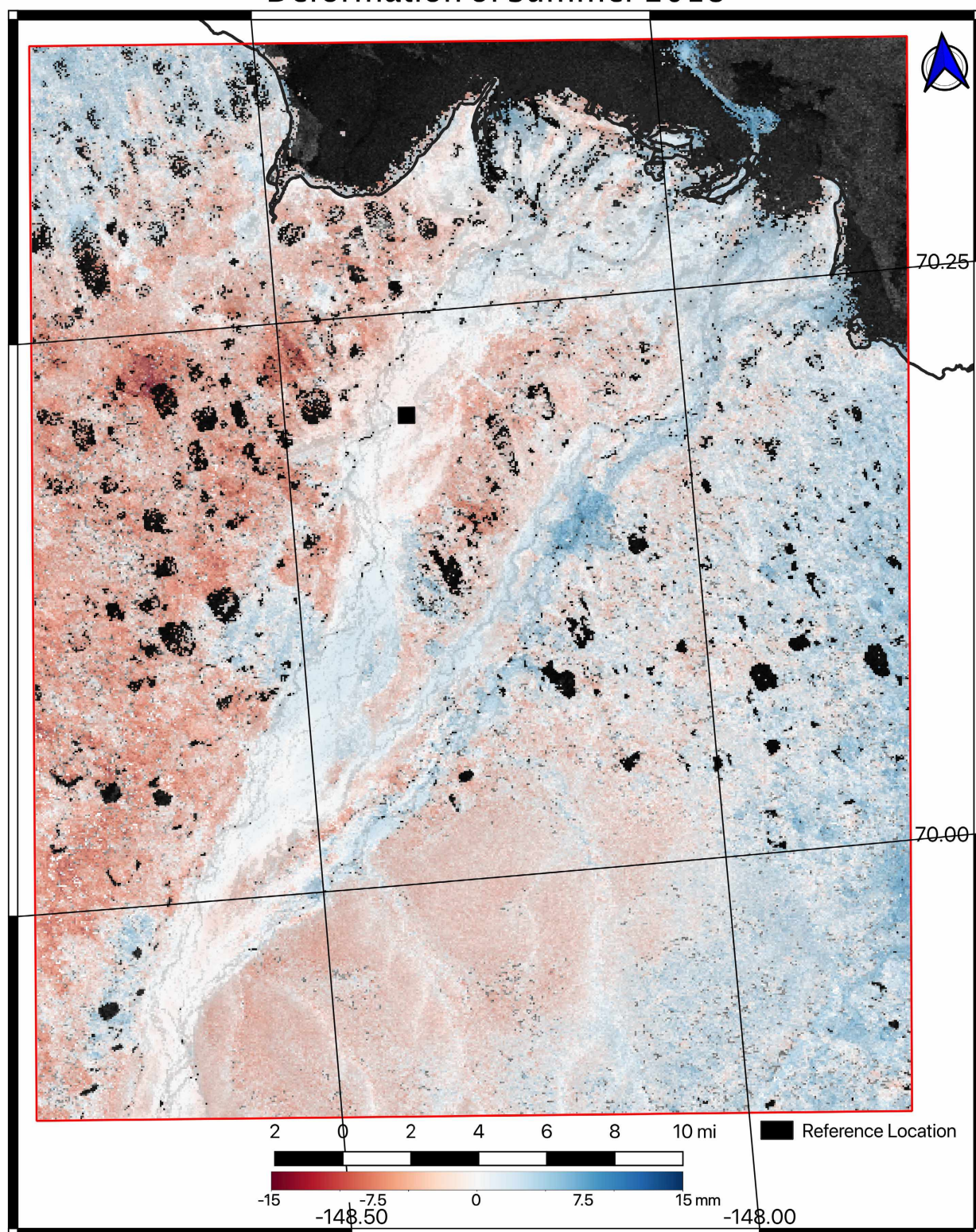


Figure 4.13: Summer 2017 subsidence and master amplitude image. An annotated version of the 2018 deformation map is shown in Figure 4.14.

Deformation of Summer 2018

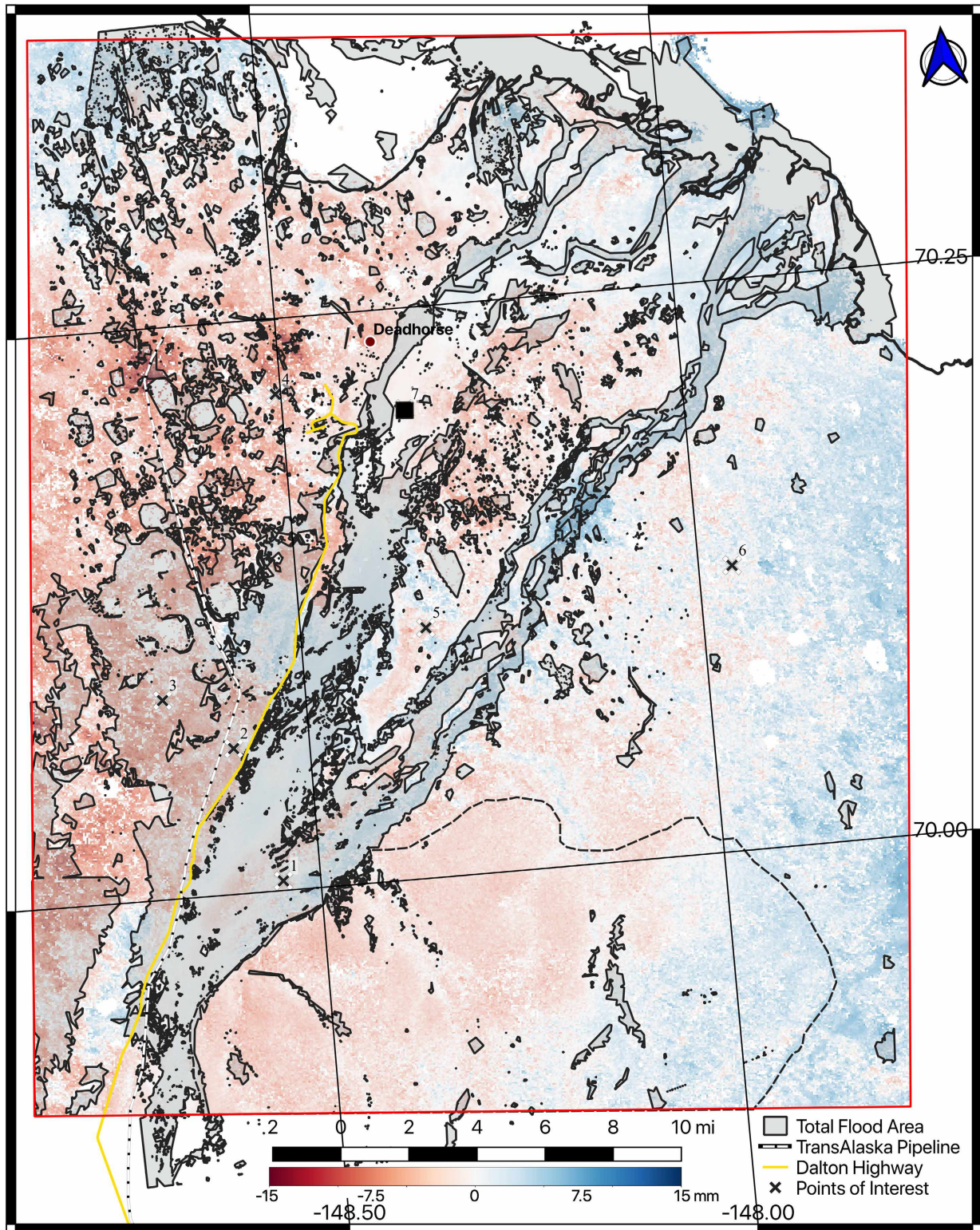


Figure 4.14: Seasonal 2018 summer subsidence. Xs show sampled locations of deformation (Figure 4.15). Light gray outlines the total 2015 Sag River flooded area (Figures 4.5). Boxes outline inset maps (Figure 4.16).

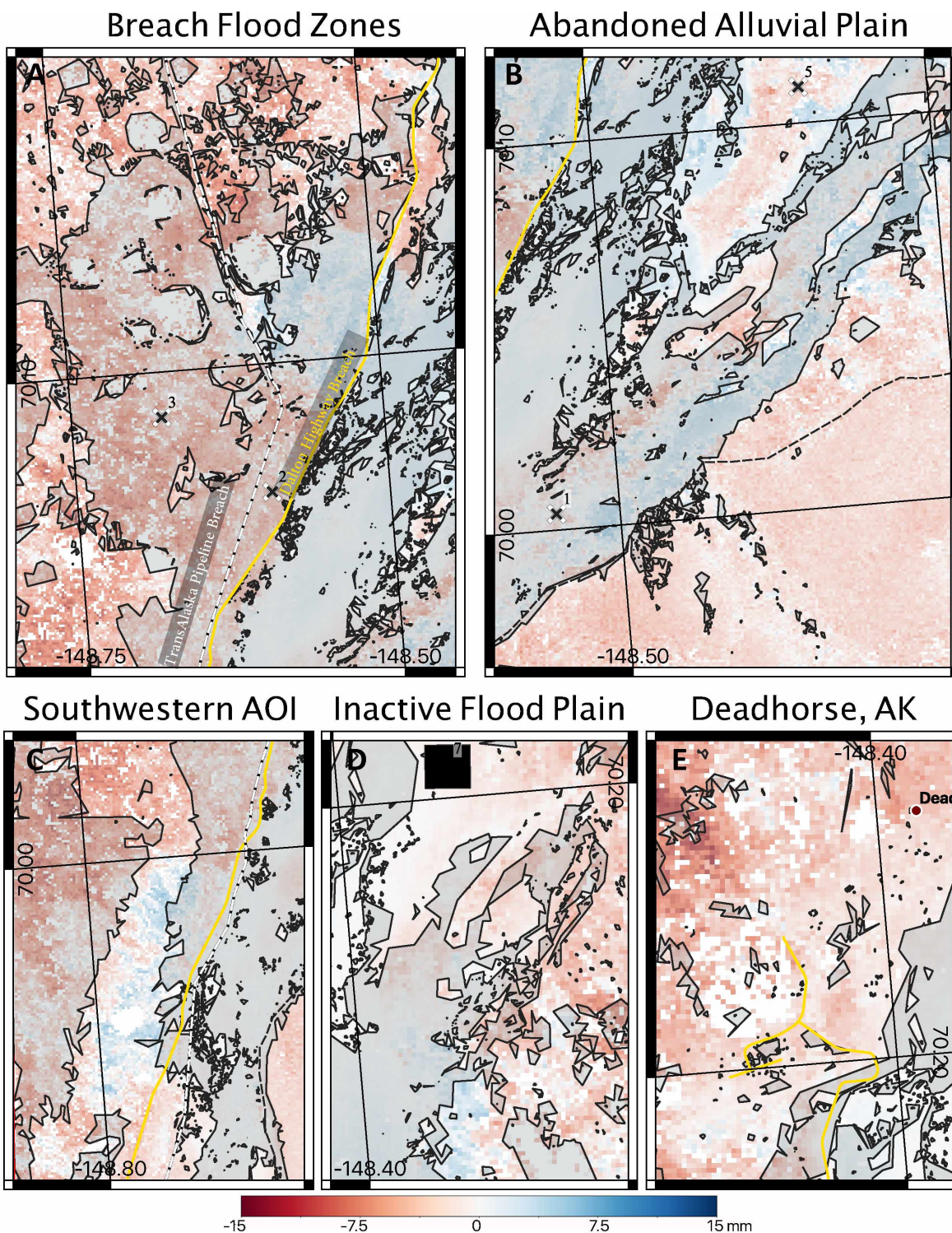


Figure 4.15: Inset maps showing estimates of summer 2018 season deformation. Insets outlined in Figure 4.14. Inset A shows the Dalton Highway breach and the TransAlaska Pipeline breach. Inset B shows an abandoned alluvial plain between the eastern Sag River channels. Inset C shows an alluvial terrace in the southwestern AOI. Inset D shows inactive floodplain east of the airport at Deadhorse, Alaska. Inset E shows manmade structures at Deadhorse. Flood mask shown in gray. See Figure 4.14 for legend.

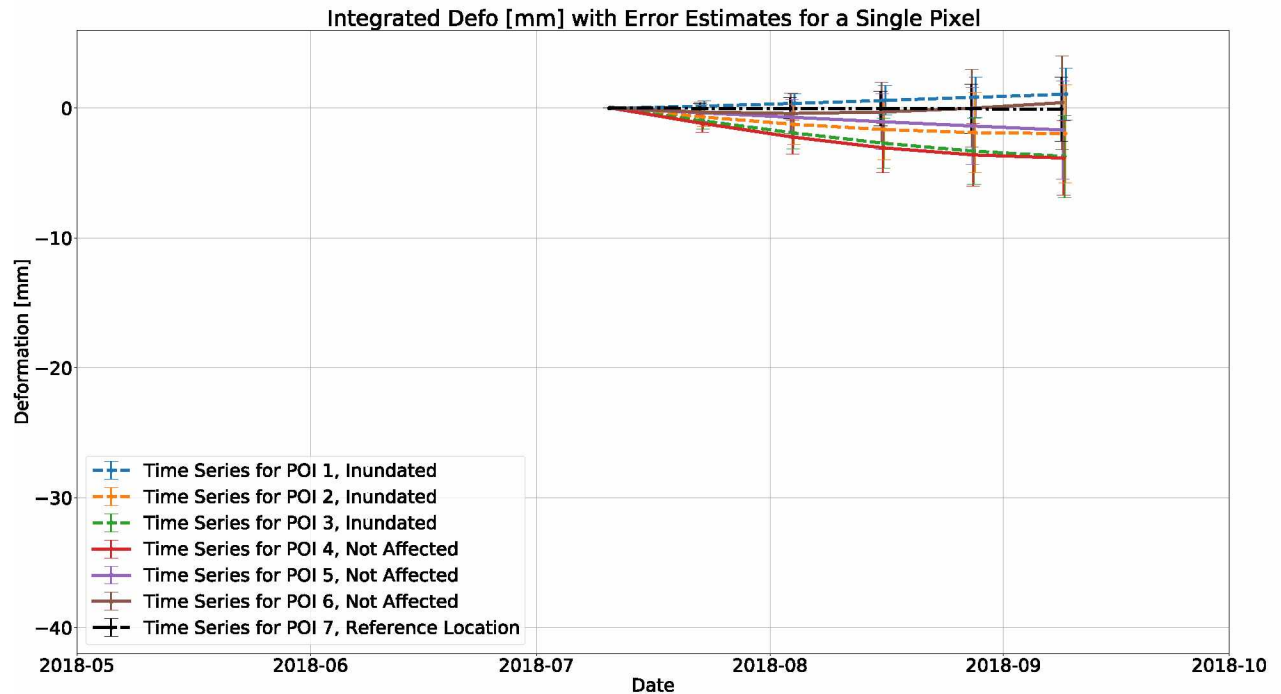


Figure 4.16: Plot showing the deformation at several locations for the 2018 summer season. The reference location is labeled as POI 7 in the deformation plot. Deformation signal processed with a 1-month temporal filter. See Figures 3.9 and 4.9 for locations of the POIs.

contact between the high subsidence and uplifting trends in an inundated area. POI 1 showed steady uplift to a cumulative deformation of +1 mm. No changes in the rate of deformation were noted (Figure 4.16). POI 5 was located in a flood-unaffected area and shows just over +1 mm of steady subsidence.

Inset C is located at the southwest corner of the AOI (Figure 4.15.C). An uplifting swell was noted in the center of Figure 4.15.C in areas not affected by the 2015 Sag River flooding events. The uplifting swell measured +6 mm, with subsidence of 0 mm to -8 mm surrounding the uplifting swell. Within the inundated areas to the east and west of the uplifting swell deformation ranged from +6 mm to -10 mm with the majority of the area showing subsidence (Figure 4.15.C).

Inset D shows the inactive floodplain east of the Deadhorse airport (Figure 4.15.D). Subsidence within this inset area was minimal. Deformation ranged between -5 mm and +5 mm. Most of the inset area displayed less than +1 mm of deformation. The highest subsidence occurred within the inactive floodplain the greatest uplift near the Sag River shore (Figure 4.15.D). POI 7, the InSAR reference location for the study is included within the inset. Deformation displayed a consistent 0 mm throughout the entire time series (Figure 4.16).

Inset E includes the manmade infrastructure at the town of Deadhorse, Alaska. Deformation around manmade structures was only observable at one location, the Deadhorse airport (Figure 4.15.E). Deformation on the runway of the airport was identifiable based on its low amplitude signature ranging from +2 to -4 mm (Figure 4.15.E). Other locations including oil pads, wells, and pump stations show up to +4 mm of uplift (see isolated blue areas, Figure 4.14). POI 4 is located just east of inset E and is placed on a well pad (Figure 4.14). POI 4 shows the highest subsidence of +4 mm with the highest rate of deformation which occurred in July 2018 (Figure 4.16).

Other general deformational trends were identified in the 2018 data set. The north portion of the Sag River Delta shows uplift from +1 to +4 mm (Figure 4.14). Generally, subsidence in areas west of the Sag River appeared slightly greater than the subsidence east of the Sag River. Small tributaries in the Franklin Bluffs showed minor subsidence. Lakes consistently showed lower coherence than rivers and were masked out during InSAR processing.

A 2018 seasonal time series of deformation at the POIs varied across the AOI and are shown in Figure 4.16. Deformation was positive at several locations due to the regional uplift, specifically in the eastern portion of the AOI but does not exceed ± 5 mm. POIs 1 and 6 both showed uplift of +1 mm and

+5 mm, respectively. POI 2 was inundated by both flood pulses of the 2015 Sag River flood and shows a cumulative subsidence of -2 mm (Figure 4.15.A). POIs 3 and 5 showed the highest subsidence of -4 mm. POI 5 showed minor subsidence of -3 mm.

4.1.2.3 Summer 2019 Surface Deformation Results

The estimated cumulative deformation for summer 2019 ranged between -61 and +41 mm over a five-month (May 1 to October 1) period (Figure 4.17). Mean deformation was -12 mm. The mode was -17 mm. See Figure 4.17 for histogram distribution of deformation of summer 2019.

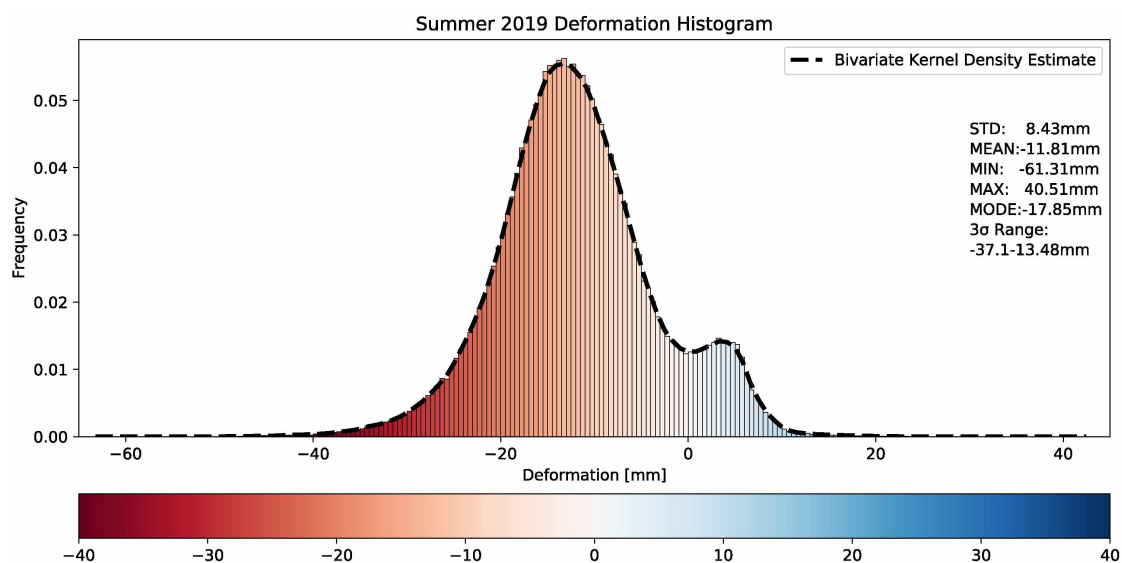


Figure 4.17: Histogram of relative deformation of the AOI during summer 2019. Pixel values in millimeters. Bins sampled every 0.5 mm. Bivariate kernel estimate of deformation shown with dashed line.

The cumulative 2019 summer deformation is shown in Figure 4.18. An annotated version of Figure 4.18 is shown in Figure 4.19. Deformation varied throughout the AOI. The following sections discuss key areas in the 2019 deformation data.

Key inset areas outlined in Figure 4.19 are shown in Figure 4.20 and Figure 4.21. For consistency, the same areas are discussed for previous years as for the summer 2019 data set. See Figure 4.20 for map insets.

Inset A shows the Dalton Highway flood breach and the TransAlaska Pipeline flood breach (Figure 4.20.A). Within areas of the Dalton Highway breach, where the distance between the highway and pipeline is less than 0.8 km, the ground showed a relative uplift trend. The northern extent of the Dalton Highway breach showed a continuation of this uplift trend along the edge of the Dalton Highway. Subsidence within the northern extension of the Dalton highway breach ranged from 0 mm to +42 mm (Figure 4.20.A). POI 2, contained within the inundated areas of the Dalton Highway breach, showed a cumulative subsidence of -8 mm (Figure 4.21). The highest rate of subsidence at POI 2 occurred during late August 2019. The TransAlaska Pipeline breach showed uplift of 0 mm to +12 mm along the western edge of the pipeline as it trended to the northeast (Figure 4.20.A). The highest subsidence of -20 mm in Inset A of -44 mm occurs in displaced arc shapes within the pipeline breach area. These subsidence arc shapes are located above ice-rich thaw lakes. The majority of the pipeline breach area shows subsidence ranging from -4 mm to -15 mm (Figure 4.20.A). POI 3 is contained within the TransAlaska Pipeline breach area and showed -12 mm of subsidence with the highest rate of subsidence occurring in August and early September 2019 (Figure 4.21).

Inset B shows deformation of the abandoned alluvial floodplain between the eastern channels of the Sag River (Figure 4.20.B). A majority of the deformation signal showed subsidence ranging from 0 mm to -39 mm. The subsidence of the abandoned floodplain area appeared to extend past the easternmost Sag River channel onto the adjacent shore. The subsidence on the adjacent shore ranged from 0 mm to -42 mm. The same abandoned floodplain showed uplift in the vicinity of POI 1 ranging

Deformation of Summer 2019

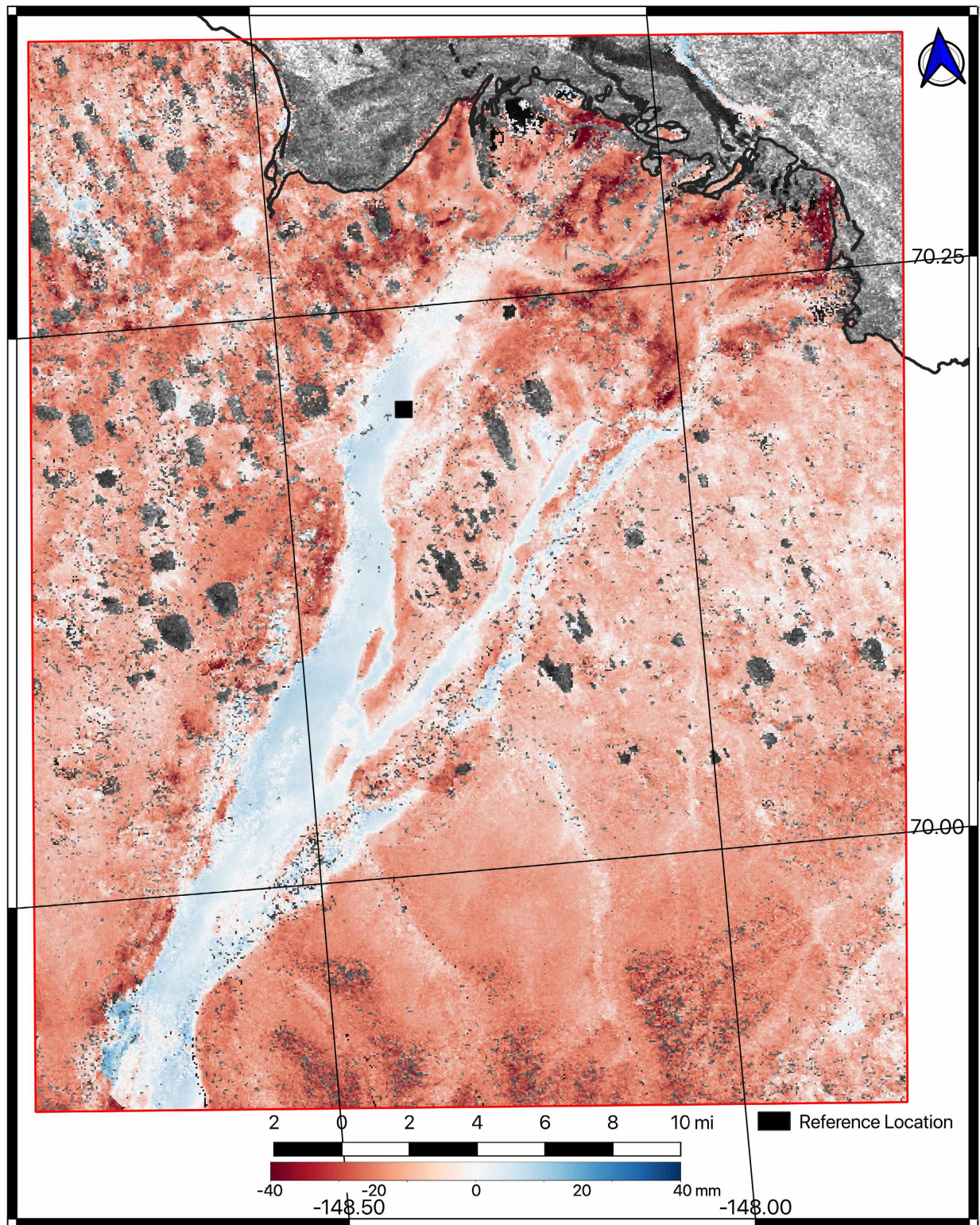


Figure 4.18: Summer 2019 subsidence and master amplitude image. An annotated version of the 2019 deformation map is shown in Figure 4.19.

Deformation of Summer 2019

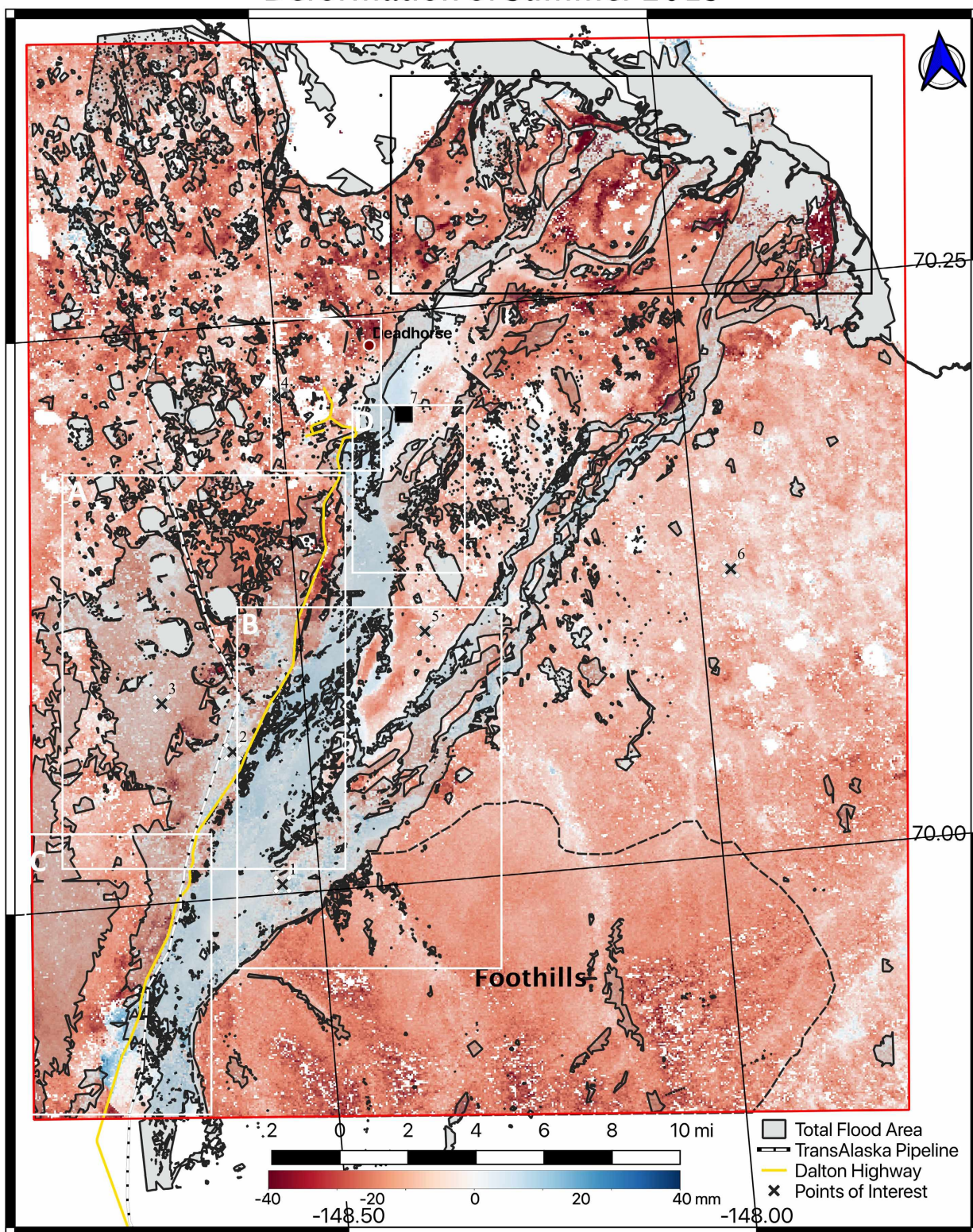


Figure 4.19: Seasonal 2019 summer subsidence. Xs show sampled locations of deformation (Figure 3.12). Gray shade areas show the total 2015 Sag River flooded area (Figure 4.6). Boxes outline inset maps (Figures 4.21 and 4.22).

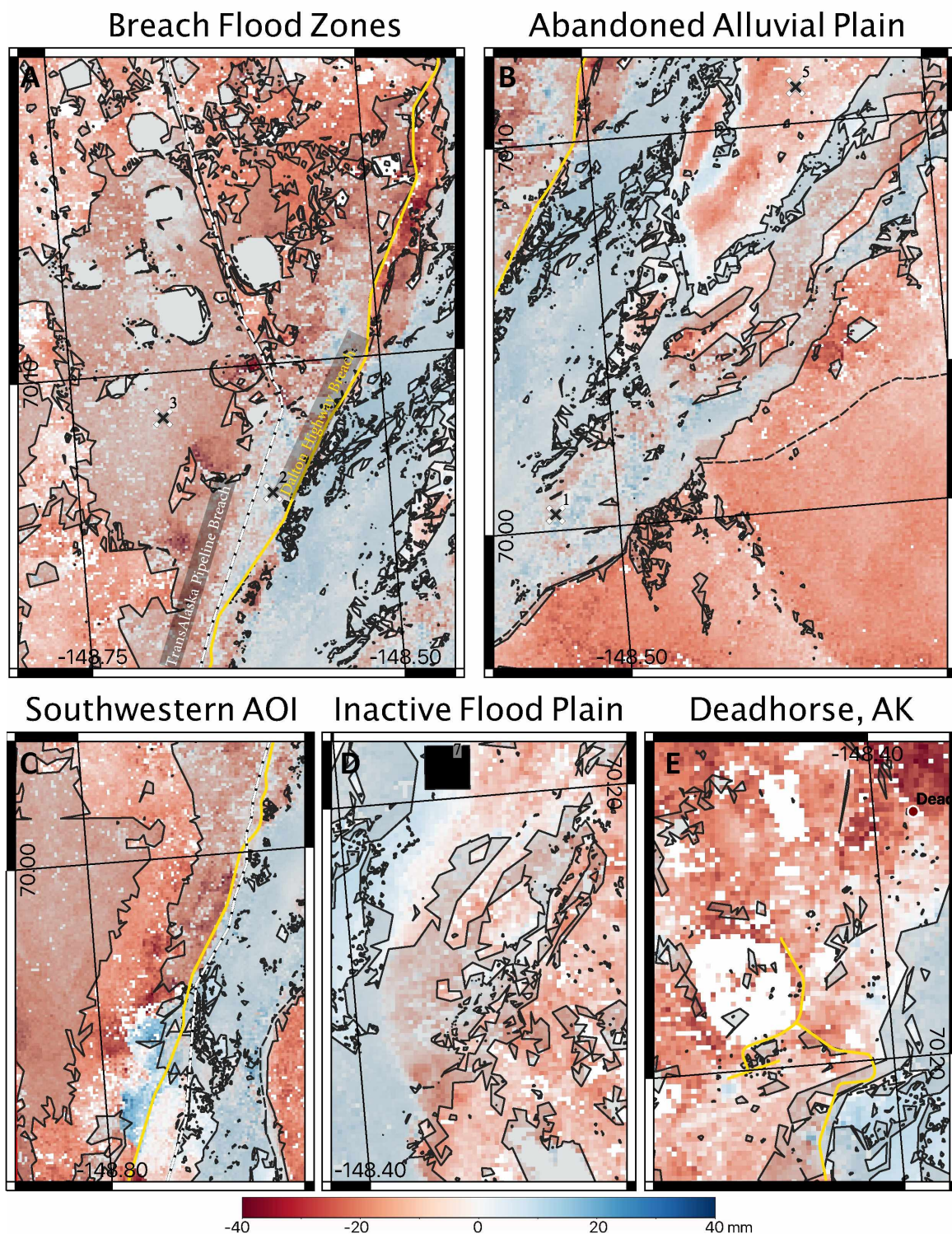


Figure 4.20: Inset maps showing estimates of the summer 2019 season deformation. Insets outlined in Figure 4.19. Inset A shows the Dalton Highway and the TransAlaska Pipeline breach areas. Inset B shows an abandoned alluvial plain between the eastern Sag River channels. Inset C shows an alluvial terrace in the southwestern AOI. Inset D shows inactive floodplain east of the airport at Deadhorse, Alaska. Inset E shows manmade structures at Deadhorse. The flood mask shown in gray. See Figure 4.19 for legend.

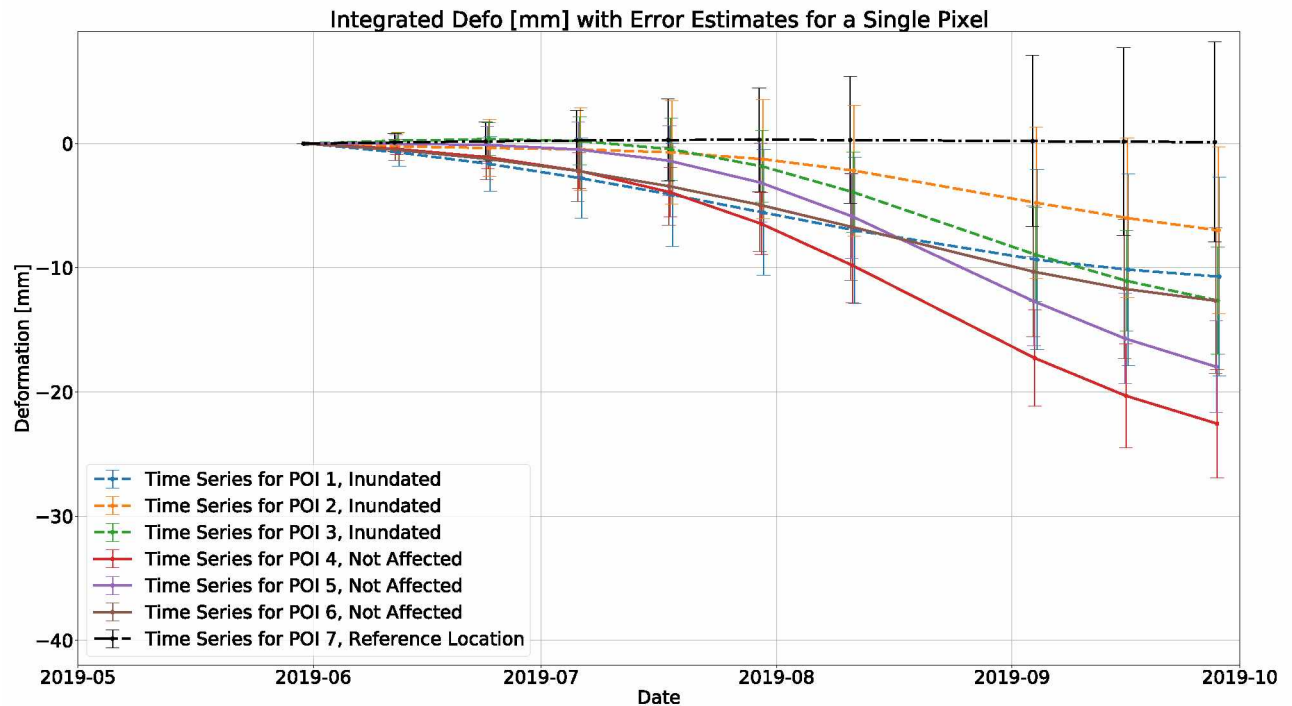


Figure 4.21: Plot showing the deformation at POI locations for the 2019 summer season. The reference location is labeled as POI 7 in the deformation plot. Deformation signal processed with a 2-month temporal filter.

from 0 mm to +17 mm (Figure 4.20.B). POI 1 is located between the subsided western edge and the uplifted eastern edge of the abandoned floodplain. POI 1 showed -10 mm of subsidence with the highest rate of deformation occurring in August 2019 (Figure 4.21). POI 5 is located in an adjacent, flood- unaffected floodplain to the north of the abandoned floodplain. POI 5 showed -18 mm of subsidence with the highest deformation rate occurring in late August 2019 (Figure 4.21).

Inset C shows the southwestern corner of the AOI (Figure 4.20.C). There appears to be a location displaying high uplift adjacent to subsidence with a sharp linear border dividing these locations. Such a phenomenon may be due to an unwrapping error producing a false jump in the data set. High subsidence within inset C parallels the Dalton Highway of its mapped extent. Subsidence ranged from 0 mm to -37 mm within this area (Figure 4.20.C).

Inset D shows the inactive floodplain east of the Deadhorse airport (Figure 4.20.D). The magnitude of deformation appears reduced when compared to the overall deformation signal of areas surrounding the TransAlaska Pipeline. Minimal uplift ranging from 0 mm to +5 mm was observed within AOI Inset D. A majority of the uplift is either sparsely distributed, mixed within subsidence or along a single linear trend located above a floodplain. Subsidence was broad and ranged from 0 mm to -24 mm. POI 7, the reference site, is located within Inset D (Figure 4.20.D). POI 7 showed minimal uplift averaging less than -1 mm over its area.

Inset E shows manmade structures near the town of Deadhorse Alaska. The only identifiable structure was the Deadhorse airport. The airport runway showed subsidence ranging from 0 mm to -1 mm (Figure 4.20.E). Other known areas of infrastructure were not identifiable based on deformational trends. POI 4 is located just east of Inset E on a well pad where deformation was the highest of the POIs, reaching a cumulative subsidence value of -22 mm (Figure 4.19). The highest rate of subsidence was during August, 2019 (Figure 4.21).

Summer 2019 analysis also displayed additional unique signals. Small tributaries in the Franklin Bluffs showed minor subsidence or uplift with locations masked due to low coherence. Lakes and rivers consistently showed lower coherence and were masked during InSAR processing. The southwestern AOI, west of the Dalton Highway, showed a small area of uplift by up to +20 mm (Figure 4.19). This area is highlighted in Inset C of Figure 4.20.C and was not affected by the 2015 flooding events. The uplift could be due to an unwrapping error in one of the interferograms of the 2019 data set. In areas that were not affected along the coastline, near the terminus of the Sag River delta, high subsidence ranged from -25 mm to -40 mm in the isolated alluvial plain and the eolian and delta deposits (black box, Figure 4.19). Inundated shorelines in Figure 4.20.D were masked due to low coherence.

The 2019 seasonal time series of deformation at the POIs varied across the AOI and are shown in Figure 4.21. The deformation data had a negative trend, having the highest rate in August 2019. POIs 1,2 and 3 were located in inundated locations and showed subsidence of -7, -11, and -13 mm. POI 4 is located at a well pad and showed the highest sampled subsidence of -23 mm. POIs 5 and 6 were located in areas that were not affected by the 2015 Sag River flooding and showed higher subsidence of -14 and -18 mm. POI 7 is placed at the reference location and showed values averaging <1 mm across the time series. Deformation at POI 7 is 0 mm within the margin of error.

4.1.3 Annual Surface Deformation Results

The estimated cumulative deformation from August 2015 to August 2019 ranged between -294 mm and +99 mm (Figure 4.22). The mean deformation was -16 mm. The mode was -33 mm. A bimodal kernel estimate of the deformation data showed a bimodal distribution with two local maxima occurring with a subsidence value of -21 mm and an uplift value of +44 mm (local maxima, Figure 4.22). See Figure 4.22 for histogram distribution of the annual deformation data set.

The cumulative multi-year surface deformation from August 2015 to August 2019 is shown in Figure 4.23. An annotated version of Figure 4.23 is shown in Figure 4.24. The areas of highest subsidence occurred within inundated regions (dark red, Figure 4.24).

Relative high subsidence, defined here as deformation lower than -60 mm in the annual deformation data set, occurred in five AOIs shown in Figure 4.26. The same AOIs as for the seasonal deformation are used. Deformation in the five AOIs is shown in Figure 4.27 and is described in the following paragraphs.

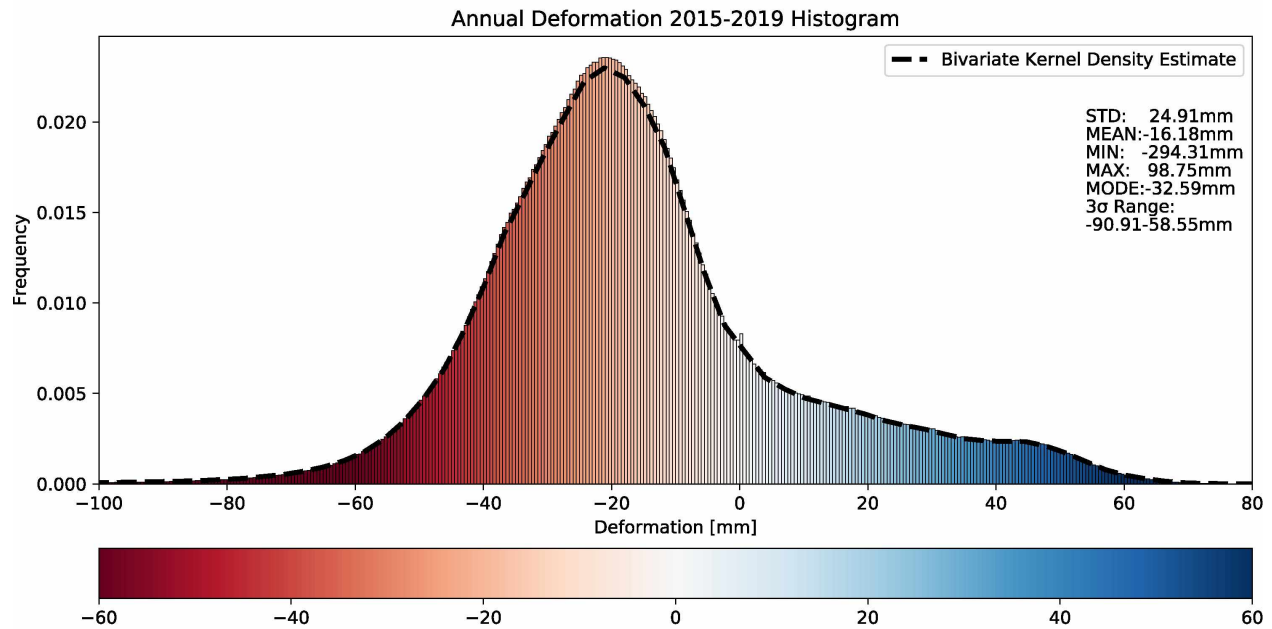


Figure 4.22: Histogram of cumulative annual relative deformation of the AOI. Deformation sampled from August 2015 to August 2019. Pixel values in millimeters. Bins sampled every 0.5 mm. Bivariate kernel estimate of deformation shown with dashed line.

Inset map A shows the areas west and southeast of the Dalton Highway and the TransAlaska pipeline that were breached during the 2015 Sag River Flood (Figure 4.27.A). Subsidence was highest in the northern areas of the Dalton Highway breach, up to -101 mm (see green and purple areas, Figure 4.27.A). A high subsidence trend in the deformation pattern appeared to be contained within a 1.6-km to 0.8-km area along most of the pipeline extent within the flooded areas (see green and purple areas, Figure 4.27.A). This high subsidence trend is most prominent in the southern TransAlaska Pipeline break, just north of the crossing point of the TransAlaska pipeline and the Dalton Highway. High subsidence ranged from -60 mm to -153 mm (see purple and yellow areas, Figure 4.27.A). The high subsidence trend parallels the TransAlaska Pipeline through the entire TransAlaska Pipeline breach area.

Inset B shows a 27-km by 2.4-km abandoned alluvial floodplain between the eastern channels of the Sag River. Subsidence values greater than -60 mm were observed over a four-year period in most

Annual Deformation August 2015 – August 2019

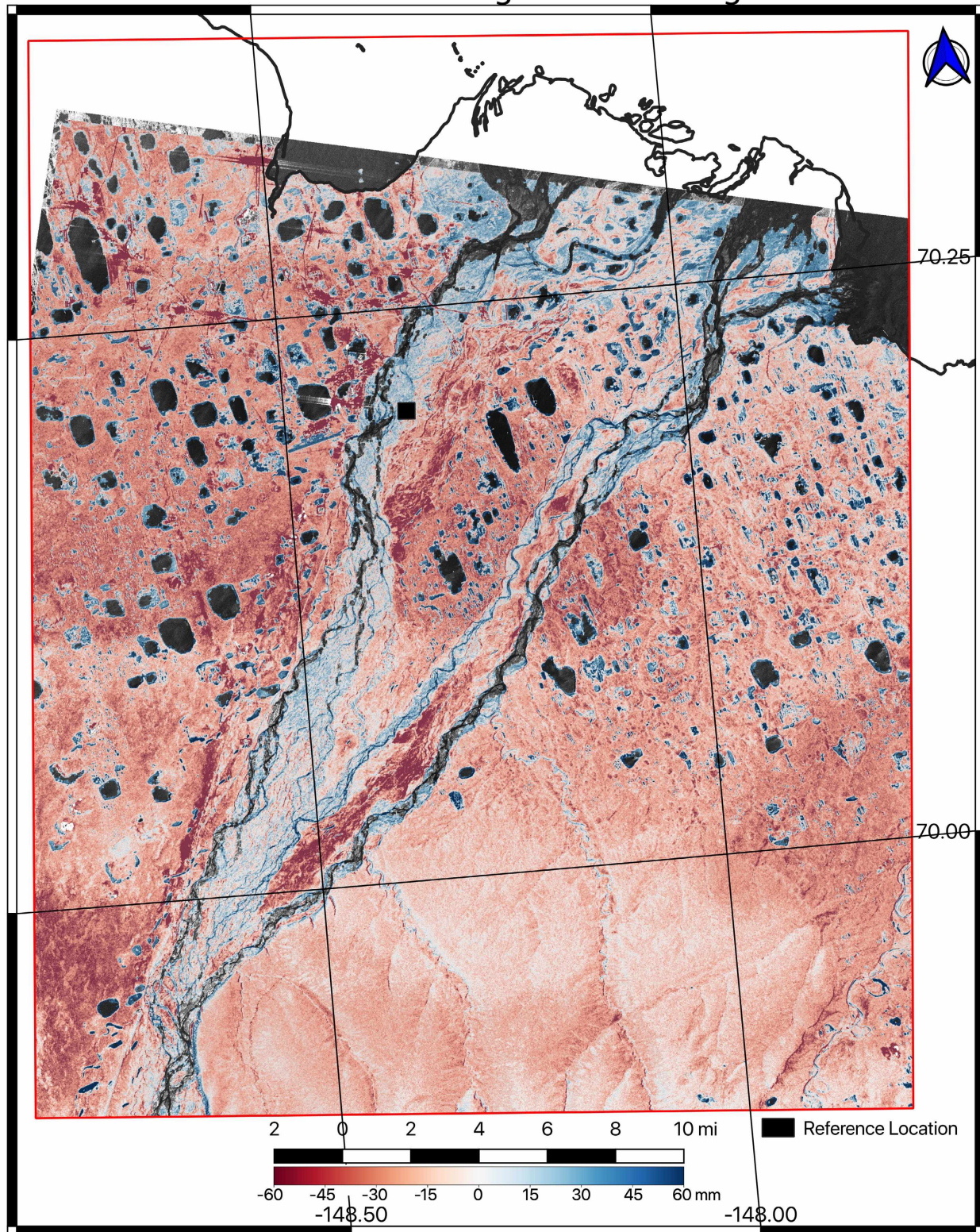


Figure 4.23: ALOS-2 cumulative deformation for the 2015-2019 period. August 2015 amplitude image shown in background. Annotated version shown in Figure 4.24.

Annual Deformation August 2015 – August 2019

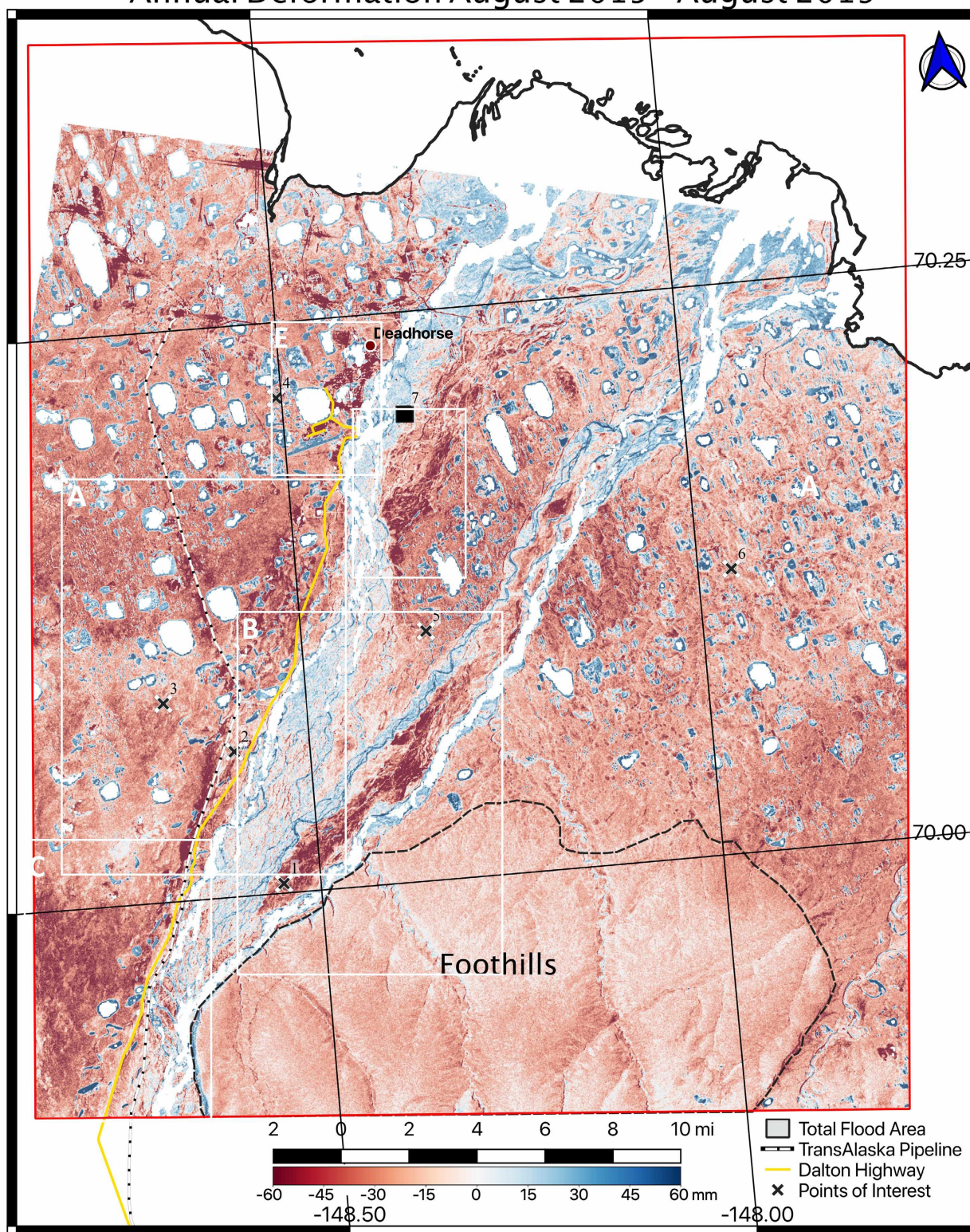


Figure 4.24: ALOS-2 Cumulative Annual subsidence from 2015 to 2019 with insets. Xs mark sampled locations of deformation (Figure 4.27). Flood affected areas shown in gray. Boxes outline inset maps (Figure 4.25).

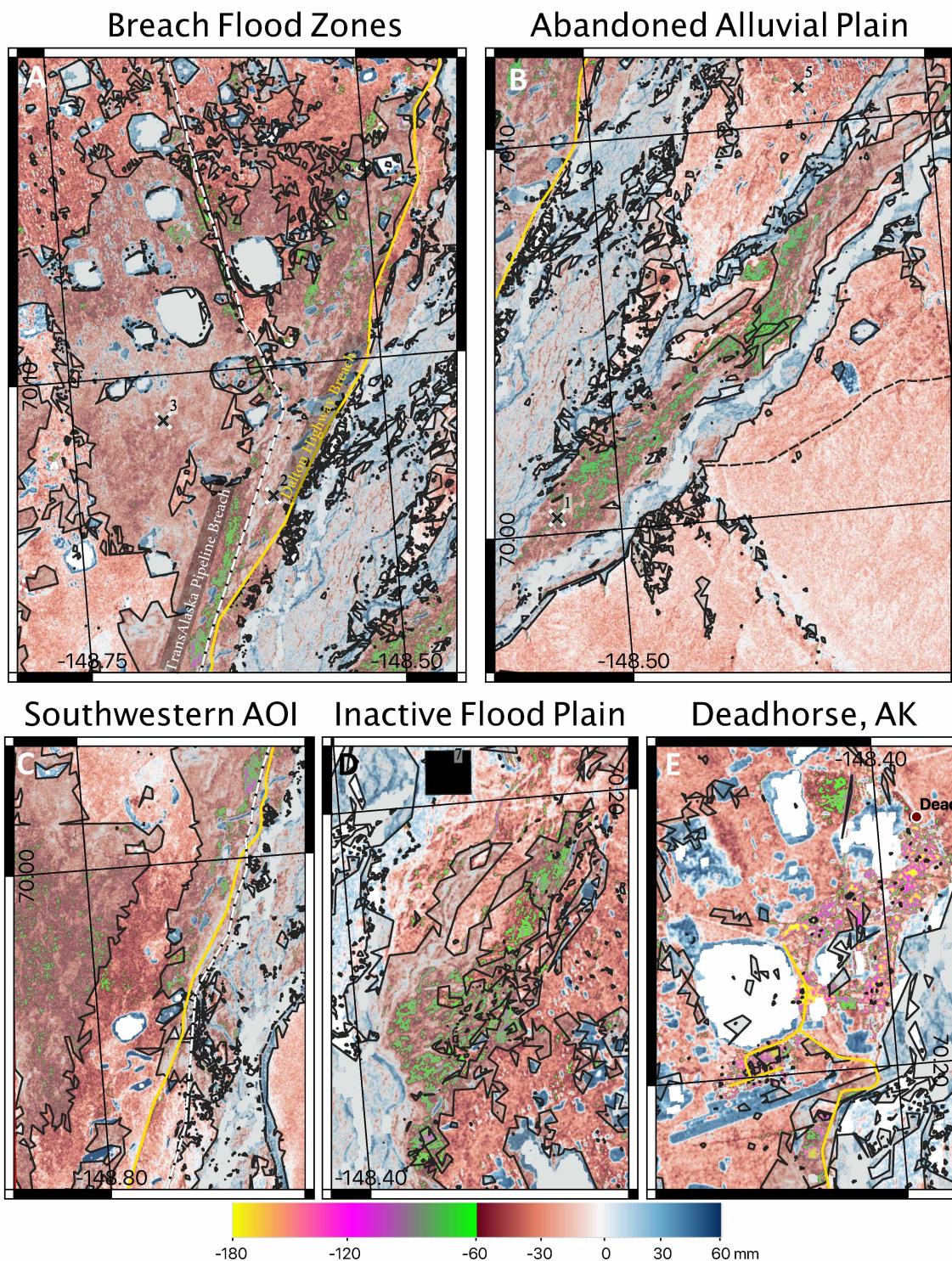


Figure 4.25: Inset maps showing estimates of ALOS-2 cumulative annual deformation. Data sampled over a four-year period, 2015-2019, outlined in Figure 4.24 as black boxes. Inset A shows the Dalton Highway and the TransAlaska Pipeline breach areas. Inset B shows an abandoned alluvial plain between the eastern Sag River channels. Inset C shows an alluvial terrace in the southwestern AOI. Inset D shows inactive floodplain east of the airport at Deadhorse, Alaska. Inset E shows manmade fabricated structures. Color bar scaled to show high subsidence. Reference Figure 4.24 for legend.

inundated locations of the alluvial plain. Areas shown in purple reached up to -97 mm of subsidence (Figure 4.25.A). The abandoned floodplain showed low subsidence to shallow uplifting areas residing over small drainages that typically flood once per year.

Inset C shows an alluvial terrace in the southwestern corner of the AOI. Sparse areas exceed -60 mm of subsidence. Isolated bullseyes of high subsidence ranging from -61 to -138 mm are contained within this inset area (Figure 4.25.C).

Inset D shows an inactive floodplain on the eastern side of the Sag River western channel, east of the Deadhorse airport. Subsidence was high and is up to -100 mm in the inundated areas (purple areas Figure 4.25.D).

Inset E shows the town of Deadhorse, Alaska (Figure 4.25.E). Deformation was the highest within Deadhorse, Alaska, ranging from +59 mm at the airport runway to -180 mm at equipment yards, buildings, well pads, and other manmade structures. (Figure 4.25.E). Across the entire AOI, the highest subsidence values of >-120 mm, occurred exclusively at manmade structures (Figure 4.24).

The ALOS 2 deformation map showing relative uplift is noted within the AOI (Figure 4.24). Although a coherence mask was utilized to mask open water areas, many of the areas showing relative uplift occurred in active floodplains. These surfaces have recurrent flooding and are part of the typical streams fluvial process. These floodplains are not discussed.

Along most of the length of the Dalton Highway, relative uplift occurred with magnitudes of +20 mm to +30 mm. This uplift pattern was 3-8 m-wide, a 1-pixel to 5-pixel width, from the center of the

road and extends from the southwestern AOI to the town of Deadhorse, Alaska (Figures 4.25 and 4.26). Uplift along the Dalton Highway is shown in Figures 4.25.A and 4.24 but, is more easily observed in the unannotated map (Figure 4.23). The Putuligayuk River showed relative uplift in areas located around most point bars on the shoreline (Figure 4.23 and 4.24). Correspondingly, cut banks of the Putuligayuk River showed high relative subsidence. The Sag River showed uplift on alluvial terraces and inactive flood plains. The Kadlershilik River in the southeastern AOI showed relative subsidence at point bars, gradual river curves and uplift at point bars around sharp curves. Cut banks showed high subsidence around tight curves and lower subsidence around gradual curves (Figure 4.23 and 4.24). Small tributaries at Franklin Bluffs showed lower subsidence than larger drainages which showed relative uplift (See foothills area, Figure 4.24). Large lakes, masked due to low coherence, showed relative uplift along their shorelines (Figure 4.23 and 4.24).

Annual deformation data were Gaussian high-pass filtered to remove long period signals. The distribution of high-pass filtered deformation of the AOI is shown in Figure 4.26. Deformation ranged between -289 mm of subsidence and +99 mm of uplift. The mean deformation value was -1 mm. The mode was -21 mm of subsidence. The data had a standard deviation of 23 mm and a 3-sigma range from -70 mm of subsidence to +68 mm of uplift. High-pass filtering leveled the data and removed most of the background values.

A Gaussian high-pass filtered version of the cumulative annual deformation data map is shown in Figure 4.27. An annotated version of Figure 4.27 is shown in Figure 4.28. The high-pass filtered deformation map was created to remove long period signals and trends from the data. The deformation signals represented in Figure 4.23 are more easily identified in the high-pass filtered map (Figure 4.27 and 4.28).

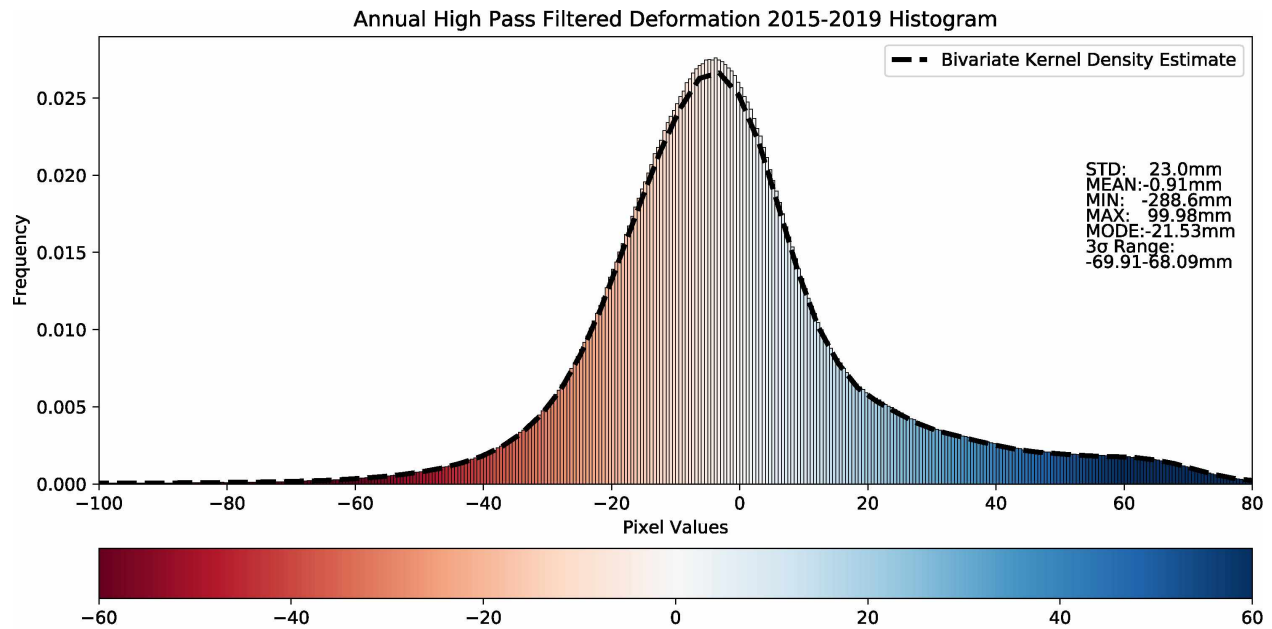


Figure 4.26: Histogram of high-pass filtered cumulative annual relative deformation of the AOI. Pixel values in millimeters. Bins sampled every 0.5 mm. Bivariable kernel density estimate of the deformation data is shown.

As we did previously, we analyzed deformation patterns within the five AOIs shown in Figure 4.28. The deformation signal in each high-pass filtered area appeared sharpened and more pronounced from the background signal after high-pass filtering. Inset A shows breached flooding east and southeast of the Dalton Highway and TransAlaska Pipeline. The high subsidence along the western edge of the pipeline areas was reduced with the long period signals removed, limited to an area 0.4 km to 0.8 km to the west. This high subsidence was lower in magnitude, just exceeding -60 mm. The extent of the high subsidence area appeared along most of the pipeline extending from the southern western edge of the AOI to the TransAlaska Pipeline pump station 1 located west of the town of Deadhorse, Alaska (Figure 4.29.A).

Inset B shows the high subsidence area along most of the inundated zones of the abandoned floodplain. High pass filtering reduced the amplitude slightly; subsidence ranged from -0.5 mm to -93 mm (Figure 4.29.B).

High Pass Filtered Annual Deformation 2015 – 2019

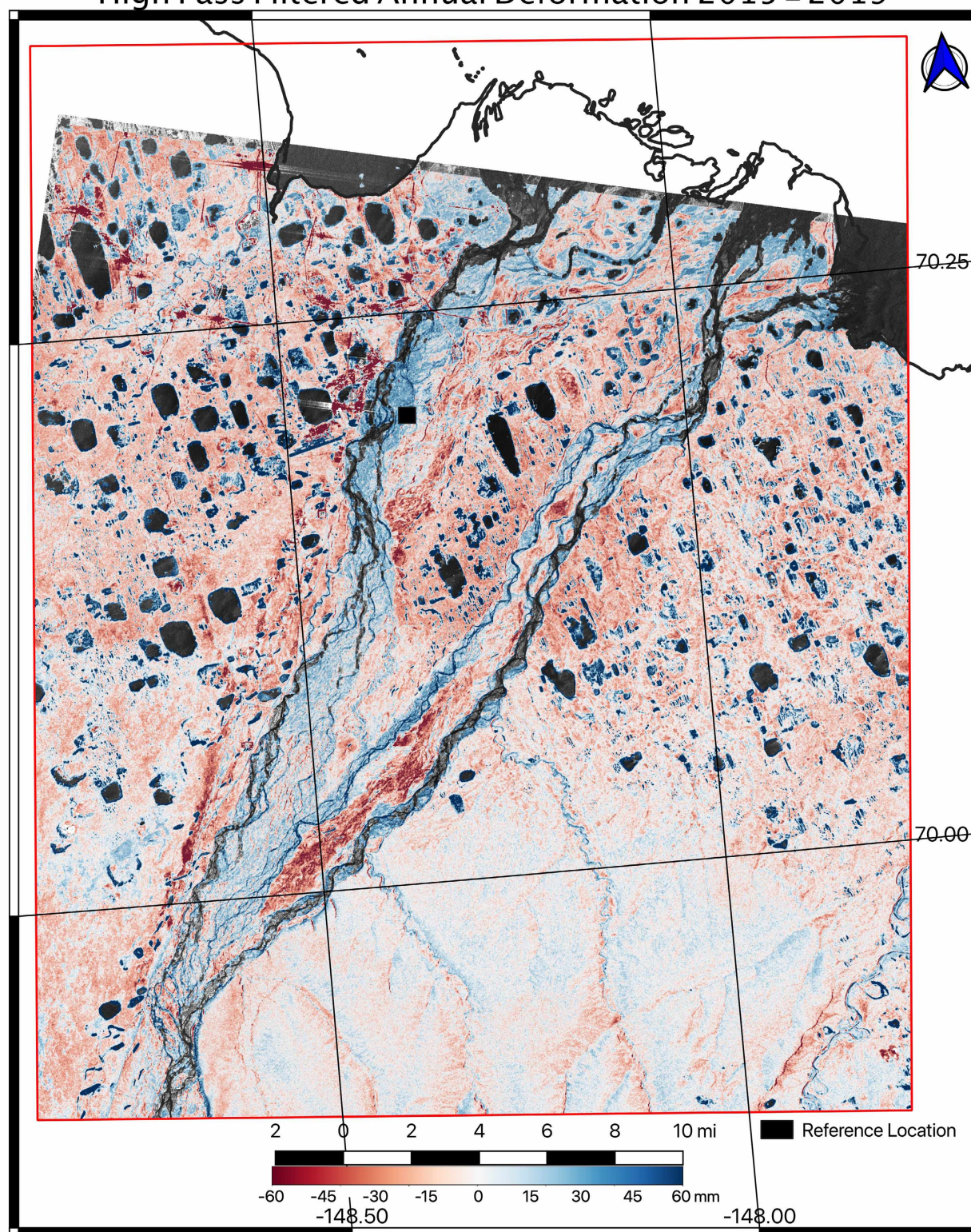


Figure 4.27: ALOS-2 Gaussian high-pass filtered annual deformation. August 2015 amplitude image shown behind deformation map. Annotated map shown in Figure 4.28.

High Pass Filtered Annual Deformation 2015 – 2019

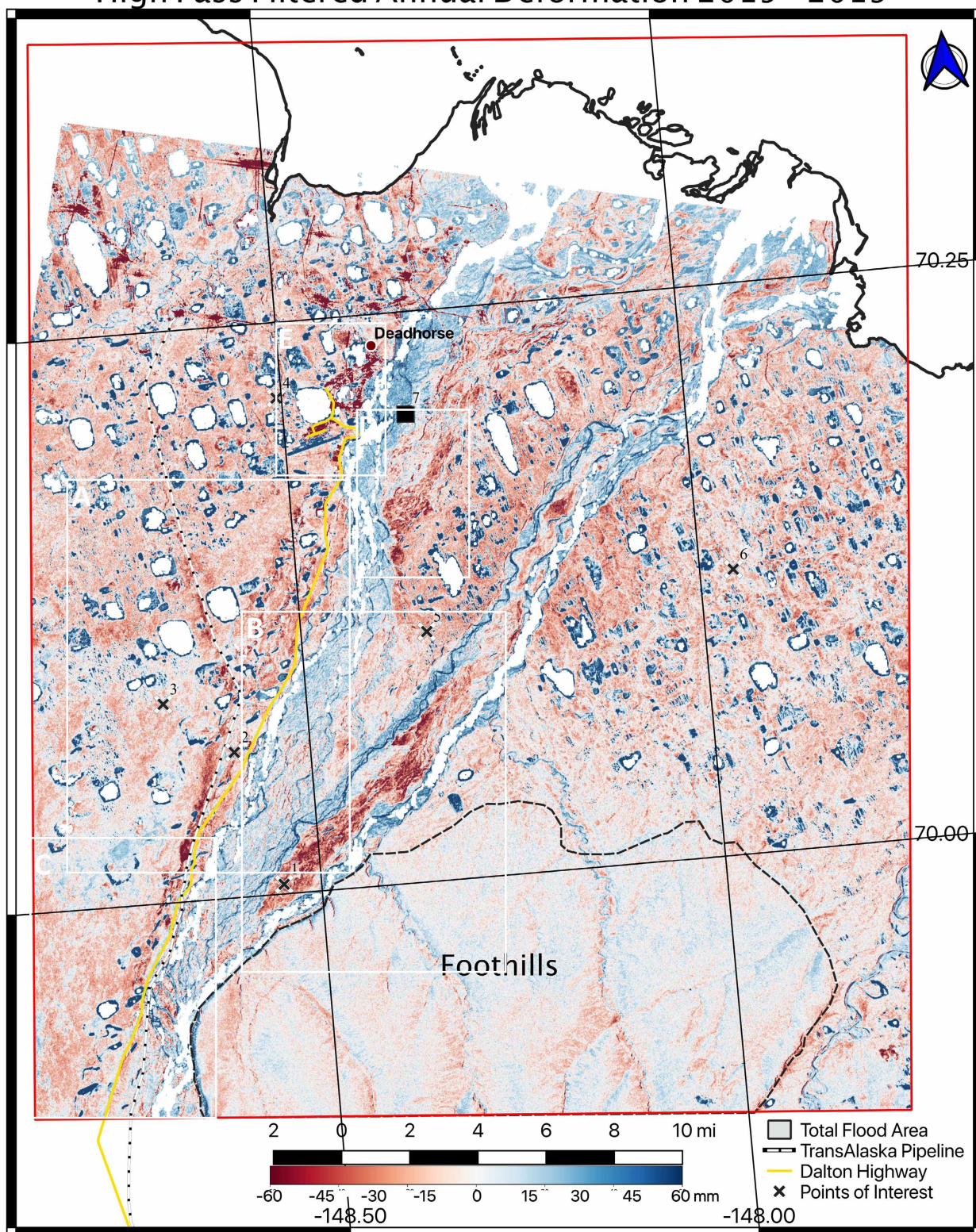


Figure 4.28: ALOS-2 Gaussian high-pass filtered annual deformation with insets. Xs mark sampled deformation (Figure 4.29). Black boxes outline inset maps (Figure 4.29).

Inset C shows an inundated terrace in the southwestern corner of the AOI. The amplitude in this area was greatly reduced and averaged -20 mm of subsidence. High subsidence was filtered out. The bullseyes of high subsidence have decreased to a range of -45 to -110 mm (see purple and yellow areas, Figure 4.29.C).

The inactive floodplain shown in Inset D displayed high subsidence up to -90 mm after filtering (Figure 4.29.D). The trend of subsidence in the inactive floodplain is sharply defined and the overall magnitude reduced.

Inset E shows manmade infrastructure at Deadhorse, Alaska. The effect of the high-pass filtering shifted the extreme values. The highest uplift of -60 mm occurred on the airport runway. The highest subsidence occurred at various equipment yards and infrastructure at the town of Deadhorse, Alaska. The majority of manmade infrastructure areas exceeded -160 mm of subsidence (yellow areas, Figure 4.29.E).

Two additional image signatures were identified in the annual deformation data set: F&G) pingos and H) the Franklin Bluffs cliff face. Pingos are primarily located in thaw lake or ice-rich thaw lake lacustrine deposits. Within the AOI, pingos rose +18 meters above the ground surface. Deformation of pingos has a unique signature in the data. The base of the pingo contains a residual lake at its base and shows a partial ring of relative uplift and the summit of the pingo showed high deformation (Figure 4.30.F&G). The Franklin Bluffs cliff face also showed relative uplift along most of its exposure (Figure 4.30.H).

A deformation time series for the seven POIs are shown in Figure 4.31. Subsidence in all POIs appeared to increase over time. POIs 1, 2, and 3 are located near the Dalton Highway in the southern

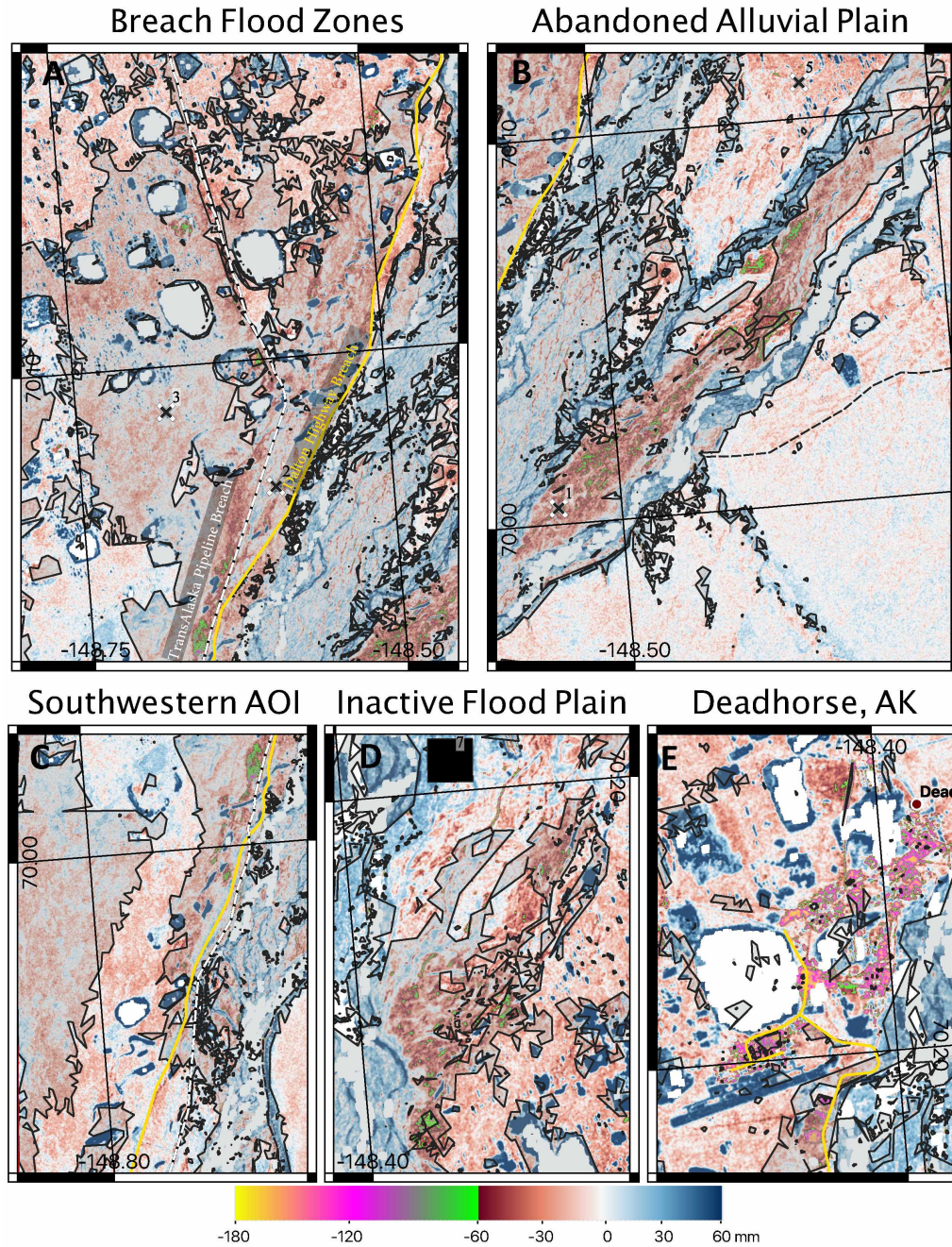


Figure 4.29: Inset maps showing estimates of high-pass filtered ALOS-2 annual deformation. from 2015 to 2019, as outlined in Figure 4.27 as white boxes. Inset A shows the Dalton Highway and the TransAlaska Pipeline breach areas. Inset B shows an abandoned alluvial plain between the eastern Sag River channels. Inset C shows an alluvial terrace in the southwestern AOI. Inset D shows an inactive floodplain east of the airport at Deadhorse, Alaska. Inset E shows manmade structures. Color bar adjusted to show high subsidence. Reference Figure 4.27 for legend.

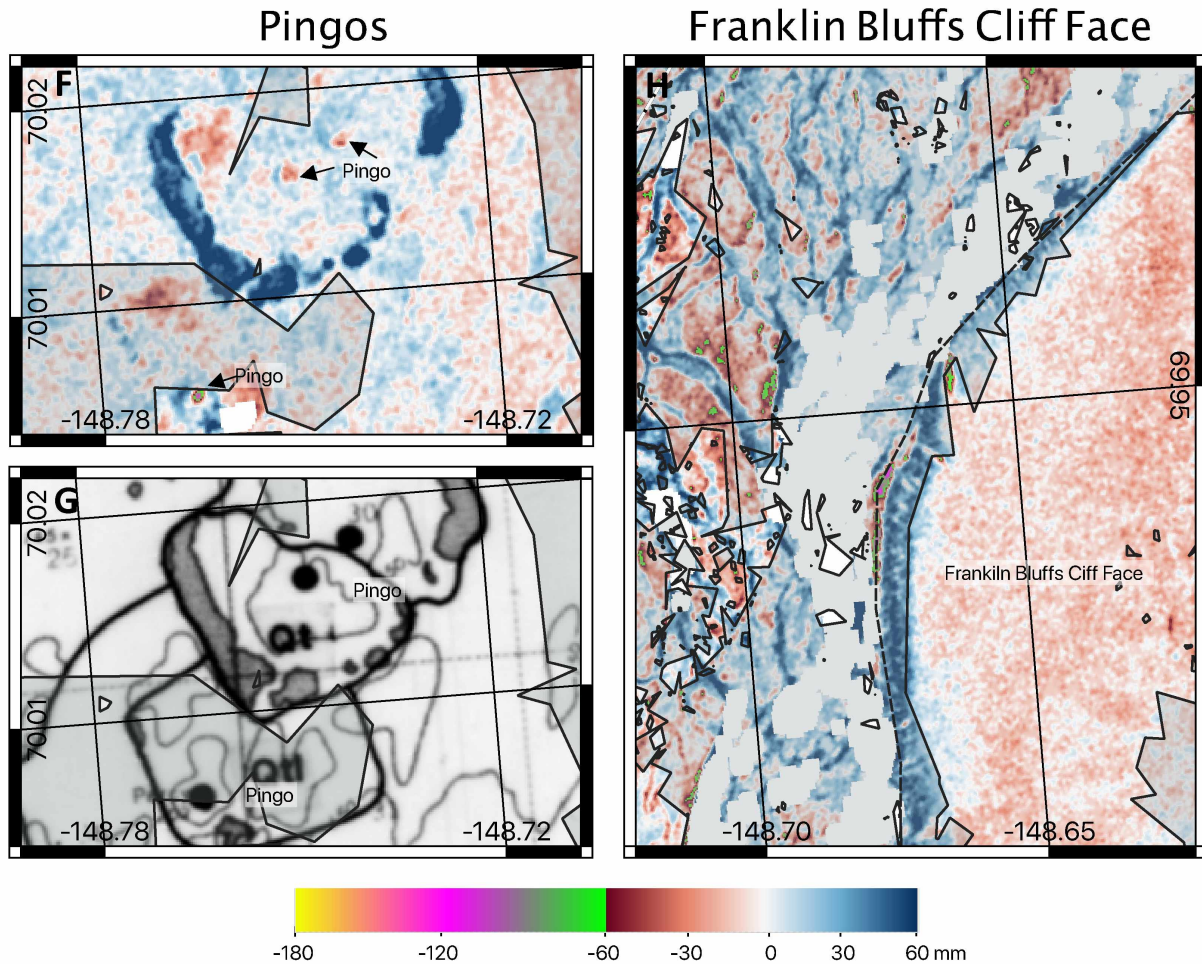


Figure 4.30: ALOS-2 cumulative annual deformation of unique structures. Inset F shows point deformation over pingos. Inset G shows the Rawlinson (1993) surficial geologic map of the areas surrounding the Pingos. Pingos mapped as black dots in Inset F. Inset H shows the Franklin Bluffs cliff face and the local deformation pattern exposed at its cliff face.

AOI near the Trans Alaska Pipeline and were inundated. These areas showed the most total, and highest rate of, subsidence over the four-year study period. POI 4 is placed directly on a well pad and showed the most subsidence of -44 mm over a four-year study period. POIs 5 and 6 are both located in areas that were not affected from the 2015 Sag River flooding events and showed the lowest subsidence over four years. POI 7 is the reference location of the ALOS-2 deformation data set, and showed minimal ~+1 mm uplift over the four-year study period. Deformation of POI 7 is 0 mm within the margin of error. See table 3.5 for description of POI sites.

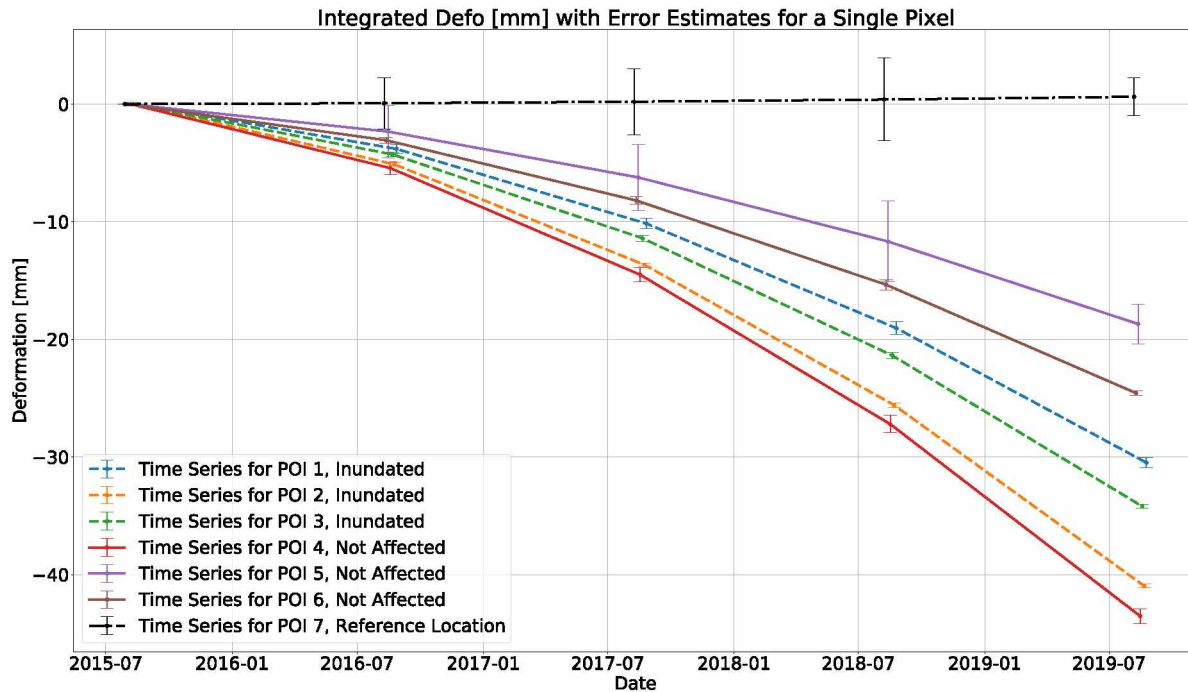


Figure 4.31: Plot showing the deformation of POI locations within the AOI. The reference location is labeled POI 7 in the deformation plot (Figures 4.24). Flood water POI inundated locations are dashed. Unaffected POIs are solid lines.

4.1.4 Summary DEM Differencing Results

Due to the high number of DEMs that have been differenced, four differenced DEMs were selected to show examples of the topographic change within the AOI. These time frames are : 1) a pre-flood time, pre-flood DEM to a time point just after the flood, May 27, 2015; 2) a pre-flood time, pre-flood DEM, to a time after the 2015 Sag River flood, June 21, 2015; 3) a comparison of after the flooding events, June 21, 2015, to a time period well after the flooding events, December 5, 2016; and 4) a comparison of time after the flooding events December 5, 2016 to February 2017. The following paragraphs describes the successfully processed differenced DEMs and discuss their results.

The pre-flood - May 27, 2015 DDEM compared a period just before the main flooding to a time just after the first flood pulse. The differenced DEM represents topographic changes that occurred immediately after the flood (Figure 4.32). A majority of Figure 4.32 shows noise in the Sag River channels or other bodies of water, such as lakes. Two notable locations of topographic change are noted in the differenced DEM. The first area is located east of the Dalton Highway and showed a topographic change of -0.5 m to -5.0 m. This location of the Dalton Highway is close to the Sag River channels. The second area is located west of the TransAlaska Pipeline and showed a negative topographic change ranging from -0.5 m to -2.5 m. Topographic change also occurs along the eastern side of the TransAlaska Pipeline but, the extent of the topographic change was less. The high degree of noise could represent open water surfaces.

An additional DDEM was measured from pre-flood time, pre-flood DEM, to a time just after the flood, June 21, 2015. A majority of this DDEM consists of high topographic noise generated in the Sag River channels (Figure 4.33). The main notable topographic change observed in the DEM occurred along the eastern edge of the Dalton Highway. Negative topographic change of -0.25 m to -5.0 m occurred within this location. A majority of the topographic change consisted of noise contained within the Sag River channels.

In order to identify the longer-term topographic change that might have occurred after the 2015 Sag River flooding, the DEM acquired on December 5, 2016 was differenced from the pre-flood DEM. No notable features outside of the Sag River channels, other than manmade structures or noise generated in open water areas were identifiable in the map (Figure 4.34). This is due to the large HoA of the 2016 DEM. The sensitivity to height with such a large HoA has reduced the ability to identify small topographic changes in the DDEM.

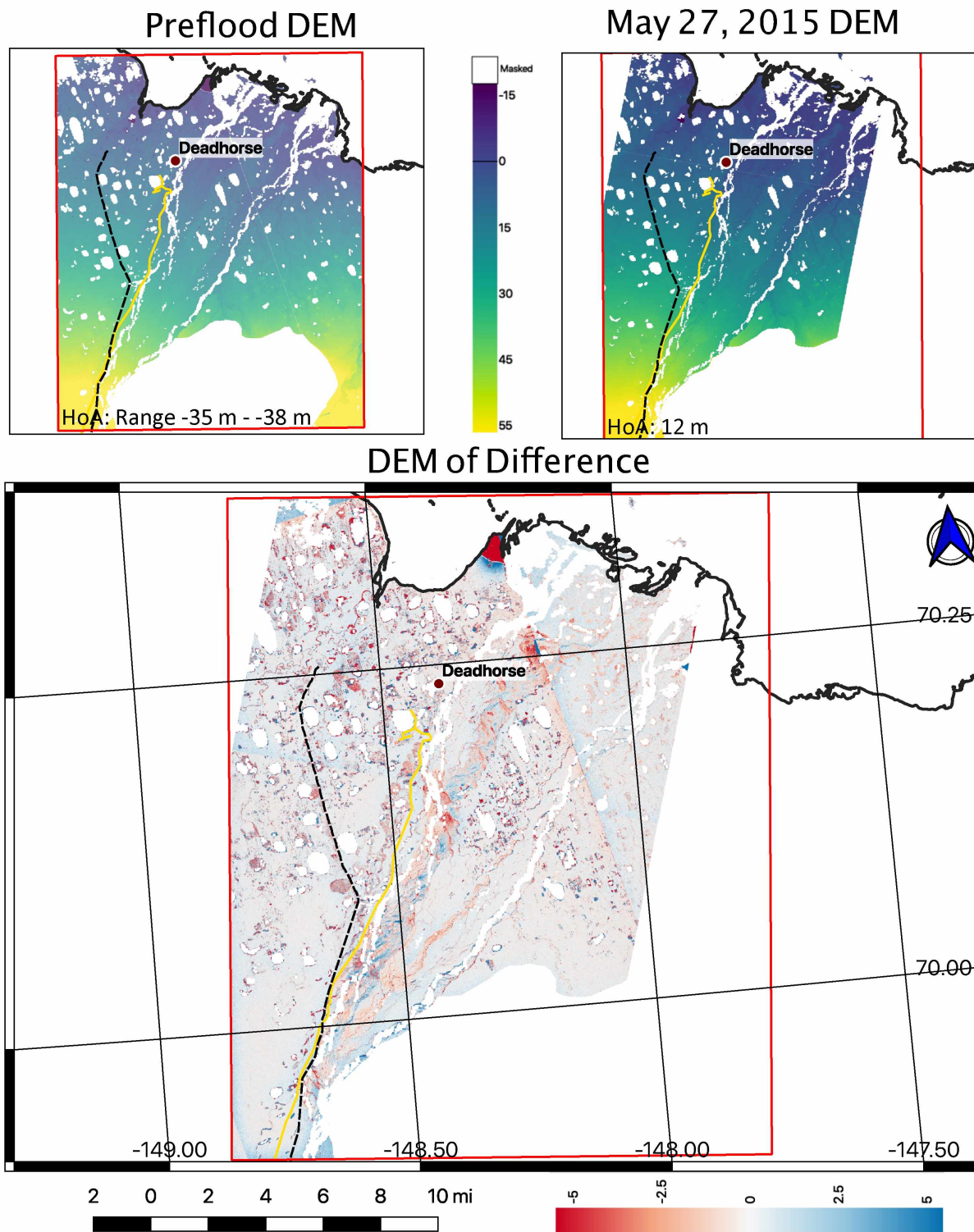


Figure 4.32: Preflood - May 27, 2015 DDEM. DDEM shows the difference from pre-flood time to just after the first flood pulse. Height of Ambiguity (HoA) shown.

The final analyzed DDEM provided a long-term comparison of DEMs, and compared a time period well after the events of the 2015 Sag River. The December 5, 2016 DEM was differenced with the February 29, 2017 (Figure 4.35). Due to a horizontal shift which could not be corrected with high-pass filtering or DEM coregistration, the DDEM contained frequent errors in the final map. The DDEM contains a high amount of noise due to the horizontal shifts moving areas of higher topography above flat lying areas. As mentioned previously the height HoA of the 2016 DEM has reduced the sensitivity to detect small scale topographic changes in the DDEM.

4.2 Joint Data Analysis

Joint data analysis was conducted in three focus areas: i) an abandoned alluvial floodplain between the eastern Sag River Channels; ii) Sag River western terrace just west of the crossing point of the Dalton Highway and TransAlaska Pipeline; and iii) Sag River eastern terrace just east of the Dalton Highway located just south of Deadhorse, Alaska (Figure 3.18). A requirement is that individual areas with similar geologic formations be contained in inundated and flood-unaffected areas. These sites were chosen to represent the effects of areas near the Dalton Highway, TransAlaska Pipeline, and the abandoned alluvial floodplain between the eastern Sag Rivers channels, an area not typically analyzed for permafrost impact. The following sections discuss the observations of each area.

4.2.1 Analysis of the Eastern Sag River Focus Area

Figure 4.38 shows the location of the eastern Sag River channel focus area. The eastern channel was selected because the flood had a limited inundation within the abandoned alluvial plain, making it an optimal area for evaluation. The boundary of the focus area was limited to the northeast and southwest by the extent of the flood-unaffected area. The northwest and southeastern extents were

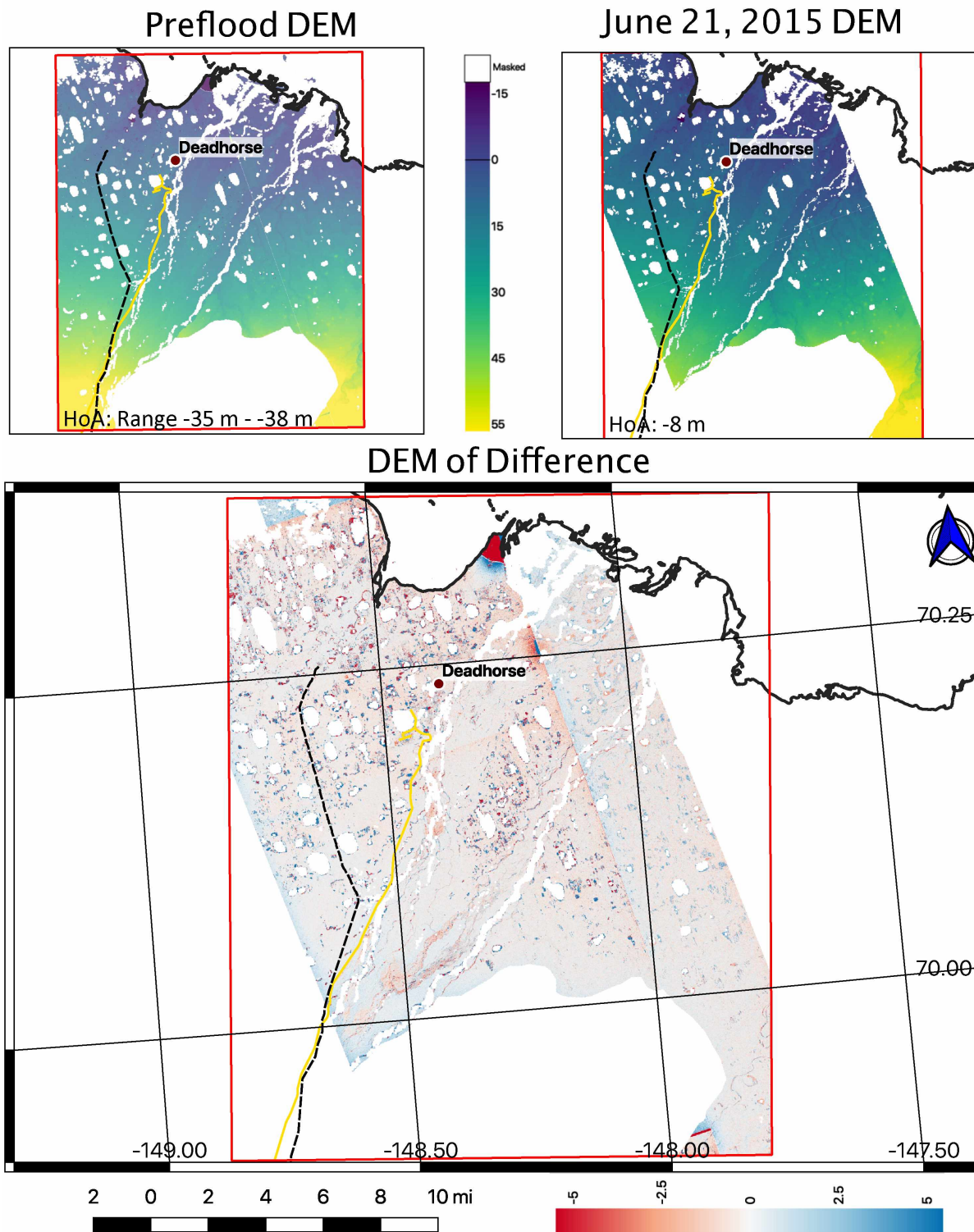


Figure 4.33: Pre-flood - June 21, 2015 DDEM. DDEMs shows the difference pre-flood time to time just after the flood. HoA shown.

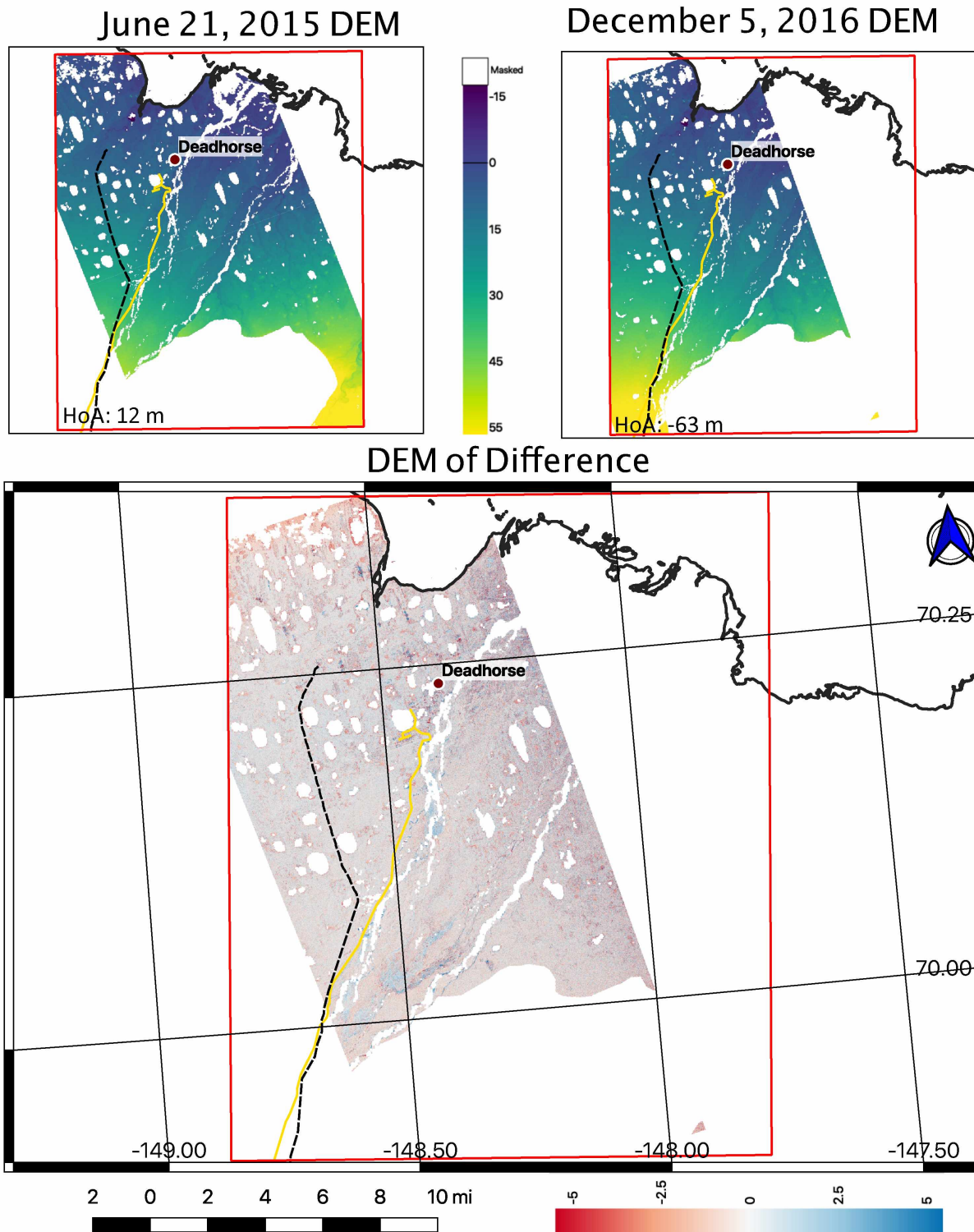


Figure 4.34: June 21, 2015 - December 5, 2016 DDEM. DDEM comparison of after the flooding events to a time well period after the flooding events. HoA shown.

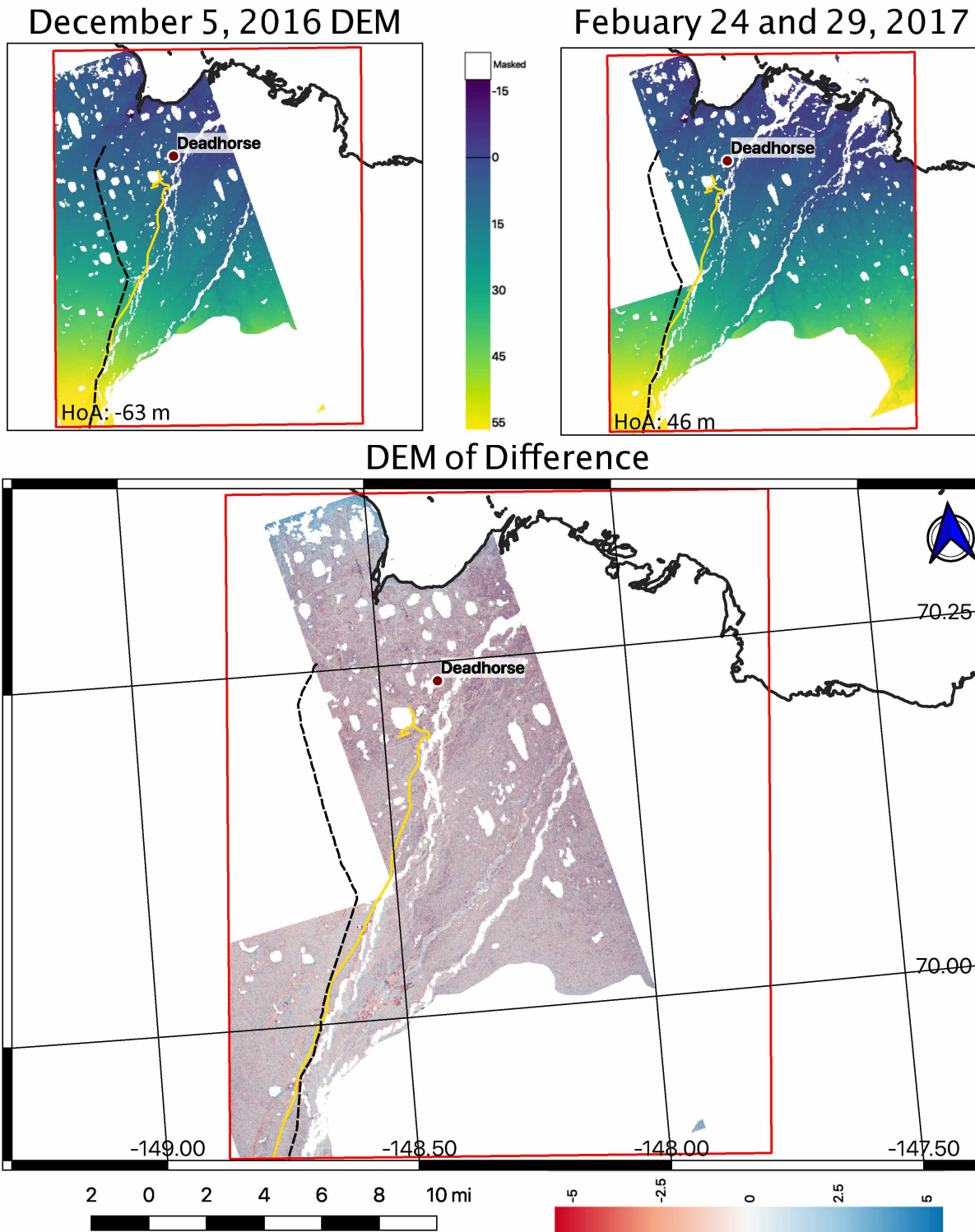


Figure 4.35: December 5, 2016 - February 2017 DDEM. DDEM covering a time period well after the flooding events. Horizontal shifts contained in the DDEM generated the high associated noise of the DDEM. HoA shown.

limited to the active floodplain in the Sag River channels. Analysis of the abandoned alluvial floodplain deposit was the primary focus of the eastern Sag River channel focus area. Additional geologic formations, including eolian sand dune and fluvial inactive floodplains, were not investigated during this evaluation due to their limited exposure within the selected study area (Figure 4.36). Active floodplain deposits present only in the Sag River channels were omitted as the entire area was inundated by the 2015 Sag River flooding events.

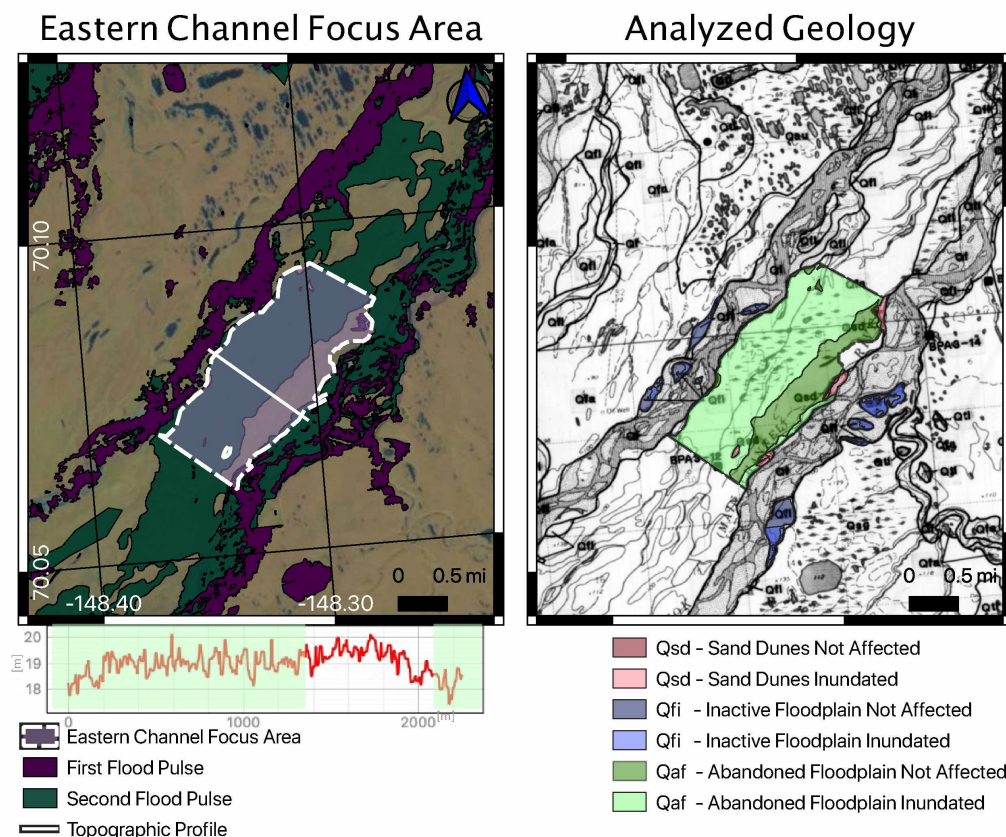


Figure 4.36: Location of the eastern channel focus area and abandoned floodplain. Analyzed geologic formation shown. Abandoned alluvial floodplain shown in green. Topographic profile of TDX reference DEM shown across the flood plain and displayed below the focus area map, with the inundated area shown in light-green. Surficial geology from Rawlinson (1993).

The total area of the abandoned alluvial floodplain focus area was 607 hectares. Flooding within the focus area was mostly confined to the western side of the abandoned floodplain. The first flood pulse did not inundate the focus area. The second flood pulse inundated 455 hectares, or 75% of the

eastern channel focus area (Figure 4.36). There was a slight rise in elevation to just over 19.5 m above sea-level, in the area between the inundated and flood-unaffected areas (refer to topographic profile, Figure 4.36). Generally, a correlation between topography and the inundation extent was noted within the sand dune or inactive alluvial plains areas. A topographic relief on the structure greater than 1 m had less inundation than areas of lower topographic difference across the feature. However, the elevation difference varied greatly within the focus area. A time series of the seasonal and annual deformations is shown in Figure 4.37 and the corresponding cumulative deformation map of the time series is also shown for visual reference (See insets for the time series A, B, C, and D; Figure 4.37).

The annual deformation of the focus area is shown in Figure 4.37.A. The focus area showed a mean subsidence value of -48 mm within inundated areas and consistently showed more subsidence than flood-unaffected areas across the deformation time series. The cumulative subsidence mean for flood-unaffected areas was -40 mm. The distribution of the violin plots shows a broad range in deformation (bottom panel of Figure 37.A). This range in flood-unaffected areas may be attributed to small depressions, showing uplift within the inundated eastern channel focus area combined with the broad subsidence in the inundated area. The flood-unaffected areas show a lower range of deformation across the entire time series (Figure 4.37.A).

Deformation for the summer 2017 season showed an increased subsidence mean value, -17 mm, in inundated areas over a five-month (May 1 to October 1) period compared to the mean subsidence value, -4 mm, in flood-unaffected areas (Figure 4.37.B). Decorrelation was also noted within inundated areas (Figure 4.37.B). The distribution of inundated areas had a single mode in the distribution of deformation measurements in the violin plot (Figure 4.37.B). This mode was slightly lower

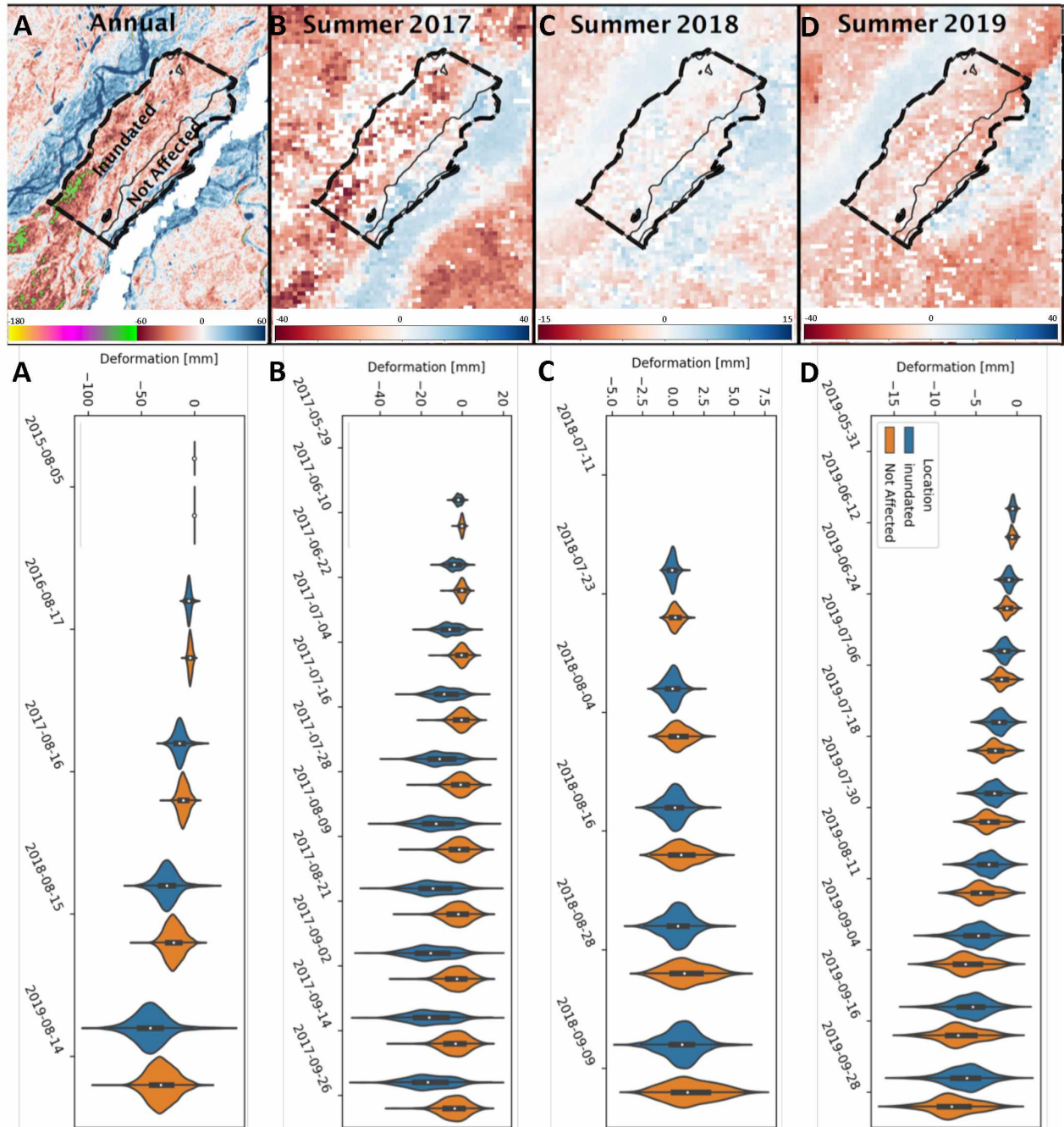


Figure 4.37: Averaged time series of deformation of abandoned floodplain. Inundated (blue) and flood-unaffected areas (orange) shown. Snapshot of cumulative deformation within the sampled area is shown.

than the mean (Figure 4.37.B). The variance in deformation measurements in both the inundated and flood-unaffected regions increases with time. The bimodal distribution within the inundated locations was related to low-magnitude subsidence at small channel depressions and and higher-magnitude subsidence in a region southwest corner of the focus area (green areas, Figure 4.37.B). The distribution

of flood-unaaffected locations in the violin plots appeared to be relatively equal and marquise-shaped throughout the time series (Figure 4.37.B).

Deformation for the summer 2018 season showed uplift in both inundated and flood-unaaffected areas over the three-month (July 1 to October 1) period (Figure 4.37.C). Uplift within inundated areas was slightly less than in flood-unaaffected areas. The cumulative mean deformation values were +1 mm in flood-unaaffected areas versus <+1 mm in flood inundated areas. The distribution of data in flood-unaaffected areas had a larger variance when compared with inundated areas (Figure 4.37.C).

Deformation for summer 2019 showed subsidence in both inundated and flood-unaaffected locations over a five-month (May 1 to October 1) period (Figure 4.37.D). The inundated locations consistently showed a mean subsidence value of -6 mm, lower than the mean subsidence of -8 mm in flood-unaaffected areas. Flood-unaaffected areas showed more subsidence though the time series. The distribution of deformation measurements consistently showed more values below the mean of the data. The data, both within inundated and flood-unaaffected areas, showed equal spread across the time series (Figure 4.37.D).

DEM differencing showed no identifiable pattern or signature of topographic change across the pairs for which offset issues could be successfully corrected. Figure 4.38 shows the pre-flood to June 21 2015 DDEM and the associated violin plot. The pre-flood-June 21, 2015 DDEM was chosen due to the variation in topographic change. Other DDEMs showed no identifiable trends related to topographic change. Within inundated areas, the mean topographic change was +1 m. Within flood-unaaffected areas the mean topographic change was +87 mm. In both areas, the distribution of height difference measurements of points was similar to the largest population just above the data mean. The distribution of points within inundated areas had a greater variance than areas not affected by the flood (Figure

4.38). The range of values within inundated areas of the DDEM could be attributed to more noise from signal decorrelation caused by flood waters after the 2015 Sag River flooding events.

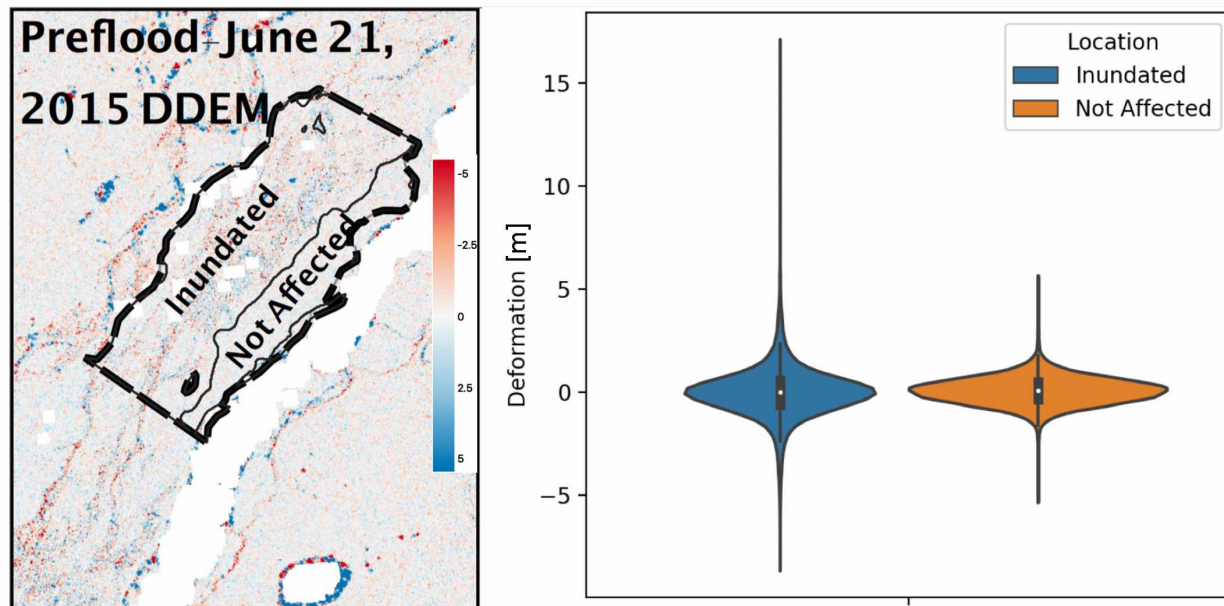


Figure 4.38: Distribution of a TDX DDEM of the pre-flood average DEM and the June 21, 2015 DEM. Associated deformation violin plot shown.

4.2.2 Analysis of the Dalton Highway Channel Analysis Area

Figure 4.39 shows the location of the Dalton Highway channel analysis area. The Dalton Highway area was selected because the flood had limited inundation within the alluvial terrace located in this area and presented an optimal area to analyze potential impacts of the flood on the TransAlaska Pipeline. The boundary of the focus area remained with the extent of Rawlinson's (1993) surficial geologic map and south boundary by geologic formations. The western and eastern extents were limited to the alluvial terrace deposit and a 427-meter buffer west of the Dalton Highway. Additional geologic formations including thaw-lake and ice-rich thaw lake deposits were not investigated due to limited water inundation within such deposits near and in the focus area (Figure 4.39). Pingos formed within thaw lake deposits were also omitted as the major deformation of their structure is likely unrelated to the 2015 Sag River flooding events.

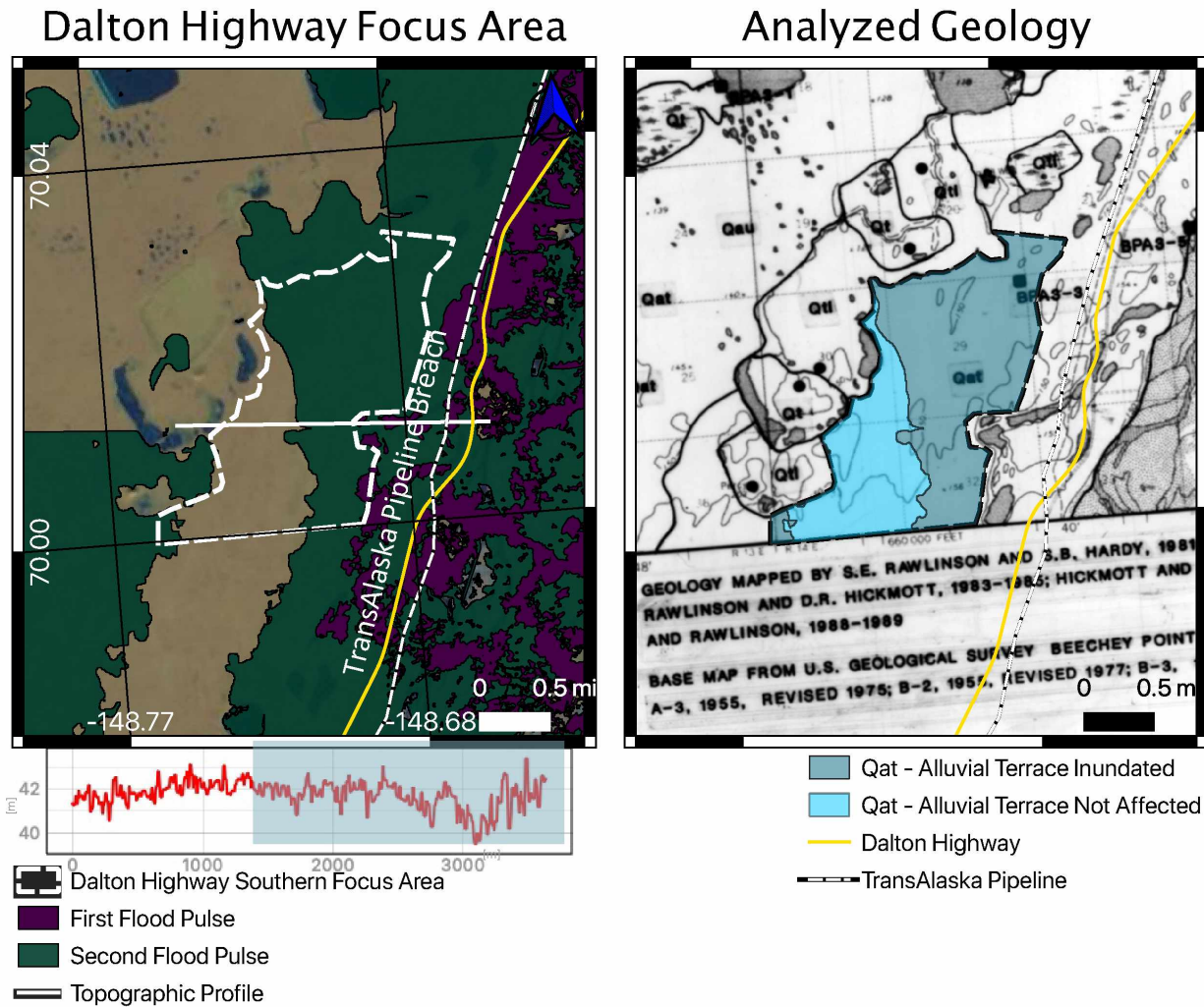


Figure 4.39: Location of the Dalton Highway focus area and analyzed geologic formation. Analyzed alluvial terrace deposit shown in blue. Topographic profile of TDX reference DEM shown across the flood plain. Inundated area shaded in light blue. Surficial geology from Rawlinson (1993).

The total area of the alluvial terrace focus area was 610 hectares. Flooding within the focus area is mostly confined to the western side of the terrace. The first flood pulse inundated a small area within the southeastern extent of the focus area. The flood waters from the second flood pulse inundated most of the focus area. The combined inundated area was 408 hectares, or 67% of the Dalton Highway alluvial terrace focus area (Figure 4.39). Note the linear processing artifact in the second flood pulse water mask (West of topographic profile solid white line, Figure 4.39). A slight rise in elevation to 42 m above sea-

level in the area between the inundated and flood-unaffected areas was noted (topographic profile, Figure 4.39). Generally, lower elevation areas west of the topographic rise had no estimated floodwaters up to the thaw lake deposits. However, the elevation difference varied greatly between the sampled locations within the focus area. Time series averages of the seasonal and annual deformation are shown in Figure 4.40.

Annual deformation sampled over a 4-year period showed slightly higher subsidence in flood inundated areas than flood-unaffected areas (Figure 4.40.A). The cumulative mean subsidence value of the ALOS-2 data set within inundated locations was -40 mm. Flood-unaffected areas showed a cumulative mean subsidence value of -36 mm. Across the time series, inundated locations expressed higher mean subsidence than flood-unaffected areas (Figure 4.40.A). The variability of estimated deformation values within inundated areas and flood-unaffected areas increased over the time series. All high deformation occurred on the eastern border of the focus areas closest to the Dalton Highway (Figure 4.40.A).

Deformation for the summer 2017 season showed an increased subsidence mean value in flood-unaffected areas compared to inundated areas over a five-month (May 1 to October 1) period. The final cumulative violin plot for summer 2017 shows mean deformation values of -10 mm in inundated areas and -14 mm within flood-unaffected areas (Figure 4.40.B). Across the entire time series, the mean value of flood-unaffected areas shows greater subsidence when compared to inundated mean value. The distribution of deformation measurements of inundated areas increases and progressively skews above the mean with time (Figure 4.40.B).

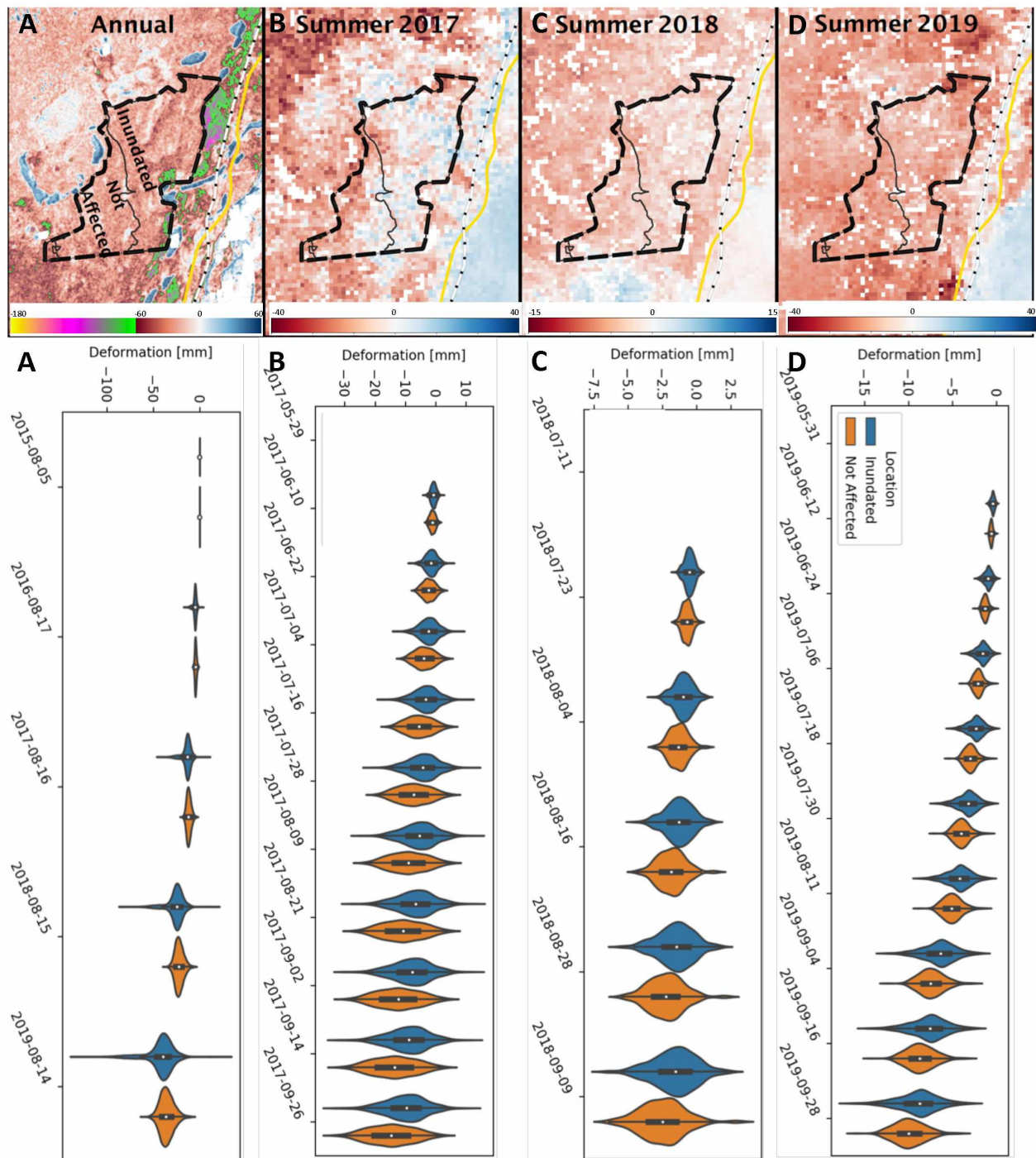


Figure 4.40: Averaged time series of deformation of alluvial terraces west of the Dalton Highway. Inundated (blue) and flood-unaaffected areas (orange) shown. Map of cumulative deformation within the sampled area is shown. Subsidence shown in red, uplift in blue.

Deformation for the summer 2018 season showed a higher subsidence mean value in flood-unaaffected areas in comparison to inundated areas over the three-month (July 1 to October 1) period

(Figure 4.40.C). The final cumulative violin plot for summer 2018 showed mean deformation values of -2 mm in inundated areas, and -3 mm within flood-unaaffected areas (Figure 4.40.C). Across the entire time series, the mean deformation of flood-unaaffected areas showed consistently higher values than the inundated area. The distribution of subsidence measurements in inundated and flood-unaaffected areas showed similarly increasing variance over time (Figure 4.40.C).

Deformation for the summer 2019 season showed more consistent subsidence when compared to the previous seasons with almost no relative uplift, although the average subsidence magnitude was higher in 2017 (Figure 4.40.D). Over the sampled five-month (May 1 to October 1) period, the cumulative mean subsidence value was -8 mm in inundated areas and -10 mm in flood-unaaffected areas. The time series consistently showed the mean value of flood-unaaffected areas was higher compared to the subsidence values of the inundated area (Figure 4.40.D).

Three DDEMs covering a time span of pre-flood to June 8, 2015, pre-flood to Dec 5, 2016, and post-flood Dec 5, 2016 to Feb 14, 2017, are shown in Figure 4.41. The DDEMs include: i) pre-flood time to just after the flood; ii) pre-flood time over one year; and iii) just after the flood to one year later. The three selected DDEMs were the only DDEMs from the TDX data with coverage in the focus area. Figure 4.41 shows no clear signal pattern or topographic trend within the DDEMs. Data from the pre-flood June 8, 2015 DDEM showed a slight positive topographic change within inundated zones and lower positive change in flood-unaaffected areas (Figure 4.41.A). The mean topographic change in inundated and flood-unaaffected areas was less than a meter, as TDX is unable to detect changes smaller than 1 meter. The pre-flood June 8, 2015 DDEM displayed no trend in topographic change and mostly resembled noise (Figure 4.41.B). Data from the June 8, 2016-February 14, 2017 DDEM were not utilized as they contained

horizontal shifts. The June 8, 2016-February 14, 2017 DDEM was displayed because it had coverage near the focus area.

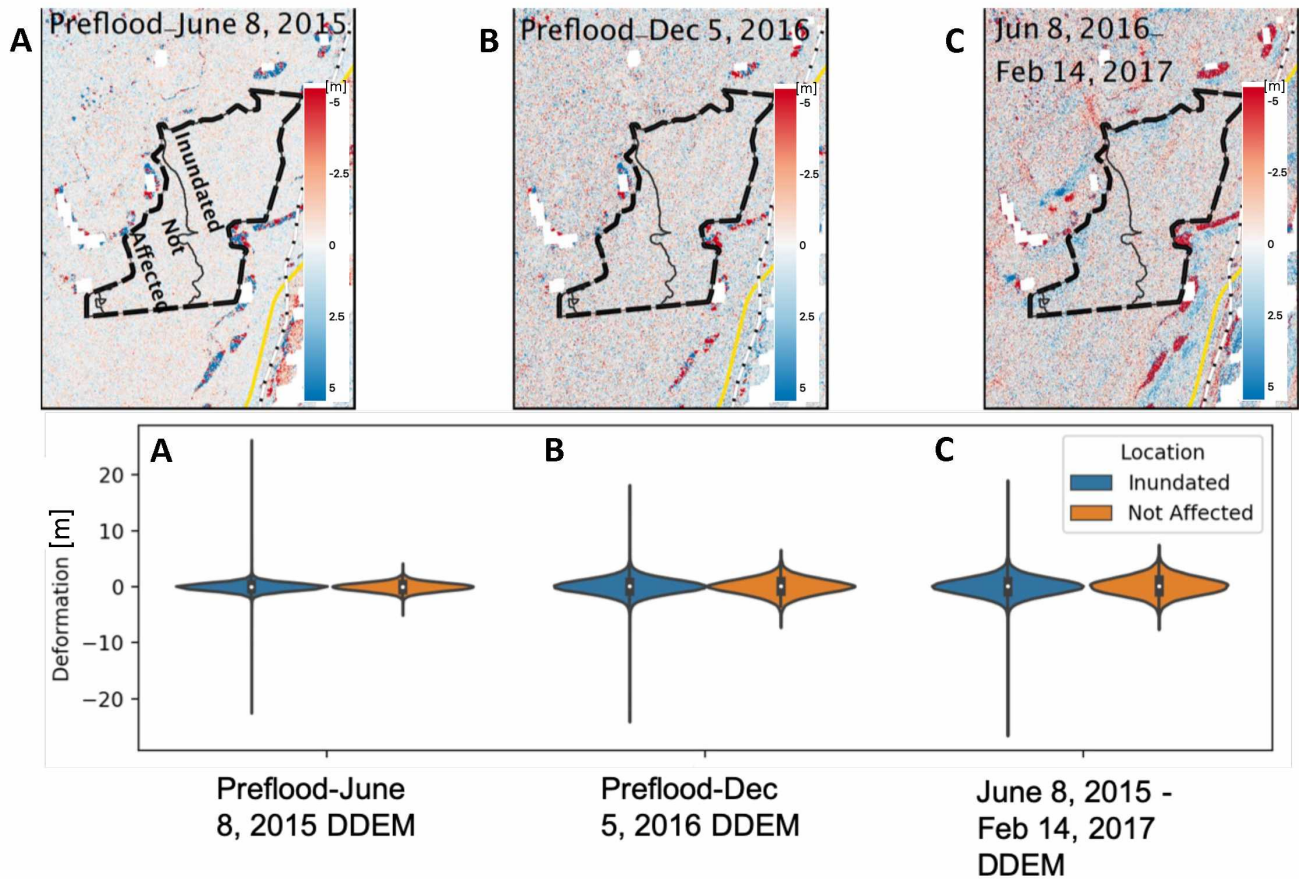


Figure 4.41: Data distribution and inset maps of three TDX DDEMs within the Dalton Highway focus area. Inset A shows the pre-flood-June 8, 2015 DDEM. Inset B shows the pre-flood-Dec 5, 2016 DDEM. Inset C shows the June 8, 2015-Feb 14, 2017 DDEM. Associated deformation violin plots shown below.

4.2.3 Analysis of the Sag River Eastern Terrace Focus Area

Figure 4.42 shows the location of the Sag River western terrace evaluation area. The Sag River western terrace focus area was selected because there was minimal inundation. The boundary of the focus area was limited to the north and south by the relative distance between the terrace eastern boundary and the Dalton Highway. The focus area was truncated in the areas where the distance between the terrace river margin and the highway was greatly reduced. The western extent was limited

to the Dalton Highway and eastern extent by the geologic contact between the analyzed terrace deposit and other surficial deposits (Figure 4.42). The western border of the analyzed area was not buffered because there was only minor inundation along the eastern edge of the Dalton Highway. The inundated area was mostly confined within the southern portion of the focus area. Shur (2015) noted complete thaw of ice wedges and photographed change in elevation alongside the Dalton Highway on the scale of meters. Analysis of the alluvial terrace presented an optimal area for evaluation of the associated permafrost deformations in areas influenced by the presence of the Dalton Highway and may show such large-scale topographic changes noted by Shur (2015).

Flooding within the focus area was mostly accomplished by the second flood pulse of the 2015 Sag River flooding events (Figure 4.42). The first flood pulse of the 2015 Sag River flooding events inundated a smaller area of the Sag River western terrace focus area (Figure 4.42). The total inundated area was 668 hectares, or 43% of the focus area. The focus area contained four small perennial lakes and a stream. These open water areas were masked. Flooding appeared to be contained within an area to the eastern side of the stream and to the Sag River. Flood water inundation appeared to be limited by the presence of the small stream. A time series of seasonal and annual deformation measurements are shown in Figure 4.43.

Annual deformation sampled over a four-year period showed similar magnitudes in inundated and non-inundated areas with indications for slightly lower subsidence in areas affected by the flood (Figure 4.43.A). The cumulative mean subsidence value of the ALOS-2 data set within inundated locations was -31 mm. Flood-unaffected areas showed a cumulative mean value of -39 mm of subsidence. The distribution within inundated areas increases over the time series. The highest deformation occurred within flood-unaffected areas just east of the Dalton Highway (Figure 4.43.A).

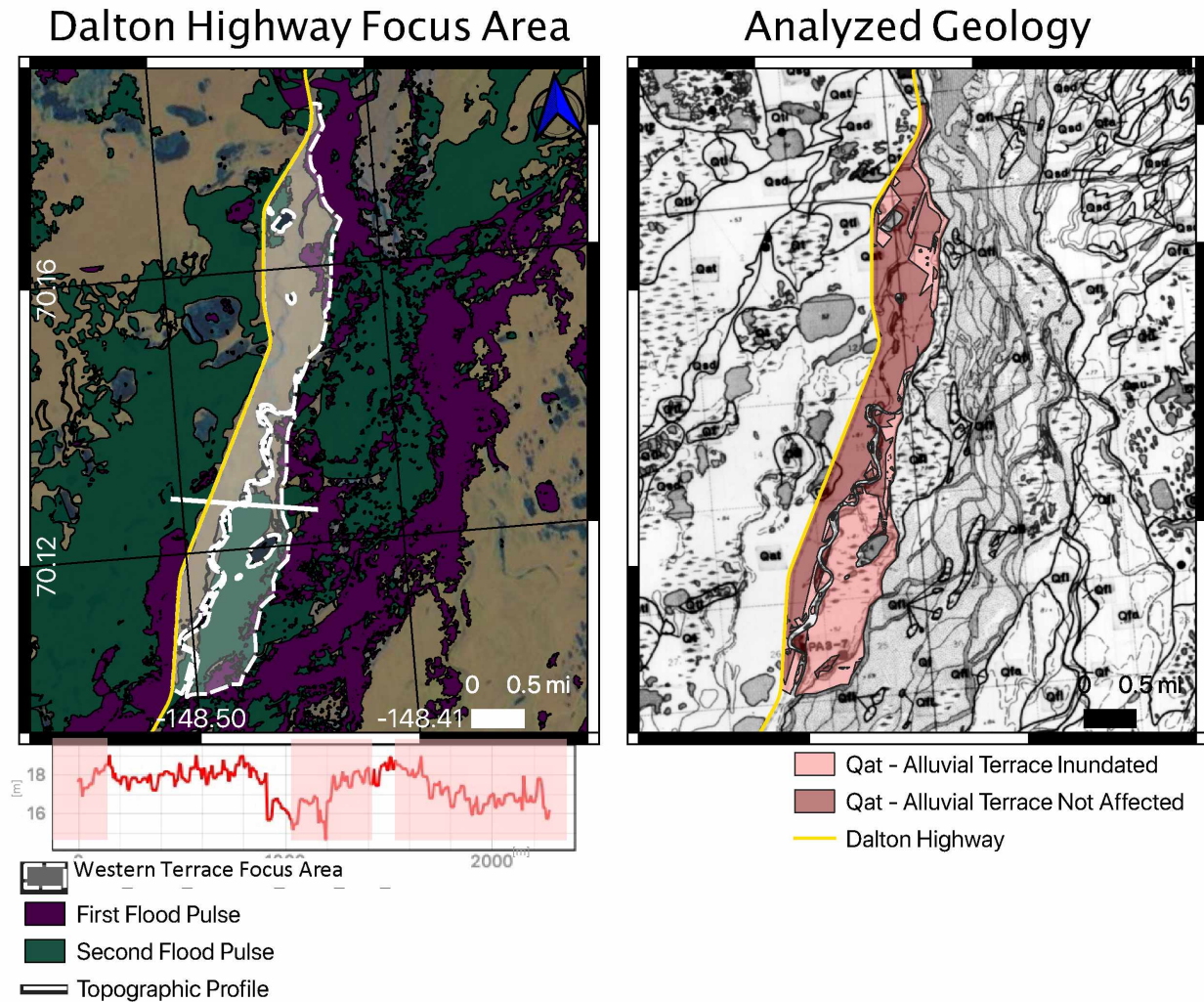


Figure 4.42: Location of the Sag River western terrace focus area and analyzed geologic formation. Analyzed alluvial terrace shown in red. Topographic profile of TDX reference DEM shown across the flood plain, inundated area shown in light red. Surficial Geology from Rawlinson (1993).

Deformation for the summer 2017 season showed increased subsidence mean values in flood-
unaffected areas in comparison to inundated areas over a five-month (May 1 to October 1) period
(Figure 4.43.B). The final cumulative violin plot for summer 2017 showed mean deformation values of -9
mm in inundated areas and -14 mm within flood-unaffected areas. Across the entire time series, the
mean value of flood-unaffected areas showed increased subsidence when compared to inundated area
mean values. The distribution of deformation measurements showed a positive bias in inundated areas

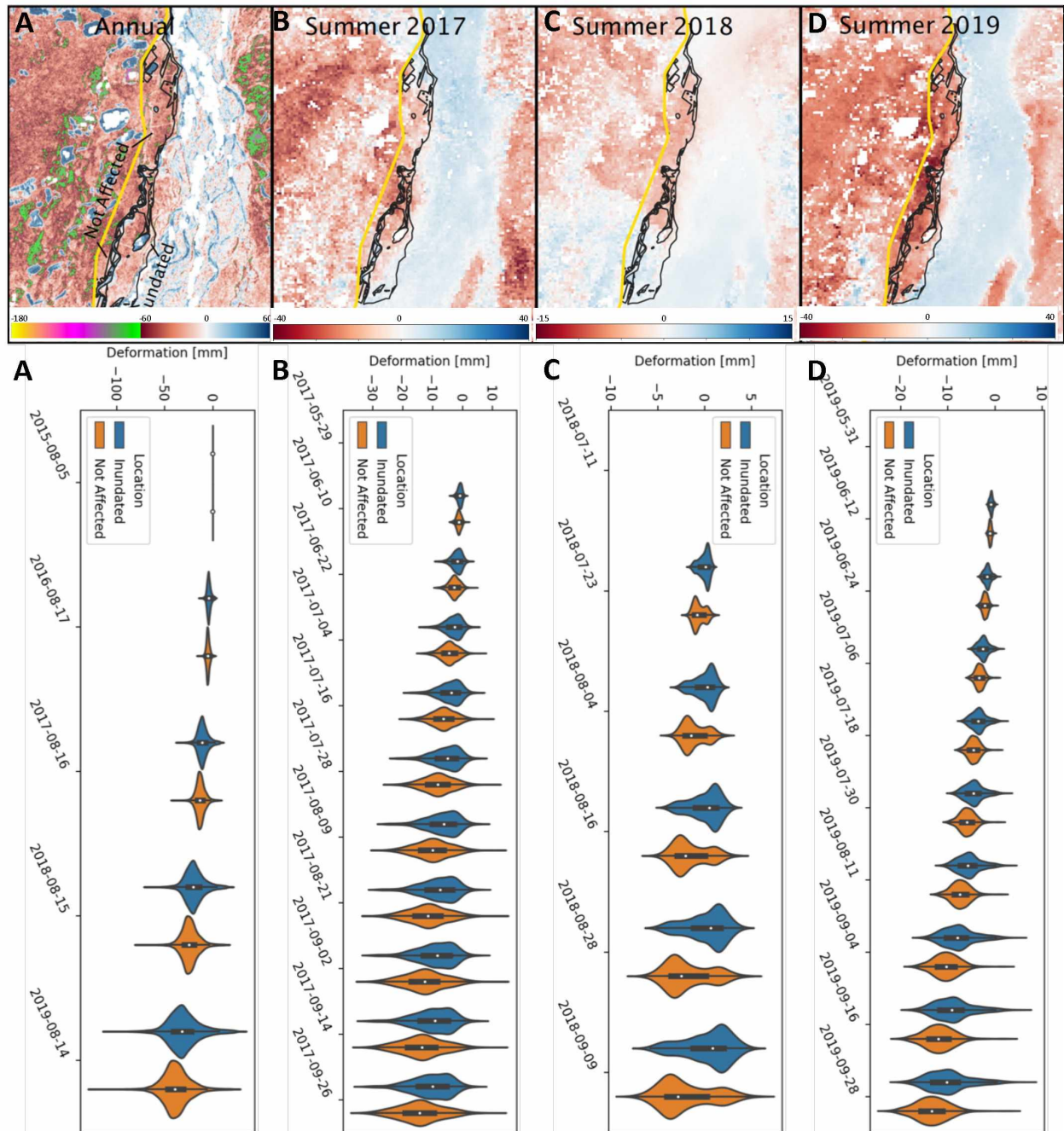


Figure 4.43: Averaged time series of deformation of the Sag River western terrace focus area. Inundated (blue) and flood-unaffected areas (orange) shown. Map of cumulative deformation within the focus area is shown.

and a negative bias in the flood-unaffected areas when compared to the mean shown in the 2017 violin plot (Figure 4.43.B).

Deformation for the summer 2018 season showed a deformation change of -3 mm in flood-affected areas, while inundated areas remained relatively flat and displayed minor uplift of +1 mm over the three-month (July 1 to October 1) sampling period (Figure 4.43). Across the entire 2018 time series, the mean value of flood-affected areas showed subsidence and was consistently less than the uplift recorded in inundated areas. The flood-affected area had a large data population below the mean value while inundated areas had a large population above the mean (Figure 4.43). Deformation for the summer 2018 season showed the majority of the inundated focus area to express relative uplift (Figure 4.43.C).

Deformation for the summer 2019 season showed more subsidence when compared to the previous summer seasons and little relative uplift. Over the sampled five-month (May 1 to October 1) period, the cumulative mean subsidence value was -10 mm in inundated areas and -13 mm in flood-affected areas. The time series consistently showed the deformation mean of flood-affected areas to be higher compared to the subsidence values of the inundated area. The violin plots showed two subsidence data populations within inundated areas. The larger population appeared higher than the mean deformation value. The flood-affected area shows two deformation data populations in the first three timesteps of the time series violin plots before becoming more evenly distributed (Figure 4.43).

Two DDEMs were sampled within this focus area: i) the pre-flood-May 21, 2015 DDEM and ii) the pre-flood-June 21, 2015 DDEM (Figure 4.44). Figure 4.44 shows the analyzed DDEMs and associated violin plots. The pre-flood-May 21, 2015 DDEM sampled the effects of the first flood pulse and showed a positive topographic change in inundated areas while flood-affected areas showed a slightly lower positive topographic change. However, these changes are of magnitudes less than a meter and beyond

the accuracy of TDX. A high degree of noise was present within channel regions of the Sag River. The second DDEM (pre-flood DEM - Jun 21, 2015 DEM) sampled the entire 2015 Sag River flood and the

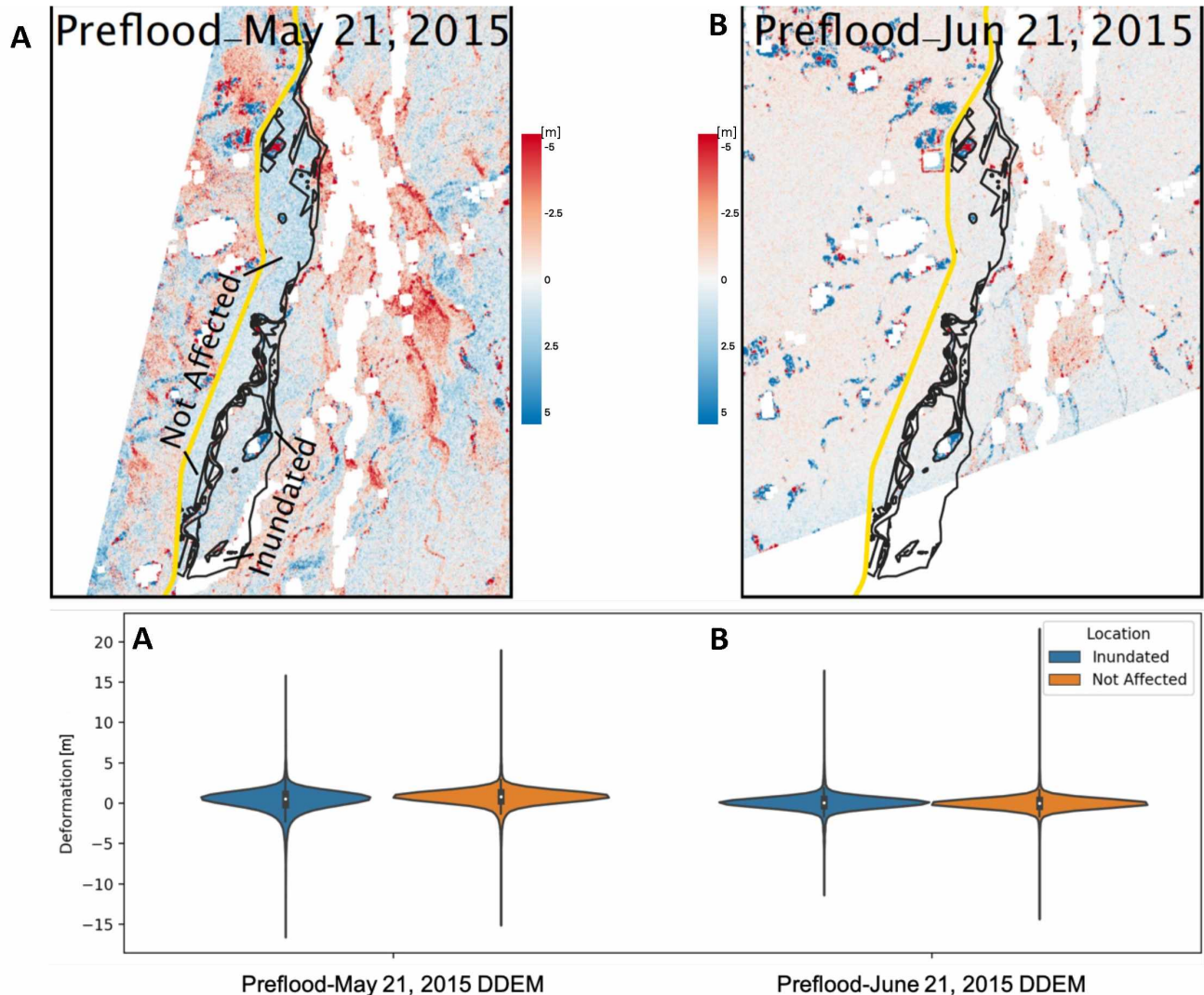


Figure 4.44: Distribution and insets of two TDX DDEMs sampled within the Sag River western terrace focus area. Inset A shows the pre-flood-May 21, 2015 DDEM. Inset B shows the pre-flood-Jun 21, 2016 DDEM. Associated deformation violin plot shown below.

events just after the flood waters receded. The DDEM showed no significant differences between inundated and non-inundated areas. Therefore, the available DDEM failed to irrefutably confirm the topographic changes reported by Shur (2015). While some indications of relative surface lowering may be present in the pre-flood-May 21, 2015 DDEM, no indications of surface lowering are evident in the

pre-flood-Jun 21, 2015 DDEM. No notable areas of topographic change were noted other than noise in both DDEMs. Longer term DDEMs were not used due to a high degree of noise and horizontal shifts in the data.

4.3 Interpretation of Data

Degradation, expressed as topographic change and spatial disturbances, intensified in areas inundated by the flooded compared to unaffected areas. The Sag River Delta, in terms of surficial geology, micro-elevation, drainage patterns, and existing permafrost degradation, expressed a high degree of heterogeneity in the AOI. The null hypothesis (H_0) of this thesis is as follows, H_0 : On average the deformation and topographic changes did not differ between inundated and flood-unaffected areas within the same geological unit. H_0 was tested in each focus area. The observations were noted in each study site are summarized in Table 4.1.

Table 4.1: Summary of observations recorded in each of the focus areas. Annual deformation sampled over a four-year period (2015-2019). The summer 2017 and 2019 seasons were sampled over a five-month (May 1 to October 1) period. The 2018 season was sampled over a three-month (July 1 to October 1) period.

<i>H_0 Test</i>	<i>Deformation and topographic change observed within inundated areas</i>				
Focus Areas	<i>Annual deformation</i>	<i>Summer 2017 deformation</i>	<i>Summer 2018 deformation</i>	<i>Summer 2019 deformation</i>	<i>DDEMs</i>
Abandoned Floodplain Eastern Channel Focus Area	Increased subsidence in river adjacent inundated area	Increased subsidence in inundated area	Decreased uplift in inundated area	Decreased subsidence in inundated area	Inconclusive
Dalton Highway Focus Area	Increased subsidence in inundated area	Decreased subsidence in inundated area	Decreased subsidence in inundated area	Decreased subsidence in inundated area	Inconclusive
Sag River Western Terrace Focus Area	Decreased subsidence in inundated area	Decreased subsidence in inundated area	Decreased subsidence in inundated areas close to zero	Decreased subsidence in inundated areas	Inconclusive

The focus areas were selected as small focus area of similar environments and area sizes to minimize the heterogeneity of the study site. Such focus areas were placed in the same geologic deposits and avoided open water and incised channels. Furthermore, each focus area was approximately equal in inundated and flood-unaaffected area. Due to a variety of ongoing processes in the Alaska North Slope permafrost, an existing background rate of deformation was expected throughout the focus areas. Flood affected areas are expected to increase deformation resulting from loss of ground ice, ice wedge degradation, thermokarstification, and other forms of permafrost degradation. There are several confounding factors that may exist within the focus areas that are inundated. Generally, in the undated areas including the Dalton Highway and TransAlaska Pipeline are at a lower elevation to the flood-unaaffected areas and usually wetter without influence of the 2015 Sag River flooding events. More ice could be contained in lower elevation areas due to wetness; however, inundated areas might contain less ground ice because aggradation of ground ice in flood-unaaffected areas might have elevated the regions in the first place. Small changes in the microtopography can cause areas to become a lot wetter triggering a range of environmental feedbacks.

Under the thesis question, flood-affected areas would be expected to display some form of increased deformation. It is assumed that there was no additional systematic difference in permafrost degradation prior or after the 2015 Sag River flooding events. Testing of H_0 was conducted on the three focus areas, summarized in Table 4.1. Annual deformation increased within two of the three inundated areas analyzed in the focus areas (Table 4.1). Inundated areas of the Dalton Highway focus area and the Sag River western terrace focus area showed decreased subsidence over all summer seasons. The abandoned floodplain eastern channel focus area showed a variable response showing both relative uplift and increased and decreased subsidence. Summer 2019 was the only summer season to show decreased subsidence in flood inundated areas. DDEMs showed no statistically notable result.

Flood inundated areas showed increased annual subsidence when compared to flood-
unaffected areas and suggested a decrease in seasonal deformation. Based on these findings, the 2015
Sag River flood could have influenced the permafrost degradation by increasing the annual deformation
and decreasing the seasonal deformation; however, these observations may be coincidental due to the
high variability of ground ice and geologic deposits the AOI. Therefore, H_0 is rejected on the basis that
there were differences in signals observed within inundated and flood-unaffected areas (Table 4.1).
Evidence suggests degradation and topographic change intensified in permafrost areas that were
inundated by the 2015 Sag River flood. The degree to which the permafrost has been affected by the
flooding remains for further study.

Chapter 5 Conclusions

The thesis sought to answer the question, “What was the response of the Sag River Delta region after the 2015 flooding in terms of deformation and topographic change?” This question was addressed by identifying the associated deformation and topographic change in three focus areas. The focus areas were selected in similar geologic formations to limit the variability within the focus area. Slight elevation differences and ice volumes exist within the focus areas. It is assumed that there was no additional systematic difference in permafrost degradation prior to or after the 2015 Sag River flooding events. H_0 was created to test the response of deformation within the focus areas. H_0 : On average the deformation and topographic changes did not differ between inundated and flood-unaaffected areas within the same geological unit. H_0 was rejected on the basis that there was enough difference in signals observed within inundated and flood-unaaffected areas to indicate an influence of the flood. There are a number of confounding factors that may exist within the focus areas that may alter the interpretation. Generally inundated areas are at lower elevations than flood-unaaffected areas. Lower elevations areas are usually wetter. Moist areas could contain more ice, but inundated areas might contain less ground ice because of aggradation. The observations indicate that the flood had an effect of intensifying degradation of the permafrost within the expanse of the 2015 Sag River Flood.

In this thesis, a series of analyses were conducted to determine the area of flood water inundation, the seasonal and annual deformation in flood-affected and flood-unaaffected regions, and topographic changes observed in flood-affected and flood-unaaffected regions. Chapter 1 provided an overview of the 2015 Sag River flooding events as recorded by ADOT&PF. Chapter 2 introduced the location AOI and provided the relevant background information related to the physical aspects of the AOI. Chapter 3 introduced the topics of SAR and InSAR analyses and an overview of the methods

utilized. Exposed surface water during the timing of the Sag River flood was identified using the Ajadi et al. (2019) unsupervised change detections method. The deformation analysis was conducted utilizing SBAS InSAR. Topographic changes at various time scales were produced using coregistered high-pass filtered TDX DEMs. The major contributions of this thesis were provided in Chapter 4, where the results and implications were discussed as they relate to the effect flooding had on the ground. The following sections describe the relevant conclusions and limitations of the analyzed data sets.

5.1 Change Detection Conclusions and Limitations

The cumulative flood waters covered an area of 69,033 hectares, approximately 30% of the AOI. Aufeis developed in isolated sections in the river channels. The water from the first flood pulse was determined to have developed around the isolated aufeis areas in the Sag River channels. As the first flood pulse progressed, water seeped to the surface and froze around aufeis. A majority of the floodwaters progressed down the river ahead of the aufeis introducing flood water into the area adjacent to the Sag River. This flood breached the Dalton Highway submerging it. The water flowed into the tundra and became confined to the lower elevation area west of the Dalton Highway. Unable to return to the Sag River drainage area, it progressed along the west side of the Dalton Highway to the north. The flood waters briefly receded after this time. The second flood pulse was caused by the early arrival of spring runoff in an aufeis-filled river. The water quickly overtopped the Dalton Highway and extended into the tundra. The Dalton Highway and TransAlaska Pipeline acted as dams, allowing further displacement of floodwaters into the tundra.

Limitations were encountered in the change detection analysis. False positives were produced that required manual editing for corrections. The false positives stemmed from an unequal distribution of new aufeis, new water, or no change identified areas. Although a manual method of correction was

applied, a more detailed preprocessing and normalization technique or utilizing more Bayesian classes in the preprocessing algorithm could have provided a more accurate result of new aufeis or new water areas.

5.2 SBAS InSAR Deformation Conclusions and Limitations

Section 4.1.2 and 4.1.3 presented the results of seasonal and annual deformation within the AOI. The Sag River flood appeared to have two unique effects related to permafrost deformation in the AOI. Annual deformation in inundated areas appeared to be higher than in flood-unaaffected areas. Seasonal subsidence showed a mix of signals within the inundated areas. However, two of three analyzed focus areas displayed lower subsidence when compared to flood-unaaffected areas. However, given the seasonal variability contained within the data, the observation may be coincidental due to confounding factors.

Deformation maps produced from Sentinel-1 SAR data have many limitations. The coarse resolution of S1 InSAR provides an 80 m x 80m pixel area that fails to capture the fine detail of the changes to the microtopography that permafrost deformation produces. Degradations to the permafrost can happen at an individual ice wedge polygon. The coarse level of resolution may produce an improper interpretation over a single pixel area. These analyses should be reexamined if higher resolution data become available at a future date. Deformation for the summer 2018 season was limited in the early timeframe of the summer by having very few interferograms with coherency. The deformation pattern for summer 2018 was likely under-sampled and deformation values underrepresented the actual deformation.

The goal in processing the annual deformation was to analyze the deformation occurring at the approximate same time of year, each year, mid-August. For two of the five years, an image in mid-August could not be acquired. To correct for the timeframe sampling inconsistency, the displacement from two images acquired from the beginning and the end of August was utilized to approximate these data. The deformation produced from the early and late August SAR scenes are averaged. The seasonal deformation was shown to have the greatest rate of seasonal permafrost subsidence in late August (Figures 4.11, 4.21). Including averaged data from late August may produce an average value greater than the actual deformation. When SAR data were processed through the temporal, spatial, and coherence filters, an increased amount of deformation may be produced. This could have been mitigated if the data set contained the same number of images per year.

5.3 DEM Differencing Conclusions and Limitations

DEM differencing did not produce a definitive result within the focus areas. A significant limitation of TDX DEM differencing was all DDEM contained notable errors that were unable to be corrected within the time frame of this thesis. Ramps and vertical shifts were present in most DEMs (and therefore DDEMs) despite coregistration and Gaussian high-pass filtering efforts. Additional error was produced from horizontal shifts in the data between ascending and descending satellite acquisitions and in all data acquired after 2016. A high degree of background noise was present in the DDEMs. Often the noise would overshadow any possible signal within focus areas. Focus areas had a similar data values to the background noise. Such noise could have been filtered out or removed with a more detailed water mask tailored to the location and timeframe of floodwater between the DDEMs. This could have been accomplished with TDX coherence data and the Sag River flood pulse maps. Restraining noise prorogation into the DDEMs is limited by the natural measurement accuracy of DEMs. DEMs have an accuracy determined by the height of ambiguity that is usually in the meter range. Topographic change

to the permafrost from the 2015 Sag River Flooding event may be in the sub-meter range and the associated changes in height would be unable to be resolved.

5.4 Data Comparisons

A null hypothesis stating no change occurred from the flood was disproved on the basis that there was sufficient evidence to suggest that the flood modified deformation in the permafrost areas. It appears that the most notable effect the flooding produced was a high degree of annual deformation in the years following the flood in partially affected areas. Seasonal signals produced a variable response. A notable limitation is the limited number of focus areas analyzed and interpreted.

To the author's knowledge, the implications from flooding from a single flooding event have not been studied in such detail along the Alaska North Slope. Applications could be investigated in addition to the results of this thesis.

5.5 Suggestions for Further Study

This thesis investigated the effect of flooding on the microtopography and the associated terrain stability of permafrost in the vicinity of the Sag River Delta. There are plenty of potential applications and additional results of this study. Future work should involve continued investigation into i) the inundated surficial geology, ii) analysis of aufeis progression during the 2015 Sag River Flooding events, iii) field investigation of the focus areas to provide direct observation, iv) parallel analysis to other rivers on the Alaska North Slope, v) reanalysis and processing of TDX DDEMs and InSAR products with additional data, and vi) continuous monitoring of the AOI to include more recent data into the analysis. Recommendations for further studies are as follows:

Continued investigation into the surficial geology to involve more analyzed focus areas and unity of the observations recorded across the AOI. This would allow for better interpretation of the effect of the 2015 Sag River flooding events and impacted areas. To that end, a current project at the DDGS is the remapping, vectorizing, and modernization of the superficial geology at Prudhoe Bay. Once this updated map is released, the surficial geology will have been accurately remapped and spatially represented. With an updated digital version of the surficial geology map, the deformation and topographic change of each geologic formation of interest within inundated and flood-unaffected areas, could be analyzed across the entire AOI. The volume changes and deformation observed within the AOI could be constrained to specific surficial lithologies and with more processing parameters.

Change detection could benefit from a detailed analysis of the progression of 2015 Sag River flooding between each image acquisition. During the first flood pulse, ADOT&PF noted a significant buildup of aufeis along the Dalton Highway. The dielectric properties of aufeis and water allows for identification with Ajayi's (2019) change detection analysis. It could be beneficial to measure aufeis extent during the flood to categorize additional impacts and effects to the Sag River permafrost. Identification of this progression could be utilized to identify ice jamming in addition to the flood waters.

Field investigation of this analysis in the focus area would take the thesis interpretations to direct observation. Having ground data of potential impacts to the permafrost is vital for understanding the changes in the permafrost and validating the methods utilized in this study. Priority should be given to areas that are less likely to have been impacted by human structures or activities. A potential first site to be analyzed is the eastern channel abandoned alluvial plain focus area. Additionally, other river adjacent communities in the Alaska Northern Slope and in the Yukon Delta are threatened by seasonal flooding. A potential parallel study could be conducted to investigate the permafrost stability after large

flooding events and provide additional information to mitigate and respond to flooding and permafrost degradation.

This research could benefit from understanding the immediate topographic change after the flooding events through DDEM reprocessing. Horizontal and vertical shifts and data ramps were present in the DDEMs after correction. DEM coregistration should be conducted again to prioritize correcting horizontal shifts in coregistered DEMs. Additionally, a detailed frequency analysis could be conducted to selectively remove specific signals and data ramps present in the data instead of using a Gaussian high-pass filter.

It is feasible to automate and expand the observations presented in the thesis to include additional SAR scenes from the various data sets. For annual and seasonal deformation analysis, additional summers and years should be added to the SBAS InSAR data sets. Additional deformation data may help provide a diagnostic response of permafrost deformation in flooded areas. Additionally, active monitoring of flood prone rivers may also prove useful in moderating degradation and reducing future threat to already flood affected permafrost regions. Analysis with upcoming missions such as TanDEM-L or NISAR will prove useful in the long-term monitoring of permafrost degradation in response to flooding on the Alaska North Slope

This page was intentionally left blank.

References

- Abolt, C.J., Young, M., Sharp, J., Johnson, J., 2015, Simulation of ice wedge polygon geomorphic transition, Prudhoe Bay, Alaska [M.Sc. Thesis]: The University of Texas at Austin, 106 p.
- Agram, P.R., Simons, J.R., Riel, B., 2012, GIANt-generic InSAR analysis toolbox: presented at 2012 AGU Fall meeting. p. 0897.
- Ajadi, O.A., Meyer, F.J., Liljedhl, A., 2017, Detection of aufeis-related flood Areas in a Timeseries of High-Resolution Synthetic Aperture Radar Images using Curvelet Transform and Unsupervised Classification [Ph.D. thesis]: Fairbanks, University of Alaska (in press).
- Alaska Department of Natural Resources, 2014, RE: MLUPNS 14-007, Geophysical Exploration Permit, Kad River 3D Seismic Survey Permit Approval: <http://dog.dnr.alaska.gov/Documents/-Permitting/NorthSlope/MLUP/2014/MLUPNS14007GlobalKadRiver3DApproval.pdf> (Accessed Nov 2019).
- Alaska Department of Transportation and Public Facilities (ADOT&PF), 2015, Dalton Highway Updates, 2015 Flooding Response: <http://www.dot.alaska.gov/nreg/dalton-updates/2015response.shtml> (Accessed Nov 2019).
- Alaska Division of Homeland Security & Emergency Management, 2018, Ch06-NaturalHazards, State Hazard Mitigation Plan (SHMP): <https://ready.alaska.gov/Plans/Mitigation/Documents/-Alaska%20State%20Mitigation%20Plan/Ch06-NaturalHazards.pdf> (Accessed June, 2020).
- Alaska Division of Geology and Geophysical Surveys (DGGS), 2019, Surficial Geology of the Beachy Point Quadrangle: (Personal Communication, 2019).
- Alaska Satellite Facility (ASF), 2019, Monitoring Deformation: <https://www.asf.alaska.edu/science-topics/volcanoes/> (accessed September 2019).
- Berardino, P., Fornaro, G., Lanari, R., Sansosti, E., 2002, A new algorithm for surface deformation monitoring based on small baseline differential SAR interferograms: IEEE Transactions on Geoscience and Remote Sensing, vol. 40, no. 11, p. 2375-2383.
- Bolin, R., 1959., Report on the Scientific Results of the "Michael Sars": North Atlantic Deep-Sea Expedition 1910, 4(2)7:1-45, doi: 10.5962/bhl.title.11322.
- Coffey, M.J., 2018, Dalton Highway Flood Response Disaster in the Arctic: presented at 2018 American Public Works Association fall conference, Seattle, Washington, 29th September.
- Couture, N.J., Irrgang, I., Pollard, W., Lantuit, H., Fritz, M., 2018, Coastal Erosion of Permafrost Soils Along the Yukon Coastal Plain and Fluxes of Organic Carbon to the Canadian Beaufort Sea: JGR: Biogeosciences, vol. 123, no. 2, p. 406-422, doi: 10.1002/2017JG004166.
- Curlander J.C., McDonough R.N., 1991, Synthetic Aperture Radar: Systems and Signal Processing. Wiley; New York.

- Ding, X.L., Li, Z.W., Zhu, J.J., Feng, G.C., Long, J.P., 2008, Atmospheric effects on InSAR measurements and their mitigation. *Sensors*, vol. 8, p. 5426–5449.
- Feirer, S.T., 2004, Ecological Framework: The Lands That and Waters That Produce Our Fish and Wildlife, Vol. B.: http://www.adfg.alaska.gov/static/species/wildlife_action_plan/section3b.pdf, (accessed December 2019).
- French, H., and Shur, Y., 2010, The principles of cryostratigraphy: *Earth-Science Reviews*, Vol. 101, no. 3-4, p. 190-206, doi: 10.1016/j.earscirev.2010.04.002.
- Engineering and Technology History, 2019, Synthetic Aperture Radar: https://ethw.org/Synthetic_Aperture_Radar (Accessed September 2019).
- European Space Agency, 2007, InSAR Principles: Guidelines for SAR Interferometry Processing and Interpretation: ESA Publications, 252 p.
- Federal Priority Streamgage Program, 2019, U.S Geological Survey Federal Priority Steam Gage Program: https://waterdata.usgs.gov/ak/nwis/uv?site_no=15908000, (accessed December 2019).
- Gabriel, A.K., Goldstein, R.M., Zebker, H.A., 1989, Mapping Small Elevation Changes Over Large Areas' Differential Radar Interferometry, *Journal of Geophysical Research*, Vol. 90, no. B7, p. 9183-9191, doi: 10.1029/JB094iB07-p09183.
- Gallant, A.L., Binnian, E.F., Omernik, J.M., and Shasby, M.B., 1995, Ecoregions of Alaska: U.S. Geological Survey Professional Paper 1567, 78 p.
- Global Forest Observation Initiative, 2018, A Layman's Interpretation Guide to L-band and C-band Synthetic Aperture Radar data, vol. 2: https://www.geosociety.org/documents/gsa/pubs/-GSA_RefGuide_Examples.pdf (accessed April 2020).
- Goldstein, R.M., Zebker H.A., Werner, C.L., 1988, Satellite radar interferometry: Two-dimensional phase unwrapping, *Radio Science* Vol. 23, no. 4, p. 713-720, doi: 10.1029/RS023i004p00713.
- Graham, L.C., 1974, Synthetic Interferometric Radar for Topographic Mapping: *Proceedings of the IEEE*, vol. 62, p. 763-768.
- Hodel, K.L., 1986, The Sagavanirktok River, North Slope Alaska: Characterization of an Arctic Stream, U.S. Geological Survey Open File Report 86-26, 28 p.
- Hogenson, K., Arko, S.A., Buechler, B., Hogenson, R., Herrmann, J. and Geiger, A., 2016. Hybrid Pluggable Processing Pipeline (HyP3): A cloud-based infrastructure for generic processing of SAR data. Abstract [IN21B-1740] presented at 2016 AGU Fall Meeting, San Francisco, CA, 12-16 December.
- Houseknecht, D.W., and Bird, K.J., 2005, Oil and gas resources of the Arctic Alaska petroleum province: U.S. Geological Survey Professional Paper 1732-A, 11 p., online at: <http://pubs.usgs.gov/pp/pp1732a/>.

- Jorgenson, M.T., Yoshikawa, K., Kanevskiy, M., Shur Y., Romanovsky, V., Marchenko, S., Grosse, G., Brown J., and Jones, B., 2008, Permafrost Characteristics of Alaska: Institute of Northern Engineering, University of Alaska, Fairbanks December update to July NICOP, scale 1: 7,200,000.
- Jorgenson, M.T., 2011, Coastal Region of Northern Alaska *in* Guidebook to Permafrost and Related Features, Guidebook 10, State of Alaska Department of Natural Resources Division of Geological & Geophysical Surveys, 209 p.
- Jorgenson, M.T., 2015, Role of ground ice dynamics and ecological feedbacks in recent ice wedge degradation and stabilization: JGR Earth Surface, Vol. 120, no. 11, doi: 10.1002/2015JF003602.
- Kane, D.L., 1981, Physical properties of aufeis growth [M.Sc. thesis]: Fairbanks, University of Alaska, 10 p.
- Kane, D. L., 2014, Hydrology and meteorology of the central Alaskan Arctic: Data collection and analysis, Final Report, Rep. No. INE/WERC 14.05, Univ. of Alaska Fairbanks, Fairbanks, AK, 274 p.
- Kanevskiy, M., Shur, Y., Jorgensonb, M.T., Stephani, E., 2011, Cryostratigraphy of late Pleistocene syngenetic permafrost (yedoma) in northern Alaska, Itkillik River exposure: Quaternary Research, Vol. 75, no. 3, p. 584-596.
- Kanevskiy, M., Shur, Y., Jorgensonb, M.T., Ping, C.-L., Michaelson, D.J., Fortierda, D., Stephania, E., Dillona, M., Tumskiye V., 2013, Ground ice in the upper permafrost of the Beaufort Sea coast of Alaska: Cold Regions Science and Technology, vol. 85, p 56-70, doi: 10.1016/j.coldregions.2012.08.002.
- Kanevskiy, M.A, Shur, Y.A., Jorgenson, T., Brown, R.N.D., Moskalenko, N., Brown, J., Walker, D.A., Raynolds, M.K., Buchhorn, M., 2017, Degradation and stabilization of ice wedges: Implications for assessing risk of thermokarst in northern Alaska: Journal of Geomorphology, Vol. 297, 41 p., doi: 10.1016/j.geomorph.2017.09.001.
- Keller, S.A., Morris, R.H., Detterman, R.L., 1961, Exploration of Naval Petroleum Reserve No. 4 And Adjacent Areas, Northern Alaska, 1944-53. U.S Geological Survey Professional Paper 303-D, 60 p.
- Kramer, H.J., 2002, Observation of the Earth and Its Environment: Survey of Missions and Sensors: Earth Sharing Observatory Resources <https://directory.eoportal.org/web/eoportal/satellite-missions/> (Accessed December 2019).
- Lachenbruch, A.H., 1962, Mechanics of thermal contraction cracks and ice-wedge polygons in permafrost. Geological Society of America Special Papers, 70, p 1-66.
- Leffingwell, E.K., 1915, Ground-ice wedges, the dominant form of ground-ice on the north coast of Alaska: Journal of Geology, vol. 23, p. 635-654.
- Leffingwell, E.K., 1919, The Canning River region, northern Alaska: U.S. Geological Survey Professional Paper 109, 251 p.
- Liljedahl, A.K, Hinzman, L.D., Schulla, J., 2012, Ice wedge polygon type controls low gradient watershed-scale hydrology: Tenth International Conference on Permafrost, vol. 1, p. 231-336.

- Liu, L., Zhang, T., and Wahr J., 2010, InSAR measurements of surface deformation over permafrost on the North slope of Alaska: *Journal of Geophysics*, vol. 115, F03023, 14 p.
- Mackay, J.R., 1983, The direction of ice wedge cracking in permafrost: downward or upward?: *Canadian Journal of Earth Science*, vol. 21, p 516-524, doi: 10.1139/e84-056.
- Mackay; 1990 Some Observations on the Growth and Deformation of Epigenetic, Syngenetic and Anti-Syngenetic Ice Wedges
- Martin, J.M., Thomas, M.A., Bull, D.L., Jones, C., 2016, The Arctic coastal erosion problem: Sandia Special Report SAND2016-9762, 122 p.
- Massonnet, D., Rossi, M., Carmona, C., Dragan, F., Peltzer, G., Feigl, K., and Rabaute, T., 1993, The displacement field of the Landers earthquake mapped by radar interferometry: *Nature*, vol 364, p. 138–142.
- McAlpin, D.B., Meyer, F.J., Gong, W., Bedet, J.E., Webley, P.W., 2017, Pyroclastic Flow Deposits and InSAR: Analysis of Long-Term Subsidence at Augustine Volcano, Alaska: *Remote Sensing*, vol. 9, no. 1, 23 p.,doi: /10.3390/rs9010004.
- McCandless, S.W., and Jackson, C.R., 2004, Principles of Synthetic Aperture Radar *in* Jackson, C.R. and Apal, J.R., eds, *Synthetic Aperture Radar Marine User's Manual: National Oceanic and Atmospheric Administration/ National Environmental Satellite, Data, and Information Service Professional Paper*, Silver Spring, MD, USA, p. 1-24.
- Meyer, F.J., 2019, Spaceborne Synthetic Aperture Radar: Principles, Data Access, and Basic Processing Techniques *in* Flores-Anderson, A.L., Herndon, K.E., Thapa, R.B., Cherrington, E., eds., *THE SAR HANDBOOK Comprehensive Methodologies for Forest Monitoring and Biomass Estimation (First edition)*; Huntsville, AL, SERVIR, 24 p., doi: 10.25966/nr2c-s697.
- Meyer, F.J., Ajadi, O.A., Schultz, L., Bell, J., Arnoult, K.M., Gens, R., and Nicoll, J.B, 2018, An Automatic Flood Monitoring Service from Sentinel-1 SAR: Products, Delivery Pipelines, and Performance Assessment: IGARSS 2018-2018 IEEE International Geoscience and Remote Sensing Symposium, p. 6576-6579.
- Milner M.A., Oswood, M.W., and Munkittrick, K.W., 2005, Rivers of Arctic North America, in Arthur C. B. and Colbert E. C. eds., *Rivers of North America: Academic Press*, p. 903-934.
- Moreira, A., Prats-Iraola, P., Younis, M., Krieger, G., Hajnsek, I., Konstantinos, P.P., 2013, A Tutorial on Synthetic Aperture Radar: *ieee Geoscience and remote sensing magazine*, doi: 2168-6831/13/\$31.00©2013IEEE, 38 p.
- Mull C.G., Houseknecht, D.W., Bird, K.J., 2003, Revised Cretaceous and Tertiary Stratigraphic Nomenclature in the Colville Basin, Northern Alaska: *U.S. Geological Survey Professional Paper* 1673, 59 p.

- National Oceanic and Atmospheric Administration (NOAA), 2020, Tides and Current Program Station: <https://tidesandcurrents.noaa.gov/stationhome.html?id=9497645&units=metric> (accessed March 2020).
- Natural Resources Canada, 2015; nrcan.gc.ca/maps-tools-publications/satellite-imagery-air-photos/remote-sensing-tutorials/microwave-remote-sensing/radar-image-distortions/9325.
- Nelson, F.E., Shiklomanov, N.I., Mueller, K.M., Hinkel, D.A., Walker, J.G., 1997, Estimating Active-Layer Thickness over a Large Region: Kuparuk River Basin, Alaska, U.S.A, *Arctic and Alpine Research*, Vol. 29, No. 4, p. 367-378.
- Nisbet, R., Miner G., and Yale, K., 2018, Model Evaluation and Enhancement *in* Elder, J., and Peterson, A., eds., *Handbook of Statistical Analysis and Data Mining Applications* (Second Edition), p. 215-233, doi: 10.1016/B978-0-12-416632-5.00011-6.
- Nonaka, T., Asaka, T., Iwashita, K., 2018, Evaluation of Atmospheric Effects on Interferograms Using DEM Errors of Fixed Ground Points: *Sensors — Open Access Journal*, vol 18, 12 p., doi: 10.3390/s18072336.
- Nuth, C., and Kääb, A. 2011, Co-registration and bias corrections of satellite elevation data sets for quantifying glacier thickness change: *Cryosphere*, vol. 5(1), p. 271–290 doi:10.5194/tc-5-271-2011.
- O’Neill, H.B., and Christiansen, H.H., 2018, Detection of Ice Wedge Cracking in Permafrost Using Miniature Accelerometers: *Journal of Geophysical Research: Earth Surface*, vol. 123, p. 642–657, doi: 10.1002/2017JF004343.
- Pelletier, M., Allard, M., Levesque, E., 2018, Ecosystem changes across a gradient of permafrost degradation in subarctic Québec (Tasiapik Valley, Nunavik, Canada): *Arctic Science, Arctic permafrost systems Special Issue*, Vol 5., 27 p.
- Permafrost Subcommittee, 1988, Glossary of permafrost and related ground ice terms. Technical Memorandum, No. 142, National Research Council of Canada, p. 156.
- Press, W.H., and Teukolsky, S.A., 1990, Savitzky-Golay Smoothing Filters: *Computers in Physics* 4, Vol. 669, 5 p., doi: 10.1063/1.4822961.
- Pullman, E.R., Jorgenson, M.T., Shur, Y., 2.16, Thaw Settlement in Soils of the Arctic Coastal Plain: *Arctic Antarctic and Alpine Research*, vol. 39, no. 3, p.468-476, doi: 10.1657/1523-0430(05-045)[PULLMAN]2.0.CO;2.
- Rawlinson, S.E., 1983, Guidebook to Permafrost and Related Features, Prudhoe Bay, Alaska: Alaska Division of Geological and Geophysical Surveys Guidebook 5, 221 p.
- Rawlinson, S.E., 1993, Surficial Geology and Morphology of The Alaskan Central Arctic Coastal Plain: Division of Geology and Geophysical Surveys Report of Investigations 93-1, 172 p.

- Rodriguez, E., Morris, C.S., Belz, J.E., Chapin, E.C., Martin, J.M., Daffer, W., Hensley, S., 2005, An assessment of the SRTM topographic products, Technical Report JPL D-31639, Jet Propulsion Laboratory, Pasadena, California, 143 p.
- Schenk, C.J., 2011, Chapter 41 Geology and petroleum potential of the West Greenland–East Canada Province *in* Spencer, A.M., Embry, A.F., Gautier, D.L., Stoupakova, A.V., Sørensen, K. eds., Geological Society, London, Memoirs, Vol. 35, p. 627-645, doi: 10.1144/M35.41
- Shur, Y.L., 1988, The upper horizon of permafrost soil: Proceedings of 5th Permafrost International Conference, presented at 1988 Permafrost International Conference Trondheim, Norway, p.867-871.
- Shur, Y., Kaneckit, M., Walker, D.A., Jorgenson, T., Buchhorn, M., Reynolds, M., Toniolo, H., 2015, Permafrost-Related Causes and Consequences of the Sagavanirktok River Delta Flooding in Spring 2015: https://www.geobotany.uaf.edu/library/talks/Shur2016-_ICOP_flooding_tal20160615.pdf (Accessed Nov 2019).
- Takashi, N., Tomohito, A., Iwashita, K., Ogushi F., 2019, The Relationships between Errors of Dem and the Height of Ambiguity of Sentinel-1: IGARSS 2019 - 2019 IEEE International Geoscience and Remote Sensing Symposium, Yokohama, Japan, 4p.,doi: 10.1109/IGARSS.2019.8899305.
- Toniolo, H., Stutzke, J., Lai, A., Youcha, E., 2017, Antecedent Conditions and Damage Caused by 2015 Spring Flooding on the Sagavanirktok River, Alaska: Journal of Cold Regions Engineering, v. 32, no. 2., 19 p., doi: 10.1061/(ASCE)CR.1943-5495.0000127.
- Uys, D., 2016, InSAR: an introduction, Australian Society of Exploration Geophysics, 7 p., doi: 10.1071/PVv2016n182p43.
- Wainwright, H.M., Dafflot, B., Smith, L.J., Hahn, M.S., Curtis, J.B., Wu, Y., Ulrich, C., Person, J.E., Torn, M.S., Hubbard, S.S., 2015, Identifying multiscale zonation and assessing the relative importance of polygon geomorphology on carbon fluxes in an Arctic tundra ecosystem: Journal of Geophysical Research: Biogeosciences, vol. 120, p. 788–808.
- Walker, D.A., Reynolds, M.K., Buchhorn, M., Peirce, J.L., 2014, Landscape and permafrost change in the Prudhoe Bay Oilfield, Alaska. Alaska Geobotany Center, University of Alaska, AGC Publication 14-01, Fairbanks, AK.
- Walvoord, M. A. and Kurylyk, B. L., 2016, Hydrologic Impacts of Thawing Permafrost – A Review, Vadose Zone Journal, v. 15, p. 1–20, doi:10.2136/vzj2016.01.0010.
- Wanty, R.B., Wang, B., Vohden, J., Day, W.C., and Gough, L.P., 2007, Aufeis Accumulations in Stream Bottoms in Arctic and Subarctic Environments as a Possible Indicator of Geologic Structure, U.S. Geological Survey Scientific Investigations Report 2007–5289–F, 14 p.
- Werner, C., Wegmüller, U., Strozzi, T., and Wiesmann, A., 2000, GAMMA Sar And Interferometric Processing Software, presented at the 2000 ENVISAT Symposium, Gothenburg, Sweden, 16-20 Oct.

- Werninghaus, R., 2004, TerraSAR-X mission: SAR Image Analysis, Modeling, and Techniques VI, vol. 5236, doi: <https://doi.org/10.1117/12.511500>.
- Wilkins, B.B., 2004, Water Research and Service in Wilkins, B.B., Browsing science research at the federal level in Canada: history, research activities and publications: Toronto: University of Toronto p. 509-590.
- Williams, J.R., 1970, Ground Water in the Permafrost Regions of Alaska: U.S. Geological Survey Professional Paper 696, 93 p.
- Woodhouse, L.H., 2015, Synthetic Aperture Radar (SAR): Introduction to Microwave Remote Sensing, Linlithgow, United Kingdom, Speckled Press, 391 p.
- Zebker, H.A., and Goldstein, R.M., 1986, Topographic mapping from interferometric synthetic aperture radar observations, *Journal of Geophysical Research*, Vol. 91, no. B5, p. 4993-4999, doi: 10.1029/JB091iB05p04993.
- Zufelt, J., Daly, S.F., 2012, Aufeis formation and remediation *in* Proceedings of the 15th International Conference on Cold Regions Engineering, Vol. 1, Quebec, Canada, August 19-22.